

Advances in Civil Engineering

Modern Solutions to Civil Engineering Problems Based on Soft Computing Techniques

Lead Guest Editor: Afaq Ahmad

Guest Editors: Vagelis Plevris and Abdul Razzaq Ghumman





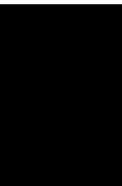
**Modern Solutions to Civil Engineering
Problems Based on Soft Computing
Techniques**

Advances in Civil Engineering

**Modern Solutions to Civil Engineering
Problems Based on Soft Computing
Techniques**

Lead Guest Editor: Afaq Ahmad

Guest Editors: Vagelis Plevris and Abdul Razzaq
Ghumman



Copyright © 2022 Hindawi Limited. All rights reserved.

This is a special issue published in "Advances in Civil Engineering." All articles are open access articles distributed under the Creative Commons Attribution License, which permits unrestricted use, distribution, and reproduction in any medium, provided the original work is properly cited.






Chief Editor

Cumaraswamy Vipulanandan, USA














Associate Editors

Chiara Bedon , Italy
Constantin Chalioris , Greece
Ghassan Chehab , Lebanon
Ottavia Corbi, Italy
Mohamed ElGawady , USA
Husnain Haider , Saudi Arabia
Jian Ji , China
Jiang Jin , China
Shazim A. Memon , Kazakhstan
Hossein Moayedi , Vietnam
Sanjay Nimbalkar, Australia
Giuseppe Oliveto , Italy
Alessandro Palmeri , United Kingdom
Arnaud Perrot , France
Hugo Rodrigues , Portugal
Victor Yepes , Spain
Xianbo Zhao , Australia

Academic Editors

José A.F.O. Correia, Portugal
Glenda Abate, Italy
Khalid Abdel-Rahman , Germany
Ali Mardani Aghabaglou, Turkey
José Aguiar , Portugal
Afaq Ahmad , Pakistan
Muhammad Riaz Ahmad , Hong Kong
Hashim M.N. Al-Madani , Bahrain
Luigi Aldieri , Italy
Angelo Aloisio , Italy
Maria Cruz Alonso, Spain
Filipe Amarante dos Santos , Portugal
Serji N. Amirkhanean, USA
Eleftherios K. Anastasiou , Greece
Panagiotis Ch. Anastasopoulos , USA
Mohamed Moafak Arbili , Iraq
Farhad Aslani , Australia
Siva Avudaiappan , Chile
Ozgur BASKAN , Turkey
Adewumi Babafemi, Nigeria
Morteza Bagherpour, Turkey
Qingsheng Bai , Germany
Nicola Baldo , Italy
Daniele Baraldi , Italy

Eva Barreira , Portugal
Emilio Bastidas-Arteaga , France
Rita Bento, Portugal
Rafael Bergillos , Spain
Han-bing Bian , China
Xia Bian , China
Huseyin Bilgin , Albania
Giovanni Biondi , Italy
Hugo C. Biscaia , Portugal
Rahul Biswas , India
Edén Bojórquez , Mexico
Giosuè Boscato , Italy
Melina Bosco , Italy
Jorge Branco , Portugal
Bruno Briseghella , China
Brian M. Broderick, Ireland
Emanuele Brunesi , Italy
Quoc-Bao Bui , Vietnam
Tan-Trung Bui , France
Nicola Buratti, Italy
Gaochuang Cai, France
Gladis Camarini , Brazil
Alberto Campisano , Italy
Qi Cao, China
Qixin Cao, China
Iacopo Carnacina , Italy
Alessio Cascardi, Italy
Paolo Castaldo , Italy
Nicola Cavalagli , Italy
Liborio Cavaleri , Italy
Anush Chandrappa , United Kingdom
Wen-Shao Chang , United Kingdom
Muhammad Tariq Amin Chaudhary, Kuwait
Po-Han Chen , Taiwan
Qian Chen , China
Wei Tong Chen , Taiwan
Qixiu Cheng, Hong Kong
Zhanbo Cheng, United Kingdom
Nicholas Chileshe, Australia
Prinya Chindaprasirt , Thailand
Corrado Chisari , United Kingdom
Se Jin Choi , Republic of Korea
Heap-Yih Chong , Australia
S.H. Chu , USA
Ting-Xiang Chu , China


Zhaofei Chu , China
Wonseok Chung , Republic of Korea
Donato Ciampa , Italy
Gian Paolo Cimellaro, Italy
Francesco Colangelo, Italy
Romulus Costache , Romania
Liviu-Adrian Cotfas , Romania
Antonio Maria D'Altri, Italy
Bruno Dal Lago , Italy
Amos Darko , Hong Kong
Arka Jyoti Das , India
Dario De Domenico , Italy
Gianmarco De Felice , Italy
Stefano De Miranda , Italy
Maria T. De Risi , Italy
Tayfun Dede, Turkey
Sadik O. Degertekin , Turkey
Camelia Delcea , Romania
Cristoforo Demartino, China
Giuseppe Di Filippo , Italy
Luigi Di Sarno, Italy
Fabio Di Trapani , Italy
Aboelkasim Diab , Egypt
Thi My Dung Do, Vietnam
Giulio Dondi , Italy
Jiangfeng Dong , China
Chao Dou , China
Mario D'Aniello , Italy
Jingtao Du , China
Ahmed Elghazouli, United Kingdom
Francesco Fabbrocino , Italy
Flora Faleschini , Italy
Dingqiang Fan, Hong Kong
Xueping Fan, China
Qian Fang , China
Salar Farahmand-Tabar , Iran
Ilenia Farina, Italy
Roberto Fedele, Italy
Guang-Liang Feng , China
Luigi Fenu , Italy
Tiago Ferreira , Portugal
Marco Filippo Ferrotto, Italy
Antonio Formisano , Italy
Guoyang Fu, Australia
Stefano Galassi , Italy

Junfeng Gao , China
Meng Gao , China
Giovanni Garcea , Italy
Enrique García-Macías, Spain
Emilio García-Taengua , United Kingdom
DongDong Ge , USA
Khaled Ghaedi, Malaysia
Khaled Ghaedi , Malaysia
Gian Felice Giaccu, Italy
Agathoklis Giaralis , United Kingdom
Ravindran Gobinath, India
Rodrigo Gonçalves, Portugal
Peilin Gong , China
Belén González-Fonteboa , Spain
Salvatore Grasso , Italy
Fan Gu, USA
Erhan Güneyisi , Turkey
Esra Mete Güneyisi, Turkey
Pingye Guo , China
Ankit Gupta , India
Federico Gusella , Italy
Kemal Hacıfendioglu, Turkey
Jianyong Han , China
Song Han , China
Asad Hanif , Macau
Hadi Hasanzadehshooiili , Canada
Mostafa Fahmi Hassanein, Egypt
Amir Ahmad Hedayat , Iran
Khandaker Hossain , Canada
Zahid Hossain , USA
Chao Hou, China
Biao Hu, China
Jiang Hu , China
Xiaodong Hu, China
Lei Huang , China
Cun Hui , China
Bon-Gang Hwang, Singapore
Jijo James , India
Abbas Fadhil Jasim , Iraq
Ahad Javanmardi , China
Krishnan Prabhakan Jaya, India
Dong-Sheng Jeng , Australia
Han-Yong Jeon, Republic of Korea
Pengjiao Jia, China
Shaohua Jiang , China

MOUSTAFA KASSEM , Malaysia
Mosbeh Kaloop , Egypt
Shankar Karuppannan , Ethiopia
John Kechagias , Greece
Mohammad Khajehzadeh , Iran
Afzal Husain Khan , Saudi Arabia
Mehran Khan , Hong Kong
Manoj Khandelwal, Australia
Jin Kook Kim , Republic of Korea
Woosuk Kim , Republic of Korea
Vaclav Koci , Czech Republic
Loke Kok Foong, Vietnam
Hailing Kong , China
Leonidas Alexandros Kouris , Greece
Kyriakos Kourousis , Ireland
Moacir Kripka , Brazil
Anupam Kumar, The Netherlands
Emma La Malfa Ribolla, Czech Republic
Ali Lakirouhani , Iran
Angus C. C. Lam, China
Thanh Quang Khai Lam , Vietnam
Luciano Lamberti, Italy
Andreas Lampropoulos , United Kingdom
Raffaele Landolfo, Italy
Massimo Latour , Italy
Bang Yeon Lee , Republic of Korea
Eul-Bum Lee , Republic of Korea
Zhen Lei , Canada
Leonardo Leonetti , Italy
Chun-Qing Li , Australia
Dongsheng Li , China
Gen Li, China
Jiale Li , China
Minghui Li, China
Qingchao Li , China
Shuang Yang Li , China
Sunwei Li , Hong Kong
Yajun Li , China
Shun Liang , China
Francesco Liguori , Italy
Jae-Han Lim , Republic of Korea
Jia-Rui Lin , China
Kun Lin , China
Shibin Lin, China

Tzu-Kang Lin , Taiwan
Yu-Cheng Lin , Taiwan
Hexu Liu, USA
Jian Lin Liu , China
Xiaoli Liu , China
Xuemei Liu , Australia
Zaobao Liu , China
Zhuang-Zhuang Liu, China
Diego Lopez-Garcia , Chile
Cristiano Loss , Canada
Lyan-Ywan Lu , Taiwan
Jin Luo , USA
Yanbin Luo , China
Jianjun Ma , China
Junwei Ma , China
Tian-Shou Ma, China
Zhongguo John Ma , USA
Maria Macchiaroli, Italy
Domenico Magisano, Italy
Reza Mahinroosta, Australia
Yann Malecot , France
Prabhat Kumar Mandal , India
John Mander, USA
Iman Mansouri, Iran
André Dias Martins, Portugal
Domagoj Matesan , Croatia
Jose Matos, Portugal
Vasant Matsagar , India
Claudio Mazzotti , Italy
Ahmed Mebarki , France
Gang Mei , China
Kasim Mermerdas, Turkey
Giovanni Minafò , Italy
Masoomah Mirrashid , Iran
Abbas Mohajerani , Australia
Fadzli Mohamed Nazri , Malaysia
Fabrizio Mollaioli , Italy
Rosario Montuori , Italy
H. Naderpour , Iran
Hassan Nasir , Pakistan
Hossein Nassiraei , Iran
Satheeskumar Navaratnam , Australia
Ignacio J. Navarro , Spain
Ashish Kumar Nayak , India
Behzad Nematollahi , Australia

Chayut Ngamkhanong , Thailand
Trung Ngo, Australia
Tengfei Nian, China
Mehdi Nikoo , Canada
Youjun Ning , China
Olugbenga Timo Oladinrin , United Kingdom
Oladimeji Benedict Olalusi, South Africa
Timothy O. Olawumi , Hong Kong
Alejandro Orfila , Spain
Maurizio Orlando , Italy
Siti Aminah Osman, Malaysia
Walid Oueslati , Tunisia
SUVASH PAUL , Bangladesh
John-Paris Pantouvakis , Greece
Fabrizio Paolacci , Italy
Giuseppina Pappalardo , Italy
Fulvio Parisi , Italy
Dimitrios G. Pavlou , Norway
Daniele Pellegrini , Italy
Gatheeshgar Perampalam , United Kingdom
Daniele Perrone , Italy
Giuseppe Piccardo , Italy
Vagelis Plevris , Qatar
Andrea Pranno , Italy
Adolfo Preciado , Mexico
Chongchong Qi , China
Yu Qian, USA
Ying Qin , China
Giuseppe Quaranta , Italy
Krishanu ROY , New Zealand
Vlastimir Radonjanin, Serbia
Carlo Rainieri , Italy
Rahul V. Ralegaonkar, India
Raizal Saifulnaz Muhammad Rashid, Malaysia
Alessandro Rasulo , Italy
Chonghong Ren , China
Qing-Xin Ren, China
Dimitris Rizos , USA
Geoffrey W. Rodgers , New Zealand
Pier Paolo Rossi, Italy
Nicola Ruggieri , Italy
JUNLONG SHANG, Singapore




Nikhil Saboo, India
Anna Saetta, Italy
Juan Sagaseta , United Kingdom
Timo Saksala, Finland
Mostafa Salari, Canada
Ginevra Salerno , Italy
Evangelos J. Sapountzakis , Greece
Vassilis Sarhosis , United Kingdom
Navaratnarajah Sathiparan , Sri Lanka
Fabrizio Scozzese , Italy
Halil Sezen , USA
Payam Shafigh , Malaysia
M. Shahria Alam, Canada
Yi Shan, China
Hussein Sharaf, Iraq
Mostafa Sharifzadeh, Australia
Sanjay Kumar Shukla, Australia
Amir Si Larbi , France
Okan Sirin , Qatar
Piotr Smarzewski , Poland
Francesca Sollecito , Italy
Rui Song , China
Tian-Yi Song, Australia
Flavio Stochino , Italy
Mayank Sukhija , USA
Piti Sukontasukkul , Thailand
Jianping Sun, Singapore
Xiao Sun , China
T. Tafsirojjaman , Australia
Fujiao Tang , China
Patrick W.C. Tang , Australia
Zhi Cheng Tang , China
Weerachart Tangchirapat , Thailand
Xiixin Tao, China
Piergiorgio Tataranni , Italy
Elisabete Teixeira , Portugal
Jorge Iván Tobón , Colombia
Jing-Zhong Tong, China
Francesco Trentadue , Italy
Antonello Troncone, Italy
Majbah Uddin , USA
Tariq Umar , United Kingdom
Muahmmad Usman, United Kingdom
Muhammad Usman , Pakistan
Mucteba Uysal , Turkey

Ilaria Venanzi , Italy
Castorina S. Vieira , Portugal
Valeria Vignali , Italy
Claudia Vitone , Italy
Liwei WEN , China
Chunfeng Wan , China
Hua-Ping Wan, China
Roman Wan-Wendner , Austria
Chaohui Wang , China
Hao Wang , USA
Shiming Wang , China
Wayne Yu Wang , United Kingdom
Wen-Da Wang, China
Xing Wang , China
Xiuling Wang , China
Zhenjun Wang , China
Xin-Jiang Wei , China
Tao Wen , China
Weiping Wen , China
Lei Weng , China
Chao Wu , United Kingdom
Jiangyu Wu, China
Wangjie Wu , China
Wenbing Wu , China
Zhixing Xiao, China
Gang Xu, China
Jian Xu , China
Panpan , China
Rongchao Xu , China
HE YONGLIANG, China
Michael Yam, Hong Kong
Hailu Yang , China
Xu-Xu Yang , China
Hui Yao , China
Xinyu Ye , China
Zhoujing Ye, China
Gürol Yildirim , Turkey
Dawei Yin , China
Doo-Yeol Yoo , Republic of Korea
Zhanping You , USA
Afshar A. Yousefi , Iran
Xinbao Yu , USA
Dongdong Yuan , China
Geun Y. Yun , Republic of Korea


Hyun-Do Yun , Republic of Korea
Cemal YİĞİT , Turkey
Paolo Zampieri, Italy
Giulio Zani , Italy
Mariano Angelo Zanini , Italy
Zhixiong Zeng , Hong Kong
Mustafa Zeybek, Turkey
Henglong Zhang , China
Jiupeng Zhang, China
Tingting Zhang , China
Zengping Zhang, China
Zetian Zhang , China
Zhigang Zhang , China
Zhipeng Zhao , Japan
Jun Zhao , China
Annan Zhou , Australia
Jia-wen Zhou , China
Hai-Tao Zhu , China
Peng Zhu , China
QuanJie Zhu , China
Wenjun Zhu , China
Marco Zucca, Italy
Haoran Zuo, Australia
Junqing Zuo , China
Robert Černý , Czech Republic
Süleyman İpek , Turkey

Contents



Use of Artificial Neural Networks to Predict Wind-Induced External Pressure Coefficients on a Low-Rise Building: A Comparative Study

Josué U. Rodríguez-Alcántara , Adrián Pozos-Estrada , and Roberto Gómez-Martínez 
Research Article (14 pages), Article ID 8796384, Volume 2022 (2022)








Shear Strength Model for Reinforced Concrete Corner Joints Based on Soft Computing Techniques

Moiz Tariq , Azam Khan, Asad Ullah, Muhammad Waseem, Hassan Nasir, and Irfan Jamil
Research Article (23 pages), Article ID 7156691, Volume 2022 (2022)






Building Information Modeling and Internet of Things Integration in the Construction Industry: A Scoping Study

Baydaa Hashim Mohammed , Hasimi Sallehuddin, Nurhizam Safie, Afifuddin Husairi, Nur Azaliah Abu Bakar, Farashazillah Yahya, Ihsan Ali , and Shaymaa AbdelGhany Mohamed
Review Article (20 pages), Article ID 7886497, Volume 2022 (2022)

Simulation of Quantity and Quality of Saq Aquifer Using Artificial Intelligence and Hydraulic Models

Abdul Razzaq Ghumman , Ghufuran Ahmed Pasha , Md. Shafiquzzaman , Afaq Ahmad , Afzal Ahmed , Riaz Akhtar Khan , and Rashid Farooq 
Research Article (22 pages), Article ID 5910989, Volume 2022 (2022)

Pothole Detection Using Deep Learning: A Real-Time and AI-on-the-Edge Perspective

Muhammad Haroon Asad , Saran Khaliq , Muhammad Haroon Yousaf , Muhammad Obaid Ullah , and Afaq Ahmad 
Research Article (13 pages), Article ID 9221211, Volume 2022 (2022)


Optimization of the Operation Rule Curves for Cascade Reservoirs Using the Cuckoo Search Algorithm

Ismail Ara  and Mutlu Yasar 
Research Article (11 pages), Article ID 8463358, Volume 2022 (2022)


Machine Learning-Based Model in Predicting the Plate-End Debonding of FRP-Strengthened RC Beams in Flexure

Tianyu Hu  and Guibing Li 
Research Article (11 pages), Article ID 6069871, Volume 2022 (2022)

An Improved Model to Calculate Pullback Force of Trenchless Horizontal Directional Drilling Pipeline

Xiao-qiang Liang, Da Hu , Yong-suo Li , Xian Yang, Lei Jiang, and Yun-yi Zhang 
Research Article (13 pages), Article ID 2346098, Volume 2022 (2022)

Classical and Bayesian Estimation of the Inverse Weibull Distribution: Using Progressive Type-I Censoring Scheme

Ali Algarni, Mohammed Elgarhy , Abdullah M Almarashi, Aisha Fayomi, and Ahmed R El-Saeed
Research Article (15 pages), Article ID 5701529, Volume 2021 (2021)

Early Warning for the Construction Safety Risk of Bridge Projects Using a RS-SSA-LSSVM Model

Gang Li , Ruijiang Ran , Jun Fang , Hao Peng , and Shengmin Wang 

Research Article (14 pages), Article ID 4449451, Volume 2021 (2021)

Research Article

Use of Artificial Neural Networks to Predict Wind-Induced External Pressure Coefficients on a Low-Rise Building: A Comparative Study

Josué U. Rodríguez-Alcántara , Adrián Pozos-Estrada ,
and Roberto Gómez-Martínez 

Instituto de Ingeniería, UNAM, Mexico City 04510, Mexico

Correspondence should be addressed to Adrián Pozos-Estrada; apozose@iingen.unam.mx

Received 2 March 2022; Accepted 12 August 2022; Published 5 September 2022

Academic Editor: Hossein Nassiraei

Copyright © 2022 Josué U. Rodríguez-Alcántara et al. This is an open access article distributed under the Creative Commons Attribution License, which permits unrestricted use, distribution, and reproduction in any medium, provided the original work is properly cited.

Wind flow on a bluff body is a complex and nonlinear phenomenon that has been mainly studied experimentally or analytically. Several mathematical methods have been developed to predict the wind-induced pressure distribution on bluff bodies; however, most of them result unpractical due to the mathematical complexity required. Long-short term memory artificial neural networks with deep learning have proven to be efficient tools in the solution of nonlinear phenomena, although the choice of a more efficient network model remains a topic of open discussion for researchers. The main objective of this study is to develop long-short term memory artificial neural network models to predict the external pressure distribution of a low-rise building. For the development of the artificial neural network models, the multilayer perceptron and the recurrent neural network were also employed for comparison purposes. To train the artificial neural networks, a database with the external pressure coefficients from boundary layer wind tunnel tests of a low-rise building is employed. The analysis results indicate that the long-short term memory artificial neural network model and the multilayer perceptron neural network outperform the recurrent neural network.

1. Introduction

The study of wind effects on low-rise buildings is carried out by using the wind-induced pressure distribution over the structure. This pressure distribution can be calculated from experimental wind tunnel tests [1] or by using computational wind engineering [2]. Based on the pressure distribution, international wind design codes and standards propose the use of external pressure coefficients (EPC) in order to calculate the wind-induced forces.

The prediction of EPC due to the incidence of wind on bluff bodies has been an important topic for researchers in the last decades. In particular, the study of the pressure distribution near the edges of the structure, since wind effects are often characterized as a nonlinear problem in these areas [3–5].

Database-assisted design (DAD) has been proposed for the design and revision of buildings under wind loads [6–9]. In

a DAD, aerodynamic information from experimental wind tunnel tests has been used; however, the scarce information on representative building models has been an obstacle to using it. Recently, researchers have developed and applied complex mathematical models to characterize or simulate the turbulent flow of wind within an environment with certain characteristics of natural roughness [10–14]. Other studies that include novel methodologies are those by Wan et al., [15] where a model based on support vector machine regression (SVR) and kernel ridge regression (KRR) was used to predict wind speed records; Wan et al. [16] developed a new universal power law based in the use of a wavelet multi-scale transform algorithm to predict wind speed; Li et al. [17] used a least-squares support-vector machine (LSSVM) model with parameter optimization to forecast wind speed; Pang et al. [18] propose a novel intelligence algorithm for airfoil design based on the combination of low wind field, considering the effects of

surface roughness on the lift coefficient and the lift-to-drag ratio of the airfoil, the instability of wind speed, and wind direction to ensure gentle stalling characteristics, and the stable power generation of wind turbines.

Recently, artificial neural networks (ANNs) offer a great advantage over complex mathematical models used in the prediction of nonlinear phenomena. The skill to simulate the role of a human brain gives ANN models the capability to solve problems from a database, combining and adapting to the conditions and changes of different input variables to find a generalized solution. Recent studies have shown the versatility and usefulness of ANN models, for example, Shaquid et al. [19] employed an ANN model to investigate a reliability model centered on the exponentiated Weibull distribution and the inverse power-law model. Moreover, Shaquid et al. [20] demonstrated that ANNs are an excellent engineering tool for predicting survival and mortality rates.

Some researchers have shown that the feed-forward neural network (FFNN) can be used to interpolate pressure coefficients for low-rise buildings [21, 22] or wind-induced pressure time series [23]. FFNNs have also been employed to predict wind-induced pressure on roofs of low-rise buildings in an efficient way [24, 25] and to estimate the dynamic along-wind response of tall buildings using ANNs as an alternative to wind tunnel tests [26, 27]. More recently, Çolak [28] employed an FFNN model to study the thermal conductivity of water-based zirconium oxide nanofluid and showed its ability to make predictions with a low margin of error.

Other studies have employed recurrent neural networks (RNN) for the study of dynamic problems, where the results obtained with the RNN outperform those obtained with the FFNN [29, 30]. It is noted that the use of RNNs in solutions of wind speed or pressure problems on structures is scarce in the literature. Likewise, in recent years, deep learning in ANNs has gained more attention for works with sequences and time series [31, 32], data for classification and regression tasks for language modeling [33, 34], speech recognition and video analysis [35, 36] with the employ of long-short term memory (LSTM) ANN; however, similar to the case of RNNs, the use of LSTM ANNs in the prediction of EPC is scarce in the literature.

In this study, a comparison of the prediction of EPC on a low-rise building by using the FFNN, RNN, and LSTM ANN models with different types of architectures is carried out. For the analyses, a database with EPC from boundary layer wind tunnel tests of a low-rise building is employed for training, validation, and testing of the ANN models. With the purpose of making this study self-contained, in the following section some basic concepts of ANNs are presented.

2. Basic Concepts of ANNs

An ANN is a tool designed primarily to mathematically model the internal architecture and operational characteristics of the human brain and nervous system, consisting of

three types of interconnected layers. The first and last layers are called input and output layers, respectively, and all other layers between the input and output layers are called hidden layers. Each layer has a certain number of artificial neurons, each connection neuron has a synaptic weight, and each layer has an activation function responsible for processing the data that the system must recognize. Moreover, each neuron has an activation value that is a function of the sum of the inputs received by other neurons, and that is multiplied by the corresponding synaptic weights of each connection.

The number of hidden layers and hidden neurons in each layer depends on several parameters, such as the complexity of the problem to be solved, the architecture of the network, the training algorithm, and the number of training cases. Throughout the development of artificial intelligence, rules have been proposed to choose the number of hidden layers and neurons [37, 38]; however, a unified procedure is still not available for all the possible cases considered. Up to date, one of the methods usually employed to identify the optimum ANN model is to vary the number of hidden layers and neurons, estimate the mean squared error (MSE), and choose the ANN with the minimum MSE as the optimal one, this method is called “Test and Error” [39] and has been extensively used in several ANN applications [40, 41].

ANN modeling usually involves three stages: training, validation, and testing. In the training stage, neurons are trained by a random input pattern to obtain a desired result. Training consists of optimizing the synaptic connection weights and modifying them after each iteration cycle until a minimum MSE is achieved. In the validation stage, optimized weights and biases are used to produce their associated output. Normally, the inputs used in the validation stage are associated with known outputs and additional comparisons of the MSE are carried out. In the testing stage, input scenarios are used to evaluate the prediction ability of the trained ANN models.

2.1. The FFNN Model. In the FFNN model, connections and data flow are unidirectional, from the input layer to the output layer, without transmission of information between neurons located in the same or previous layer. The FFNN model has been used to solve dynamic problems; however, this type of ANN does not offer any retention of information, making it less effective than the RNN to solve certain types of problems [42]. An FFNN has one of the simplest architectures for training and getting good results for static problems where the behavior of the values to be predicted does not depend on time.

If an ANN model with a single output neuron and two hidden layers are considered, the mathematical expression that relates the output neuron in the output layer with the neurons in the input and hidden layers is given by the following equation [43]:

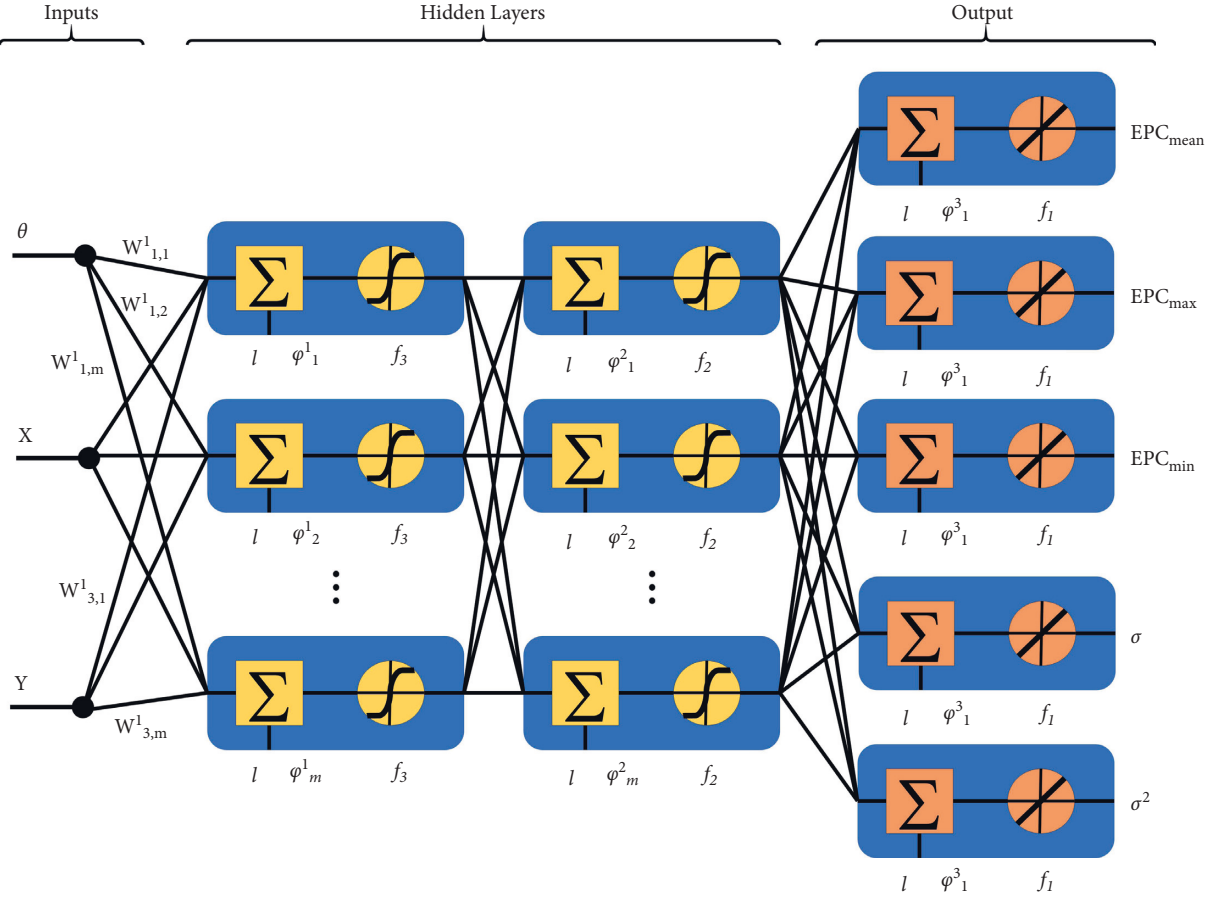


FIGURE 1: FFNN architecture with two hidden layers.

$$Y_{\text{Output}} = f_1 \left(\sum_{k=1}^m \left([W_3]_{k,1} f_2 \left(\sum_{j=1}^m \left([W_2]_{j,k} f_3 \left(\sum_{i=1}^n ([W_1]_{i,j} x_i) + (\varphi_1)_j \right) \right) + (\varphi_2)_k \right) \right) + (\varphi_3)_1 \right), \quad (1)$$

where n is the total number of input neurons; m is the total number of neurons in each hidden layer; x_i is the i -th neuron of the input layer; $[W_1]_{i,j}$ is the matrix of synaptic weights that optimize the connection between the input layer and the first hidden layer; $[W_2]_{j,k}$ is the matrix of synaptic weights that optimize the connection between the first and second hidden layers; $[W_3]_{k,1}$ is the matrix of synaptic weights that optimize the connection between the second hidden layer and the output layer; $(\varphi_1)_j$ is the vector associated with the results of the first hidden layer; $(\varphi_2)_k$ is the vector associated with the results of the second hidden layer; $(\varphi_3)_1$ is the vector associated with the results of the output layer; $f_3(\bullet)$ and $f_2(\bullet)$ are each a Hyperbolic Sigmoid Tangent activation function used between input and hidden layers and within the hidden layers; and $f_1(\bullet)$ is a Linear activation function used between the second hidden layer and the output layer. Figure 1 presents the architecture of the FFNN model used in this study.

2.2. The RNN Model. RNNs employ feedforward and feedback connections, the latter refers to the information that can be interchanged between neurons that are in the

same or previous layers and subsequent layers, this type of connection gives them an advantage over the FFNNs when it comes to identifying and controlling a dynamic problem [44]. The RNN is mainly composed of three layers (Figure 2), the first one is the input layer with two types of neurons: the external input neurons (x_i) responsible for feeding the RNN with external information, and the internal input neurons or context units (o_r), which receive information from the neurons of the hidden layers (recurrent information). The function of the context units is to store knowledge generated by the network in each iteration, this knowledge will replace the external input to achieve the appropriate adjustment of the trained model; this ability provides the advantage of solving problems where the variable is changing over time. In the hidden layer, the combination of x_i and o_r is carried out by considering their corresponding synaptic weight matrix (w_{ij}) and recurrent synaptic weight matrix (w_{rj}). Finally, the output of the hidden layer (O_j) is obtained by applying the activation function $f(\bullet)$ to the combination. Equation (2) mathematically summarizes the calculation of O_j [43] as follows:

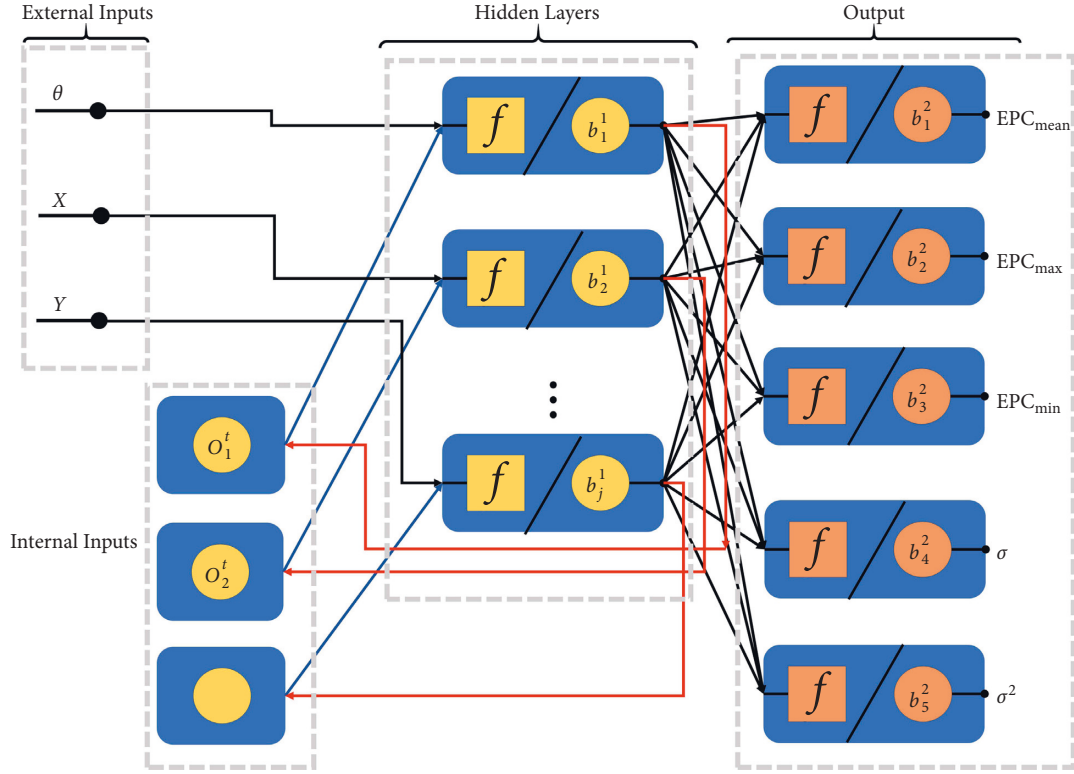


FIGURE 2: Recurrent neural network (RNN) architecture used. For simplicity, the synaptic weights between input layer (external and internal) and hidden layer have been omitted.

$$O_j = f\left(\sum_{i=1}^N x_i w_{ij} + \sum_{r=1}^R O_r w_{rj}\right), \quad (2)$$

where N is the total number of external neurons, and R is the total number of internal neurons.

The output of the hidden layer, O_j , becomes the internal input (O_r) for the next time step t , according to the following equation [43]:

$$O_r^t = O_j^{t-1}. \quad (3)$$

Finally, the output or solution from the RNN is obtained by using the following equation [43]:

$$O_k = g\left(\sum_{j=1}^J O_r w_{jk}\right), \quad (4)$$

where w_{jk} is a synaptic weight matrix, g is a linear activation function, J is the total number of hidden neurons, and k is the number of outputs.

2.3. The LSTM ANN Model. This kind of ANN model uses backpropagation through the time training algorithm [45] and deep learning in order to reduce the short-term dependencies that are generated due to the decrease in gradient, while the information from each step declines [46–48]. This network aims to reach a generalized solution to the problem. Such is done by overcoming the setbacks of the

declined gradients, selecting the information by filters or gates; thus, relevant information is retained, whereas irrelevant information is forgotten. Reduced vulnerability in time steps makes LSTM ANN better for data stream treatment compared to FFNN and conventional RNN models.

The general architecture of this kind of ANN is illustrated in Figure 3(a), where the main components of an LSTM ANN are shown. The input vectors that feed the LSTM ANN are also included in Figure 3(a). The h_t and c_t variables denote the hidden outputs or states, and the state of the cell in time t , respectively.

The network arrangement will have as many LSTM blocks as the number of time steps that need to be analyzed. Each block uses a predefined number of hidden units that will process the information within them.

The expression given in equation (5) is used for the calculation of the cell state (c_t) in the time step t [49].

$$c_t = f_t c_{t-1} + i_t g_t, \quad (5)$$

where c_{t-1} is the initial cell state, g_t is the memory cell, i_t is the input gate, and f_t is the forget gate. The expressions to calculate g_t , i_t , and f_t are given, respectively, by the following equations [49]:

$$g_t = \sigma_c(W_g x_t + R_g h_{t-1} + b_g), \quad (6)$$

$$i_t = \sigma_g(W_i x_t + R_i h_{t-1} + b_i), \quad (7)$$

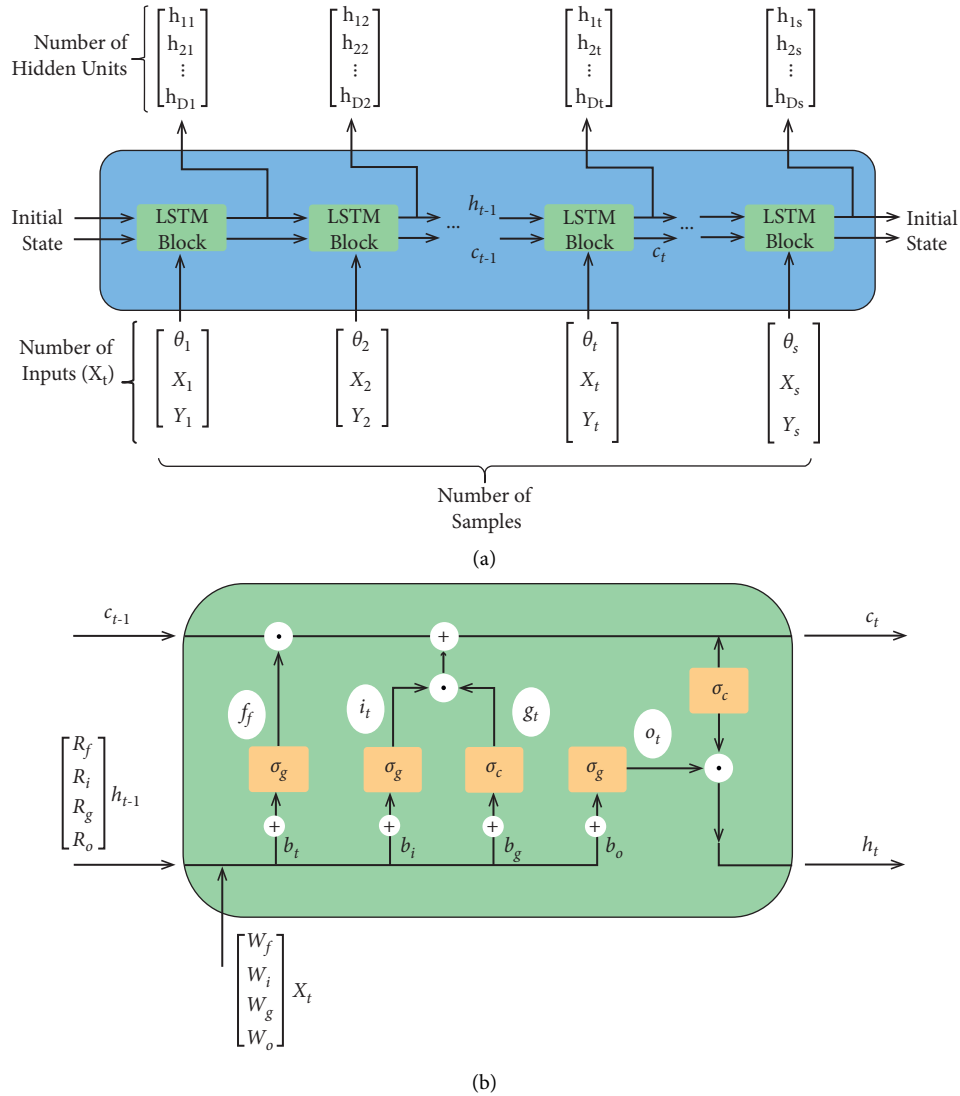


FIGURE 3: LSTM ANN: (a) architecture; (b) LSTM block.

$$f_t = \sigma_g(W_f x_t + R_f h_{t-1} + b_f), \quad (8)$$

where $W_g, W_i,$ and W_f are the synaptic weights matrices by cell state, input gate, and forget gate, respectively; $R_g, R_i,$ and R_f are the recurrent synaptic weights matrices by cell state, input gate, and forget gate, respectively; $b_g, b_i,$ and b_f are the biases by cell state, input gate, and forget gate, respectively; x_t is the signal data associated with the database time step t , and h_{t-1} is the previous hidden output or state.

In the case of h_t , it will be updated according to the following equation (49):

$$h_t = o_t \sigma_c(c_t), \quad (9)$$

where o_t is the output gate given by the following equation [49]:

$$o_t = \sigma_g(W_o x_t + R_o h_{t-1} + b_o), \quad (10)$$

where $W_o, R_o,$ and b_o are the synaptic weights matrix, the recurrent synaptic weights matrix, and biases of the output gate, respectively; h_{t-1} is the previous network status; x_t is the signal data associated with time step t . In equations (7), (8), and (10), σ_g denotes the gate activation function, and in equations (6) and (9), σ_c denotes the state activation function.

The status of each block depends on h_t , which contains the output of the LSTM block for the appropriate time step t , and the state of c_t , which contains the knowledge from previous time steps. Internally, at each block and at each time step, cell state information is added or removed by controlling gates (Figure 3(b)).

More specifically, the forget gate is used to control the volume of information that will be discarded from past time steps selecting the value of the vector f_t , if the result of the function is close to 1, the information stored by the state of the cell is retained; however, when the function value is close to 0, the cell state will discard the information.

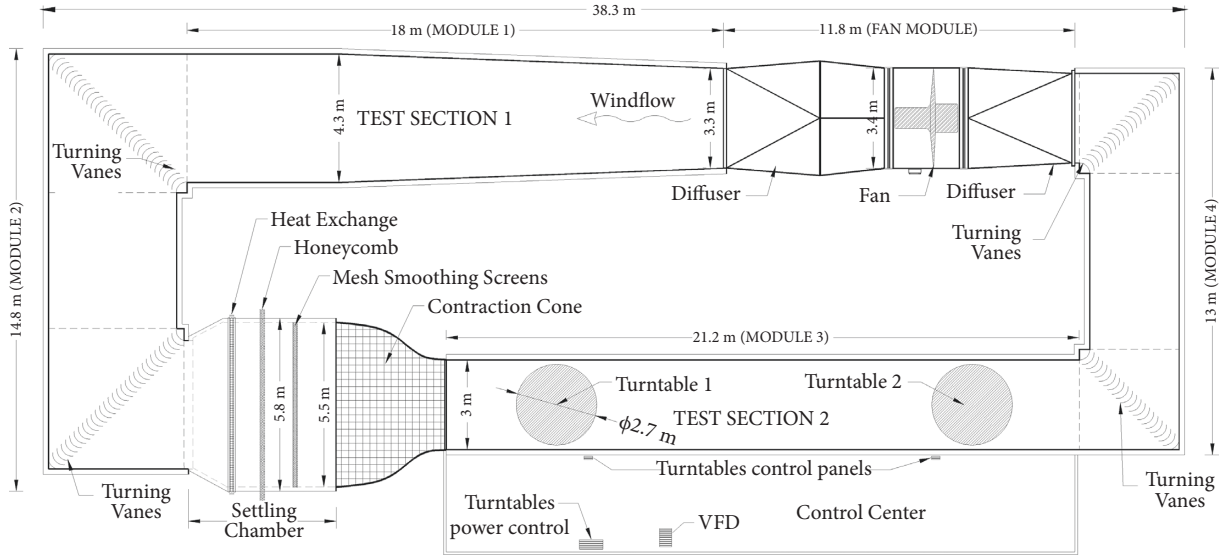


FIGURE 4: Sketch of the boundary layer wind tunnel of institute of engineering, UNAM.

In this way, the current memory g_t and the long-term memory c_{t-1} are combined in the LSTM, resulting in a new cellular state c_t . The information contained at a predefined time can be preserved by the control of the forget gate f_b , while the current inessential information is removed from memory by the control of the input gate i_t . The output gate o_t is configured to control the amount of memory information to update at the next time step, similar to the input gate calculation.

3. Analysis Procedure

3.1. Experimental Input and Output Parameters. To assemble the experimental database of wind-induced EPC of a generic low-rise building, wind tunnel tests at the boundary layer wind tunnel (BLWT) of the National Autonomous University of Mexico (UNAM for its acronym in Spanish) were carried out. The UNAM BLWT is of the closed-circuit type and is composed of four modules that form a rectangular configuration in plan (Figure 4). Modules 1 and 3 are approximately 38 m long, whereas modules 2 and 4 are 13.9 and 12.6 m long, respectively. Module 3 is the module for replicating the atmospheric boundary layer (ABL), it is 3 m wide, and the height ranges from 2 m at the contraction cone exit to 2.35 m behind the second turntable. The length of the test section permits the placement of roughness elements and turbulence generators to adequately characterize the ABL and turbulence intensity profile for a predefined terrain category [50]. All the experimental tests were carried out in Module 3. A complete description of the BLWT employed for the experimental tests can be found in Amaya-Gallardo et al. [51].

For the wind simulation, a wind speed scale of 1 : 2.3 was selected. The reference wind speed for testing was obtained from the Mexican wind standard for an urban terrain category. For the simulation of the mean wind profile and

turbulence characteristics, a passive turbulence generator was installed in Test Section 2, which consisted of roughness elements, a castellated barrier, and spines (Figure 5). A total of 27 measures of wind speed at different heights were obtained by using a digital hot-wire anemometer. These measurements were used to determine the mean wind speed profile and turbulence indicators (i.e., turbulence profile and power spectral density function (PSDF)). Figure 6(a) shows a comparison of the experimental mean wind velocity (U_x) profile with the classical theoretical power law (POW) adopted by several international wind design codes. Also, in Figure 6(b), the turbulence intensity profile is shown. The mathematical expressions that defined the power-law mean wind velocity profile and longitudinal turbulence intensity are defined, respectively, as [52]:

$$U_x = \bar{U}_{\text{ref}} \left(\frac{z}{z_{\text{ref}}} \right)^{\alpha} I_{U_x} = \frac{\sigma_U}{U_x}, \quad (11)$$

where α is the power law exponent, \bar{U}_{ref} is a reference mean wind velocity, z_{ref} a reference height, in this work considered as 0.2 m (which is equivalent to 10 m above ground in full scale), and σ_U is the standard deviation of the longitudinal turbulence wind component.

To determine the experimental power-law exponent α , a fitting exercise based on the least square method was carried out, resulting in a value of $\alpha = 0.295$ (urban terrain category). Furthermore, it is observed in Figure 6(b) that the longitudinal turbulence intensity values range from about 25% near the wind tunnel floor level, up to 8% in the upper part of the longitudinal turbulence profile. To further evaluate the turbulence simulated in the wind tunnel, Figure 7 presents the PSDF of the longitudinal turbulence component and its comparison with the Von Karman Spectrum, which is considered a suitable representation of the velocity spectrum [52] and is given by the following equation:

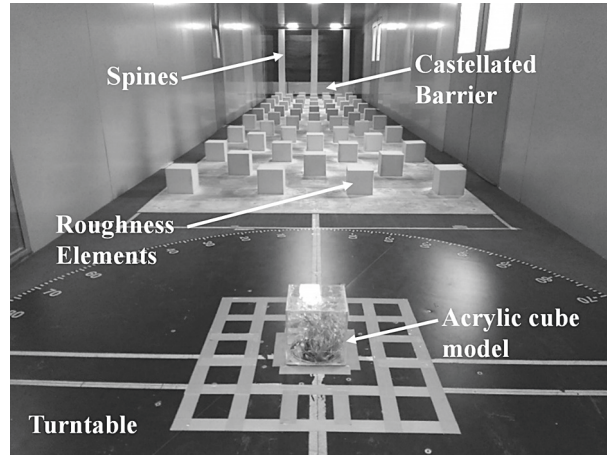


FIGURE 5: Wind tunnel set-up and passive turbulence generator.

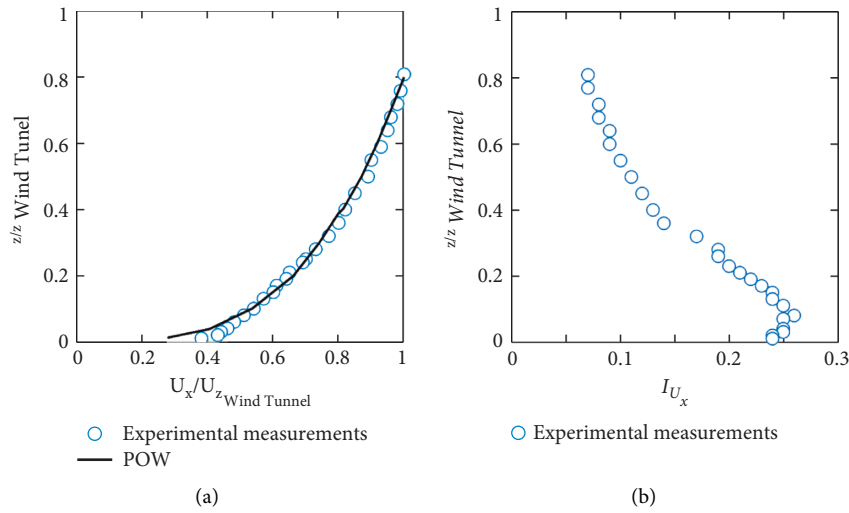


FIGURE 6: Longitudinal wind profiles: (a) mean wind speed; (b) turbulence intensity.

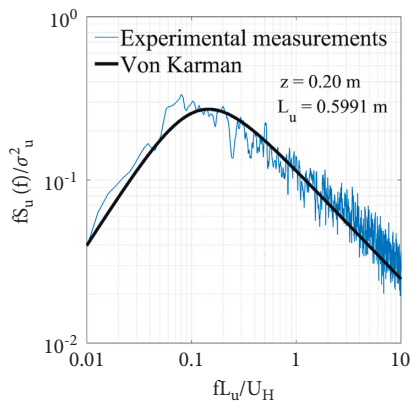


FIGURE 7: Comparison of experimental PSDF and von karman PSDF.

$$\frac{fS_u(f)}{\sigma_u^2} = \frac{4fL_u/U_x}{[1 + 70.8(fL_u/U_x)^2]^{5/6}}, \quad (12)$$

where f is frequency, L_U is the turbulence integral length scale in the longitudinal direction, S_U is the power spectral density of the fluctuating wind component. Figure 7 presents a comparison of the normalized PSDF obtained at $z = 0.2$ m and the Von Karman Spectrum. It is observed in Figure 7 a good comparison of the experimental and theoretical PSDFs.

The parameters used as input neurons for the FFNN and RNN models were θ , as well as the x - and y -coordinates of each tap. The output neurons were EPCmean, PCmax, EPCmin, σ , and σ^2 . For the LSTM ANN model, input vectors containing the coordinates (x, y) of the taps and predefined θ values were used, and the output neurons were the same as those for the FFNN and RNN models.

3.2. ANN Data Sets and Training. For the ANN training, a subset of the experimental database was used, where 75% of the data were randomly selected and employed to train, while the remaining 25% of the data were used as a first validation set to monitor the training process to avoid overtraining. A second validation set was used to identify the optimum ANN models. With the optimum ANN models,

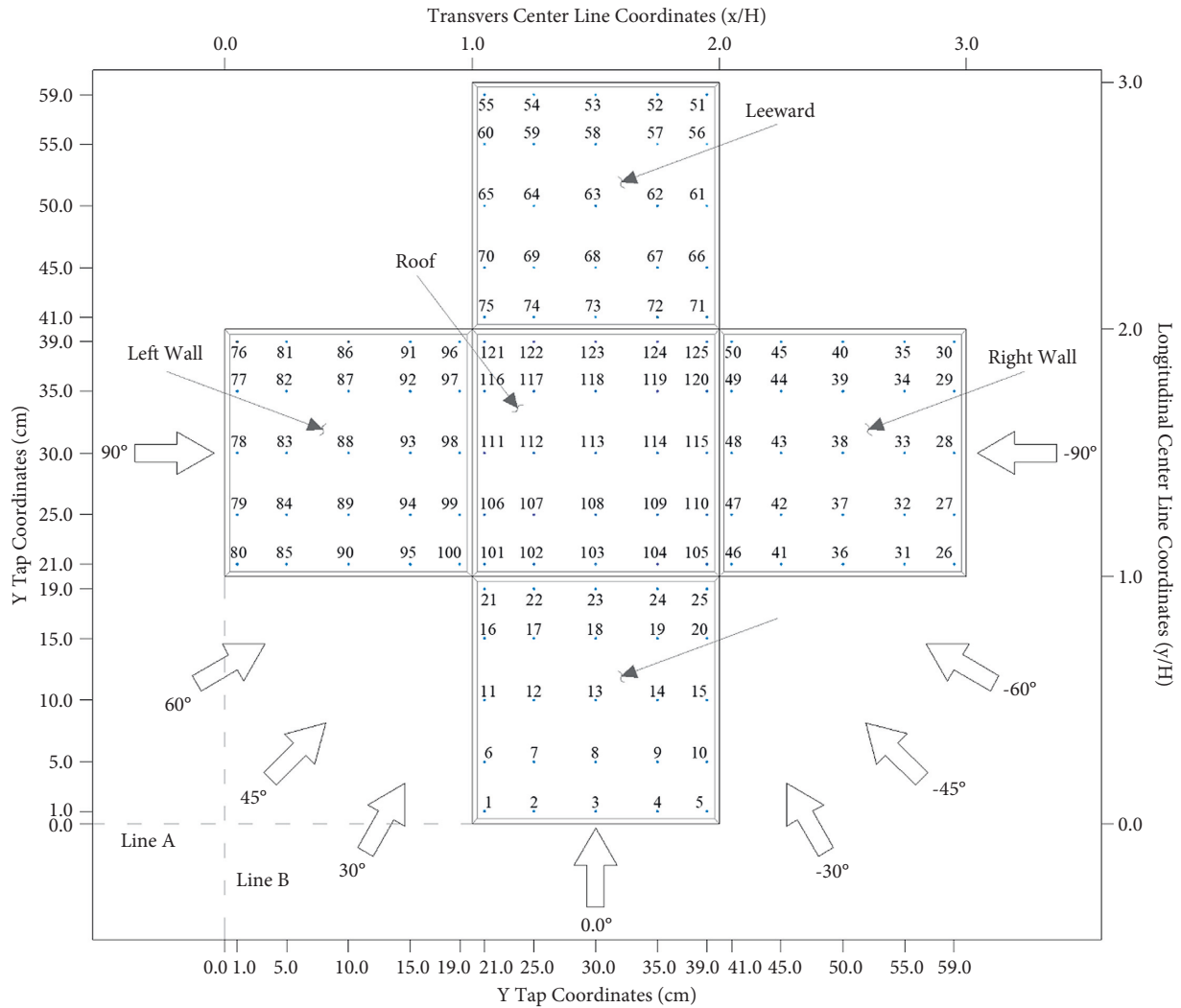


FIGURE 8: Coordinates of the taps located in the low-rise building tested in wind tunnel and wind directions.

TABLE 1: Training, validation, and test data.

Subsets	Wind direction (°)					
Training set ¹	-90.0	-45.0	0.0	45.0	90.0	—
Validation set ²	-60.0	-30.0	30.0	60.0	—	—
Testing set	-80.0	-70.0	-50.0	-40.0	-20.0	-10.0
	80.0	70.0	50.0	40.0	20.0	10.0

Note. 1) For this set, 75% was used for training and 25% for the first validation; 2) Second validation set.

case scenarios were evaluated with a testing set. The training, first, and second validation, as well as test subsets, are summarized in Table 1.

For the development of FFNNs, models with one and two hidden layers with 3 to 50 hidden neurons per hidden layer, and the sigmoidal hyperbolic tangent and linear activation functions were considered. The variation of hidden layers and neurons is with the aim of avoiding the lack of learning and the inability of predicting outcomes for the scenarios that are not used in training (i.e., overfitting).

One of the algorithms used to train the FFNN is the back-propagation [54], where the error is propagated backward by adjusting the weights from the output to the

input layer. For training the FFNN models, the following steps were followed:

- (1) Provide the ANN model with sample inputs and known outputs;
- (2) Evaluate an error function in terms of the difference between the predicted and observed output;
- (3) Minimize the error function (MSE) by adjusting the weights and biases of all the layers from the output to the input layer.

In order to evaluate the impact of using different types of minimization algorithms on the prediction effectiveness of the

TABLE 2: Best FFNN models identified in the validation stage with 1 and 2 hidden layers.

Training algorithm	MSE		ρ	
	1HL	2HL	1HL	2HL
L-M	0.345 (30)	0.210 (20)	0.947	0.968
BR	0.246 (50)	0.227 (10)	0.967	0.960
BFGS	0.434 (50)	0.280 (50)	0.929	0.961
VLRGD	0.676 (15)	0.799 (25)	0.853	0.841
GDM	0.966 (5)	0.768 (40)	0.814	0.855
GD	0.867 (15)	0.799 (30)	0.817	0.853

1HL = 1 hidden layer; 2HL = 2 hidden layers. The values inside brackets indicate the number of hidden neurons.

TABLE 3: Best RNN models identified in the validation stage with 1, 2, and 3 delays.

Training algorithm	MSE			ρ		
	1D	2D	3D	1D	2D	3D
BFGS	0.607 (11)	0.662 (11)	0.674 (7)	0.341	0.320	0.333
BR	0.671 (11)	0.790 (11)	0.858 (7)	0.335	0.306	0.325
GD	0.699 (11)	0.894 (7)	0.941 (11)	0.309	0.302	0.296
VLRGD	0.765 (8)	0.791 (6)	0.850 (4)	0.321	0.308	0.310
GDM	0.774 (7)	0.815 (11)	0.804 (10)	0.701	0.692	0.319
L-M	0.777 (6)	0.727 (7)	0.847 (2)	0.334	0.325	0.302

1D = 1 delay; 2D = 2 delays; 3D = 3 delays. The values inside brackets indicate the number of hidden neurons.

FFNN models, the minimization of the MSE was carried out using the following algorithms [54]: Gradient Descent (GD), Gradient Descent with Momentum (GDM), Variable Learning Rate Gradient Descent (VLRGD), Levenberg-Marquardt (L-M), BFGS Quasi-Newton (BFGS), and Bayesian Regularization (BR).

In the case of the RNN, models with 1 to 3 delays, and with two groups of hidden neurons were considered. The first group includes 3, 5, 10, 15, 20, 25, 30, 40, and 50 hidden neurons, while the second group includes 2, 4, 6, 7, 8, 9, and 11 hidden neurons. The second group was included to evaluate with more precision the use of a small number of hidden neurons compared to the first group.

For the training of the RNN, the same steps followed for the training of the FFNN were adopted, except that the internal input neurons are also included in the minimization procedure by adjusting the recurrent synaptic weight matrix and biases of all the layers from the output to the input layer.

To develop the LSTM ANN models, a regression LSTM network with sequence output where the targets are the training sequences with values shifted over a time step was used. To create an LSTM regression network architecture, the next steps were followed:

- (1) Determine a sequence input layer that has an input size that matches the number of channels of the input data. In this case 3 inputs data.
- (2) Define the number of hidden units in each LSTM block. For the LSTM ANN models, each LSTM block considered 100, 200, 300, 400, and 500 hidden units.
- (3) Include a fully connected layer with an output size that matches the number of channels of the output targets.
- (4) Include a regression layer.

TABLE 4: Best LSTM NN models identified in the validation stage with ADAM training algorithm and a batch equal to 30.

HU	MSE	ρ
400	0.022	0.982
300	0.023	0.981
100	0.032	0.977
500	0.069	0.982
200	0.073	0.982

HU = Hidden unit.

For the training of the LSTM ANN, the algorithm used was the Adaptive Moment Estimation (ADAM) optimizer, which is an adaptive learning rate method. An ADAM optimizer is a stochastic gradient descent for use in Deep Learning on non-convex optimization problems.

4. Analysis Results and Discussion

4.1. Identification of the Best ANN Models. To evaluate the impact of record selection on the trained ANN models, a total of 100 trials were carried out. For each trial, a new set of randomly selected values (75% of the data used for training) were used. The second validation set was used to identify the best ANN models. Tables 2 and 3 summarize the results obtained from the best ANN models identified (i.e., the ANN models with the smallest MSE) for the FFNN and RNN, respectively, while Table 4 presents the best models identified for the LSTM ANN. Also, in Tables 2-4, the correlation coefficient (ρ) between the predicted and the actual values are included.

It is observed in Table 2, that for the FFNN models, the optimum number of neurons and hidden layers that provide the lowest MSE for the trained model depends on the selected data. It is also observed that, in general, the optimum

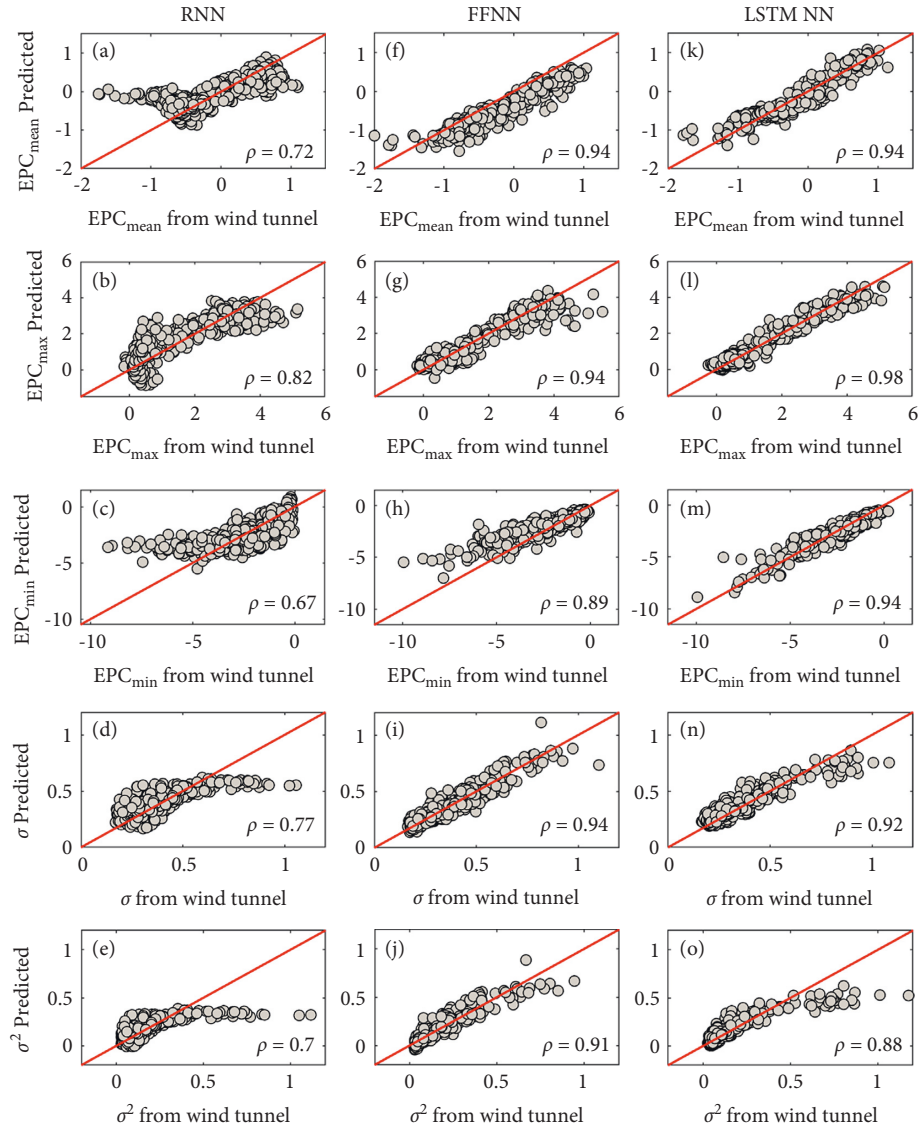


FIGURE 9: Comparison of the EPC_{mean} , EPC_{max} , EPC_{min} , σ , and σ^2 values predicted by the trained ANN models and the second validation set and those obtained from wind tunnel tests: (a), (b), (c), (d), (e) RNN; (f), (g), (h), (i), (j) FFNN; (k), (l), (m), (n), (o) LSTM NN. The red line indicates the ideal fit.

number of neurons is greater than 10, and that the 2-hidden-layers models outperform those of 1 hidden layer. The minimum MSE and maximum ρ are associated with the L-M training algorithm, although the BR and BFGS produce comparable results to those obtained with the L-M algorithm. Based on these observations, the use of 20 neurons and the ANN model with 2 hidden layers is selected for the prediction of EPC_{mean} , EPC_{max} , EPC_{min} , σ , and σ^2 values, with associated values of MSE and ρ equal to 0.210 and 0.968, respectively.

The results summarized in Table 3 for RNN models indicate that the optimum number of neurons and the optimum number of delays also depend on the selected data. The optimum number of neurons is between 2 and 11. The RNN models with 1 delay outperform those with 2 and 3 delays. The minimum MSE and maximum ρ are associated with the BFGS training algorithm. From the RNN

models presented in Table 3, the use of 11 neurons and 1 delay is selected for the prediction of EPC_{mean} , EPC_{max} , EPC_{min} , σ , and σ^2 values. The associated values of MSE and ρ for this RNN model are equal to 0.607 and 0.341, respectively.

The results presented in Table 4 for the LSTM ANN show that, in general, as the hidden units increase, the MSE reduces and ρ increases. Based on this observation, the best model selected for the prediction of EPC_{mean} , EPC_{max} , EPC_{min} , σ , and σ^2 values are with 400 hidden units and with 30 batches, with associated values of MSE and ρ equal to 0.0219 and 0.9824, respectively.

4.2. Comparison of Trained ANN Models. The comparison between the predicted EPC_{mean} , EPC_{max} , EPC_{min} , σ , and σ^2 by using the best FFNN, RNN, and LSTM trained models,

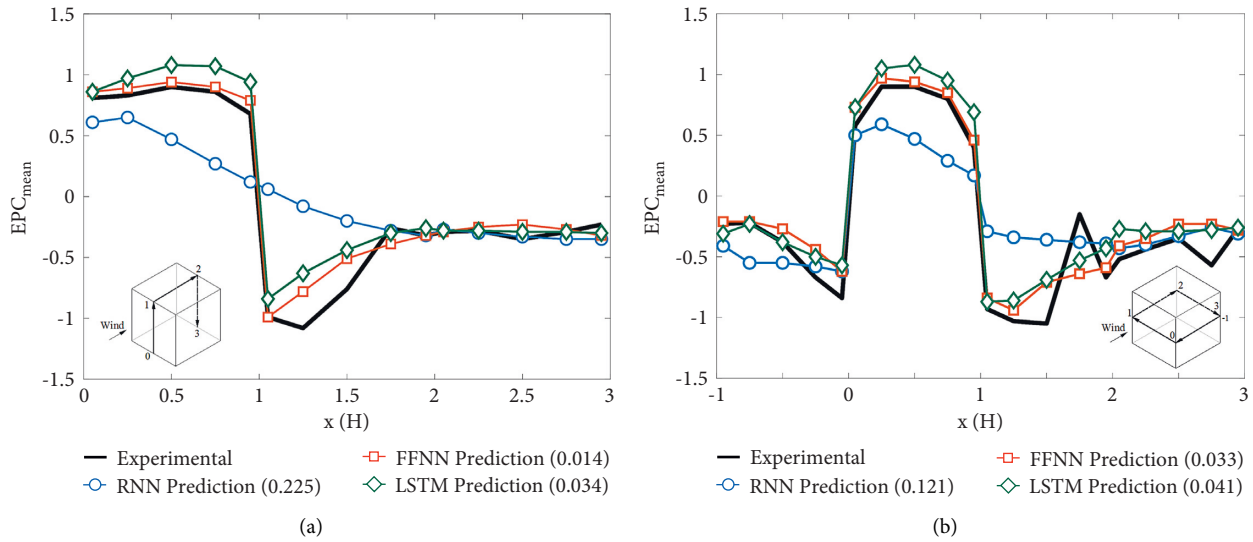


FIGURE 10: Comparison of the experimental EPC_{mean} and those predicted by the trained ANN models for $\theta = -10^\circ$: (a) along the longitudinal center line; (b) along the transverse center line. Numbers inside brackets indicate the MSE values.

obtained with the second validation set, and those obtained from the actual experimental database is shown in Figure 9. It is observed from Figure 9 that, in general, there is good agreement between the predicted and the observed values. The computed correlation coefficients range between 0.67 and 0.98. The best correlation is observed for the values predicted with the FFNN and LSTM models, while the worst correlation is obtained when the RNN model is employed. It is also observed in Figure 9 that there is no clear preference among the trained LSTM and FFNN models for providing the best estimates. Figure 9 also shows that the parameters best predicted by the LSTM ANN are EPC_{mean} , EPC_{max} , and EPC_{min} , with correlation coefficients greater than 92%. On the other hand, the parameters best predicted by the FFNN models are EPC_{mean} , EPC_{max} , and σ , with correlation coefficients greater than 91%. The previous observation indicates that, for preliminary design purposes, the use of the LSTM ANN model would be preferred, since the parameters EPC_{max} and EPC_{min} are generally used in the design of cladding, while EPC_{mean} is used for the design of the main structure. Moreover, the prediction made with the RNN models is not robust because they produce undesirable behavior for predicting EPC_{mean} , EPC_{min} , σ , and σ^2 .

To further evaluate the ability of the ANN models developed, in the following, the discussion is focused on the EPC_{mean} since it is widely used for wind design in codes and standards. For the comparison between the results predicted by using the testing set and the experimental ones, a case scenario of wind direction equal to -10° is considered. This wind direction was not included in the training set nor in the validation sets. By using the testing set, Figure 10 shows a comparison of predicted and experimental EPC_{mean} values along the longitudinal and transverse central lines for $\theta = -10^\circ$. It is observed in Figure 10 that the EPC_{mean} values predicted with the LSTM and the FFNN models follow closely those from the experimental test, and that the RNN model is the one with less predictive ability, with abrupt

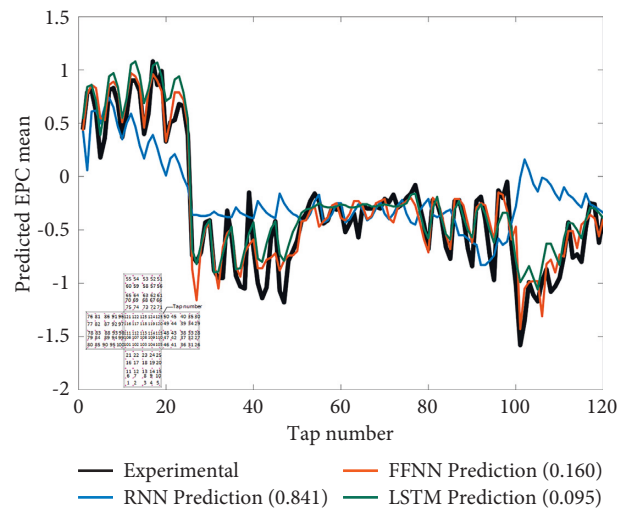


FIGURE 11: Comparison of the experimental EPC_{mean} and those predicted by the trained ANN models for all the taps for $\theta = -10^\circ$. Numbers inside brackets indicate the MSE values.

changes in the prediction of EPC_{mean} along the longitudinal and transverse central lines. The MSE obtained based on the experimental and predicted values for the three compared ANN models are included in Figure 10, where the minimum MSE is associated with the FFNN. It is further observed in Figure 10(a) that the predictions of EPC_{mean} made with both the FFNN and the LSTM ANN models for the windward wall (from point 0 to point 1) are the best, contrary to the predictions made with the RNN, which present a sudden drop compared to the experimental results. For the roof (from point 1 to point 2), the three ANN models considered do not reach the minimum EPC_{mean} values from experimental tests; however, the FFNN and LSTM ANN models are able to mimic the sudden change from pressure to suction. The latter is not observed for the predictions made with the RNN model. For the leeward zone (from point 2 to point 3), the

TABLE 5: Variation of MSE on the faces of the low-rise building for different wind direction by using the trained ANN models.

θ (°)	Right wall			Windward wall			Left wall			Leeward wall			Roof		
	RNN	FFNN	LSTM	RNN	FFNN	LSTM	RNN	FFNN	LSTM	RNN	FFNN	LSTM	RNN	FFNN	LSTM
-80	0.212	0.029	0.018	0.141	0.025	0.022	0.014	0.015	0.031	0.023	0.007	0.039	0.199	0.026	0.149
-70	0.306	0.017	0.015	0.152	0.024	0.017	0.015	0.015	0.033	0.029	0.013	0.044	0.194	0.033	0.135
-50	0.340	0.023	0.061	0.205	0.033	0.032	0.059	0.023	0.044	0.033	0.010	0.022	0.305	0.081	0.073
-40	0.240	0.017	0.021	0.157	0.016	0.033	0.108	0.028	0.056	0.022	0.010	0.024	0.311	0.065	0.067
-20	0.141	0.027	0.018	0.141	0.018	0.018	0.193	0.034	0.062	0.010	0.015	0.015	0.456	0.039	0.083
-10	0.128	0.033	0.026	0.178	0.020	0.039	0.276	0.047	0.048	0.011	0.014	0.010	0.546	0.035	0.062
10	0.065	0.010	0.013	0.130	0.026	0.021	0.193	0.053	0.055	0.017	0.019	0.010	0.515	0.035	0.035
20	0.056	0.017	0.019	0.114	0.019	0.012	0.096	0.037	0.038	0.015	0.018	0.009	0.489	0.039	0.064
40	0.047	0.016	0.007	0.067	0.019	0.026	0.187	0.055	0.040	0.024	0.019	0.010	0.483	0.085	0.075
50	0.040	0.012	0.008	0.024	0.030	0.025	0.263	0.050	0.052	0.031	0.018	0.012	0.389	0.069	0.061
70	0.032	0.011	0.012	0.144	0.025	0.040	0.296	0.038	0.046	0.054	0.025	0.015	0.357	0.039	0.050
80	0.027	0.013	0.011	0.244	0.022	0.039	0.331	0.036	0.051	0.099	0.026	0.025	0.334	0.039	0.052
Mean	0.139	0.018	0.018	0.137	0.022	0.028	0.164	0.035	0.047	0.031	0.016	0.020	0.376	0.050	0.075

predictions of the three models (i.e., FFNN, LSTM, and RNN) are in good agreement with the experimental results. Similar observations to those drawn from Figure 10(a) are also applicable to Figure 10(b), except that the RNN model is not able to mimic the behavior observed from the experimental results for the lateral walls (from point -1 to 0 and from 1 to 2) and the windward wall (from point 0 to 1).

A generic low-rise building represented by a cube with a side dimension equal to 10 m was considered for the experimental tests. This type of low-rise building has been widely studied worldwide and is referred to as the Silsoe cube [53]. A length scale equal to 1:50 was selected for the modeling. The model was built with rigid acrylic plates with 4 mm thickness. The pressure tap layout consisted of a total of 125 pressure taps, with 25 pressure taps per face (Figure 8). Plastic tubes made of urethane with an internal diameter of 8.6×10^{-4} m and an exterior diameter of 1.68×10^{-3} m were used to connect the pressure taps to the pressure scanners. During the experimental tests, the temperature was controlled with a heat exchanger, the average temperature during the tests was 15°C. The pressure scanners were set with a sampling rate equal to 256 Hz and a sampling time of 21 s. Wind direction (θ) was varied within -90° to 90° with increments of 10° ; additional angles of 45° and -45° were also considered (Figure 8). From the experimental tests, a total of 1125 time-history records of EPC were registered and processed to calculate mean EPC (EPCmean), maximum EPC (EPCmax), minimum EPC (EPCmin), root mean square of EPC (σ), and variance of EPC (σ^2), which are typical measures to evaluate the wind-induced forces in structures [1]. With the information processed and organized, an experimental input and output database was assembled, which included EPCmean, EPCmax, EPCmin, σ , and σ^2 values, which were associated with predefined θ values and coordinates (x , y) for each tap (Figure 8). For simplicity, the instrumented faces of the cube were unfolded as shown in Figure 8, and the reference system to define the coordinates for each tap was located at the intersection of the lines A and B. The total number of elements in the experimental database was equal to 5625.

To further investigate whether the LSTM and FFNN models outperform the RNN model, Figure 11 presents a comparison of the experimental and predicted EPC_{mean} values for all the taps and for wind direction -10° . It is observed in Figure 11 that, in general, the LSTM and FFNN models are able to mimic the behavior of the EPC_{mean} values, with very good predictions for the upper and lower bounds of EPC_{mean} (i.e., the greatest positive values of EPC_{mean} and the lowest negative values). It is also observed from Figure 11 that the RNN model provides predictions of the EPC_{mean} values from taps 1 to 25 that follow a similar trend to that of the experimental values, but with lower magnitude; from taps 26 to 50 and from taps 101 to 125, the RNN predictions are considerably different to those from the experimental tests; and from taps 50 to 100, the RNN model provides EPC_{mean} values that follow an average trend to that of the experimental values.

The comparison shown in Figure 11 was repeated, except that a wide range of wind directions (not included in the training set nor in the validation sets) and the prediction at each face of the low-rise building were considered, the results of this comparison in terms of the MSE are summarized in Table 5. Similar observations to those drawn for Figure 11 are applicable to the results presented in Table 5, indicating that the LSTM and FFNN models are the ones with better predictive ability. Among all the cases considered in Table 5, the predictions with the three ANN models at the leeward wall are associated with the minimum MSE values and those at the roof with the maximum. It is also observed from the results of Table 5 that, on average, the FFNN is the model associated with the minimum MSE values.

5. Conclusions

Numerical analyses were carried out to investigate whether the FFNN, RNN, and LSTM models could adequately predict the mean, maximum, minimum, root mean square, and variance of external pressure coefficients of a low-rise building. For the analysis, 1125 time-history records of external pressure coefficients calculated from wind tunnel tests were considered.

The main observations that can be drawn from the analysis results are:

- (1) The best-trained FFNN and RNN models require more than 10 hidden neurons, while the LSTM ANN requires 400 hidden units and 30 batches. The latter indicates that the developed ANN-based models need a considerable number of hidden neurons and units to provide predictions with low error values for the cases considered.
- (2) The input neurons employed in all the ANN models showed to be adequate and concordant with the physical phenomenon where the external pressure coefficients depend on the wind direction and location
- (3) For preliminary design purposes, the use of the LSTM ANN model would be preferred, since it provides the best predictions for the maximum, minimum, and mean external pressure coefficients, which are used in the design of cladding and the main structure.
- (4) The RNN models are not robust because they produce undesirable behavior for predicting EPC_{mean} , EPC_{min} , σ , and σ^2 .

Data Availability

The manuscript has no associated data.

Conflicts of Interest

The authors declare that there are no conflicts of interest regarding the publication of this article.

Acknowledgments

This work was supported by the Institute of Engineering of the National Autonomous University of Mexico (UNAM) and the National Council on Science and Technology of Mexico (CONACYT). We thank Osvaldo Martín del Campo Preciado for providing insightful comments and suggestions to improve this work.


References

- [1] V. Guzmán-Solis, A. Pozos-Estrada, and R. Gómez-Martínez, "Experimental study of wind-induced shear, bending, and torsional loads on rectangular tall buildings," *Advances in Structural Engineering*, vol. 23, no. 14, 2020.
- [2] P. J. Richards and R. P. Hoxey, "Appropriate boundary conditions for computational wind engineering models using the $k-\epsilon$ turbulence model," *Journal of Wind Engineering and Industrial Aerodynamics*, vol. 46-47, pp. 145-153, 1993.
- [3] J. X. Lin, D. Surry, and H. W. Tieleman, "The distribution of pressure near roof corners of flat roof low buildings," *Journal of Wind Engineering and Industrial Aerodynamics*, vol. 56, no. 2-3, pp. 235-265, 1995.
- [4] J. X. Lin and D. Surry, "The variation of peak loads with tributary area near corners on flat low building roofs," *Journal of Wind Engineering and Industrial Aerodynamics*, vol. 77-78, pp. 185-196, 1998.
- [5] H. Kozmar, "Surface pressure on a cubic building exerted by conical Vortices," *Journal of Fluids and Structures*, vol. 92, Article ID 102801.
- [6] A. Rigato, P. Chang, and E. Simiu, "Database-assisted design, standardization, and wind direction effects," *Journal of Structural Engineering*, vol. 127, no. 8, pp. 855-860, 2001.
- [7] Y. Chen, G. A. Kopp, and D. Surry, "Interpolation of pressure time series in an aerodynamic database for low buildings," *Journal of Wind Engineering and Industrial Aerodynamics*, vol. 91, no. 6, pp. 737-765, 2003.
- [8] G. A. Kopp and Y. Chen, "Database-assisted design of low-rise buildings: aerodynamic considerations for a practical interpolation scheme," *Journal of Structural Engineering*, vol. 132, no. 6, pp. 909-917, 2006.
- [9] T. C. E. Ho, D. Surry, D. Morrish, and G. A. Kopp, "The UWO contribution to the NIST aerodynamic database for wind loads on low buildings: Part 1. Archiving format and basic aerodynamic data," *Journal of Wind Engineering and Industrial Aerodynamics*, vol. 93, no. 1, pp. 1-30, 2005.
- [10] K. R. Gurley, M. A. Tognarelli, and A. Kareem, "Analysis and simulation tools for wind engineering," *Probabilistic Engineering Mechanics*, vol. 12, no. 1, pp. 9-31, 1997.
- [11] R. Popescu, G. Deodatis, and J. H. Prevost, "Simulation of homogeneous non-Gaussian stochastic vector fields," *Probabilistic Engineering Mechanics*, vol. 13, no. 1, pp. 1-13, 1998.
- [12] M. Gioffre, V. Gusella, and M. Grigoriu, "Simulation of non-Gaussian field applied to wind pressure fluctuations," *Probabilistic Engineering Mechanics*, vol. 15, no. 4, pp. 339-345, 2000.
- [13] M. Gioffre, V. Gusella, and M. Grigoriu, "Non-Gaussian wind pressure on prismatic buildings II: numerical simulation," *Journal of Structural Engineering*, vol. 127, no. 9, pp. 990-995, 2001.
- [14] Y. Chen, *Time Series Simulation of Wind-Induced Pressures on Low Buildings*, Faculty of Graduate Studies the University of Western Ontario, London, UK, 2002.
- [15] J. Wan, G. Ren, J. Liu, Q. Hu, and D. Yu, "Ultra-short-term wind speed prediction based on multi-scale predictability analysis," *Cluster Computing*, vol. 19, no. 2, pp. 741-755, 2016.
- [16] J. Wan, J. Liu, G. Ren et al., "A universal power-law model for wind speed uncertainty," *Cluster Computing*, vol. 22, no. S4, Article ID 10347, 2019.
- [17] Y. Li, P. Yang, and H. Wang, "Short-term wind speed forecasting based on improved ant colony algorithm for LSSVM," *Cluster Computing*, vol. 22, no. S5, Article ID 11575, 2019.
- [18] X. Pang, H. Wang, and J. Chen, "Intelligence algorithm for optimization design of the low wind speed airfoil for wind turbine," *Cluster Computing*, vol. 22, no. S4, pp. 8119-8129, 2019.
- [19] A. Shafiq, A. B. Çolak, and T. N. Sindhu, "Reliability Investigation of Exponentiated Weibull Distribution Using IPL through Numerical and Artificial Neural Network Modeling," *Quality and Reliability Engineering International*, pp. 1-16, Wiley, Hoboken, NJ, USA, 2022.
- [20] A. Shafiq, A. Batur Çolak, T. Naz Sindhu, S. Ahmad Lone, A. Alsubie, and F. Jarad, "Comparative study of artificial neural network versus parametric method in COVID-19 data analysis," *Results in Physics*, vol. 38, Article ID 105613, 2022.
- [21] K. Varshney and K. Poddar, "Prediction of wind properties in urban environments using artificial neural network," *Theoretical and Applied Climatology*, vol. 107, no. 3-4, pp. 579-590, 2012.
- [22] X. Gavalda, J. Ferrer-Gener, G. A. Kopp, and F. Giralt, "Interpolation of pressure coefficients for low-rise buildings of

- different plan dimensions and roof slopes using artificial neural networks,” *Journal of Wind Engineering and Industrial Aerodynamics*, vol. 99, no. 5, pp. 658–664, 2011.
- [23] Y. Chen, G. A. Kopp, and D. Surry, “Interpolation of wind-induced pressure time series with an artificial neural network,” *Journal of Wind Engineering and Industrial Aerodynamics*, vol. 90, no. 6, pp. 589–615, 2002.
- [24] J. Y. Fu, S. G. Liang, and Q. S. Li, “Prediction of wind-induced pressures on a large gymnasium roof using artificial neural networks,” *Computers & Structures*, vol. 85, no. 3-4, pp. 179–192, 2007.
- [25] Y. Chen, G. A. Kopp, and D. Surry, “Prediction of pressure coefficients on roofs of low buildings using artificial neural networks,” *Journal of Wind Engineering and Industrial Aerodynamics*, vol. 91, no. 3, pp. 423–441, 2003.
- [26] T. J. Nikose and R. S. Sonparote, “Dynamic along wind response of tall buildings using Artificial Neural Network,” *Cluster Computing*, vol. 22, no. S2, pp. 3231–3246, 2019.
- [27] T. J. Nikose and R. S. Sonparote, “Dynamic wind response of tall buildings using artificial neural network,” *The Structural Design of Tall and Special Buildings*, vol. 28, no. 13, 2019.
- [28] A. B. Çolak, “Experimental study for thermal conductivity of water-based zirconium oxide nanofluid: developing optimal artificial neural network and proposing new correlation,” *International Journal of Energy Research*, vol. 45, no. 2, pp. 2912–2930, 2021.
- [29] A. Thammano and P. Ruxpakawong, “Nonlinear dynamic system identification using recurrent neural network with multi-segment piecewise-linear connection weight,” *Memetic Computing*, vol. 2, no. 4, pp. 273–282, 2010.
- [30] Y. You and M. Nikolaou, “Dynamic process modeling with recurrent neural networks,” *AIChE Journal*, vol. 39, no. 10, pp. 1654–1667, 1993.
- [31] F. A. Gers, D. Eck, and J. Schmidhuber, “Applying LSTM to time series predictable through time-window approaches,” in *Artificial Neural Networks - ICANN 2001*. ICANN 2001, G. Dorffner, H. Bischof, and K. Hornik, Eds., Vol. vol 2130, Springer, Berlin, Germany, 2001.
- [32] C. J. Su and Y. Li, “Recurrent neural network based real-time failure detection of storage devices,” *Microsystem Technologies*, vol. 28, no. 2, pp. 621–633, 2019.
- [33] Y. Ma, H. Peng, T. Khan, E. Cambria, and A. Hussain, “Sentic LSTM: a hybrid network for targeted aspect-based sentiment analysis,” *Cognitive Computation*, vol. 10, no. 4, pp. 639–650, 2018.
- [34] W. Ying, L. Zhang, and H. Deng, “Sichuan dialect speech recognition with deep LSTM network,” *Frontiers of Computer Science*, vol. 14, no. 2, pp. 378–387, 2020.
- [35] A. Graves, D. Eck, N. Beringer, and J. Schmidhuber, “Biologically plausible speech recognition with LSTM neural nets,” in *Biologically Inspired Approaches to Advanced Information Technology*. BioADIT 2004, A. J. Ijspeert, M. Murata, and N. Wakamiya, Eds., Vol. 3141, Springer, Berlin, Germany, 2004.
- [36] J. Liu, A. Shahroudy, D. Xu, and G. Wang, “Spatio-temporal LSTM with trust gates for 3D human action recognition,” in *Computer Vision - ECCV 2016*. ECCV 2016, B. Leibe, J. Matas, N. Sebe, and M. Welling, Eds., Vol. 9907, Springer, Cham, Switzerland, 2016.
- [37] S. Lawrence, C. L. Giles, and A. C. Tsoi, “Lessons in neural network training: overfitting may be harder than expected,” in *Proceedings of the Fourteenth National Conference on Artificial Intelligence*, Providence, RI, USA, July 1997.
- [38] S. Geman, E. Bienenstock, and R. Doursat, “Neural networks and the bias/variance dilemma,” *Neural Computation*, vol. 4, no. 1, pp. 1–58, 1992.
- [39] D. R. Hush and B. G. Horne, “Progress in supervised neural networks,” *IEEE Signal Processing Magazine*, vol. 10, no. 1, pp. 8–39, 1993.
- [40] A. Pozos-Estrada, R. Gómez, and H. P. Hong, “Use of Neural network to predict the peak ground accelerations and pseudo spectral accelerations for Mexican Inslab and Interplate Earthquakes,” *Geofísica Internacional*, vol. 53, no. 1, pp. 39–57, 2014.
- [41] R. Flores-Mendoza, J. U. Rodríguez-Alcántara, A. Pozos-Estrada, and R. Gómez, “Use of artificial neural networks to predict strong ground motion duration of interplate and inslab Mexican earthquakes for soft and firm soils,” *Geofísica Internacional*, vol. 61, no. 3, pp. 153–179, 2022.
- [42] D. T. Pham and S. J. Oh, “A recurrent backpropagation neural network for dynamic system identification,” *Journal of Systems Engineering*, vol. 2, no. 4, pp. 213–223, 1992.
- [43] C. Principe, N. R. Euliano, and W. C. Lefebvre, *Neural and Adaptive Systems: Fundamentals through Simulation*, John Wiley & Sons, New York, NY, USA, 1999.
- [44] D. T. Pham and D. Karaboga, “Training Elman and Jordan networks for system identification using genetic algorithms,” *Artificial Intelligence in Engineering*, vol. 13, no. 2, pp. 107–117, 1999.
- [45] P. J. Werbos, “Backpropagation through time: what it does and how to do it,” *Proceedings of the IEEE*, vol. 78, no. 10, pp. 1550–1560, 1990.
- [46] Y. Bengio, P. Simard, and P. Frasconi, “Learning long-term dependencies with gradient descent is difficult,” *IEEE Transactions on Neural Networks*, vol. 5, no. 2, pp. 157–166, 1994.
- [47] J. F. Kolen and S. C. Kremer, “Gradient flow in recurrent nets: the difficulty of learning long-term dependencies,” in *A Field Guide to Dynamical Recurrent Networks*. IEEE Press, Piscataway, NJ, USA, 2001.
- [48] W. Kong, Z. Y. Dong, Y. Jia, D. J. Hill, Y. Xu, and Y. Zhang, “Short-term residential load forecasting based on LSTM recurrent neural network,” *IEEE Transactions on Smart Grid*, vol. 10, no. 1, pp. 841–851, 2019.
- [49] A. Zemmari and J. Benois-Pineau, *Deep Learning in Mining of Visual Content*, Springer, Cham, Switzerland, 2020.
- [50] J. Counihan, “Adiabatic atmospheric boundary layers: a review and analysis of data from the period 1880–1972,” *Atmospheric Environment*, vol. 9, no. 10, pp. 871–905, 1975.
- [51] E. Amaya-Gallardo, A. Pozos-Estrada, and R. Gómez, “Characteristics and calibration of the Mexican boundary layer wind tunnel at UNAM,” *Ingeniería: Investigación y Tecnología*, vol. XXIII, no. 1, 2022.
- [52] E. Simiu and R. H. Scanlan, *Wind Effects on Structures*, John Wiley & Sons, New York, NY, USA, 1996.
- [53] P. J. Richards, R. Hoxey, B. D. Connell, and D. P. Lander, “Wind-tunnel modelling of the Silsoe cube,” *Journal of Wind Engineering and Industrial Aerodynamics*, vol. 95, no. 9-11, pp. 1384–1399, 2007.
- [54] L. V. Fausset, *Fundamentals of Neural Networks: Architecture, Algorithms, and Applications*, Prentice-Hall, Englewood Cliffs, NJ, USA, 1994.

Research Article

Shear Strength Model for Reinforced Concrete Corner Joints Based on Soft Computing Techniques

Moiz Tariq ¹, Azam Khan,¹ Asad Ullah,¹ Muhammad Waseem,² Hassan Nasir,³ and Irfan Jamil²

¹*NUST Institute of Civil Engineering (NICE), Sector H-12, Islamabad, Pakistan*

²*Department of Civil Engineering, University of Engineering and Technology, Peshawar, Pakistan*

³*Water Sanitation Services Peshawar (WSSP), Peshawar, Pakistan*

Correspondence should be addressed to Moiz Tariq; mtariq.ms18@nice.nust.edu.pk

Received 5 February 2022; Revised 25 March 2022; Accepted 4 June 2022; Published 4 August 2022

Academic Editor: Afaq Ahmad

Copyright © 2022 Moiz Tariq et al. This is an open access article distributed under the Creative Commons Attribution License, which permits unrestricted use, distribution, and reproduction in any medium, provided the original work is properly cited.

The shear strength of cyclically loaded RC corner joints, resulting in opening and closing moments, has not been extensively studied. In addition, experimental studies of the joint shear strength are time-consuming and expensive. Therefore, to overcome this challenge, two separate gene expression programming (GEP) based empirical models are developed for the shear strength of the corner joints, one under the opening moment and the other under the closing moments. One of the key parameters overlooked in previous studies is the joint shear reinforcement, which has been incorporated in the GEP models. These models are developed by compiling an experimental database of 59 specimens in terms of the concrete compressive strength, the joint aspect ratio, the reinforcement tensile strength, and the reinforcement compressive strength. A detailed statistical study is undertaken that indicates superior accuracy of the proposed models and a high potential for their application in the design practice.

1. Introduction

Beam-column joints made from reinforced concrete (RC) have attracted considerable attention in the last few decades [1–10] because of the difficulty in predicting their behavior. Although extensive effort has been put forward to studying various conventional RC joints, a reliable prediction method for the beam-column corner joints is rare. Corner joint response is more complex in nature, which can be because of the joint opening; resulting in compression outside the joint, or the joint closing; resulting in compression inside the joint. In addition, the corner joints' behavior is uncertain when supported by a column that is lightly loaded. Despite this complexity and uncertainty, the seismic building codes place little emphasis on the corner joint design.

When the corner joint opens and closes, different load-resisting mechanisms are triggered, thereby further complicating the joint's behavior. Therefore, various models are developed for the shear strength of these joints. For example, Priestley et al. [11] proposed a shear strength model in terms

of the principal tensile $0.29\sqrt{f'_c}$ and the principal compressive stresses $0.3f'_c$ MPa. Later, Megget's [12] revised the corner joint shear strength to $0.1f'_c$, which was also adopted by New Zealand Standard [13]. However, several experimental investigations have shown that the corner joint behaves differently in the opening and the closing action, so a single expression of the shear capacity is not sufficient [14–17]. A weaker diagonal concrete strut during the corner joint opening almost halves the shear capacity as compared to the capacity during the joint closing action [18, 19]. Thus, their seismic efficiency is more dependent on the opening than the closing shear stress.

Corner joints are not included in any of the major design codes, such as the New Zealand design standard [13], EC 8 [20], Chinese Seismic Code [21], or Architectural Institute of Japan [22]. As a result, the exterior joint provisions are applied to the corner joint design. ACI318-19 [23] and ACI352R-02 [24] recommend only one expression for the corner joint's nominal shear strength. Besides these actions, the corner joint has normally lower axial load than joints in

other locations because of a discontinuous column. Due to all these differences, Moiz et al. [25] proposed two regression models, one for corner joint opening and the other for the corner joint closing. The model showed satisfactory predictive ability, however, it tends to omit the joint shear reinforcement ratio, which has a significant influence on the shear strength of the RC corner joint.

Various experts have put forth analytical and computational models for determining the shear capacity of RC joints. In this respect, the compression field theory has been successfully applied by Hwang et al. [26]. Similarly, the rotating-angle softened truss model (RA-STM) [27] and the modified rotating angle softened truss theory (MRA-STM) [28] have been implemented for predicting RC joint shear capacities. Other models include the softened truss theory (FA-STM) [29] and an improved strut and tie-based shear strength model [30]. However, these models are not able to accurately predict the behavior of corner joints. For the corner joints' shear capacity, very few analytical models exist that can determine the capacity under the opening and closing actions [31, 32]. Attempts have also been made to simulate corner joints using a computationally complex finite element analysis approach [33].

Due to the requirement of expertise and involvement of the computational complexity of the existing models, the design capacity of corner joints needs to be reexamined using a technique that can predict the response based on the existing experimental evidence. As a result, the current research aims to develop two reliable shear capacity models using the Gene Expression Programming by consulting experimental results for 59 specimens. The proposed soft computing models are validated and compared statistically with the existing models.

2. Research Significance

The transfer of the shear and the moment forces from one structural element to another is ensured by the use of beam-column joints. RC structures in earthquake-prone areas frequently collapse due to the shear failure of joints [34–41]. One of the failure causes is the treatment of joints as a rigid element in structural design, which ignores the shear strength of joints, thereby challenging its design and detail for better seismic performance. Only a few reliable models exist that can predict the shear capacity of joints based on the ductility requirements [41–53]. In most of the existing models, the concrete compressive strength is the only influencing parameter, but other factors, such as the joint geometric properties, joint shear reinforcement, and member longitudinal reinforcement, are often overlooked. Attempts have been made, without success, to apply these shear capacity models on the corner joints because of the lack of corner joint-specific models. Hence, the current research aims to develop two soft computing models, incorporating the influence of horizontal and vertical joint shear reinforcement, for assessing the complex behavior of corner joints under the joint opening and closing actions, respectively.

3. Parameters Affecting the Shear Strength of RC Corner Joint

Essentially, all of the variables influencing the shear capacity of RC corner joints so that an improved model is developed. Research [4, 7, 52–68] shows that the shear strength of corner joints depends on a variety of factors including the concrete compressive strength, the longitudinal tension reinforcement ratios, the joint horizontal and vertical shear reinforcement, and the joint aspect ratio. These studies have confirmed that joint shear strength is positively correlated with the concrete compressive strength when the joint is tending to close, and the shear strength is negatively correlated when the joint is tending to open.

Another factor influencing corner joint shear strength is the joint aspect ratio (beam to column depth ratio), which is positively correlated with the shear strength, regardless of whether the joint is opening or closing [12, 14, 15, 18, 31, 32, 69–71, 72]. Surprisingly, the design code of practices neglects the influence of joint aspect ratio on the strength of the corner joints. It has also been shown [69] that adequate anchorage can increase the joint shear capacity of a longitudinal reinforcement (Figure 1). In addition, the shear capacity can be improved if a corner joint column is wider than the beam, because of the indirect confinement offered by the column. It is concluded from this finding that, under the joint closing, the flexural moment capacity reduces if the opening to the closing moment of the joint is higher. Contrarily, under the joint opening, the capacity reduces if the opening to the closing capacity of the joint is lower.

4. Experimental Investigation and Existing Shear Capacity Models

When it comes to studying corner joints, the Loma Prieta Earthquake of 1989 may be seen as a turning point. Since then, numerous experimental studies have been undertaken, especially involving cyclic loading. Before 1989, most of the experimental studies involved the monotonic loading of corner joints. This section examines some of the most significant studies into cyclically loaded corner joints.

4.1. Current Experimental Database. A database of 59 experiments is compiled based on the key influencing parameters discussed in Section 3. Out of these 59 specimens, 40 are used to build the GEP model, and the remaining 19 samples are used to test the model. Few experiments are excluded because of inconsistencies in the specimen geometry, material and reinforcement properties, etc. Table 1 summarizes the available specimens in the database.

4.2. Previous Experimental Investigations. Several experimental studies [15–17] have noted anomalous results for corner joint shear capacities when using the empirical expression proposed by ACI 352-02 [24]. A similar difference [14] is noted in the New Zealand Code of Practice (NZS 3101-2006). This disparity is because of leaving out various key influencing factors from the code proposed expressions [30, 32, 72]. Material, geometry, and reinforcement properties have

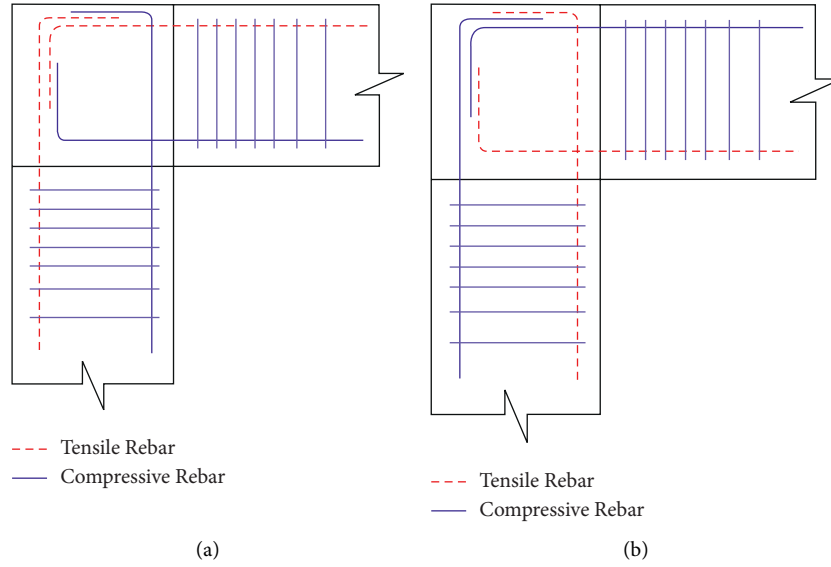


FIGURE 1: Corner joint longitudinal reinforcement. (a) Closing moment (b) Opening moment.

TABLE 1: RC specimens dimensions and properties.

Specimen ID	F_c' (MPa)	f_{yb} (MPa)	b_j (mm)	h_j (mm)	ρ_{bT}	ρ_{jT}
Mogili and Kuang [73]						
KJ-NO	37.60	526.00	300.00	300.00	0.020	0.024
KJ-N1	36.80	526.00	300.00	300.00	0.024	0.024
KJ-F0	34.50	560.00	300.00	420.00	0.020	0.026
KJ-F1	29.20	560.00	300.00	420.00	0.024	0.026
KJ-S0	27.80	560.00	300.00	300.00	0.011	0.026
KJ-S1	26.80	560.00	300.00	300.00	0.013	0.026
Zhang [31]						
KJ-NS	38.40	500.00	300.00	300.00	0.024	0.000
KJ-F	36.50	500.00	300.00	300.00	0.024	0.011
KJ2-H12V10	29.30	520.00	300.00	300.00	0.024	0.013
KJ3-H10V12	32.20	500.00	300.00	300.00	0.024	0.013
KJ-H8V10	35.40	500.00	300.00	300.00	0.024	0.009
KJ-BD500	30.90	500.00	300.00	300.00	0.014	0.008
KJ-CW430	30.80	500.00	365.00	300.00	0.024	0.011
KJ-BD700	32.50	500.00	300.00	300.00	0.010	0.008
KJ-CD500	32.30	500.00	300.00	500.00	0.024	0.008
KJ-CW600	33.20	500.00	450.00	300.00	0.024	0.013
Mazzoni et al. [15]						
KJ#1	42.10	503.00	254.30	304.80	0.024	0.004
KJ#2	42.10	503.00	254.30	304.80	0.024	0.008
KJ#3	32.85	503.00	254.30	304.80	0.024	0.008
Cote and Wallace [16]						
KJ#1	45.70	448.00	317.50	406.40	0.014	0.011
KJ#2	49.80	448.00	317.50	406.40	0.014	0.011
KJ#3	45.00	448.00	317.50	406.40	0.014	0.005
KJ#4	45.60	448.00	317.50	406.40	0.014	0.011
McConnell and Wallace [17]						
KJ#5	31.50	448.00	342.50	406.40	0.015	0.006
KJ#6	33.00	448.00	342.50	406.40	0.015	0.005
KJ#7	32.90	448.00	342.50	406.40	0.015	0.010
KJ#8	36.30	448.00	342.50	406.40	0.015	0.006
KJ#9	38.50	448.00	342.50	406.40	0.015	0.005
KJ#10	37.90	448.00	342.50	406.40	0.015	0.010
KJ#11	35.00	448.00	342.50	406.40	0.015	0.006
KJ#12	32.90	448.00	342.50	406.40	0.015	0.005

TABLE 1: Continued.

Specimen ID	F_c' (MPa)	f_{yb} (MPa)	b_j (mm)	h_j (mm)	ρ_{bT}	ρ_{iT}
KJ#13	31.70	448.00	342.50	406.40	0.015	0.010
Megget [12, 14]						
KJ-1	27.80	358.00	225.00	250.00	0.020	0.006
KJ-2	27.80	358.00	225.00	250.00	0.018	0.006
KJ-3	34.00	328.00	225.00	250.00	0.026	0.011
KJ-4	34.00	328.00	225.00	250.00	0.022	0.010
KJ-5	33.60	355.00	225.00	250.00	0.022	0.001
KJ-6	33.60	325.00	225.00	250.00	0.022	0.011
KJ-7	50.00	333.00	225.00	250.00	0.041	0.017
KJ-8	40.40	340.00	225.00	250.00	0.022	0.001
KJ-9	39.80	333.00	225.00	250.00	0.022	0.006
KJ-10	39.70	333.00	225.00	250.00	0.022	0.006
KJ-11	26.80	333.00	225.00	250.00	0.022	0.006
Angelakos [33]						
KJ-1	45.70	448.00	340.00	400.00	0.014	0.011
KJ-2	49.70	448.00	340.00	400.00	0.014	0.011
KJ-3	45.00	448.00	340.00	400.00	0.014	0.005
KJ-4	45.60	448.00	340.00	400.00	0.014	0.011
KJ-5	31.50	461.00	340.00	400.00	0.022	0.006
KJ-6	33.00	461.00	340.00	400.00	0.022	0.005
KJ-7	32.90	461.00	340.00	400.00	0.022	0.010
KJ-8	36.30	461.00	340.00	400.00	0.016	0.006
KJ-9	38.50	461.00	340.00	400.00	0.016	0.005
KJ-10	37.90	461.00	340.00	400.00	0.016	0.010
KJ-11	35.00	461.00	340.00	400.00	0.019	0.006
KJ-12	32.90	461.00	340.00	400.00	0.019	0.005
KJ-13	31.70	461.00	340.00	400.00	0.019	0.010
KJ-14	33.60	448.00	340.00	400.00	0.019	0.006
KJ-15	36.90	434.00	340.00	400.00	0.015	0.010
KJ-16	37.20	487.00	340.00	400.00	0.015	0.010
KJ-1	45.70	448.00	340.00	400.00	0.014	0.011
KJ-2	49.70	448.00	340.00	400.00	0.014	0.011
KJ-3	45.00	448.00	340.00	400.00	0.014	0.005
KJ-4	45.60	448.00	340.00	400.00	0.014	0.011
KJ-5	31.50	461.00	340.00	400.00	0.022	0.006
KJ-6	33.00	461.00	340.00	400.00	0.022	0.005
KJ-7	32.90	461.00	340.00	400.00	0.022	0.010
KJ-8	36.30	461.00	340.00	400.00	0.016	0.006
KJ-9	38.50	461.00	340.00	400.00	0.016	0.005
KJ-10	37.90	461.00	340.00	400.00	0.016	0.010
KJ-11	35.00	461.00	340.00	400.00	0.019	0.006
KJ-12	32.90	461.00	340.00	400.00	0.019	0.005
KJ-13	31.70	461.00	340.00	400.00	0.019	0.010
KJ-14	33.60	448.00	340.00	400.00	0.019	0.006
KJ-15	36.90	434.00	340.00	400.00	0.015	0.010
KJ-16	37.20	487.00	340.00	400.00	0.015	0.010

a significant influence on the joint shear strength [30, 72]. As a result of this precedent, it is necessary to develop an expression that incorporates all these factors as input parameters.

4.3. Review of Existing Shear Capacity Models. Extensive variation exists in the proposed empirical expressions of corner joint shear strength. However, many of these expressions produce results that are invalid and impractical.

There are many proposed corner joint shear capacity equations; for instance, $0.58\sqrt{f'_c}$ [17] and $0.58\sqrt{f'_c}$ [33, 72, 74]. Similarly, other researchers [12, 14] have proposed $0.12f'_c$ for the joint closing and $0.10f'_c$ for the opening shear capacity. Some investigators [11] have bounded the principal tensile stress in the corner joint to $0.29\sqrt{f'_c}$, rather than predicting the joint shear capacity. An identical variable trend in the shear capacity equations is also

observed in the expressions of building codes. Some of the empirical models used in the subsequent comparative study are discussed in Table 2

5. Fundamentals of Gene Expression Programming

An artificial intelligence-based technique called Gene Expression Programming (GEP) is an evolutionary algorithm that generates mathematical models and processes the input data in a domain-independent manner [75]. GEP differs from the Genetic Algorithms (GAs) and the Genetic Programmings (GPs) in the sequence of chromosome representation. GEP algorithm can produce a linear and nonlinear sequence of chromosomes creating a robust computer-based solution of complex and challenging problems. The algorithm iteratively alters the number of chromosomes and genes, head size, and the linking functions to generate an influential model that can perform a broad range of estimation and prediction tasks. An interesting feature of having more genes and chromosomes is that the function can be more complex, but the results can still be exact. Because of this tradeoff, it is possible to achieve a simplified mathematical model and control the number of genes/chromosomes, as well as achieve the desired level of accuracy [76].

As the GEP algorithm progresses, it tries to achieve convergence on the global optimal solution. There may be

times when the algorithm is unable to choose the best solution from a pool of possible ones, thereby leading to an endless loop or producing an illogical expression, depending on the state. Changing the number of genes and chromosomes, or changing the linking function, can solve this numerical problem. This numerical problem was effectively resolved herein whilst developing two models for predicting the shear capacity of corner joints, one related to the joint opening and the other to joint closing.

6. Development of GEP Based Shear Capacity Model

To develop a GEP model, the population involving 40 data points is randomly extracted from a total of 59 datasets (Table 2). The influencing factors of the joint shear strength, including, the column and beam cross-sections, the concrete compressive strength and yielding stress of reinforcing bars, the area of longitudinal tension reinforcement, and the area of longitudinal compression reinforcement, are selected as input parameters to establish two independent GEP models, one for closing action and the other for opening action of joints. These models are validated using the remaining 19 datasets of the experimental database. The following expression is derived for the shear capacity during the joint closing.

$$v_{jh_c} = v_{jh_{c1}} + v_{jh_{c2}} + v_{jh_{c3}} \text{ (MPa)}, \quad (1)$$

$$v_{jh_{c1}} = \left(-0.25 \frac{b_j}{h_j} \right) \left(\frac{d_b \rho_{hj} f_{yb}}{d_c \sqrt{f'_c}} \right) \left(\sqrt{f'_c} - \frac{d_b}{d_c} - \frac{\rho_{cb} f_{yb}}{\sqrt{f'_c}} - 2.16 \right) \left(\frac{b_j}{h_j} + \frac{\rho_{cb} f_{yb}}{\sqrt{f'_c}} \right), \quad (2)$$

$$v_{jh_{c2}} = \left[\left(\sqrt{f'_c} \right)^{\frac{1}{4}} - \left(\frac{b_b}{d_b} \right)^5 \right] \left(10.49 \frac{\rho_{cb} f_{yb}}{\sqrt{f'_c}} \right), \quad (3)$$

$$v_{jh_{c3}} = \left[\left(f'_c \right)^{\frac{1}{4}} - 0.942 \left(\frac{\rho_{vj} f_{yb}}{\sqrt{f'_c}} \right)^2 \right] - \left(\frac{b_c}{d_b} \right), \quad (4)$$

and the following during the joint opening,

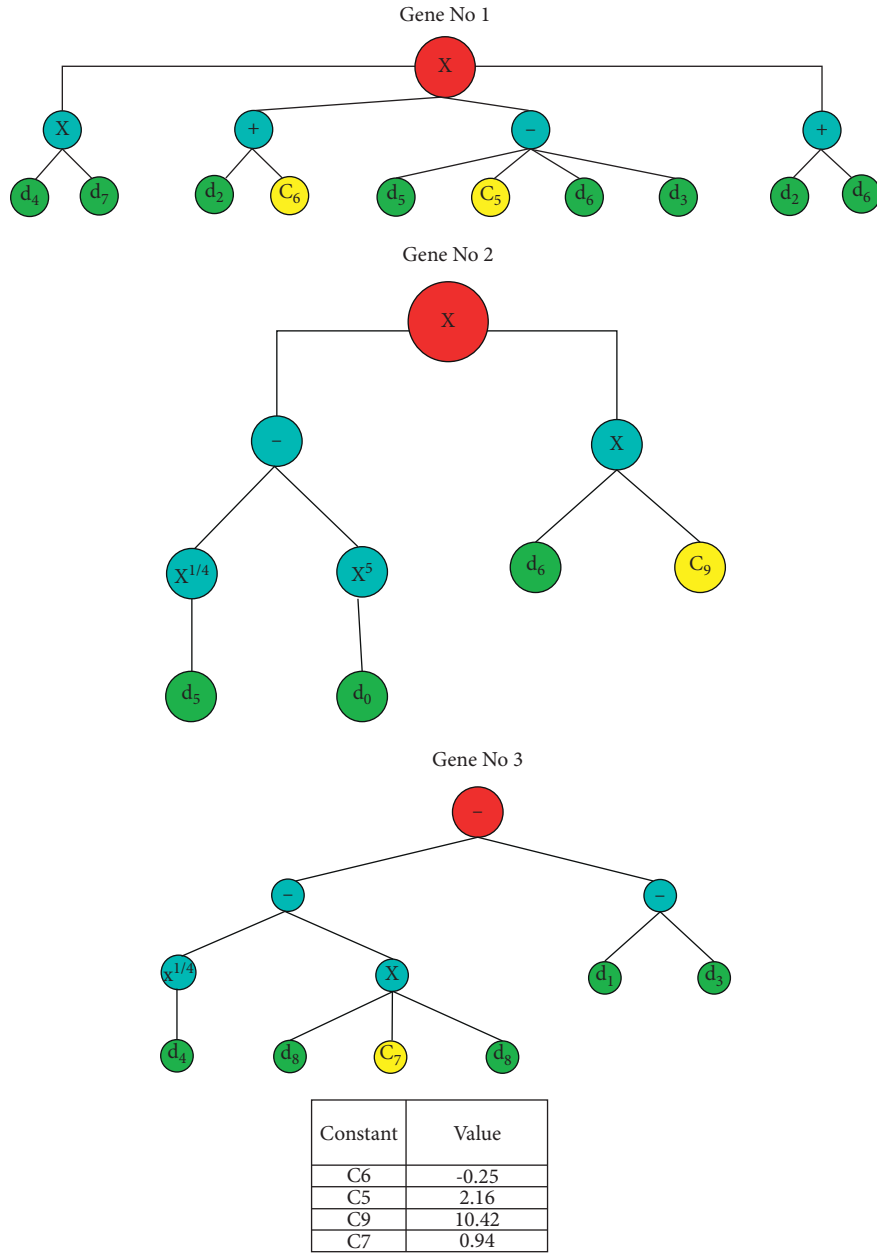
$$v_{jh_o} = v_{jh_{o1}} + v_{jh_{o2}} + v_{jh_{o3}} \text{ (MPa)}, \quad (5)$$

$$v_{jh_{o1}} = \left[\left(0.87 \sqrt{f'_c} \frac{b_j}{h_j} \right) - 3 \frac{\rho_{vj} f_{yb}}{\sqrt{f'_c}} \right] \left(\frac{\rho_{hj} f_{yb}}{\sqrt{f'_c}} \frac{b_c}{d_c} \right) \left(2.44 \frac{\rho_{tb} f_{yb}}{\sqrt{f'_c}} \right), \quad (6)$$

$$v_{jh_{o2}} = \frac{b_j}{h_j} \left[0.27 \frac{\rho_{tb} f_{yb}}{\sqrt{f'_c}} \right] \left(3 \frac{b_j}{h_j} + f'_c \right), \quad (7)$$

TABLE 2: Previously proposed empirical models.

Name	Empirical formula	Limitations
New Zealand Code of practice (3101-2006) [13]	$V_{jh} \leq \min [0.2f_c' b_j h_j; 10b_j h_c]$	Extending the provisions of exterior joint on corner joint
Chinese Standards 50011:2010 [21]	$V_{jh} \leq (1/\gamma_{RE})(0.3\eta_j \beta_c f_c' b_j h_j)$ $\gamma_{RE} = 0.85$ $\eta_j = 1$	Extending the provisions of interior joint on corner joint
Architectural Institute of Japan [22]	$V_{ju} = k\phi F_j D_j$ $V_{ju} = 0.272 f_c'^{0.7} b_j D_j$ $k = 0.4$	Reduction factor is same for both closing and opening behaviour
American Concrete Institute [24]	$V_n = 0.083 \gamma_c \sqrt{f_c' A_j}$ $V_n = \gamma_c \sqrt{f_c' A_j}$	Reduction factor is same for both closing and opening behaviour
Eurocode 8 [20]	$V_{jhd} = \lambda \eta f_{c,d} \sqrt{(1 - (\nu_d/\eta)) b_j h_j}$ $\eta = 0.6 (1 - (f_{ck}/250))$	Extending the provisions of exterior joint on corner joint
Tariq et al. [25]	$v_{jh_c} = -0.438 / [-1.23 (h_b/h_c)^2] - [-1.23 - (h_b/h_c)] + [f_c' (- (h_b/h_c) / 2.31 (f_c'/f_y))]^{(1/4)} + [(\rho_b f_{yb} / \sqrt{f_c'}) (h_b^2/b_j h_c)] (MPa)$ $v_{jh_o} = 1 / (\rho_b f_y \sqrt{f_c' - 4.967})^{(1/2)} + [1.33 + (h_b/h_c) + (h_b/h_c) - 0.37 (b_j/h_c)] + [1.54 ((f_c'/f_{yb}) - (h_b/h_b)) (h_b/b_b)]^{(1/4)} + [(h_b/b_b)^4 (\rho_b f_{yb} / \sqrt{f_c'})^3] (MPa)$	Does not incorporate the effect joint vertical and horizontal joint transverse reinforcement



$$d_0 = \frac{b_b}{d_b} \quad d_1 = \frac{b_c}{d_b} \quad d_2 = \frac{b_j}{h_j} \quad d_3 = \frac{d_b}{d_c} \quad d_4 = f'_c \quad d_5 = \sqrt{f'_c} \quad d_6 = \frac{\rho_{tb} f_{yb}}{\sqrt{f'_c}} \quad d_7 = \frac{\rho_{hj} f_{yb}}{\sqrt{f'_c}} \quad d_8 = \frac{\rho_{vj} f_{yb}}{\sqrt{f'_c}}$$

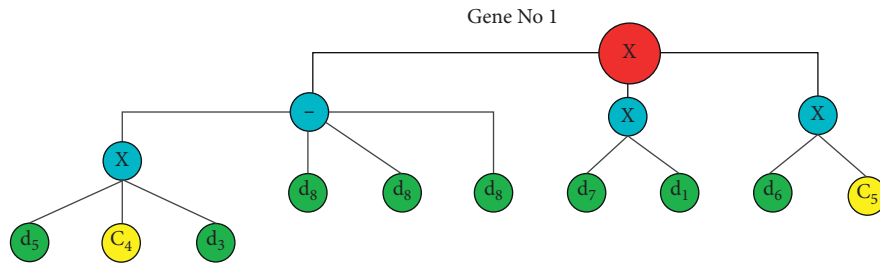
FIGURE 2: Gene expression for the closing model.

$$v_{jh_{o3}} = \left(\frac{b_b}{d_b} \right)^{25} \left(\frac{d_b}{d_c} - \frac{b_j}{h_j} - \frac{b_c}{d_c} - 0.188 \right) \left(3 \frac{\rho_{tb} f_{yb}}{\sqrt{f'_c}} + 0.45 \right), \tag{8}$$

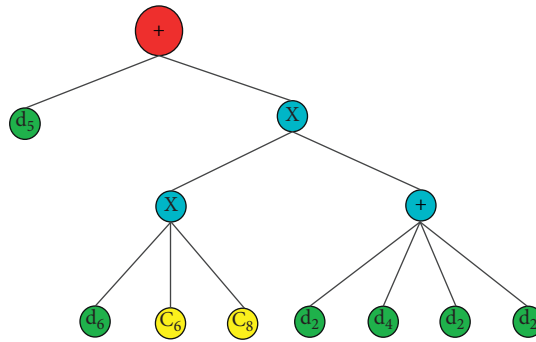
where d_b = depths of beam member, d_c = depth of column members, b_j = joint effective width, h_j = joint effective depth, ρ_{cb} = longitudinal tensile reinforcement under closing, ρ_{tb} = longitudinal tensile reinforcement under opening behavior, ρ_{vj} = represent the joint vertical shear reinforcement, ρ_{hj} represent the joint horizontal shear reinforcement,

f'_c = concrete compressive strength, and f_{yb} = reinforcement tensile yield. Moreover, v_{jh_c} and v_{jh_o} represent the joint shear capacity in MPa.

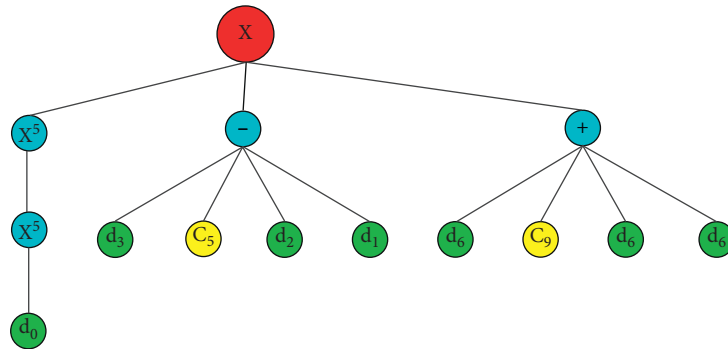
Figures 2 and 3 depict the proposed model for the joint closing and opening capacities, and Table 3 provides some additional details related to the proposed models.



Gene No 2



Gene No 3



Constant	Value
C5	2.43
C4	0.87
C0	-0.51
C8	-0.52
C5	0.19
C9	0.45

$$d_0 = \frac{b_b}{d_b} \quad d_1 = \frac{b_c}{d_b} \quad d_2 = \frac{b_j}{h_j} \quad d_3 = \frac{d_b}{d_c} \quad d_4 = f'_c \quad d_5 = \sqrt{f'_c} \quad d_6 = \frac{\rho_{tb}f_{yb}}{\sqrt{f'_c}} \quad d_7 = \frac{\rho_{hj}f_{yb}}{\sqrt{f'_c}} \quad d_8 = \frac{\rho_{vj}f_{yb}}{\sqrt{f'_c}}$$

FIGURE 3: Gene expression for the opening model.

7. Statistical Assessment of the Proposed Model

After developing any regression-based model, it is essential to set out criteria for evaluating the model's performance. A variety of statistical indicators are available to assess the predictive ability of the model.

The coefficient of variation (CoV) is commonly used to evaluate model performance. CoV can be calculated as follows:

$$CoV (\%) = \left\{ \frac{\sigma}{\mu} \right\} \times 100, \tag{9}$$

TABLE 3: Model construction parameter.

Function set	$+, -, /, \times, x^{1/2}, \sqrt[4]{}, 2, 3, 4, 5$
Chromosomes	100
Head size	5
Linking function	Addition
Number of genes	3
Mutation rate	0.044
Inversion rate	0.1
One-point recombination rate	0.3
Two-point recombination rate	0.3
Gene recombination rate	0.1
Gene transposition rate	0.1
Constants per gene	2
Lower/upper bound of constants	-20/20

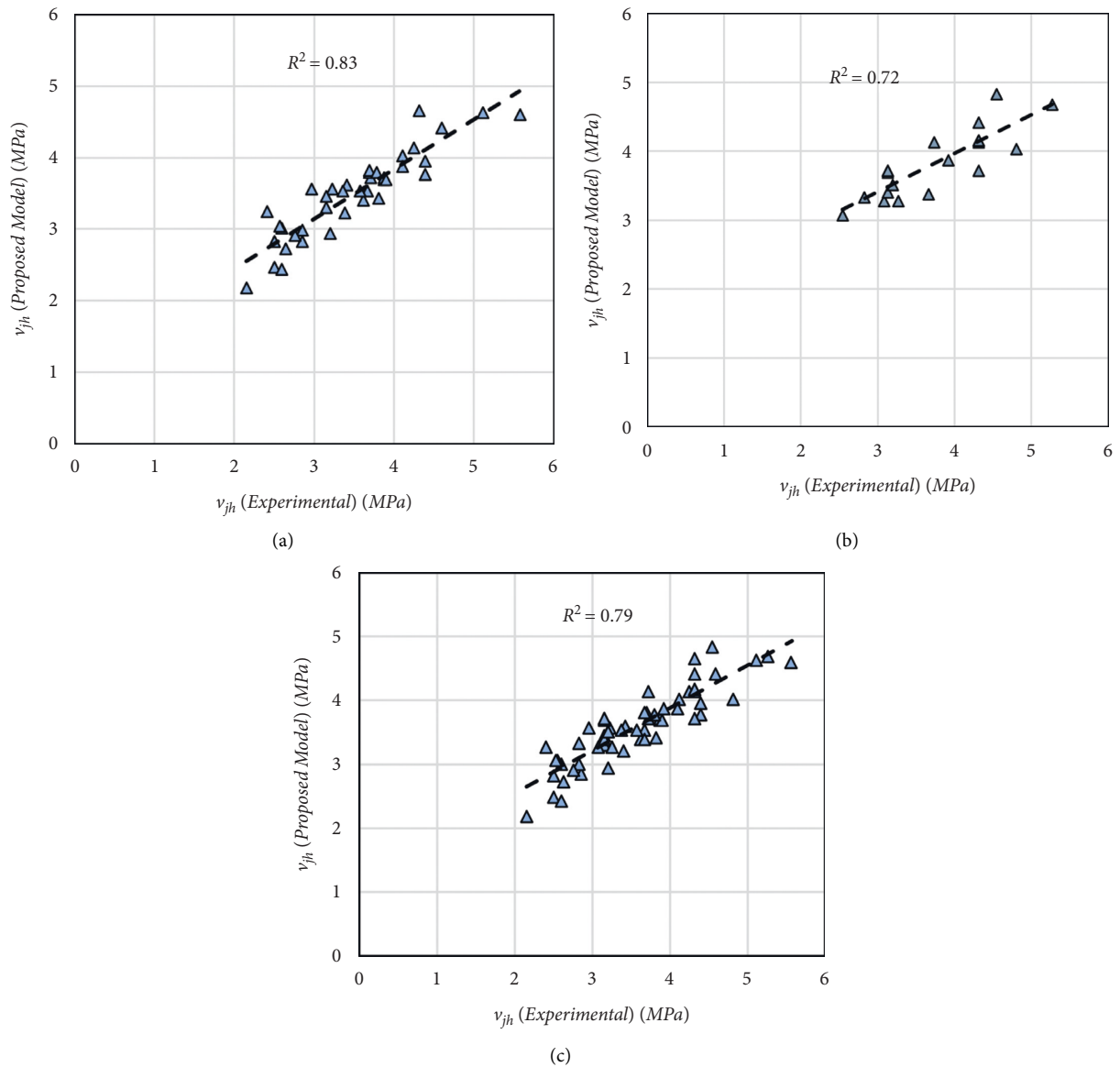


FIGURE 4: Estimated shear strength versus experimental shear strength for joint closing. (a) Training. (b) Validation. (c) All data.

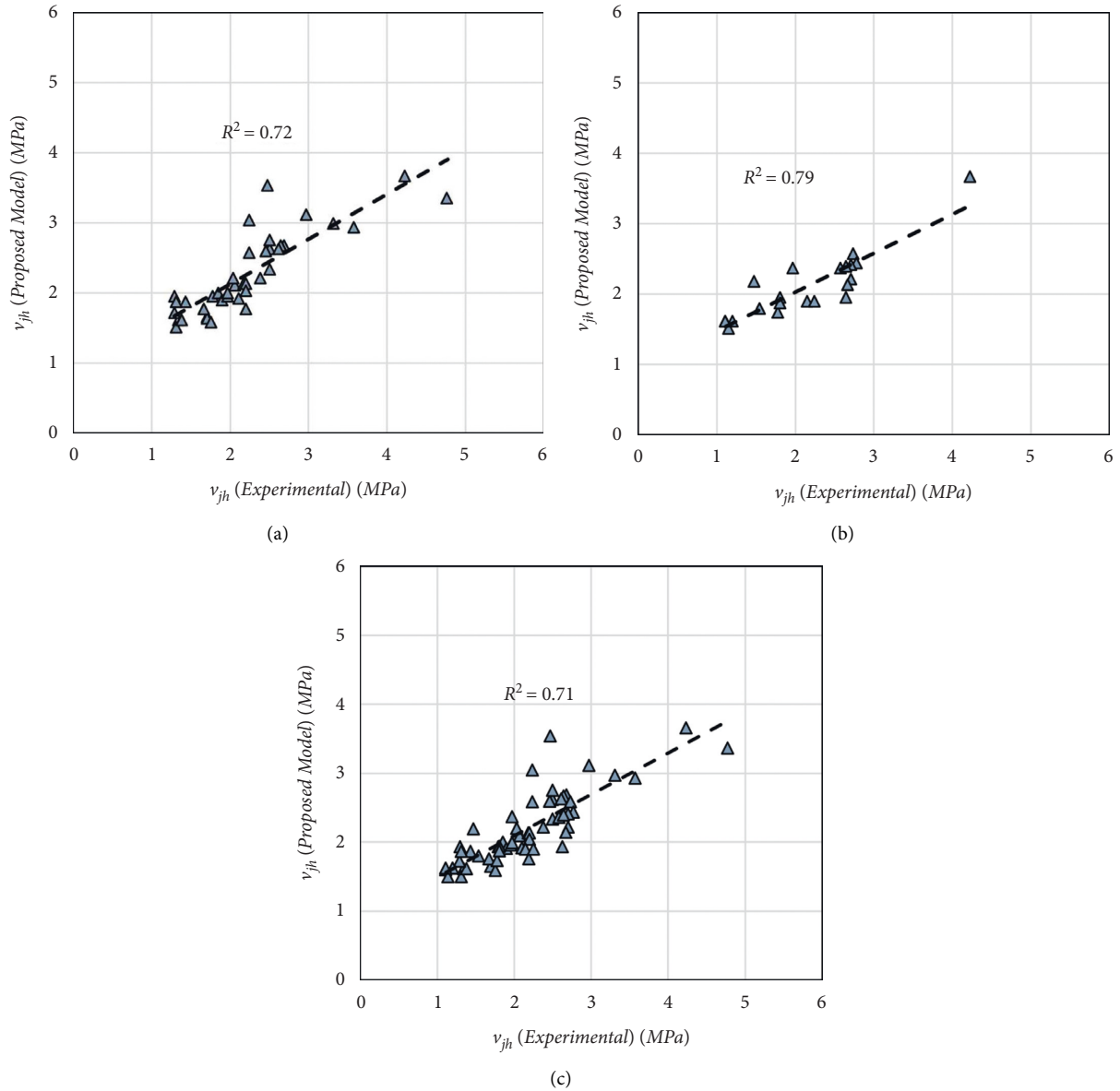


FIGURE 5: Estimated shear strength versus experimental shear strength for joint opening. (a) Training. (b) Validation. (c) All data.

where σ is the standard deviation and μ is the sample mean. A smaller value of CoV indicates less data spread.

The average absolute error (AAE) is another measure of validation. The AAE is defined as follows:

$$AAE(\%) = \frac{1}{n} \sum \left[\frac{|V_{jh}^{Exp} - V_{jh}^{Est}|}{V_{jh}^{Exp}} \right], \quad (10)$$

where n is the number of test specimens.

The performance of the regression model can be challenged by measuring the coefficient of determination (R^2), defined as follows:

$$R^2 = 1 - \frac{\sum [V_{jh}^{Exp} - V_{jh}^{Est}]^2}{\sum [V_{jh}^{Exp} - V_{jh(Mean)}^{Exp}]^2}, \quad (11)$$

where the performance of a model is considered very good if R^2 is close to 1. The performance of the joint closing and opening models is demonstrated in Figures 4 and 5, respectively. As seen in the joint closing model in Figure 4, the coefficient of determination (R^2) is 0.82 for the training, 0.73 for the validation, and 0.79 for the overall data. In the same way, the coefficients for the opening action are 0.72, 0.79, and 0.75, respectively, for the training, the validation, and the overall data. These values clearly show better prediction capability of both the closing and opening models.

Another measure of the prediction accuracy is the t-statistic [77] for the evaluation and comparison of the corner joints. The null hypothesis is $H_0: \mu_D = 0$, where $\mu_D = \text{experimental and predicted shear stress difference (MPa)}$. In comparison, the alternative hypothesis is $H_1: \mu_D \neq 0$. The t-statistic is defined as follows:

TABLE 4: *t*-Statistics results.

Description	Opening		Closing	
	v_{jh}^{Exp} (MPa)	v_{jh}^{Est} (MPa)	v_{jh}^{Exp} (MPa)	v_{jh}^{Est} (MPa)
Mean	2.16	2.20	3.58	3.60
Variance	0.50	0.30	0.58	0.33
Observations	59	59	59	59
Pearson correlation		0.83		0.90
Hypothesized mean difference		0.00		0.00
Df	58	58	58	58
<i>t</i> -stat		-0.32		-0.18
<i>t</i> -critical two-tail		-2.00/2.00		-2.00/2.00

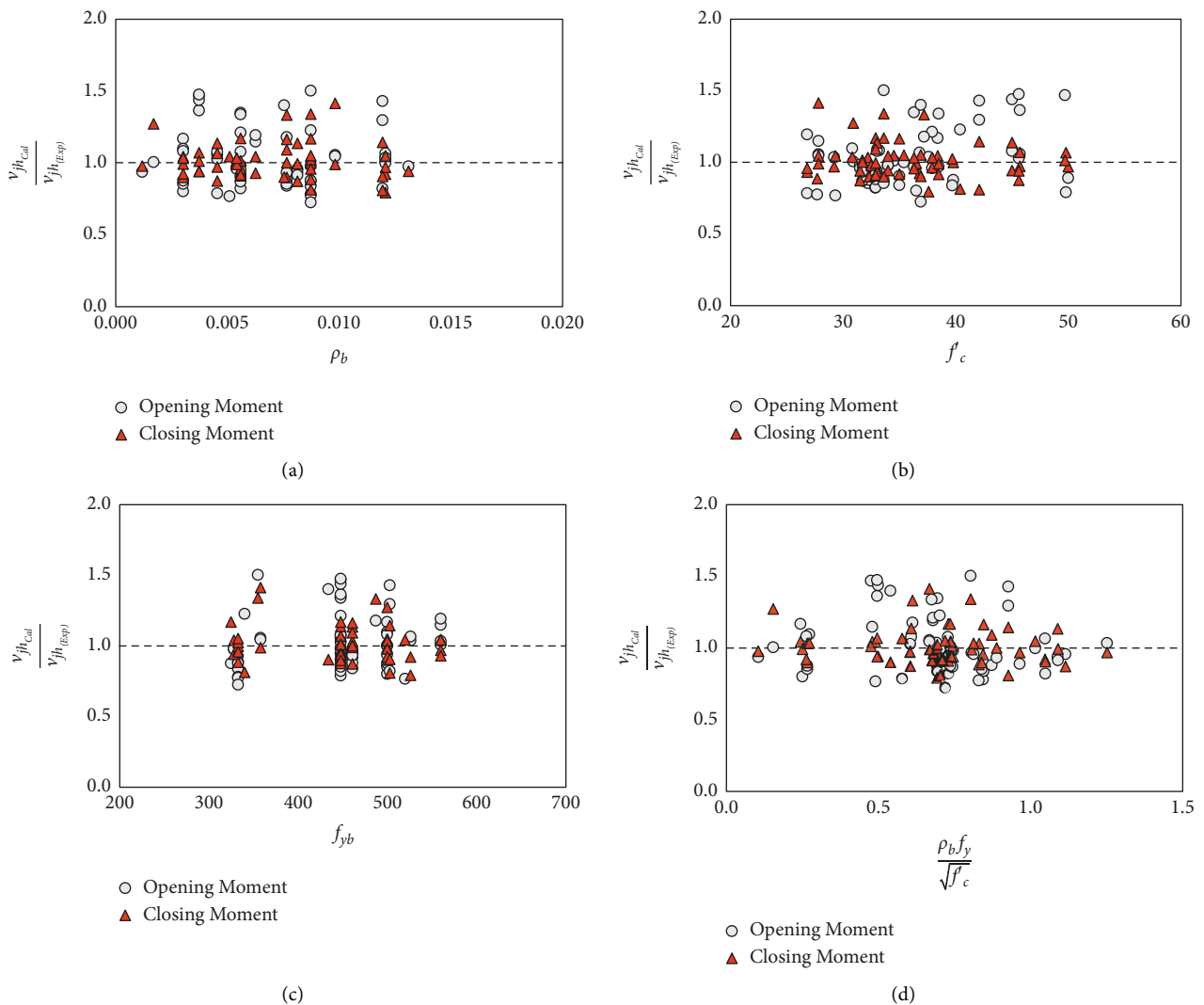


FIGURE 6: Continued.

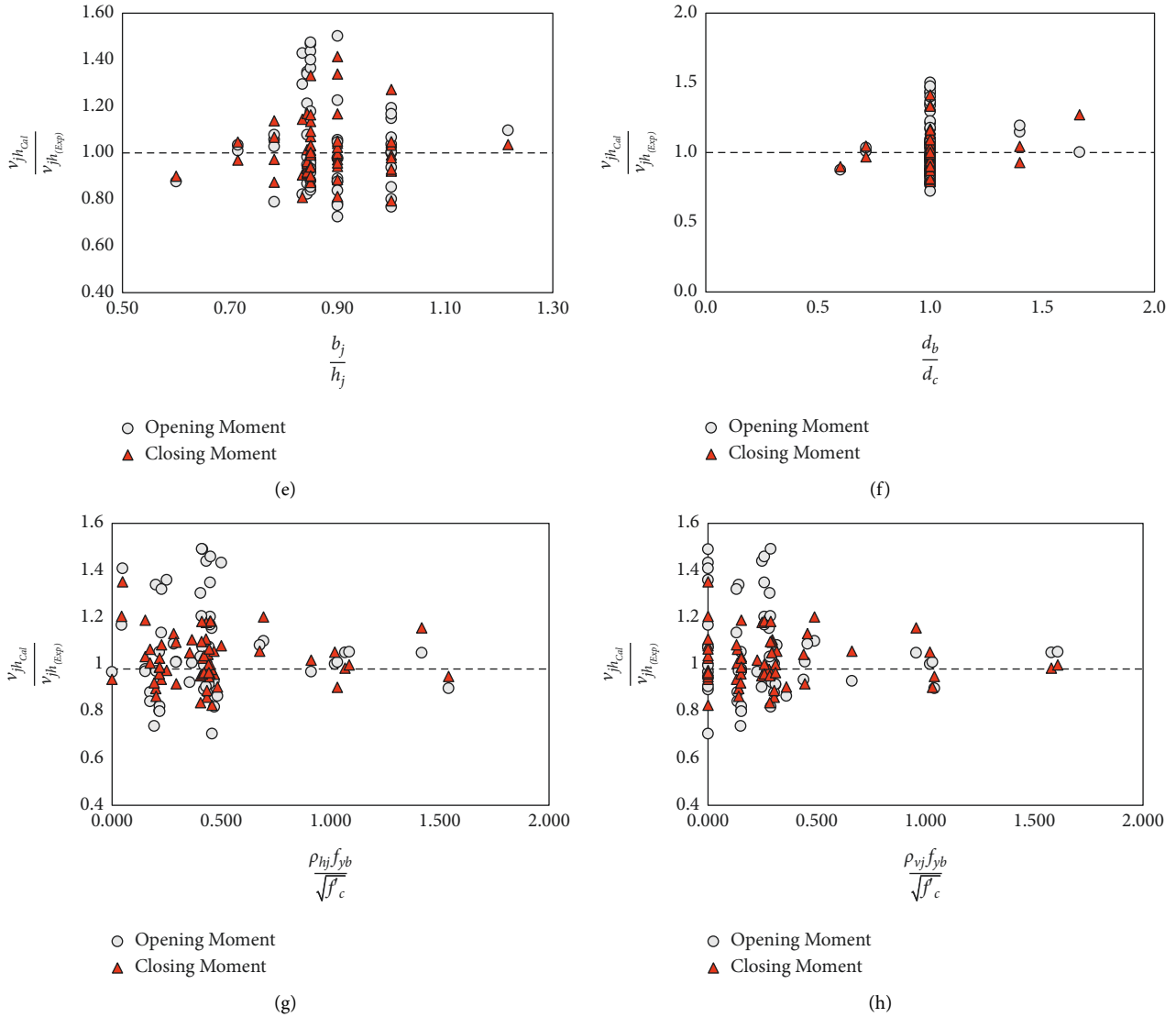


FIGURE 6: Performance of GEP models considering key parameters.

TABLE 5: Joint shear capacity under the closing.

Specimen ID	fc' (MPa)	v_{jh}^{Est} (MPa)	v_{jh}^{Exp} (MPa)	$v_{jh}^{Exp}/v_{jh}^{Est}$	$v_{jh}^{Exp}/v_{jh}^{ACI}$	$v_{jh}^{Exp}/v_{jh}^{Eurocode}$	$v_{jh}^{Exp}/v_{jh}^{NZS\ 3101}$	$v_{jh}^{Exp}/v_{jh}^{AIJ}$	$v_{jh}^{Exp}/v_{jh}^{GB50010}$
Mogili and Kuang [73]									
KJ-NO	37.60	3.60	3.42	0.98	0.84	0.39	0.45	0.90	0.30
KJ-N1	36.80	3.96	4.39	1.02	1.09	0.51	0.60	1.17	0.40
KJ-F0	34.50	3.00	2.60	0.85	0.67	0.32	0.38	0.73	0.25
KJ-F1	29.20	3.21	3.39	0.82	0.94	0.48	0.58	1.06	0.39
KJ-S0	27.80	2.46	2.61	0.74	0.72	0.37	0.45	0.82	0.30
KJ-S1	26.80	2.84	2.85	0.76	0.83	0.44	0.53	0.95	0.35
Zhang [31]									
KJ-NS	38.40	2.43	2.60	0.92	0.63	0.29	0.34	0.67	0.23
KJ-F	36.50	3.29	3.16	1.13	0.79	0.37	0.43	0.85	0.29
KJ2-H12V10	29.30	3.56	2.96	1.01	0.82	0.42	0.51	0.93	0.34
KJ3-H10V12	32.20	2.99	2.84	1.05	0.75	0.37	0.44	0.83	0.29
KJ-H8V10	35.40	2.92	3.19	1.25	0.81	0.39	0.45	0.88	0.30
KJ-BD500	30.90	4.40	4.60	1.36	1.25	0.62	0.74	1.39	0.50
KJ-CW430	30.80	2.90	2.75	1.02	0.75	0.37	0.45	0.83	0.30
KJ-BD700	32.50	4.02	4.11	0.97	1.08	0.53	0.63	1.20	0.42
KJ-CD500	32.30	2.82	2.50	1.11	0.66	0.33	0.39	0.73	0.26

TABLE 5: Continued.

Specimen ID	fc' (MPa)	ν_{jh}^{Est} (MPa)	ν_{jh}^{Exp} (MPa)	$\nu_{jh}^{Exp}/\nu_{jh}^{Est}$	$\nu_{jh}^{Exp}/\nu_{jh}^{ACI}$	$\nu_{jh}^{Exp}/\nu_{jh}^{Eurocode}$	$\nu_{jh}^{Exp}/\nu_{jh}^{NZS3101}$	$\nu_{jh}^{Exp}/\nu_{jh}^{AIJ}$	$\nu_{jh}^{Exp}/\nu_{jh}^{GB50010}$
KJ-CW600	33.20	2.18	2.15	0.78	0.56	0.27	0.32	0.62	0.22
Mazzoni et al. [15]									
KJ#1	42.10	4.13	4.25	1.03	0.99	0.45	0.50	1.03	0.34
KJ#2	42.10	4.64	4.31	1.04	1.00	0.45	0.51	1.05	0.34
KJ#3	32.85	4.60	5.57	1.33	1.18	0.72	0.85	1.61	0.57
Cote and Wallace [16]									
KJ#1	45.70	3.71	3.71	1.06	0.83	0.37	0.41	0.85	0.27
KJ#2	49.80	3.69	3.88	1.09	0.83	0.36	0.39	0.84	0.26
KJ#3	45.00	3.40	3.63	1.04	0.82	0.36	0.40	0.84	0.27
KJ#4	45.60	3.71	3.87	1.10	0.86	0.38	0.42	0.89	0.28
McConnell and Wallace [17]									
KJ#5	31.50	3.88	4.10	1.20	1.10	0.55	0.65	1.22	0.43
KJ#6	33.00	3.52	3.67	1.07	0.96	0.47	0.56	1.06	0.37
KJ#7	32.90	3.77	4.38	1.28	1.15	0.56	0.67	1.27	0.44
KJ#8	36.30	3.80	3.70	1.07	0.93	0.44	0.51	1.00	0.34
KJ#9	38.50	3.42	3.81	1.10	0.92	0.43	0.49	0.99	0.33
KJ#10	37.90	3.70	3.89	1.12	0.95	0.44	0.51	1.02	0.34
KJ#11	35.00	3.82	3.68	1.07	0.94	0.45	0.53	1.02	0.35
KJ#12	32.90	3.53	3.57	1.04	0.94	0.46	0.54	1.03	0.36
KJ#13	31.70	3.79	3.79	1.11	1.01	0.50	0.60	1.12	0.40
Megget [12, 14]									
KJ-1	27.80	3.04	2.56	0.81	0.73	0.38	0.46	0.83	0.31
KJ-2	27.80	2.73	2.64	0.86	0.75	0.39	0.47	0.86	0.32
KJ-3	34.00	3.57	3.23	0.93	0.83	0.40	0.48	0.91	0.32
KJ-4	34.00	3.45	3.15	0.91	0.81	0.39	0.46	0.89	0.31
KJ-5	33.60	3.26	2.41	0.67	0.63	0.30	0.36	0.69	0.24
KJ-6	33.60	3.54	3.37	0.98	0.88	0.43	0.50	0.96	0.33
KJ-7	50.00	4.62	5.11	1.16	1.09	0.47	0.51	1.10	0.34
KJ-8	40.40	3.06	2.54	0.71	0.60	0.28	0.31	0.64	0.21
KJ-9	39.80	3.28	3.08	0.87	0.74	0.34	0.39	0.78	0.26
KJ-10	39.70	3.28	3.26	0.92	0.78	0.36	0.41	0.83	0.27
KJ-11	26.80	3.38	3.67	1.07	0.97	0.56	0.68	1.22	0.46
Angelakos [33]									
KJ-1	45.70	3.72	3.14	0.94	0.70	0.31	0.34	0.72	0.23
KJ-2	49.70	3.70	3.14	0.93	0.67	0.29	0.32	0.68	0.21
KJ-3	45.00	3.40	3.14	0.95	0.71	0.31	0.35	0.73	0.23
KJ-4	45.60	3.72	3.14	0.95	0.70	0.31	0.34	0.72	0.23
KJ-5	31.50	4.84	4.54	1.05	1.22	0.61	0.72	1.35	0.48
KJ-6	33.00	4.43	4.31	1.00	1.13	0.55	0.65	1.24	0.44
KJ-7	32.90	4.69	5.27	1.23	1.38	0.68	0.80	1.52	0.53
KJ-8	36.30	4.13	4.31	1.15	1.08	0.51	0.59	1.16	0.40
KJ-9	38.50	3.73	4.31	1.15	1.05	0.49	0.56	1.12	0.37
KJ-10	37.90	4.02	4.81	1.28	1.18	0.55	0.63	1.26	0.42
KJ-11	35.00	4.16	4.31	1.15	1.10	0.53	0.62	1.19	0.41
KJ-12	32.90	3.88	3.92	1.05	1.03	0.50	0.60	1.13	0.40
KJ-13	31.70	4.16	4.31	1.16	1.15	0.57	0.68	1.28	0.45
KJ-14	33.60	4.13	3.73	1.02	0.97	0.47	0.56	1.06	0.37
KJ-15	36.90	3.34	2.82	0.88	0.70	0.33	0.38	0.75	0.25
KJ-16	37.20	3.52	3.21	0.96	0.79	0.37	0.43	0.85	0.29
Average performance factor				0.99	0.90	0.44	0.51	0.98	0.34

$$t = \frac{\bar{X} - \mu_D}{s/\sqrt{N}}, \quad (12)$$

N = Sample size
 ν = Degree of free do m

where

- \bar{X} = Sample mean difference
- μ_D = Population mean
- s = Standard deviation

The significant level $\alpha = 0.05$ with $\mu = 58$ degrees of freedom.

Table 4 indicates that the $t_{Calculate} < t_{(0.025,60)}$, i.e., $-0.18 < 2.00$ and $-0.32 < 2.00$ for the corner joint under both the closing and the opening, respectively, with a degree

TABLE 6: Joint shear capacity under the opening moment.

Specimen ID	f_c' (MPa)	v_{jh}^{Est} (MPa)	v_{jh}^{Exp} (MPa)	$v_{jh}^{Exp}/v_{jh}^{Est}$	$v_{jh}^{Exp}/v_{jh}^{ACI}$	$v_{jh}^{Exp}/v_{jh}^{Eurocode}$	$v_{jh}^{Exp}/v_{jh}^{NZS3101}$	$v_{jh}^{Exp}/v_{jh}^{AIJ}$	$v_{jh}^{Exp}/v_{jh}^{GB50010}$
Mogili and Kuang [71]									
KJ-NO	37.60	2.68	2.68	0.92	0.86	0.31	0.36	0.71	0.24
KJ-N1	36.80	2.67	2.64	0.90	0.89	0.31	0.36	0.71	0.24
KJ-F0	34.50	3.12	2.97	1.05	0.97	0.37	0.43	0.83	0.29
KJ-F1	29.20	2.98	3.31	1.00	1.28	0.47	0.57	1.04	0.38
KJ-S0	27.80	2.63	2.50	0.83	1.27	0.37	0.45	0.81	0.30
KJ-S1	26.80	2.59	2.46	0.80	1.32	0.38	0.46	0.82	0.31
Zhang [30]									
KJ-NS	38.40	1.65	1.71	1.04	0.81	0.19	0.22	0.44	0.15
KJ-F	36.50	2.34	2.50	1.46	0.85	0.29	0.34	0.67	0.23
KJ2-H12V10	29.30	2.75	2.50	1.08	0.99	0.36	0.43	0.78	0.28
KJ3-H10V12	32.20	2.21	2.38	1.27	0.88	0.31	0.37	0.70	0.25
KJ-H8V10	35.40	2.09	2.07	1.46	0.77	0.25	0.29	0.57	0.19
KJ-BD500	30.90	2.93	3.57	1.68	1.68	0.48	0.58	1.08	0.39
KJ-CW430	30.80	1.94	1.79	0.92	0.83	0.24	0.29	0.54	0.19
KJ-BD700	32.50	2.58	2.24	0.95	1.45	0.29	0.34	0.65	0.23
KJ-CD500	32.30	2.21	2.03	1.32	0.71	0.27	0.31	0.59	0.21
KJ-CW600	33.20	1.65	1.7	0.90	0.92	0.22	0.26	0.49	0.17
Mazzoni et al. [15]									
KJ#1	42.10	3.04	2.24	0.94	0.73	0.24	0.27	0.54	0.18
KJ#2	42.10	3.54	2.47	1.04	0.76	0.26	0.29	0.60	0.20
KJ#3	32.85	4.00	4.77	1.57	1.38	0.61	0.73	1.38	0.48
Cote and Wallace [16]									
KJ#1	45.70	1.61	1.34	0.95	0.76	0.13	0.15	0.31	0.10
KJ#2	49.80	1.59	1.76	1.39	0.97	0.16	0.18	0.38	0.12
KJ#3	45.00	1.50	1.32	0.93	0.79	0.13	0.15	0.31	0.10
KJ#4	45.60	1.61	1.38	0.98	0.78	0.14	0.15	0.32	0.10
McConnell and Wallace [17]									
KJ#5	31.50	2.00	1.86	0.90	1.07	0.25	0.30	0.55	0.20
KJ#6	33.00	1.76	1.67	0.83	0.91	0.21	0.25	0.48	0.17
KJ#7	32.90	1.91	1.90	0.94	0.98	0.24	0.29	0.55	0.19
KJ#8	36.30	1.94	1.3	0.85	0.95	0.19	0.22	0.43	0.15
KJ#9	38.50	1.73	1.29	0.84	0.83	0.17	0.19	0.39	0.13
KJ#10	37.90	1.86	1.43	0.94	0.91	0.20	0.23	0.45	0.15
KJ#11	35.00	1.95	1.96	1.02	0.91	0.24	0.28	0.54	0.19
KJ#12	32.90	1.76	2.19	1.09	1.04	0.28	0.33	0.63	0.22
KJ#13	31.70	1.92	2.10	1.02	0.96	0.28	0.33	0.62	0.22
Megget [12, 14]									
KJ-1	27.80	2.14	2.18	0.84	1.07	0.32	0.39	0.71	0.26
KJ-2	27.80	2.14	2.20	0.85	1.08	0.33	0.40	0.72	0.26
KJ-3	34.00	2.63	2.61	1.06	0.94	0.33	0.38	0.74	0.26
KJ-4	34.00	1.99	1.97	0.94	0.85	0.25	0.29	0.56	0.19
KJ-5	33.60	1.86	1.32	0.61	0.83	0.17	0.20	0.38	0.13
KJ-6	33.60	2.03	2.20	1.05	0.94	0.28	0.33	0.63	0.22
KJ-7	50.00	3.66	3.50	2.05	0.90	0.32	0.35	0.75	0.23
KJ-8	40.40	1.80	1.54	0.84	0.83	0.17	0.19	0.39	0.13
KJ-9	39.80	1.90	2.15	1.16	0.87	0.24	0.27	0.54	0.18
KJ-10	39.70	1.90	2.25	1.21	0.91	0.25	0.28	0.57	0.19
KJ-11	26.80	1.94	2.63	1.08	1.23	0.40	0.49	0.88	0.33
Angelakos [32]									
KJ-1	45.70	1.62	1.20	0.94	0.72	0.13	0.14	0.30	0.09
KJ-2	49.70	1.60	1.11	0.96	0.65	0.11	0.12	0.26	0.08
KJ-3	45.00	1.50	1.14	0.93	0.76	0.13	0.14	0.30	0.10
KJ-4	45.60	1.62	1.11	0.89	0.69	0.12	0.13	0.28	0.09
KJ-5	31.50	2.58	2.73	1.13	1.55	0.36	0.43	0.81	0.29
KJ-6	33.00	2.22	2.7	1.12	1.39	0.33	0.39	0.75	0.26
KJ-7	32.90	2.44	2.77	1.07	1.27	0.32	0.38	0.72	0.25
KJ-8	36.30	1.94	1.81	0.96	1.06	0.21	0.25	0.49	0.17
KJ-9	38.50	1.73	1.78	0.99	0.98	0.20	0.23	0.46	0.15
KJ-10	37.90	1.87	1.81	1.00	0.96	0.21	0.24	0.47	0.16

TABLE 6: Continued.

Specimen ID	f_c' (MPa)	v_{jh}^{Est} (MPa)	v_{jh}^{Exp} (MPa)	$v_{jh}^{Exp}/v_{jh}^{Est}$	$v_{jh}^{Exp}/v_{jh}^{ACI}$	$v_{jh}^{Exp}/v_{jh}^{Eurocode}$	$v_{jh}^{Exp}/v_{jh}^{NZS3101}$	$v_{jh}^{Exp}/v_{jh}^{AIJ}$	$v_{jh}^{Exp}/v_{jh}^{GB50010}$
KJ-11	35.00	2.41	2.70	1.06	1.05	0.28	0.33	0.64	0.22
KJ-12	32.90	2.14	2.67	1.05	1.12	0.31	0.36	0.69	0.24
KJ-13	31.70	2.36	2.58	1.04	1.10	0.32	0.38	0.72	0.26
KJ-14	33.60	2.39	2.64	1.04	1.08	0.29	0.34	0.65	0.23
KJ-15	36.90	2.19	1.47	0.94	0.86	0.22	0.26	0.51	0.17
KJ-16	37.20	2.38	1.97	0.93	0.88	0.23	0.26	0.52	0.18
Average performance factor				1.00	0.99	0.30	0.32	0.60	0.21

TABLE 7: Statistical parameters of shear strength GEP model under the closing moment.

Author	$PF = v_{jh}^{Exp}/v_{jh}^{Est}$ Mean	Std. deviation	COV (%)	AAE (%)	R^2
Mogili et al. [32]	1.13	0.190	17.3	15.0	0.34
Kim et al. [74]	1.28	0.28	28.0	21.0	0.02
ACI 352R [24]	0.90	0.180	20.0	22.0	0.07
Eurocode [20]	0.44	0.101	23.0	141.8	0.02
Chinese code [21]	0.34	0.083	24.5	212.6	0.02
Newzealand standard [13]	0.51	0.125	24.5	108.4	0.001
Architectural institute of Japan [22]	0.98	0.210	23.0	19.7	0.95
Megget [12, 14]	0.34	0.240	24.0	30.4	0.02
McConnell and Wallace [17]	1.03	0.224	22.0	17.8	0.001
Wallace et al. [72]	1.20	0.260	22.0	19.0	0.02
Angelakos [33]	1.20	0.260	22.0	19.0	0.02
Priestly et al. [11]	1.26	0.274	22.0	20.9	0.02
Tariq et al. [25]	0.98	0.130	13.0	10.0	0.49
Proposed	1.00	0.127	12.7	9.4	0.79

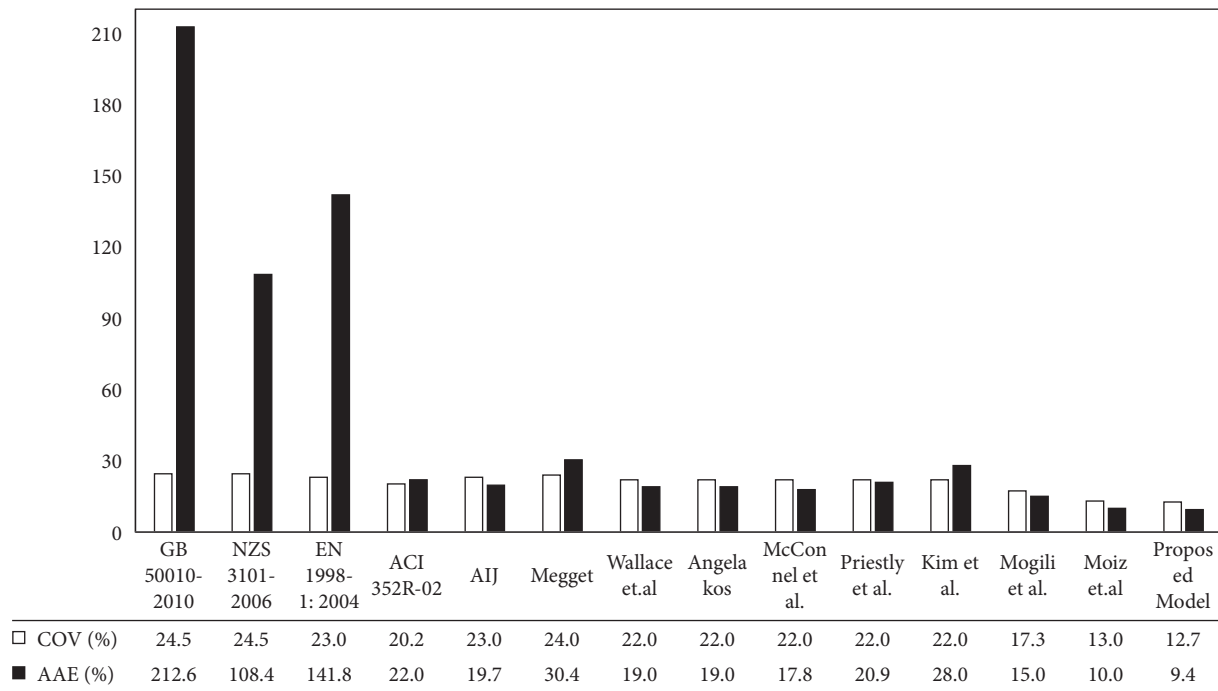


FIGURE 7: Statistical measures of the predicted values against the available models (joint closing).

of freedom (ν) = 60 and not in the rejection region. Therefore, the null hypothesis is accepted at a 5% significance level.

In addition to the above-given statistical indicators, the overall performance of both the opening and the closing models can be examined by varying the levels of the primary

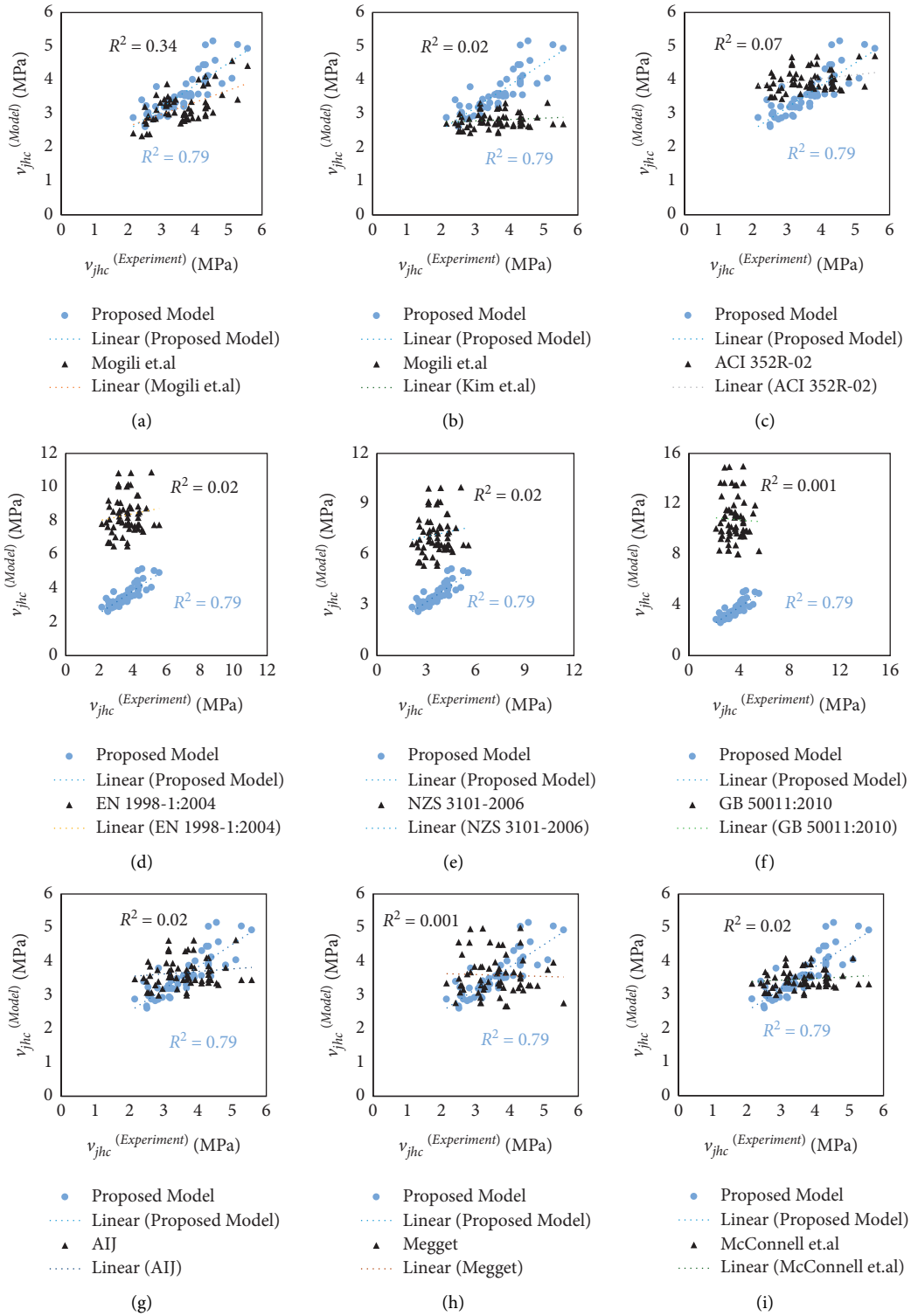


FIGURE 8: Continued.

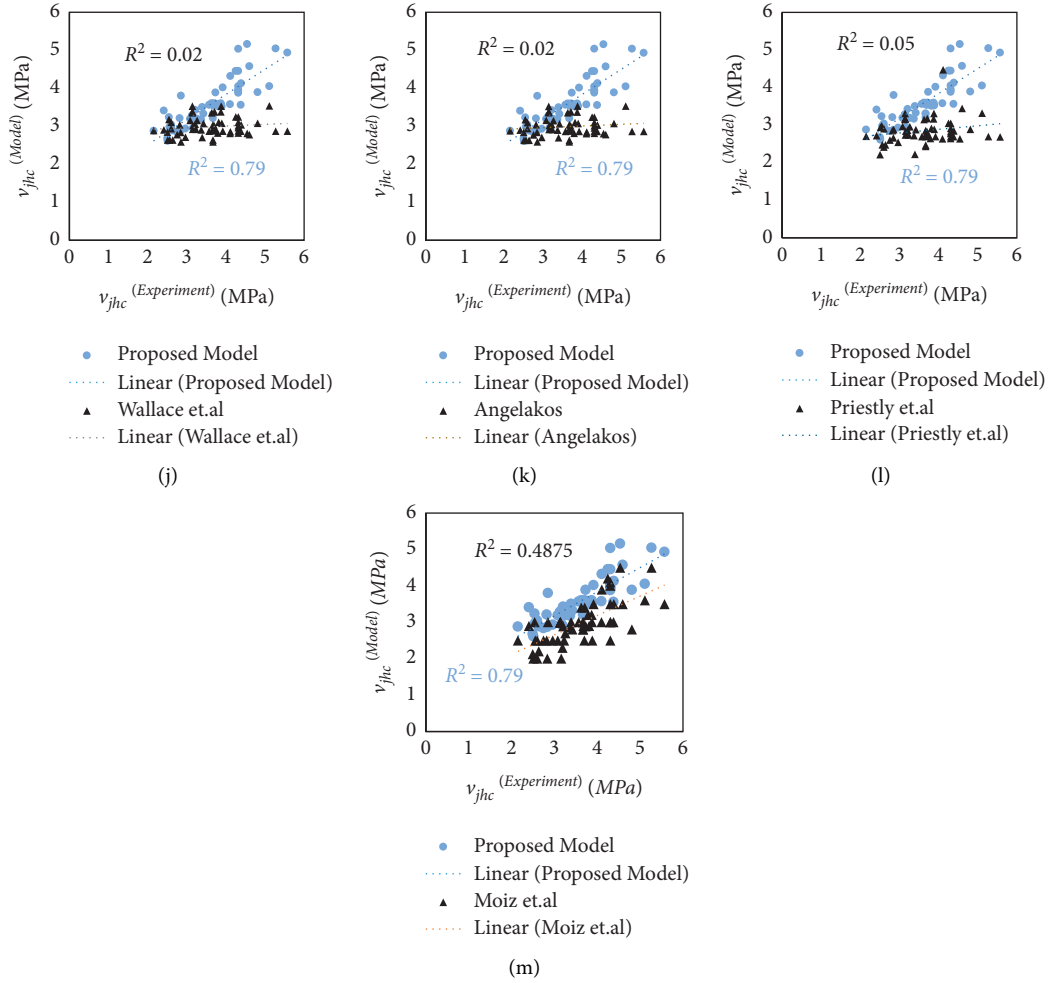


FIGURE 8: Correlation analysis of corner joint shear strength subject to closing: (a) Proposed equation (b) Mogili et al. (c) Kim et al. (d) American concrete institute (e) Euro code 8 (f) New Zealand standard (g) Chinese seismic standard (h) Architectural Institute of Japan (i) Megget et al. (j) McConnell et al. (k) Angelakos et al. (l) Priestly et al. (m) Moiz et al.

TABLE 8: Statistical parameters of shear strength GEP model under an opening moment.

Author	$PF = v_{jh}^{Exp} / v_{jh}^{Est}$ Mean	Std. deviation	COV (%)	AAE (%)	R^2
Mogili et al. [32]	0.98	0.210	22.0	18.0	0.45
Kim et al. [74]	0.79	0.260	31.0	46.0	0.13
ACI 352R [24]	0.55	0.160	29.0	101.0	0.03
Eurocode [20]	0.27	0.097	36.0	323.0	0.14
Chinese code 2011 [21]	0.21	0.079	37.0	450.3	0.14
Newzealand standard 2006 [13]	0.31	0.113	36.0	266.8	0.14
Architectural institue of Japan [22]	0.61	0.200	33.0	87.3	0.14
Megget [12, 14]	0.62	0.214	34.0	81.4	0.13
McConnell et al. [17]	0.63	0.192	31.0	73.6	0.14
Wallace et al. [72]	0.73	0.223	31.0	51.4	0.14
Angelakos [33]	0.73	0.223	31.0	51.4	0.14
Priestly et al. [11]	0.77	0.250	32.4	47.1	0.03
Tariq et al. [25]	1.00	0.220	22.0	18.0	0.50
Proposed	1.00	0.200	20.0	16.0	0.71

influencing parameters. Figure 6 demonstrates the variation of the joint shear strength ratio (ratio of shear calculated to the experimental value) with $\rho_b, f'_c, f_{yb}, \rho_b f_y / \sqrt{f'_c}, h_b / h_c,$

$b_j / h_c, \rho_{vj} f_{yb} / \sqrt{f'_c}, \rho_{hj} f_{yb} / \sqrt{f'_c}$ and for opening and closing behavior. This shear strength ratio shows a virtual average of 1.00 within the interval [0.7, 1.5] in Figure 6(a)

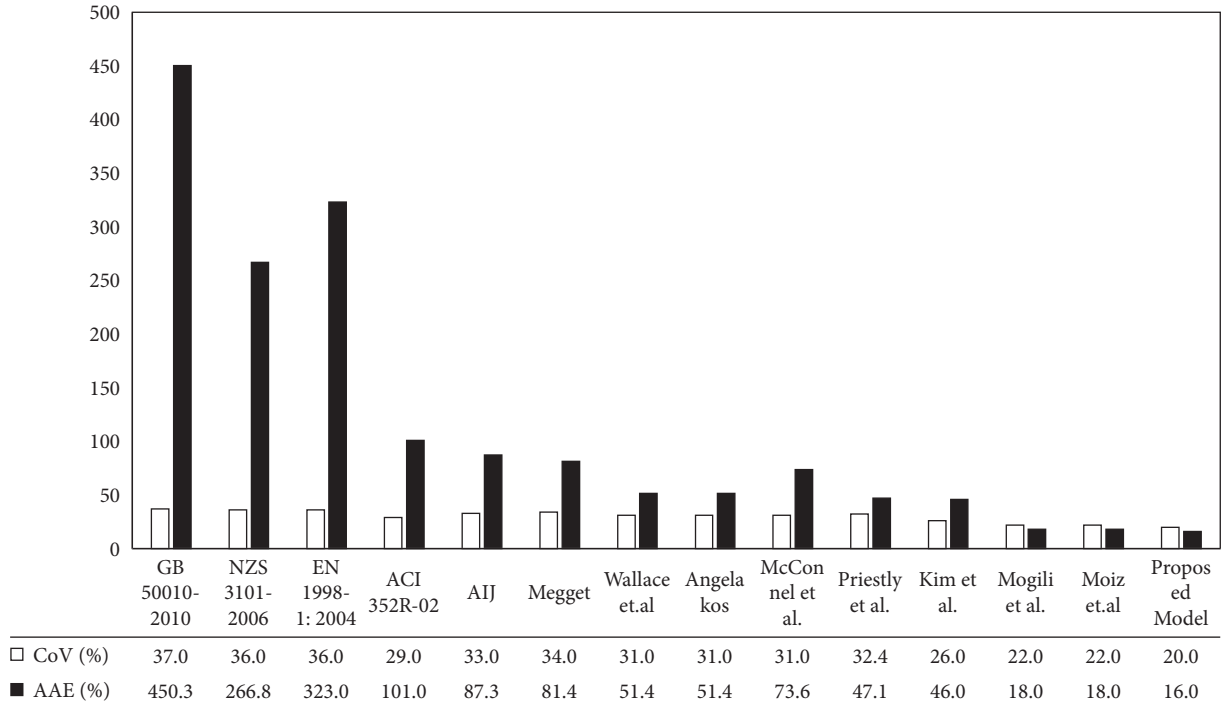


FIGURE 9: Statistical measures of the predicted values against the available models (joint opening).

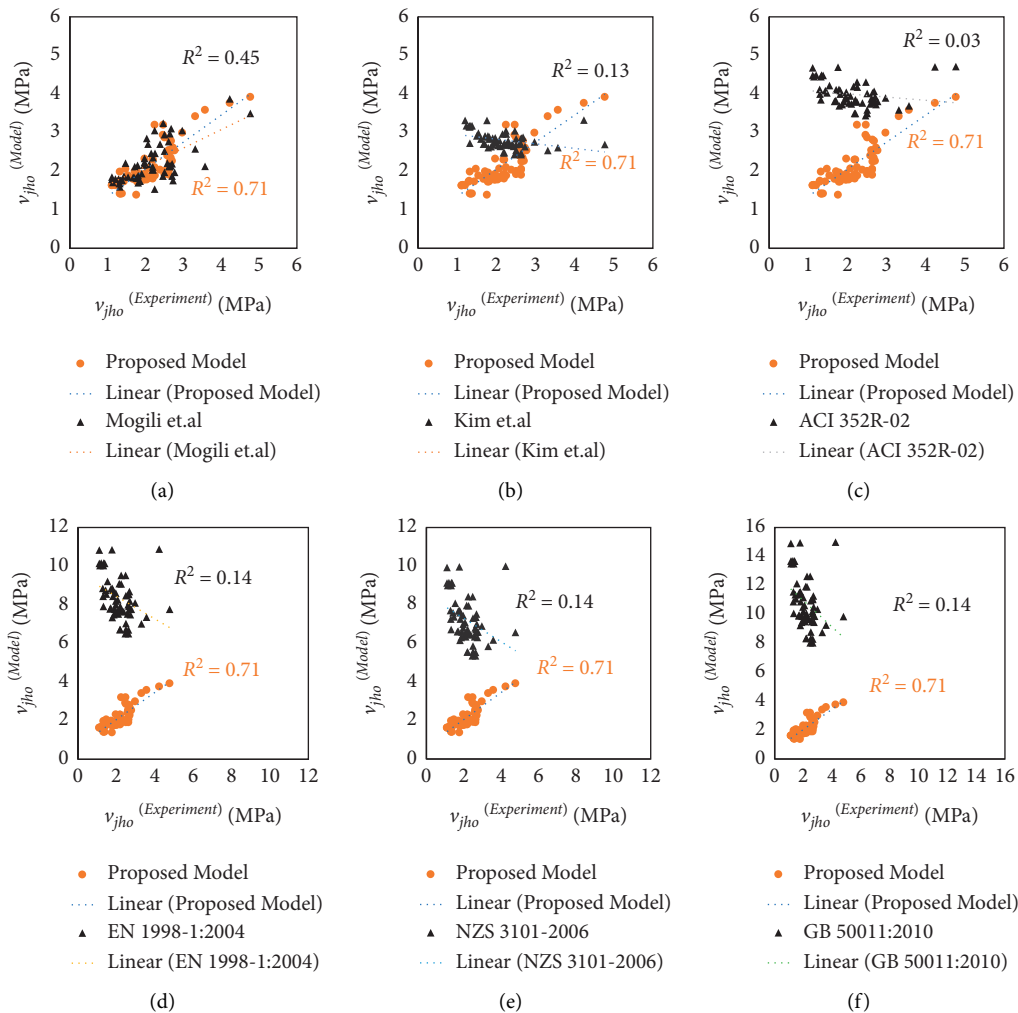


FIGURE 10: Continued.

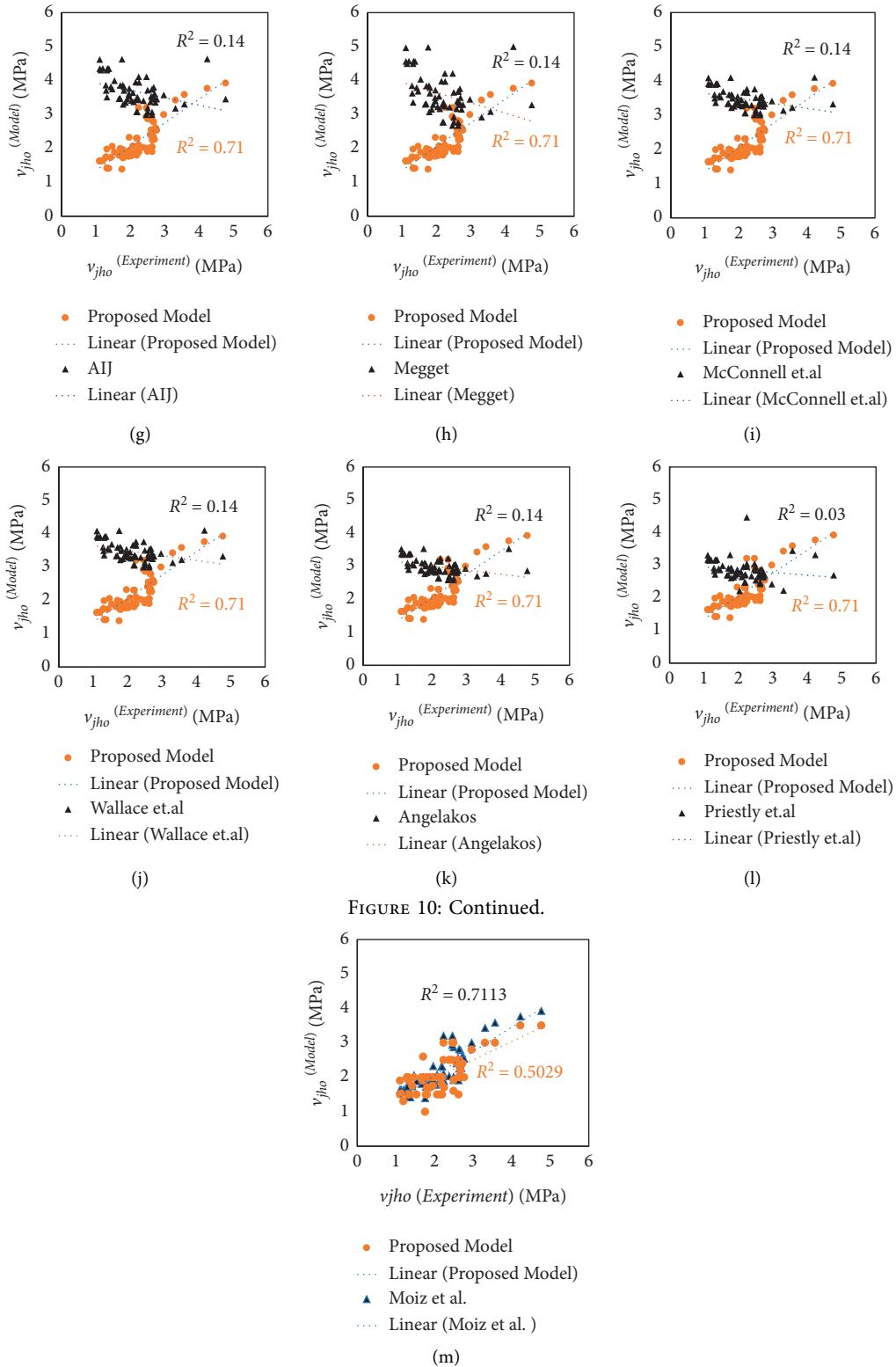


FIGURE 10: Continued.

FIGURE 10: Correlation analysis of corner joint shear strength subject to opening (a) Proposed equation (b) Mogili et al. (c) Kim et al. (d) American concrete institute (e) Euro code 8 Proposed equation (b) Mogili et al. (c) Kim et al. (d) American concrete institute (e) Euro code 8 (f) New Zealand standard (g) Chinese seismic standards (h) Architectural Institute of Japan (i) Megget et al. (j) McConnell et al. (k) Anglakos et al. (l) Priestly et al. (m) Moiz et al.

corresponding to various levels of ρ_b , which represents the suitable model performance in both closing and opening.

Similarly, in Figure 6(b), it is shown that the results of the joint shear strength ratio are comparable in terms of f'_c values. Even though the proposed joint shear model is slightly overestimated for the case of the experimental joint specimens with higher f'_c , the model performance is adequate within the interval [0.7, 1.5]. Generally speaking, the closed-joint performed better than their open-joint counterparts.

Better results are also obtained for f_{yb} , the index of $\rho_b f_y / \sqrt{f'_c}$, b_j/h_c , h_b/h_c , horizontal shear reinforcement, and vertical shear reinforcement, as is clear from Figure 6(c) till 6(h). In short, the foregoing shows that the proposed model shows better predictive performance.

8. Results and Discussions

The robustness and the predictive capability of the proposed GEP models can be assessed by comparing the results with the existing models. The existing models are either available in literature or adopted by the code of practices. The database comprising the shear strength tests is reported in Tables 5 and 6.

8.1. Assessment of Shear Capacity GEP Model during Joint Closing. The overall performance of the proposed joint closing model can be assessed from the comparison results of Table 7. The results of the previous models indicate that the closing joint shear strength is not estimated accurately, mainly due to the omission of important influencing factors in the models. For instance, the models proposed by various codes of practices incorporate the influence of only three key parameters, thus resulting in lower accuracy. The table shows that the model proposed by Moiz et al. [25] provides acceptable accuracy, although this model omits the influence of the joint shear reinforcement ratio. The proposed model incorporating all the important influencing parameters possesses the highest value of the coefficient of determination ($R^2 = 0.79$), and the lowest value of both the coefficient of variation (CoV = 12.7) and the average absolute error (AAE = 9.4%), which clearly shows the accuracy and reliability of the model. Apart from the Moiz et al. [25] model, all the other models have the coefficient of determination of less than 50%. Similarly, the performance factor of the formulations proposed by the code of practices is less than 50%. The comparison of these models is also shown in Figures 7 and 8. These results surely confirm robust predictions of the current model compared to all the other models.

8.2. Assessment of Shear Capacity GEP Model during Joint Opening. The performance of the joint opening model can be assessed from the comparison results of Table 8. Clearly, the previous models do not predict the shear strength accurately because they overlook the influence of key factors in the models. For instance, the models proposed by various

codes of practices incorporate only three influencing parameters, thus resulting in lower accuracy. Again, the model proposed by Moiz et al. [25] provides acceptable accuracy during the joint opening, although this model omits the influence of the joint shear reinforcement ratio. The proposed model possesses the highest value of the coefficient of determination ($R^2 = 0.71$), and the lowest value of both the coefficient of variation (CoV = 20) and the average absolute error (AAE = 16%), which clearly shows the accuracy and reliability of the model. Apart from the Moiz et al. [25] model, all the other models have the coefficient of determination of less than 50%. Likewise, the performance factor of the formulations proposed by the code of practices is less than 50%. The comparison of these models is also shown in Figures 9 and 10. These results surely confirm robust predictions of the opening joint model compared to all the other models.

8.3. Practical Application. Both the opening and closing models can be used for calibration and prediction of corner joint shear strength because the models are based on a wider range of influencing parameters. Therefore, the corner joint shear behavior can be quantitatively assessed for different values of key parameters. Being able to be easily implemented in Excel or MATLAB, the quantitative assessment can offer a useful tool for design and engineering decisions.

9. Conclusion

Based on the algorithm of the Gene Expression Program (GEP), two shear strength prediction models are established and the results are compared with other models. Specifically, one of the models is capable of determining the shear strength during the corner joint closing, and the other during the joint opening. The conclusions of the current study are outlined as follows:

- (i) Sensitivity and parametric study identified the main influencing factors as the geometric properties of the structural elements, the joint aspect ratio, the tensile strength of steel, the concrete compressive strength, and the longitudinal tensile reinforcement ratio.
- (ii) Based on the dataset of 59 experiments, the corner joint closing model shows the best performance with the average absolute error (AAE) of 9.4%, Coefficient of variation (CoV) of 12.7%, the coefficient of determination (R^2) of 0.79, and the performance factors of 1.01.
- (iii) The results of the corner joint opening model show the average absolute error (AAE) of 16.0%, the Coefficient of variation (CoV) of 20% the coefficient of determination (R^2) of 0.75, and the performance factors of 1.04. These all prove the efficacy of the model.
- (iv) The performance of both models is checked against the expressions proposed by various design building

codes. These models show better prediction of corner joint shear strength than codes, such as American Concrete Institute (ACI 352R-02) [24], Architectural Institute of Japan (AIJ) [22], New Zealand Code of practice (NZS 3101-2006) [13] and Chinese Code of practice [21] and Eurocode (EN 1998-1:2004) [20].

Data Availability

The data used to support the study are included in the paper.

Conflicts of Interest

The authors declare that they have no conflicts of interest.

References

- [1] J. Shafaei and S. A. Nezami, "Effect of different size of joint enlargement on seismic behavior of gravity load designed RC beam-column connections," *The Structural Design of Tall and Special Buildings*, vol. 28, pp. 1–27, 2019.
- [2] S. Pampanin, G. M. Calvi, and M. Moratti, "Seismic behaviour of RC beam-column joints designed for gravity loads," *12th Eur Conf Earthq Eng*, vol. 726, pp. 1–10, 2002.
- [3] U. Akguzel and S. Pampanin, "Assessment and design procedure for the seismic retrofit of reinforced concrete beam-column joints using FRP composite materials," *Journal of Composites for Construction*, vol. 16, pp. 21–34, 2012.
- [4] N. Mitra and L. N. Lowes, "Evaluation, calibration, and verification of a reinforced concrete beam-column joint model," *Journal of Structural Engineering*, vol. 133, pp. 105–120, 2007.
- [5] P. G. Bakir and H. M. Bodurođlu, "A new design equation for predicting the joint shear strength of monotonically loaded exterior beam-column joints," *Engineering Structures*, vol. 24, pp. 1105–1117, 2002.
- [6] M. L. Moretti, T. P. Tassios, and E. Vintzileou, "Behavior and design of corner joints under opening bending moment," *ACI Structural Journal*, vol. 111, pp. 3–13, 2014.
- [7] L. N. Lowes and A. Altoontash, "Modeling reinforced-concrete beam-column joints subjected to cyclic loading," *Journal of Structural Engineering*, vol. 129, pp. 1686–1697, 2003.
- [8] U. Akguzel and S. Pampanin, "Effects of variation of axial load and bidirectional loading on seismic performance of GFRP retrofitted reinforced concrete exterior beam-column joints," *Journal of Composites for Construction*, vol. 14, pp. 94–104, 2010.
- [9] G. L. Wang, J. G. Dai, and J. G. Teng, "Shear strength model for RC beam-column joints under seismic loading," *Engineering Structures*, vol. 40, pp. 350–360, 2012.
- [10] M. Anderson, D. Lehman, and J. Stanton, "A cyclic shear stress-strain model for joints without transverse reinforcement," *Engineering Structures*, vol. 30, pp. 941–954, 2008.
- [11] M. J. N. Priestley, F. Seible, and G. Calvi, *Seismic Design and Retrofit of Bridge*, John Wiley & Sons, NJ, USA, 1st edition, 1996.
- [12] L. M. Meggeta, "The seismic design and performance of reinforced concrete beam-column knee joints in buildings," *Earthquake Spectra*, vol. 19, pp. 863–895, 2003.
- [13] "Concrete Structures Standard," 2006.
- [14] L. M. Megget, "The seismic behaviour of small reinforced concrete beam-column knee joints," *Bull New Zeal Natl Soc Earthq Eng*, vol. 31, pp. 215–245, 1998.
- [15] S. Mazzoni, J. P. Moehle, and C. R. Thewalt, *Cyclic response of RC beam-column knee joints test and retrofit*, University of California, CA, USA, 1991.
- [16] P. A. Cote and J. W. Wallace, "A study of reinforced concrete knee-joints subjected to cyclic lateral loading," vol. 94, pp. 1–154, 1994, Rep No CU/CEE.
- [17] S. W. McConnell and J. W. Wallace, *Behavior of Reinforced Concrete Beam-Column Knee-Joints Subjected to Reversed Cyclic Loading*, vol. 95, 1995.
- [18] N. Zhang, J. S. Kuang, and S. Mogili, *Cyclic Behaviour of Reinforced Concrete Beam-Column Knee Joints*, 16th World Conf. Earthq. Eng. 16WCEE, 2017.
- [19] S. Mogili and J. S. Kuang, "Cyclic vulnerability of RC knee connections under relatively high opening shear stresses," in *16th Eur Conf Earthq Eng*, Thessaloniki, Greece, June 2018.
- [20] EN 1998-1, *Eurocode 8: Design of Structures for Earthquake Resistance—Part 1: General Rules, Seismic Actions and Rules for Buildings*, CEN European Committee for Standardization, Brussels, Belgium, 2004.
- [21] The People's Republic of China National Standard, "GB50010-2010: Code for Seismic Design of Buildings," p. 237, 2010.
- [22] "Architectural Institute of Japan," *Structural Design Guidelines for Reinforced concrete Buildings*, 1999.
- [23] A. Concrete Institute, "An ACI Standard Building Code Requirements for Structural Concrete (ACI 318-19) Commentary on Building Code Requirements," 2016.
- [24] J. A.-A. Committee, "Recommendations for Design of Beam-Column Connections in Monolithic Reinforced Concrete Structures," vol. 02, 2010.
- [25] M. Tariq, A. Khan, J. Shayanfar, M. U. Hanif, and A. Ullah, "A regression model for predicting the shear strength of RC knee joint subjected to opening and closing moment," *Journal of Building Engineering*, vol. 41, Article ID 102727, 2021.
- [26] S. J. Hwang and H. J. Lee, "Analytical model for predicting the shear strength of exterior reinforced concrete beam-column joints," *ACI Structural Journal*, vol. 96, pp. 846–858, 1999.
- [27] T. T. C. Hsu, "Softened truss model theory for shear and torsion," *ACI Structural Journal*, vol. 85, pp. 624–635, 1988.
- [28] S. H. F. Wong and J. S. Kuang, "Predicting shear strength of RC exterior beam-column joints by modified rotating-angle softened-truss model," *Computers and Concrete*, vol. 8, pp. 59–70, 2011.
- [29] X. B. Pang and T. T. C. Hsu, "Fixed angle softened truss model for reinforced concrete," *ACI Structural Journal*, vol. 93, pp. 197–207, 1996.
- [30] M. Pauletta, D. Di Luca, and G. Russo, "Exterior beam column joints - shear strength model and design formula," *Engineering Structures*, vol. 94, pp. 70–81, 2015.
- [31] N. Zhang, *Seismic Performance and Shear Strength of Reinforced Concrete Beam-Column Knee Joints*, The Hong Kong University of Science and Technology, Hong Kong, China, 2017.
- [32] S. Mogili, J. S. Kuang, and S. J. Hwang, "Predicting shear strength of reinforced concrete knee joints in closing and opening actions," *Journal of Structural Engineering*, vol. 146, pp. 1–11, 2020.
- [33] B. Angelakos, "The Behavior of Reinforced concrete Knee Joints under Earthquake Loads," 1999.
- [34] A. C. Lynn, J. P. Moehle, S. A. Mahin, and W. T. Holmes, "Seismic evaluation of existing reinforced concrete building columns," *Earthquake Spectra*, vol. 12, pp. 715–739, 1996.

- [35] H. Sezen, *Seismic Behavior and Modeling of Reinforced concrete Building Columns*, University of California at Berkeley, CA, USA, 2002.
- [36] H. Ousalem, T. Kabeyasawa, A. Tasai, and Y. Ohsugi, "Experimental study on seismic behavior of reinforced concrete columns under constant and variable axial loadings," *Proc Japan Concr Inst*, vol. 24, pp. 229–234, 2002.
- [37] K. Elwood and J. P. Moehle, "Shake Table Tests and Analytical Studies on the Gravity Load Collapse of Reinforced concrete Frames," 2003.
- [38] K. J. Elwood, "Modelling failures in existing reinforced concrete columns," *Canadian Journal of Civil Engineering*, vol. 31, pp. 846–859, 2004.
- [39] K. J. Elwood and J. P. Moehle, "Axial capacity model for shear-damaged columns," *ACI Structural Journal*, vol. 102, pp. 578–587, 2005.
- [40] K. J. Elwood and J. P. Moehle, "Drift capacity of reinforced concrete columns with light transverse reinforcement," *Earthquake Spectra*, vol. 21, pp. 71–89, 2005.
- [41] C. Del Vecchio, M. Del Zoppo, M. Di Ludovico, G. M. Verderame, and A. Prota, "Comparison of available shear strength models for non-conforming reinforced concrete columns," *Engineering Structures*, vol. 148, pp. 312–327, 2017.
- [42] M. J. N. Priestley, R. Verma, and Y. Xiao, "Seismic shear strength of reinforced concrete columns," *Journal of Structural Engineering*, vol. 120, pp. 2310–2329, 1994.
- [43] J. C. M. Ho and H. J. Pam, "Inelastic design of low-axially loaded high-strength reinforced concrete columns," *Engineering Structures*, vol. 25, pp. 1083–1096, 2003.
- [44] M. Moretti and T. P. Tassios, "Behaviour of short columns subjected to cyclic shear displacements: experimental results," *Engineering Structures*, vol. 29, pp. 2018–2029, 2007.
- [45] M. Ascheim and J. P. Moehle, "Shear strength and deformability of RC bridge columns subjected to inelastic cyclic displacements," Rep to Calif Dep Transp Rep No UCBIERC-92J04 Earthq Eng Res Center, 1992.
- [46] H. Sezen and J. P. Moehle, "Shear strength model for lightly reinforced concrete columns," *Journal of Structural Engineering*, vol. 130, pp. 1692–1703, 2004.
- [47] H. G. Park, K. K. Choi, and J. K. Wight, "Strain-based shear strength model for slender beams without web reinforcement," *ACI Structural Journal*, vol. 104, pp. 638–639, 2007.
- [48] H. G. Park, E. J. Yu, and K. K. Choi, "Shear-strength degradation model for RC columns subjected to cyclic loading," *Engineering Structures*, vol. 34, pp. 187–197, 2012.
- [49] H. G. Park, S. Kang, and K. K. Choi, "Analytical model for shear strength of ordinary and prestressed concrete beams," *Engineering Structures*, vol. 46, pp. 94–103, 2013.
- [50] a Niroomandi, S. Pampanin, and R. Dhakal, "Comparison of alternative assessment procedures to predict seismic performance of RC columns," *Tenth Pacific Conf. Earthq. Eng. (PCEE)*, pp. 1–10, 2015.
- [51] E. Osorio, J. M. Bairán, and A. R. Mari, "Analytical modeling of reinforced concrete columns subjected to bidirectional shear," *Engineering Structures*, vol. 138, pp. 458–472, 2017.
- [52] A. Nouali and M. Matallah, "A simplified approach to assess the size effect on the shear-flexure interaction in RC elements," *Engineering Structures*, vol. 144, pp. 151–162, 2017.
- [53] S. Pampanin, G. Magenes, and A. Carr, "Modelling of shear hinge mechanism in poorly detailed RC beam-column joints," *Proc. fib Symp. 2003 Concr. Struct. Seism. Reg.*, pp. 126–127, 2003.
- [54] L. N. Lowes and A. Altoontash, "Modeling reinforced-concrete beam-column joints subjected to cyclic loading," *Journal of Structural Engineering*, vol. 129, pp. 1686–1697, 2003.
- [55] M. Shin and J. M. Lafave, "Modeling of cyclic joint shear deformation contributions in RC beam-column connections to overall frame behavior," *Structural Engineering & Mechanics*, vol. 18, pp. 645–669, 2004.
- [56] H. F. Wong, *Shear Strength and Seismic Performance of Non-seismically Designed Reinforced concrete Beam-Column Joints*, pp. 205–230, Hong Kong Univ Sci Technol, Hong Kong, China, 2005.
- [57] N. Mitra and L. N. Lowes, "Evaluation, calibration, and verification of a reinforced concrete beam-column joint model," *Journal of Structural Engineering*, vol. 133, pp. 105–120, 2007.
- [58] M. J. Favvata, B. A. Izzuddin, and C. G. Karayannis, "Modelling exterior beam-column joints for seismic analysis of RC frame structures," *Earthquake Engineering & Structural Dynamics*, vol. 37, pp. 1527–1548, 2008.
- [59] O. C. Celik and B. R. Ellingwood, "Seismic fragilities for non-ductile reinforced concrete frames - role of aleatoric and epistemic uncertainties," *Structural Safety*, vol. 32, pp. 1–12, 2010.
- [60] A. Niroomandi, A. Maheri, M. R. Maheri, and S. S. Mahini, "Seismic performance of ordinary RC frames retrofitted at joints by FRP sheets," *Engineering Structures*, vol. 32, pp. 2326–2336, 2010.
- [61] A. Sharma, R. Eligehausen, and G. R. Reddy, "A new model to simulate joint shear behavior of poorly detailed beam-column connections in RC structures under seismic loads, Part I: exterior joints," *Engineering Structures*, vol. 33, pp. 1034–1051, 2011.
- [62] A. Niroomandi, M. A. Najafgholipour, and H. R. Ronagh, "Numerical investigation of the affecting parameters on the shear failure of Nonductile RC exterior joints," *Engineering Failure Analysis*, vol. 46, pp. 62–75, 2014.
- [63] M. J. Favvata and C. G. Karayannis, "Influence of pinching effect of exterior joints on the seismic behavior of RC frames," *Earthq Struct*, vol. 6, pp. 89–110, 2014.
- [64] J. Shafaei, M. S. Zareian, A. Hosseini, and M. S. Marefat, "Effects of joint flexibility on lateral response of reinforced concrete frames," *Engineering Structures*, vol. 81, pp. 412–431, 2014.
- [65] J. S. Jeon, L. N. Lowes, R. DesRoches, and I. Brilakis, "Fragility curves for non-ductile reinforced concrete frames that exhibit different component response mechanisms," *Engineering Structures*, vol. 85, pp. 127–143, 2015.
- [66] M. Omid and F. Behnamfar, "A numerical model for simulation of RC beam-column connections," *Engineering Structures*, vol. 88, pp. 51–73, 2015.
- [67] A. Borghini, F. Gusella, and A. Vignoli, "Seismic vulnerability of existing R.C. buildings: a simplified numerical model to analyse the influence of the beam-column joints collapse," *Engineering Structures*, vol. 121, pp. 19–29, 2016.
- [68] J. Shayanfar and H. A. Bengar, "Numerical model to simulate shear behaviour of RC joints and columns," *Computers and Concrete*, vol. 18, pp. 877–901, 2016.
- [69] J. Shayanfar, H. Akbarzadeh Bengar, and A. Niroomandi, "A proposed model for predicting nonlinear behavior of RC joints under seismic loads," *Materials & Design*, vol. 95, pp. 563–579, 2016.
- [70] M. Laterza, M. D'Amato, and R. Gigliotti, "Modeling of gravity-designed RC sub-assemblages subjected to lateral loads," *Engineering Structures J*, vol. 130, pp. 242–260, 2017.

- [71] J. Kim and J. M. LaFave, "Key influence parameters for the joint shear behaviour of reinforced concrete (RC) beam-column connections," *Engineering Structures*, vol. 29, pp. 2523–2539, 2007.
- [72] J. W. Wallace, S. W. McConnell, P. Gupta, and P. A. Cote, "Use of headed reinforcement in beam-column joints subjected to earthquake loads," *ACI Structural Journal*, vol. 95, pp. 590–606, 1998.
- [73] S. Mogili and J. S. Kuang, "Reversed cyclic performance of reinforced concrete knee joints under variable closing and opening stresses," *Engineering Structures*, vol. 178, pp. 116–127, 2019.
- [74] J. Kim, M. James, and J. M. LaFave, "A simplified approach to joint shear behavior prediction of RC beam-column connections," *Earthquake Spectra*, vol. 28, pp. 1071–1096, 2012.
- [75] J. R. Koza, "Genetic programming as a means for programming computers by natural selection," *Statistics and Computing*, vol. 4, pp. 87–112, 1994.
- [76] M. Tariq, A. Khan, A. Ullah, J. Shayanfar, and M. Niaz, "Improved shear strength prediction model of steel fiber reinforced concrete beams by adopting gene expression programming," *Materials*, vol. 15, p. 3758, 2022.
- [77] W. Navidi, "Statistics for Engineers and Scientists," 2011.

Review Article

Building Information Modeling and Internet of Things Integration in the Construction Industry: A Scoping Study

Baydaa Hashim Mohammed ^{1,2}, **Hasimi Sallehuddin**,¹ **Nurhizam Safie**,¹
Afifuddin Husairi,³ **Nur Azaliah Abu Bakar**,⁴ **Farashazillah Yahya**,⁵ **Ihsan Ali** ⁶,
and Shaymaa AbdelGhany Mohamed⁷

¹Faculty of Information Science and Technology, Universiti Kebangsaan Malaysia, Bangi 43600, Selangor, Malaysia

²Medical Instrumentation Department, AL-Esraa University College, Baghdad, Iraq

³Pusat Citra Universiti, Universiti Kebangsaan Malaysia (UKM), Bangi 43600, Selangor, Malaysia

⁴Razak Faculty of Technology and Informatics, Universiti Teknologi Malaysia, Kuala Lumpur, Malaysia

⁵Faculty of Computing Informatics, Universiti Malaysia Sabah, Sabah, Malaysia

⁶Department of Computer System and Technology, Faculty of Computer Science and Information Technology, University of Malaya, Kuala Lumpur 50603, Malaysia

⁷University of Technology, Baghdad, Iraq

Correspondence should be addressed to Baydaa Hashim Mohammed; baidaa81@gmail.com

Received 28 January 2022; Accepted 5 May 2022; Published 1 June 2022

Academic Editor: Abdul Razzaq Ghumman

Copyright © 2022 Baydaa Hashim Mohammed et al. This is an open access article distributed under the Creative Commons Attribution License, which permits unrestricted use, distribution, and reproduction in any medium, provided the original work is properly cited.

Building Information Modeling (BIM) has emerged as a prospective technology used to advance the practices of construction projects. Also, Internet of Things (IoT), as a technology that connects sensing devices to share information across platforms, has become essential in building and construction environment. The integration of BIM-IoT in the construction industry, a high-risk industry, might increase overall performance and reduce related hazards. However, there is a dearth of studies on the integration of BIM and IoT in the construction industry. Scoping review of literature was performed using various databases such as IEEE Xplore, Science Direct, ACM, Emerald Insight, and Taylors & Francis databases to explore the study demographics, research direction, category, adoption, and performance of the BIM-IoT integration for the construction industry. Out of 2270 articles identified, a total of 81 key and vital articles were found and collected in scoping review to formulate the research questions. The study results revealed that the literature related to BIM-IoT integration and adoption is moderately steady, with constant output in the last four years. Twelve of the contributions were identified, and five were identified to be proposed more and conducted by researchers: investigation, evaluation, model, framework, and system. Also, fifteen (18.51%) studies were identified from the selected works that were evaluated using performance measurement. The findings shed light on some of the most significant difficulties in research related to BIM-IoT integration in the construction industries as well as potential future initiatives.

1. Introduction

Of recent, Building Information Modeling (BIM) has emerged as a prospective technology used to advance the delivery practices of construction projects. A project that utilized BIM is generally accurate and sustainable [1, 2]. Conversely, the Internet of Things (IoT), as a technology that connects sensing devices to share information across

platforms, has become essential in building and construction environment. BIM adoption in the construction industry has been rigorously studied in the last decade [3–7]. Also, the factors that affect its adoption are examined and critically studied. However, the incorporation of BIM and IoT devices is a relatively innovative development. Generally, BIM and IoT complement each other by providing a key view of a given project. Hence, the two technologies supplement each

other's limitations [8–10]. BIM provides a high depiction of the project at the component level, while IoT improves this information by offering a real-time feed of operations in construction and operation.

Therefore, real-time data integration and BIM-IoT adoption provide a strong archetype for applications to increase construction operation efficiencies. Hence, the connection of real-time data from the speedily growing set of IoT sensor networks to the highly reliable BIM models offers many benefits. In recent years, various reviews and survey papers were published on BIM adoption and its integration with various technologies [1, 11–23, 26]. Also, Baydaa et al. conducted a systematic mapping study on the integration of BIM and IoT technologies. The study gives the trends and current challenges in the field of study [27]. However, based on our knowledge, no scoping review on integrating and adopting BIM-IoT technologies in the construction industry was found. Hence, in this study, we aim to fill this research gap.

This paper utilized a scoping review methodology that is evidence-based to guarantee that significant investigations on BIM and IoT coordination and appropriation in the development business in the previous decade (2011–2021) are found and gathered. The approach has a thorough determination and assessment strategies with a repeatable studies selection cycle. Also, this work gives results with regards to the studies selected overall characteristics and demographics, and the research focus of the studies selected. Besides, the contributions of the papers selected, the construction industry attitude toward the integration and adoption of BIM and IoT technologies, and the performance measures used in the research area were also reported. The key contributions of this paper are outlined as follows:

- (i) A broad systematic review on BIM- IoT integration and adoption.
- (ii) The critical synthesis of the current literature in the exploration area.
- (iii) The identification of current challenges in the research area with areas that require more attention from the researchers.

Several studies have reported the applications of BIM in various dimensions. Eadie et al. surveyed the alleged changes necessary for adopting and accepting BIM in the United Kingdom (UK). The current issues and implications were outlined by the authors [11]. Jacobsson and Merschbrock also reviewed the BIM coordinator's role, practices, and responsibilities in the construction industry. The authors highlight the primary responsibilities of coordinators concerning the studied publications [12]. A review was done in a study by Noor and Yi to map out BIM utilization in the construction industry. The authors further highlight the existing research gaps [13]. Moreover, Jin et al. review recent studies on the BIM acceptance and application in the construction industry. The authors also gave future research directions for further research [14]. A study by Al-Yami and Sanni-Anibire highlights the current state of BIM implementation in Saudi Arabia. Furthermore, the advantages and obstacles of BIM implementation were presented [15].

Another study by Ayam and Al-Ghamdi presented a review of BIM and green buildings. The shortcomings and issues of BIM in green buildings are discussed and articulated [16].

Dixit et al. also conducted a review on integrating BIM and facility management (FM) in the construction industry. The key issues and challenges in the research area were highlighted and discussed [17]. A survey in [18] examines the main advantages of BIM implementation and sustainability practices in the construction industry. The study identified the advantages of BIM adoption and sustainability practices. Moreover, Witt and Kohkonen conducted a systematic review of BIM-enabled education [19]. Issues and challenges were further outlined. Another study also conducted a review on BIM for construction education [20].

A review of the integration of BIM and IoT devices was conducted by Tang et al. [1]. The authors highlight the trends in the field of study. In another review by Wang et al., a review on integrating BIM and geographical information systems (GIS) in a sustainable built environment was conducted [21]. Furthermore, a bibliometric analysis was also given by the authors. Another paper also works on BIM integration with existing technologies [22]. The research in [23, 24] explores the recent works on BIM for off-site construction. The authors also identify some key research trends and gaps in the area of study. Also, Baydaa et al. conducted a systematic mapping study on the integration of BIM and IoT technologies. The study gives the trends and current challenges in the field of study [25]. Recent papers also conducted an extensive review on BIM in the construction industry [26–28]. However, no scoping review works on BIM and IoT devices integration and adoption in the construction industry based on the identified review studies. Hence, this study aims to close this research gap.

2. Research Method

To conduct a scoping review, the finding, assessment, interpretation, and reporting of the related research in a given field is required by a researcher [29]. This study was based on [30, 31] studies. This method was designed to allow the inclusion of quality studies and give a comprehensive overview of a study field. Thus, to lead a scoping review, a search plan must be used that is clear and impartial. Subsequently, the search plan needs to ensure the culmination of the search [32, 33]. Currently, to the best of our knowledge, no scoping review paper gives a critical review and analysis of existing research on the integration or adoption of BIM-IoT technologies in the construction industry. Hence, this work aim is to close the gap in research. The current scoping review process comprises many stages that have to be done in an organized and orderly manner. These stages shown in Figure 1 comprise the building of the paper protocol in terms of formulating the appropriate research questions, the conduction of the review, the analysis of the acquired results, results in visualization, results on reporting, and lastly, a discussion of the outcome.

2.1. Research Questions. This study aims to understand works on the integration or adoption of BIM-IoT technologies in the

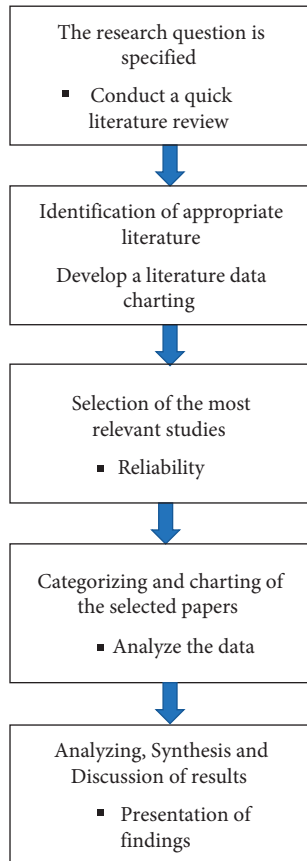


FIGURE 1: The schematic representation of the approach adopted in the scoping review.

construction industry. For a complete outlook of this research area, the study outlines, and answers five vital research questions (RQs). These RQs will help categorize further and understand the current works to find the limitations and future works proposed in the domain. The five defined RQs are given as follows:

- (i) RQ1: what are the selected studies, demographics, and characteristics?
- (ii) RQ2: what is the research focus of the selected studies?
- (iii) RQ3: what are the contributions proposed by the selected studies, and how they can be categorized?
- (iv) RQ4: what theories are used to study BIM adoption by the selected studies?
- (v) RQ5: what are the different performance measures used in the research domain?

2.2. Data Sources. Normally, Table 1 features the five databases used for essential works retrieval. Thus, we believed these databases to be the prime hotspots for recovering any potentially related works in this examination.

2.3. Search Terms. To effectively locate the papers, key terms are essential for the search. Keele [29] reported that

TABLE 1: The data sources.

Database name	Link
IEEE Xplore	https://ieeexplore.ieee.org/
Science Direct	https://sciencedirect.com/
ACM	https://dl.acm.org/
Emerald Insight	https://emerald.com/insight/
Taylor & Francis	https://tandfonline.com/

population, intervention, comparison, and outcome (PICO) viewpoints were adopted by various SLRs and mapping works [34–36]. The following are the search terms for the viewpoints:

- (i) Population: BIM and IoT
- (ii) Intervention: integration and adoption
- (iii) Outcome: construction and AEC

In this investigation, regarding the PICO structure's overall premise, we built a conventional Search string to continue searching on numerous databases. Therefore, to lead the programmed search, the blueprint nonexclusive Search string fills in as a guide.

Generic: ((Building information modeling OR BIM) OR (Internet of things OR IoT) AND (Integration OR adoption) AND (construction OR AEC))

Because each database has unique interfaces for advanced search, these particular search strings were utilized on the five selected databases to search for related articles. In Table 2, the search string for each database is presented.

2.4. Studies on Selection Procedure. In this stage (study choice cycle), the primary point is to distinguish successfully considers that are critical to our investigation's goals. In Figure 2, the examination choice technique (SSP) of this investigation is introduced. The examination choice cycle is in three stages; every one of these stages was refined through a top to bottom agreement meeting between the scientists to ensure high certainty with the least predisposition in the investigation SSP. Consequently, if a specific report is in different sources, we just bring one into considered concerning our hunt request. We at first discovered 2270 examination through our search. The examination's query items were coordinated for various searchers by the 1st author, the 2nd author, the 3rd author, and the 4th author. The authors also conduct an early screening of the 2270 studies retrieved regarding their titles, abstracts, and conclusion. Hence, for each screened, the study was examined by two researchers so as to agree if the study is to be added lastly. Hence, for a study that was critic contrarily, further deliberation was conducted by the two researchers who done the examination of studies they find concrete agreement. The purpose of this evaluation was to largely eliminate works that were obviously not significant, duplicate, or studies that did not tackle the issue of integration or adoption of BIM-IoT technologies in the construction industry.

2.5. Inclusion and Exclusion Criteria. In the mission to answer the characterized RQs in this study, we planned and

TABLE 2: Search strings.

Database name	Search string
IEEE Xplore	“Document Title”: Building information modeling) OR “Document Title”: BIM) OR “Document Title”: internet of things) OR “Document Title”: IoT AND “Abstract”: integration) OR “Abstract”: adoption) AND “All Metadata”: construction) OR “All Metadata”: AEC)
Science Direct	BIM, IoT, construction, AEC
ACM	[[Publication Title: building information modeling] OR [[Publication Title: bim] AND [Publication Title: internet of things]] OR [Publication Title: iot]] AND [[Abstract: integration] OR [Abstract: adoption]] AND [[Abstract: construction] OR [Abstract: aec]]
Emerald Insight	Title: “building information modeling” OR (title: “internet of things”) AND (abstract: “integration”) OR (abstract: “adoption”) AND (abstract: “construction”) OR (abstract: “AEC”)
Taylor & Francis	[Publication Title: building information modeling] AND [All: construction] AND [[All: industry] OR [All: aec]]

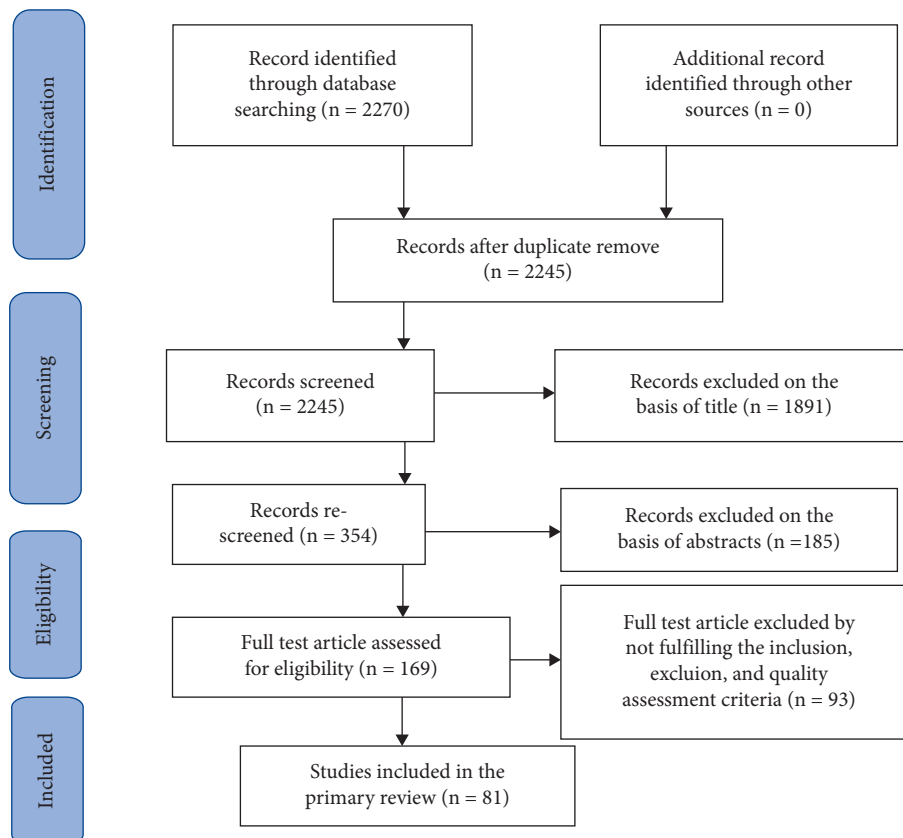


FIGURE 2: Studies of selection procedure.

utilized all around expressed consideration (IC) and avoidance (EC) measures to help in picking forthcoming investigations from the chose information bases. The rules were utilized on all the examinations gathered in the various degrees of the SSP. The period was set from 2011 to 2021 (11 years) for contemplates search, and this is to ensure that modern investigations were the just one’s incorporated. We likewise incorporate early referred to contemplates, as long as the full examination content was accessible.

In Table 3, we delineated the IC and EC standards utilized in this SLR. These rules were used in the second and third SSP degrees (as portrayed in Figure 1). The IC and EC models were utilized on the subsequent level, dependent on the investigations’ titles, modified works, and ends. In this

manner, 169 out of 354 examinations were separated in the subsequent level. In the third level, to improve the certainty on examinations inclusion, we used a snowballing methodology on 169 full text considers inspected. On a similar note, a retrogressive and forward snowballing was directed. For in reverse snowballing, the analysts search through investigation reference rundown and eliminate considers that do not meet this examination’s models. For forward snowballing, the specialists investigated the examinations dependent on the examinations’ referring to the assessed investigation. With this, each examination referring to a specific report is assessed. Consequently, in this investigation, we consider incorporating and avoiding an examination dependent on the measures in Table 3 and the quality

TABLE 3: Inclusion/exclusion criteria.

Inclusion criteria	
IC1	Papers which are peer-reviewed
IC2	Papers that concentrate on BIM and IoT integration or adoption in the construction industry
IC3	Important papers published from 2011 to 2021
IC4	Papers that have the prospective to answer the formulated RQs
Exclusion criteria	
EC1	Papers that are written in other languages that are not English
EC2	Papers that are not related to the research questions
EC3	Gray studies: for illustration, articles with no data such as publication date/type, volume, and issue numbers were removed
EC4	Duplicate studies (addition of latest study when multiple studies have the same theme)
EC5	Papers with results and findings that are unclear

credits illustrated in Section 2.6. Henceforth, both criteria were utilized simultaneously to the full texts of all the 169 studies. Finally, 81 studies were lastly chosen for this work.

2.6. Quality Assessment Criteria (QA). QA is essential and exceptionally significant in each scoping review. QA of the investigations was directed in the third degree of the SSP. The IC and EC with the QA measures were utilized to recover examinations in the second SSP degree. One hundred nine (109) examinations were gathered by the specialists in the third level, where the scientists analyzed each investigation to eliminate inclination.

Therefore, to assess the nature of the chose articles, we planned a poll. The planning survey was propelled by a previous efficient investigation [35, 37].

- (1) QA1: does the article contribute to the integration or adoption of BIM and IoT technologies? The potential answers are “Yes (+1),” “Partially (+0.5),” and “No (+0).”
- (2) QA2: does the paper offer an adequate review of the literature in the domain of research? The potential answers are “Yes (+1),” “Partially (+0.5),” and “No (+0).”
- (3) QA3: does the paper define the objectives and goals of the study? The potential answers are “Yes (+1),” “Partially (+0.5),” and “No (+0).”
- (4) QA4: are the contributions and limitations of the article visibly outlined? The potential answers are “Yes (+1)” and “No (+0).”
- (5) QA5: the paper has been published in a well-recognized and reliable publication source. To answer these quality criteria, for Conferences, Symposium, and Workshops, we deliberated the computer science conference ranking (CORE) (A, B, and C) [38]. For the journal articles, the Journal Citation Report (JCR) lists were used. Hence, the answers to these defined criteria can be as follows:

Journals:

- (+2) if rated Q1,
- (+1.5) if rated Q2,
- (+1) if rated Q3 or Q4,
- (+0) if it has no JCR ranking.

Conferences, Symposium, and Workshops:

- (+1.5) if rated CORE A,
- (+1) if rated CORE B,
- (+0.5) if rated CORE C,
- (+0) if not in CORE ranking.

Others; (+0).

The quality criterion score in (QA5) indicates that Journals have more weight than Proceedings (Conferences, Symposiums, and Workshops) because the chances of publishing a paper in Q1 or Q2 Journal can be hard in comparison with other published sources. Consequently, a scale of 1–6 will stay as the final quality score for a specific study.

2.7. Extraction of Data. After the second degree of the examination choice method, we chose the survey groups and then analyzed articles. In this way, each article’s full content was investigated by, in any event, two specialists. Therefore, imperative data were additionally mined to a given information extraction structure. The structure was an assortment of the critical rundown of things as per the following:

- (i) Title
- (ii) The year of publication
- (iii) The venue of publication
- (iv) The type of contribution
- (v) The research focuses
- (vi) The utilized performance measures for evaluation
- (vii) The citation counts of a study.

3. Results

This section presents the results for the RQs of this SLR paper.

3.1. RQ1: What Are the Selected Studies, Demographics, and Characteristics? Out of the 169 records analyzed and utilizing all the characterized models, 93 records were excluded, and only 81 articles were selected for this investigation. We firmly and fundamentally investigated the 81 articles selected to answer all the RQs introduced in Section 3.1. In Table 4, all the chose contemplates are delineated in detail.

TABLE 4: Overview of selected studies.

Identifier	Study reference	Publication year	Publication channel	Citation count
S1	[39]	2020	Journal	0
S2	[40]	2020	Journal	1
S3	[41]	2020	Journal	1
S4	[42]	2015	Journal	30
S5	[43]	2012	Journal	20
S6	[44]	2017	Journal	65
S7	[45]	2019	Conference	0
S8	[46]	2016	Journal	19
S9	[47]	2019	Conference	0
S10	[48]	2011	Conference	23
S11	[49]	2012	Conference	162
S12	[50]	2017	Conference	6
S13	[51]	2013	Symposium	2
S14	[52]	2014	Conference	11
S15	[53]	2018	Conference	1
S16	[54]	2013	Symposium	15
S17	[55]	2018	Journal	24
S18	[56]	2018	Journal	8
S19	[57]	2018	Journal	6
S20	[58]	2015	Journal	178
S21	[59]	2019	Journal	1
S22	[60]	2018	Journal	22
S23	[61]	2019	Journal	1
S24	[62]	2017	Conference	7
S25	[63]	2016	Journal	26
S26	[64]	2019	Journal	0
S27	[3]	2019	Journal	2
S28	[65]	2017	Journal	4
S29	[66]	2019	Journal	4
S30	[5]	2017	Journal	28
S31	[67]	2018	Journal	15
S32	[68]	2018	Journal	8
S33	[69]	2020	Journal	2
S34	[70]	2014	Journal	24
S35	[71]	2019	Journal	3
S36	[72]	2014	Journal	110
S37	[73]	2013	Journal	82
S38	[74]	2018	Journal	28
S39	[75]	2017	Journal	8
S40	[76]	2015	Journal	53
S41	[77]	2017	Conference	1
S42	[78]	2019	Conference	0
S43	[79]	2017	Journal	23
S44	[80]	2019	Journal	3
S45	[81]	2019	Journal	16
S46	[82]	2019	Journal	2
S47	[83]	2019	Journal	5
S48	[84]	2014	Journal	26
S49	[85]	2015	Journal	110
S50	[6]	2015	Journal	34
S51	[86]	2018	Journal	19
S52	[4]	2015	Journal	84
S53	[87]	2020	Journal	2
S54	[88]	2020	Journal	2
S55	[89]	2019	Journal	2
S56	[90]	2013	Journal	48
S57	[91]	2015	Journal	4
S58	[92]	2019	Journal	0
S59	[93]	2020	Journal	0
S60	[94]	2019	Journal	3

TABLE 4: Continued.

Identifier	Study reference	Publication year	Publication channel	Citation count
S61	[95]	2016	Journal	35
S62	[96]	2018	Workshop	2
S63	[97]	2013	Journal	83
S64	[98]	2012	Journal	42
S65	[99]	2016	Conference	1
S66	[100]	2020	Journal	5
S67	[101]	2018	Journal	32
S68	[102]	2013	Conference	7
S69	[103]	2013	Conference	35
S70	[104]	2018	Journal	17
S71	[105]	2019	Journal	3
S72	[106]	2018	Journal	7
S73	[107]	2019	Journal	0
S74	[108]	2018	Journal	12
S75	[7]	2019	Conference	1
S76	[109]	2019	Journal	3
S77	[110]	2021	Journal	2
S78	[111]	2021	Journal	8
S79	[112]	2021	Conference	12
S80	[113]	2021	Journal	1
S81	[114]	2021	Journal	12

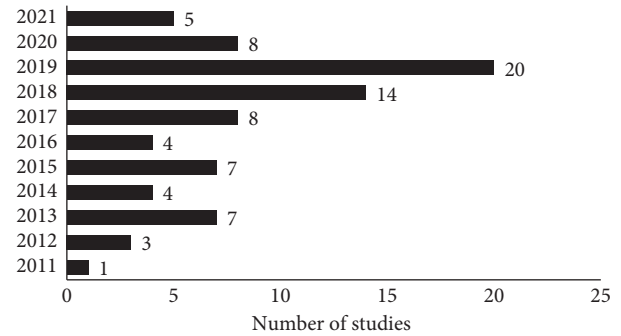


FIGURE 3: Articles published per year.

3.1.1. *Publication Over Time.* Figure 3 gives the all-out number of distributed works depending on the time of distribution (2011–2021). Over the most recent ten years, there is a significant measure of consideration given to scientists’ research area at a reformist enthusiasm. We found that 2011 was the most undynamic year, with just one investigation distributed (S10). Subsequently, high positioning CORE procedures (Conferences, Symposium, and Workshops) and Journals have not distributed an investigation in the exploration area. Consequently, the investigation distributed in the year 2011 (S10) was distributed in the First International Technology Management Conference.

Notwithstanding, consistently, we have seen an expanded awareness from specialists, especially from 2017 to 2021. This can be clarifying by recognizing the development from 2011 to 2016, where a stable quantity of studies has been produced. In these years (2011–2016), key works have been produced, for example, S20, S25, S34, S40, S48, S49, S50, and S61 that for both new and veteran researchers to

TABLE 5: Quality assessment of the studies selected.

Study	QA1	QA2	QA3	QA4	QC5	Total score
S1	1	1	1	1	2	6
S2	1	1	1	1	2	6
S3	1	0.5	1	1a	1.5	5
S4	1	0	1	0	1	3
S5	1	0.5	1	0	1.5	4
S6	1	1	1	1	2	6
S7	1	0	0.5	0	0	1.5
S8	1	1	1	1	2	6
S9	1	0	0.5	0	0	1.5
S10	1	0	0.5	0	0	1.5
S11	1	0.5	0.5	1	1	4
S12	1	0	0.5	0	0	1.5
S13	1	0.5	0	0	0	1.5
S14	1	0.5	0	0	0	1.5
S15	1	0	0.5	0	0	1.5
S16	1	0	0	0	0	1
S17	1	1	1	1	2	6
S18	1	1	1	1	1.5	5.5
S19	1	0.5	1	1	1.5	5
S20	1	0.5	1	1	1	4.5
S21	1	1	0.5	1	1	4.5
S22	1	0.5	0	1	0	2.5
S23	1	1	1	1	2	6
S24	1	1	1	1	1.5	5.5
S25	1	1	1	1	2	6
S26	1	1	1	1	2	6
S27	1	0	0.5	0	0	1.5
S28	1	1	1	1	2	6
S29	1	1	1	1	2	6
S30	1	1	1	1	2	6
S31	1	1	1	1	2	6
S32	1	0	0.5	0	0	1.5
S33	1	1	1	1	2	6
S34	1	1	1	1	2	6
S35	1	0.5	0.5	1	1.5	4.5
S36	1	1	1	1	2	6
S37	1	1	1	1	2	6
S38	1	0.5	1	1	2	5.5
S39	1	0.5	1	1	2	5.5
S40	1	1	1	1	2	6
S41	1	0	0.5	0	0	1.5
S42	1	0	0.5	0	0	1.5
S43	1	0.5	1	1	1.5	5
S44	1	1	1	1	2	6
S45	1	1	1	1	2	6
S46	1	0.5	1	1	2	5.5
S47	1	0.5	0.5	1	1	4
S48	1	1	1	1	2	6
S49	1	1	1	1	2	6
S50	1	0.5	1	1	2	5.5
S51	1	0.5	1	1	2	5.5
S52	1	1	1	1	2	6
S53	1	1	1	1	1.5	5.5
S54	1	1	1	1	2	6
S55	1	1	1	1	2	6
S56	1	1	1	1	2	6
S57	1	0	0.5	0	0	1.5
S58	1	1	1	1	1.5	5.5
S59	1	1	1	1	2	6
S60	1	0.5	0.5	0	0	2
S61	1	1	1	1	2	6

TABLE 5: Continued.

Study	QA1	QA2	QA3	QA4	QC5	Total score
S62	1	0	0.5	0	0	1.5
S63	1	0.5	1	1	2	5.5
S64	1	1	1	1	1.5	5.5
S65	1	0.5	0.5	1	0	3
S66	1	1	1	1	2	6
S67	1	1	1	1	2	6
S68	1	1	0.5	1	1	4.5
S69	1	1	0.5	1	1	4.5
S70	1	1	1	1	2	6
S71	1	1	1	1	2	6
S72	1	0.5	1	1	2	5.5
S73	1	0.5	0.5	1	1	4
S74	1	0.5	1	1	2	5.5
S75	1	0	0.5	1	0.5	3
S76	1	1	1	1	2	6
S77	1	1	1	1	2	6
S78	1	1	1	1	2	6
S79	1	1	1	1	0	4
S80	1	1	1	1	0	4
S81	1	1	1	1	2	6

contribute to this new and interesting research area. The reader will likewise see that in the year 2019, there are numerous works published in contrast with the remaining years. We observed that there are high-level journals that contribute the most works in this domain, and these Journals are Journal of Engineering Construction and Architectural Management and Construction Innovation. All in all, regardless of a moderate beginning in the early years (2011 to 2016), the exploration movement in the field of study keeps on picking up force with consistent development, chiefly in the subsequent four years (2017 to 2020). It can be observed that there is growing interest in the awareness on BIM-IoT as indicated by S77–S81 in year 2021.

3.1.2. Publication Channel and Quality Scores. In Table 4, we recorded the distribution channels, distribution year, and reference means for each investigation. Four diverse distribution channels were distinguished and large: Journal, Conference, Workshop, and Symposium. We found that the dominant part of the examinations was distributed in Journals with 63 investigations (77.78%) of the examinations chose, 15 investigations (18.52%) distributed in Conference, two examinations (2.46%) were distributed in Symposium; lastly, one investigation (1.23%) was distributed in Workshop. With this, the general nature of the investigations selected is self-evident because 77.78% of the selected contemplates were distributed in Journals.

We likewise inspected the selected quality score readings for the characterized quality measures in Section 2.6. In Table 5, we introduced the quality score for each investigation. The consequences of the quality examination exhibit that all investigations have scored over 1, just one investigation score of 1, which is S16. Thirty-three investigations score 6 (S1, S2, S6, S8, S17, S23, S25, S26, S28, S29, S30, S31, S33, S34, S36, S37, S40, S44, S45, S48, S49, S52, S54, S55, S56,

S59, S61, S70, S71, S76, S77, S78, and S81), and thirteen examinations score 5.5 (S18, S24, S38, S39, S46, S50, S51, S53, S58, S63, S64, S72 and S74), while two investigations (S79) scored 4.

3.1.3. Publication Source. Table 6 summarizes the studies based on their publication sources. The publication sources will help to evaluate at a glance the distribution pattern of the various research themes and clusters in the years under study. Altogether, 43 publication sources from various publishers were identified. Publication sources such as Engineering Construction and Architectural Management, Construction Innovation, and Automation in Construction have more papers with 14, 8, and 6, respectively. It was also found that most of the examinations distributed in the top publication sources (for example, S1, S2, S17, S25, S26, S28, S29, S30, S31, S33, S34, S44, S45, S48, S49, S52, S55, S54, S59, S66, and S67) have a great score of 6.5 or more from the evaluation done in Table 5. In Table 6, we discovered five distributors who are Taylor & Francis, with 13 distribution sources, trailed by IEEE (13), Emerald Insight (10), ACM (4), and Elsevier (4). The least publication source was recorded by MDPI and Springer with 1 each.

3.2. RQ2: What Is the Research Focus of the Selected Studies?

In this section, we present the research focus of the studies selected. Based on the analysis conducted of the studies selected in this paper, we categorized the selected studies into two research focus, which are BIM adoption and BIM integration. From Table 7, 50.62% of the selected studies focus on BIM adoption, and 49.38% of the selected studies focus on BIM and IoT devices integration. Hence, the following sections (Section 3.2.1 and Section 3.2.2) present and discussed the studies that focused on both research angles in the field of study.

3.2.1. BIM Adoption. There are 41 studies that work on BIM adoption in the construction industry from the selected studies. We observed that out of the 41 studies focused on BIM adoption, 13 studies (S47, S35, S26, S9, S75, S46, S29, S44, S45, S55, S21, S27, and S73) were published in 2019. This makes the year (2019) the most active year for the studies in BIM adoption. They were followed by 2018, 2017, and 2015 with 10, 4, and 4. Consequently, studies on BIM adoption will be presented. Shrivastava and Chini explore the use of BIM to examine the initial embodied energy of a building. The authors demonstrate BIM flexibility to modify the model [43]. In work by Davies and Harty, the authors define scales development used to assess the views about the significances of BIM and its use in the United Kingdom (UK) [73]. The result shows that BIM use is harmonious with current ways of working. Hence, their research is focused on understanding UK construction organizations concerning BIM adoption. Singh presents a behavioural perspective on system innovation adoption decisions in AEC [70]. The finding shows that the systematic innovation-related needs in the AEC network are interrelated. Enegbuma et al.

investigate the factors affecting BIM adoption in Malaysia. Hence, the authors developed a model to do just that [84]. The findings serve as a guide for BIM adoption and effective and careful policymaking on BIM implementation in Malaysia.

Demian and Walters conducted a case study on the efficacy of BIM for transferring information within a building team [72], a study on existing concrete fabrication facilities, using four information management systems, such as e-mail, an Enterprise Resource Planning system, construction project extract tool, and a new BIM-based system. It was concluded that the use of a BIM-based system averted information flow via building models. With the growing attention given to BIM globally, Ding et al. conducted a study to know the apparatus for BIM adoption by architects in China [4]. In doing so, the authors formulate a questionnaire for architects in Shenzhen, China. The result shows that factors such as technical defects of BIM, motivation, and BIM ability affect the adoption of BIM techniques. Shafiq et al. evaluate carbon footprint in Malaysia's low-rise buildings by utilizing BIM technology [42]. The result is to help practitioners in selecting the best combination of structural materials. In another study by Rogers et al., to determine the obstacles and perceptions of BIM adoption, the authors explore BIM adoption from Malaysian construction organizations' perspective. The result shows that even though the organizations have a good concept of BIM, they lack well-trained personnel.

Singh and Holmstrom investigate BIM adopting a hierarchy of needs [6]. The finding shows that not just individuals, organizations also show the hierarchical ordering of innovation-related needs. Gledson researched to acquire an insight into employees' opinions about organizational BIM adoption [63]. A case study was conducted that focused on initial BIM projects conveyed by an early adopter organization. The findings show that organizations often have to utilize hybrid project conveyance methods on initial adopter projects. Mustaffa et al. investigate BIM adoption experiences in various countries, such as USA, UK, and Finland [50]. These countries are known to be early BIM adopters. The authors hope that the experiences explored will be useful for BIM implementation and adoption in Malaysia. Ngowtanasuwan and Hadikusumo proposed a new model to explain and forecast the Thai construction industry's adoption of behaviours. The authors used a system dynamic (SD) approach with four selected companies for a case study [65]. The result illustrates that BIM training is the best way to enhance the performance of a company. Gledson and Greenwood used Rogers' innovation diffusion theory to investigate the adoption of 4D BIM in the UK construction industry [5]. The authors surveyed 97 construction practitioners to assess 4D BIM innovation acceptance in a time. The result shows the advantages of 4D BIM, and also we understand the reason for its adoption and rejection.

Juan et al. examined the existing prominence of BIM adoption in 224 Taiwanese architectural firms. The authors find out the acceptability and readiness of these firms in implementing BIM [79]. The authors also proposed a predictive model which can be utilized by companies that are

TABLE 6: Publication source.

Publication source	Publishers	Studies	No.	%
Engineering Construction and Architectural Management	Emerald Insight	S1, S29, S30, S31, S44, S45, S49, S50, S51, S52, S55, S74, S76, S77	14	17.28
Construction Innovation	Emerald Insight	S25, S26, S28, S33, S34, S46, S48, S54	8	9.87
Automation in Construction	Elsevier	S2, S17, S59, S66, S67, S81	6	7.41
Construction Management and Economics	Taylor & Francis	S36, S37, S40, S63	4	4.93
Journal of Engineering, Design and Technology	Taylor & Francis	S3, S19, S58	3	3.70
Architectural Engineering and Design Management	Taylor & Francis	S22, S39, S72	3	3.70
International Journal of Construction Management	Taylor & Francis	S5, S35	2	2.46
Built Environment Project and Asset Management	Emerald insight	S20, S47	2	2.46
International Journal of Computer Integrated Manufacturing	Taylor & Francis	S56, S70	2	2.46
International Conference on Research and Innovation in Information Systems	IEEE	S9, S12	2	2.46
International Journal of Sustainable Building Technology and Urban Development	Taylor & Francis	S4	1	1.23
Journal of Cleaner Production	Elsevier	S6	1	1.23
Facilities	Emerald Insight	S8	1	1.23
Journal of Facilities Management	Emerald Insight	S18	1	1.23
Journal of Financial Management of Properties and Construction	Emerald Insight	S21	1	1.23
Structure and Infrastructure Engineering	Taylor & Francis	S23	1	1.23
International Journal of Architectural Research	Emerald Insight	S27	1	1.23
International Journal of Management Projects in Business	Emerald Insight	S32	1	1.23
Production and Planning Control	Taylor & Francis	S38	1	1.23
Journal of Civil Engineering and Management	Taylor & Francis	S43, S64	1	1.23
International Journal of Building Pathology and Adaptation	Emerald Insight	S53	1	1.23
Engineering Project Organization	Taylor & Francis	S57	1	1.23
Procedia Computer Science	Elsevier	S60	1	1.23
Journal of Building Performance Simulation	Taylor & Francis	S61	1	1.23
International Journal of Geographical Information	Taylor & Francis	S71	1	1.23
Intelligent Buildings International	Taylor & Francis	S73	1	1.23
First International Technology Management Conference	IEEE	S10	1	1.23
International Conference on Robots and Intelligent System	IEEE	S15	1	1.23
Workshop on Human-Habitat for Health (H3): Human-Habitat Multimodal Interaction for Promoting Health and Well-Being in the Internet of Things Era	ACM	S62	1	1.23
International Conference on Information Management	IEEE	S7	1	1.23
Conference on Electrical, Communication, and Computer Engineering	IEEE	S42	1	1.23
Nordic Conference on Construction Economics and Organization	Emerald Insight	S75	1	1.23
International Conference on Virtual Systems and Multimedia	IEEE	S11	1	1.23

TABLE 6: Continued.

Publication source	Publishers	Studies	No.	%
International Conference on Management of Engineering and Technology	IEEE	S24	1	1.23
International Conference on Applied Systems Innovation	IEEE	S41	1	1.23
Chinese Control and Decision Conference	IEEE	S65	1	1.23
Proceedings of the Winter Simulation Conference	ACM	S14	1	1.23
International Symposium on Instrumentation and Measurement, Sensor Network, and Automation	IEEE	S13	1	1.23
Symposium on Theory of Modelling and Simulation-DEVs Integrative M&S	ACM	S16	1	1.23
International Conference on Research Challenges	IEEE	S68	1	1.23
International Conference on Cloud Computing Technology and Science Sustainability	IEEE	S69	1	1.23
	MDPI	S78	1	1.23
6th International Conference on Communication and Electronics Systems	IEEE	S79	1	1.23
Frontiers of Engineering Management	Springer	S80	1	1.23

TABLE 7: Research focus in the field of study.

Research focus	Studies	No.	%
BIM adoption	S3, S4, S5, S9, S12, S15, S17, S18, S19, S21, S25, S26, S27, S28, S29, S30, S31, S32, S33, S34, S35, S36, S37, S38, S43, S44, S45, S46, S47, S48, S49, S50, S51, S52, S53, S54, S55, S72, S73, S74, S75	41	50.62
BIM and IoT integration	S1, S2, S6, S7, S8, S10, S11, S13, S14, S16, S20, S22, S23, S24, S39, S40, S41, S42, S56, S57, S58, S59, S60, S61, S62, S63, S64, S65, S66, S67, S68, S69, S70, S71, S76, S77, S78, S79, S80, S81.	40	49.38

considering adopting BIM. The result shows that most of the firms investigated have adopted BIM tools. Ahankoob et al. explore the level of positive association that occurs between BIM adoption and organizational learning [106]. Hence, based on a survey on Australian building contractors, the general effect of BIM maturity couple with years of experience by contractors to embrace new information is examined. The result indicates that the level of organization experience with BIM is a much better forecaster of learning performance than the difficulty of BIM utilization in a given organization. By utilizing the unified theory of acceptance and use of technology (UTAUT), Addy et al. examine the factors facilitating BIM adoption among quantity surveyors in Ghana [57]. Hence, the study's findings give a useful framework in policy development with a clear pathway for BIM implementation in Ghana. Ahmed and Kassem develop a unified BIM adoption Taxonomy (UBAT) and further identify the taxonomy concepts that impact the first three BIM adoption process stages [55]. Hence, the study is mainly planned to enhance the reader's knowledge of the BIM adoption process.

Wang et al. apply BIM technology in construction management [53]. The result shows that BIM application facilitates the integration, visualization, and automation of power engineering construction management. Zhao et al. model the risk routes related to BIM adoption in the Chinese AEC industry [67]. The result confirmed risk categorization with 15 hypothetical risk paths that are statistically important. In the study by Jin et al., the authors show an instructive practice in a task-based appraisal of AEC understudies interdisciplinary structure configuration work receiving BIM [86]. The perception of students with regards

to BIM effects in integrated project design is also examined. The result shows that adopting BIM helps motivate students to have a broader design and construction strategy. To know organization differences in BIM adoption speed and its rationale, Ayinla and Adamu investigate the causes of this digital divide and provide some solutions for bridging the gap [108]. Based on a questionnaire conducted to over 240 global respondents, the findings show that organization size is often not significant concerning the speed they adopt BIM. Olapade and Ekemode investigate the general awareness and usage of BIM for facility management (FM) in Nigeria [56]. The findings show that there is a low-level of alertness and adoption of BIM for FM. In a study by Matthews et al., the general insights on how BIM adoption influenced the partnership and change management practices within a project are attained [74]. The finding demonstrates that little knowledge and experience to provide a model for asset management mostly caused the project team to have problems.

Almuntaser et al. proposed a BIM adoption framework in the Saudi Arabia AEC sector [68]. The finding shows that BIM adoption gives several benefits and efficiency. In a study by Oyewole and Dada, the authors examine the gaps in training between the expected and perceived understanding of BIM adoption practice among Nigeria construction professionals [83]. Based on a questionnaire survey conducted, the findings show that there is a substantial gap in training design creation and organization among Nigeria construction professionals. Concerning BIM adoption in the industry, Ahankoob et al. examine the level to which previous BIM experiences influences experts view on BIM prospective advantages [71]. Hence, based on a survey

conducted by the authors, the result shows that BIM familiarity is a key factor in knowing the prospective BIM advantages. In understanding the potential benefits, BIM adoption and implementation by construction organizations will be more comfortable. Ahmed and Suliman proposed an adoption model based on structural equation modeling (SEM). The proposed model analyzes the relationship between key indicators which drives BIM adoption [64]. The result demonstrates that people and the environment are the key indicators facilitating BIM adoption. Shehzad et al. examined the factors that impact BIM adoption in the construction industry [47]. The authors identified 74 factors which were classified into organizational, technology, and environmental dimensions. Therefore, the study will aid researchers in understanding the factors that influence BIM adoption. Ullah et al. conducted a study to study the existing position of BIM adoption, its advantages, and the limitations of BIM adoption in the construction industry globally [7]. The finding shows the BIM adoption rate in several countries' construction companies with eighteen identified obstacles to BIM adoption identified.

Hilal et al. proposed a hybrid conceptual model for BIM adoption in FM. The model incorporates the technology task fit (TTF) and the UTAUT theories [82]. The study is done to help improve the understanding of BIM acceptance and adoption by FM. Marefat et al. examine the effect of BIM for critical safety projects and obstacles to adoption [66]. The authors distributed the questionnaire to 200 construction companies. The result highlights some of the factors that lead to failure in BIM adoption, specifically in Iran. Chen et al. explore the factors influencing BIM adoption in the construction industry and its benefits to research and practice [80]. Given the technology-organization-environment (TOE) framework, the creators built up a research model that consolidates the primary achievement factors associated with BIM innovation implementation. The creators locate that the general preferred position of BIM was a key factor that permitted BIM reception. Hong et al. proposed a model for BIM selection and execution at little and medium-sized development associations [81]. The proposed model accesses BIM adoption benefits, cost, and also its challenges faced by these organizations. Park et al. proposed an acceptance model for BIM. The authors also examined external factors extracted by interviews that facilitate the adoption of BIM technologies [89]. The results show that both compatibility and organizational support play a key part in adopting BIM technologies. Babatunde et al. conducted a study to recognize and analyze the utilization of BIM-based cost estimating software [59]. The study also examines BIM adoption drivers in the Nigerian quantity survey firms. The findings show that most Nigerian quantity survey firms are aware of BIM but have not adopted BIM-based cost estimation software. To promote sustainable policies for enhancing developing countries' economies and environmental performance, Akdag and Maqsood highlight the potential for BIM in such countries, particularly Pakistan [3]. The authors conducted surveys and interviews with BIM users and non-BIM users' architects in Pakistan. The authors highlight strategies that will enhance the adoption and implementation of BIM in Pakistan.

In a study by Rathnasiri and Jayasena, a new framework for adopting green BIM technology for Sri Lankan buildings was developed [107]. The research findings reveal the challenges of green BIM application when building data are not sufficiently available. Babatunde et al. investigate the key drivers of BIM adoption among professionals in the Nigeria construction industry. The authors conducted a preliminary study and a questionnaire survey [41]. The findings recognized 23 key drivers to BIM adoption with the significance of each driver. Vidalakis et al. explore the implementation and adoption of BIM among small- and medium-sized enterprises (SMEs). These SMEs are specifically in the UK AEC industry. Hence, the study tackles the issue of the lack of uniformity in the SME sector regarding BIM adoption [69]. The findings show that SME familiarity with the current BIM software is very low, contributing to the sector's lack of adoption. Saka and Chan develop a hierarchical model for investigating inter-relationships of the obstacles to adopt BIM. The work is intended at examining the main obstacles to BIM adoption [88]. These barriers are analyzed through the viewpoint of SMEs in Nigeria. The finding shows that obstacles are mainly from sociotechnical circumstance; hence, the SMEs can drive BIM adoption by looking to their internal environment. Babatunde et al. investigates BIM implementation barriers and explore means to enhanced BIM adoption in Nigerian construction firms [87]. The authors identified 20 obstacles to BIM implementation with ten ways to enhance BIM adoption in Nigerian construction firms.

3.2.2. BIM and IoT Integration. We found 40 studies that work on BIM and IoT integration from the selected studies (as presented in Table 7). Conversely, from the studies, 2019 was the most active year with the most studies published (S7, S23, S42, S58, S60, S71, and S76), respectively. We followed by 2013, 2017, and 2018 with 6, 4, and 4 studies. Accordingly, studies on BIM-IoT integration will be presented.

Ghosh et al. try to integrate the BIM and enterprise resource planning (ERP) system to help in the sustainable governance process [48]. Dore and Murphy proposed an approach for the maintenance of cultural heritage places [49]. The findings expose some enhancement. In another study by Ren et al., a framework for integrating BIM and e-commerce in a material procurement process was proposed [98]. The framework is designed to improve design-construction integration. The result shows some promise. Melzner et al. present a customizable automatic rule-based checking system for BIM models [97]. The system is built to be an add-on to current BIM software and can check models for safety threats in the early stages of design and preparation processes. The result shows that BIM can play a significant role in safety design and planning. Juan proposed a framework for innovative cloud-based building information interaction [51]. The proposed framework shows some improvement. Wang et al. integrate BIM and Discrete Event Systems Specification (DEV) [54]. The work helps designers in understanding different building properties. Hwang et al. conducted a study to implement a prototype for BIM and GIS (Geographic Information System) interoperability

[102]. The result shows that the prototype shows some promise.

Mahamadu et al. highlight the existing challenges to BIM-cloud integration [103]. Hence, the study focuses on privacy and security concerns as key issues that hinder technology integration. Grilo et al. introduced a model that uses an interdisciplinary way to gather significant components answerable for joint effort execution [90]. The proposed model is incorporated with a multimeasure dynamic apparatus, named Analytical Network Process (ANP). A case study shows the application of the proposed model and ANP; the result shows that the relationship between business interoperability needs to be improved. Zhang et al. integrate BIM with the rule-based system to assess the design and building performance [52]. The authors get data by utilizing a Real-Time Location System (RTLS). The result shows some promise. Love et al. investigate BIM value and the issues stopping its adoption in FM applications [58]. The findings demonstrate a lack of methodologies that illustrate the key advantages of BIM in FM.

Korpela et al. conducted an investigative study by asking three key questions: what sort of information tools is utilized for FM, how to design data are handled, and how facility managers integrate BIM models with maintenance information systems [76]. The result shows the possible steps to the integration of the two systems. With the current hope that BIM tools can increase process integration and support multidisciplinary planning practices, Kovacic and Filzmoser move to test this assumption using various BIM tools [91]. The authors conducted an experimental study. The result demonstrates that BIM tools are perceived as very valuable, but they are not interoperable. Shengyi and Jia explore the research studies on the mix of BIM innovation and computer-generated reality innovation [99]. This coordination makes the use of VR innovation in the development extends much better. Jeong et al. proposed a structure for the reconciliation of BIM, and the article arranged actual demonstrating based on building energy modeling (BEM) [95]. The proposed system is centred on warm reproduction that helps dynamic in the planning cycle. Given a contextual investigation, the proposed system was approved. Golabchi et al. proposed a robotized approach that shows the chance of using BIM to create calculations that computerize dynamic for FM applications [46]. These calculations are to computerize the way toward recognizing failing warming ventilation and cooling (HVAC) hardware. The outcome exhibits that the proposed approach can be valuable in FM rehearse by improving efficiency and cost reduction with regards to decision-making.

In a Larsen study, the author presents a change management process with the Change Control System (CCS) to manage changes in detail, and also to access BIM utilization in identifying the consequences of changes [75]. The finding shows that CCS combined with BIM can help in keeping control of alterations in detailed design. Tsai et al. explore BIM and GIS spatial technology integration in managing pipelines of building [77]. The result shows that the management of such a pipeline with integrated technologies will enhance building maintenance effectiveness. Arslan et al.

build up a framework that uses BIM programming and a remote sensor innovation, fundamentally to build up proactive well-being, the board framework [62]. The proposed system indicated to be suitable by decreasing safety hazards during FM phase of a building. Li et al. developed a Radio Frequency Identification Device (RFID) integrated into a BIM platform that encapsulates many stakeholders, data flow, and so on [44]. The result shows that the developed platform improves the achievement of everyday operations and decision-making. Bueno et al. develop an integration interface of manufacturer-based life cycle assessment (LCA) data into a BIM platform [60]. The result shows some promise. Louis and Rashid introduced BIM as an operating system for the smart house application [96]. The investigation of the proposed application demonstrates some potential.

Davtatab et al. proposed a product stage for the assortment and investigation of information from BIM models [101]. The outcome shows some guarantee. To tackle transportation issues, wasteful administration of assets and wasteful creation, and on-location get together of pre-assembled components, Chen et al. build up another framework, named Physical Internet-empowered BIM System (PI-BIMS) [104]. This framework incorporates BIM, auto-ID advancements, and distributed computing, giving constant correspondence, assortment, and representation of data. The outcome shows some guarantee. Usmani et al. build up output to as-fabricated BIM work process. This device will use a 3D laser scanner to review and create as-fabricated structure data models for Malaysian offices dependent on a contextual investigation [92]. The outcome demonstrates that the instrument can be valuable. Lokshina et al. proposed a framework that utilized a blockchain innovation to make sure about and control the system that incorporates coordinated IoT and BIM advances [94]. The proposed incorporated framework displays some guarantee. In an examination by Tariq et al., the creators research the usage of Virtual Reality (VR) innovation through the reconciliation with BIM in the Pakistan development industry [78]. The discovering shows that the combination of BIM and VR can help in the fast dynamic and improves correspondence and cooperation between venture members. Xiang et al. proposed another incorporation model [45]. The model guides in changing over BIM models to GIS models capably. The outcome reveals that the proposed coordinated model achieves well. Munir et al. attempt to distinguish the innovations for leveling out Asset Management (AM) frameworks for BIM-based reconciliation. A contextual investigation is utilized to comprehend the execution cycle of incorporating BIM with AM frameworks [109]. The examination traces key methodologies in embracing BIM-based cycles by a resource proprietor, the execution cycle, issues, and the points of interest.

To explore the outlined detection problem in integrating BIM and GIS, Zhou et al. proposed a new algorithm, named OutDet. The calculation picks agent perception, changes and tasks the BIM mathematical information in an organized framework and recognizes the detectable offices [105]. In light of an observational examination directed, the outcome exhibits that the proposed calculation (OutDet) can

TABLE 8: Contributions proposed by the selected studies.

Contribution	No.	Studies
Investigation study	26	S16, S20, S40, S41, S62, S42, S76, S3, S12, S15, S18, S21, S27, S30, S33, S47, S49, S50, S74, S72, SS53, S51, S77, S78, S80, S81
Evaluation study	13	S69, S14, S57, S4, S5, S9, S19, S29, S35, S34, S36, S37, S38
Model	13	S56, S7, S26, S28, S31, S43, S44, S45, S46, S48, S55, S54, S52
Framework	7	S10, S64, S13, S61, S67, S32, S73
System	7	S63, S39, S24, S6, S70, S60, S1
Approach	4	S11, S68, S8, S59
Tool	3	S22, S58, S23
Exploration study	4	S65, S25, S75, S79
Algorithm	1	S71
Taxonomy	1	S17
Protocol	1	S66
Method	1	S2

TABLE 9: Adoption theories utilized by the selected studies.

Theories	No.	Studies
Innovation diffusion theory (IDT)	4	S30, S34, S54, and S74
Technology acceptance theory (TAM)	3	S37, S43, and S55
Technology-organization-environment (TOE) framework	2	S44 and S54
Unified theory of acceptance and use of technology (UTAUT)	2	S19 and S46
BIM maturity model	1	S72 and 74
Technology task fit (TTF)	1	S46
Conceptual adoption model	1	S48
Institutional theory (INT)	1	S54
Organizational readiness model	1	S43

adequately call a massive part of unnecessary highlights when delivering BIM models in GIS. In another work by Boddupalli et al., a representation device is suggested that empowers a robotized sensor information stock into BIM climate [61]. The proposed device gives methodical upkeep and danger to the executives. The examination shows that the proposed instrument is conceivably easy to use and a key financial structure. Zhang et al. proposed a method to integrate BIM and 3D web-based GIS to implement micro and macro information in a unified environment [40]. Hence, this method is aimed at addressing the differences in geometric visualization and transformation coordination. The result shows some promise. Tang et al. proposed the use of Building Automation and Control Networks (BACNET) and BIM standard industry establishment class (IFC) [100]. The outcome shows that the convention can help open the planned future brilliant structure data trade and coordination. Mohamed et al. proposed another methodology for existing structure offices [93]. The proposed structure exhibits some guarantee. Yuan et al. proposed a BIM-based Performance Management System (BPMS). The proposed framework joins BIM with web and cloud innovation to accomplish execution estimation, execution observing, and execution-based instalment [39]. The proposed framework shows some guarantee concerning managing partners in improving work capability with BIM and different advances.

3.3. RQ3: *What Are the Contributions Proposed by the Selected Studies, and How They Can Be Categorized?* To fully know

the contributions proposed by the chosen studies, we plan and categorize the existing known proposals from the studies selected and further classified the studies based on which contribution they proposed. In Table 8, the contribution with regards to the studies that proposed it is presented. In totality, we identify 12 contributions. These contributions are Investigation study with 26 studies, followed by Evaluation (13), Model (13), Framework (7), System (7), Approach (4), Tool (3), Exploration study (3), Algorithm (1), Taxonomy (1), Protocol (1), and Method (1).

The result reveals that investigative study is the most conducted in research (as shown in Table 8). Additionally, we observed that 11 out of the 13 studies that proposed Model are studies that work on BIM adoption, while 10 out of the 13 studies that conducted an Evaluation study works on BIM adoption. Also, five out of the seven studies that proposed Framework works on BIM and IoT integration.

3.4. RQ4: *What Are the Theories Used to Examine BIM Adoption in the Construction Industry by the Selected Studies?* Out of 41 studies that worked on BIM adoption, we identified 12 studies that used adoption theories when studying BIM adoption in the construction industry. Hence, these studies (the 12 studies) amount to 29.27% of the studies that worked on BIM adoption. Furthermore, we identified nine different theories that were adopted from these studies. These theories concerning the studies that used them are presented in Table 9. Some of the most popular theories are innovation diffusion theory (IDT) (S30, S34, S54, and S74),

TABLE 10: Performance measures utilized by the selected studies.

Performance measures	No.	Studies
Performance	7	S1, S22, S26, S37, S57, S61, S64
Effectiveness	2	S41, S71
Accuracy	1	S2
Efficiency and accuracy	1	S7
Efficiency and effectiveness	1	S28
Efficiency	1	S70
Accuracy and effectiveness	1	S63
Complexity, compatibility, interoperability	1	S54

technology acceptance theory (TAM) (S37, S43, and S55), technology-organization-environment (TOE) framework (S44 and S54), BIM maturity model (S72 and 74), and unified theory of acceptance and use of technology (UTAUT) (S19 and S46).

3.5. RQ5: What Are the Different Performance Measures Used in the Research Domain? In noting this RQ, we distinguished 15 (19.74%) concentrates out of the chosen considers pre-owned execution measure for assessment. The exhibition estimates, for example, adequacy, exactness, productivity, execution, unpredictability, similarity, and interoperability, were found. A portion of these investigations utilizes a blend of more than one execution measures. We further saw that 11 out of the 15 examinations used presentation measure chips away at BIM and IoT incorporation. This is clear since deals with the mix are predominantly arrangement proposition-driven. An analyst needs to propose a new framework, model, or calculation to help mix the two advancements (BIM and IoT). However, this observation is negligible because most of the studies (80.26%) have no performance measure in their studies evaluation process. This is a huge problem, particularly when it comes to proper and factual evaluation to ascertain a specific phenomenon or trend in the field of study. Hence, researchers in this field need to apply more performance measures to evaluate ones work to enhance result credibility and generalization. Table 10 outlines the performance measures utilized by the studies selected.

4. Discussion

In this article, we led an SLR on BIM and IoT coordination and reception in the development business. BIM and IoT reconciliation and reception have increase generous consideration from the exploration network over the most recent 11 years. Of later, the reception and IoT innovations mix with BIM have become a critical and significant issue in the examination area. In this part, the outcomes identified with the RQs are summed up and examined through the introduction of the examination discoveries, research difficulties, and the future work course.

4.1. Research Findings. The key objective of this SLR is to assess the existing literature in the area of research. Hence, 169 papers were rigorously investigated using our IC and EC criteria, together with our quality assessment criteria.

Finally, 81 studies were choosing that meet those criteria for further analysis. The key findings concerning the answered RQs are outlined as follows:

- (i) BIM and IoT device integration and adoption have been gaining attention from the research community since 2013. We found that 2011 was the minimum active year with a single work published (S10). We found that in high-ranking Journals, such as Engineering Construction and Architectural Management, Construction Innovation, and Automation in Construction, there are no works published in the year 2011. For the studies selected, we observed that 77.78% of the selected studies were published in Journals sources, while 22.22% were published proceedings such as Conferences, Symposium, and Workshops. Therefore, with the research activity in the research area continuing to gain momentum with steady growth, particularly during the last 4 years, we forecast that the research area will gain significant attention in the years to come.
- (ii) The results of the QA reveal that all works score more than 1. However, only one study scores 1, which is S16. 40.74% of the selected studies score 6, and 16.04% scores 5.5, which amounts to 56.78% of the total selected paper. This displays the universal quality of the studies selected. With regards to the publication source, we found three more visible sources. These sources are Engineering Construction and Architectural Management, Construction Innovation, and Automation in Construction were the top contributors with 13, 8, and 5 publications, respectively. We also identified five publishers, which are Taylor & Francis, with 13 publication sources, followed by IEEE (12), Emerald Insight (10), ACM (4), and Elsevier (3).
- (iii) Concerning the research focus of the studies selected, we found out that BIM adoption in the construction industry is the most conducted. This is because 53.95% of the selected studies focused on this area, while 46.05% focused on BIM and IoT device integration. This is understandable because researchers are working extremely hard in the last decade to make sure that counties are adopting BIM in their construction policies before moving towards its integration with IoT devices. However, looking at the potential of integrating these two

technologies in recent years, researchers in the field of researcher are encouraging their integration and proposing new solutions to ease this transition in a challenging sector such as construction.

- (iv) In answering RQ3, we identify 12 contributions. Out of the 12 found contributions, five were observed to be more proposed and conducted by researchers: Investigation, Evaluation, Model, Framework, and System with 32.09%, 16.04%, 16.04%, 8.64%, and 8.64%, respectively. Out of 41 studies that worked on BIM adoption, we identified 29.27% of the studies that used adoption theories when studying BIM adoption in the construction industry. Hence, we identified 9 different theories that were adopted from these studies. Some of the most popular theories are IDT (S30, S34, S54, and S74), TAM (S37, S43, and S55), TOE framework (S44 and S54), BIM maturity model (S72 and 74), and UTAUT (S19 and S46).
- (v) Regarding execution measures, we distinguished 15 (19.74%) concentrates out of the chosen examines that preowned execution measure for assessment. We further saw that 11 out of the 15 examinations used presentation measure chips away at BIM and IoT joining. This is evident because taking a shot at joining is overwhelmingly arrangement proposition-driven, where a specialist ordinarily needs to propose a new framework, model, or calculation to help combine the two advances (BIM and IoT). However, this observation is negligible because most of the studies (80.26%) have no performance measure in their study evaluation process.

4.2. Identified Issues. After the rigorous analysis of the PS, this section gives some identified issues from the result obtained. We observed that more than 90% of the studies are not tailored to solution proposals. Both investigative studies and evaluation studies are gaining significant attention from the researchers in this domain. This trend should be tailored to the proposition of new ways (in terms of framework, techniques, and so on) to help construction industries to adopt such technologies rather than just investigations and general evaluations. This problem limits the chances of a solution proposition that will facilitate BIM adoption. Hence, we encourage researchers to proposed new solutions for BIM adoption in the construction industry. Other problems are with regard to the methodology of this study. Important papers can be missed during the paper collection process. This issue can cause important papers to be excluded. However, we mitigate this issue by conducting our search on five key data sources where many Journals and Proceedings in the domain are indexed. Another issue is with respect to bias on data synthesis. Not all papers selected clearly outline the information we needed to extract. Hence, we have to infer this information based on the experience of the authors. The final decision on a data item extracted is finalized by all the authors in this paper to mitigate this. Hence, this issue can be reduced.

4.3. Challenges and Direction for Future Work. In this study, we conducted a broad review of the studies selected. Henceforth, the findings will help researchers understand the current contributions concerning integrating and adopting BIM and IoT in the construction industry. Furthermore, this study will also help researchers identify the most proposed contributions, the most used adoption theories, and the utilized performance measures by the studies selected in the field of study. Hence, in this section, the identified challenges are highlighted regarding the scope of this study. We further provide future research directions as a pathway for researchers to follow.

From the result in Figure 2, we observed that despite the slow start from 2011 to 2016, the research area's research activity continues gaining momentum with steady growth, particularly during the last four years. Nevertheless, despite the steadiness, the research output is not consistent and proportional where year like 2019 has a large share of papers compared to other prominent years. Even though a conclusion cannot be driven for 2020 due to our search cap, we urge the research community to be more active. With 53.95% of the studies selected, BIM adoption works is the most conducted, while works on BIM and IoT integration are less than 50%. We encourage researchers to focus more on BIM and IoT integration in the construction industry in both developed and underdeveloped countries for future works. We observed that a massive chunk of the selected studies, 28.95% investigated their contributions. At this stage, we could have seen many works by researchers proposing new solutions on the technologies integration rather than investigation. Hence, we urge new and experienced researchers to propose new solutions in the research domain.

We further observed that 11 out of the 15 studies that utilized performance measure works on BIM and IoT integration. This is obvious because integration works are dominantly solution proposal-driven, where a researcher usually has to propose a new model, system, or algorithm to help integrate the two technologies (BIM and IoT). However, this observation is negligible because most of the studies (80.26%) have no performance measure in their studies evaluation process. This is a huge problem, particularly when it comes to proper and factual evaluation to ascertain a specific phenomenon or trend in the field of study. Hence, researchers in this field need to apply more performance measures to evaluate one work to enhance result credibility and generalization.

4.4. Threat to Validity. This survey's impediments must be considered to have a general examination of the outcomes gained from this audit. This way, the principal errors to this study's legitimacy are the error of information extraction, predispositions on examination choice, and incorrectness of information extraction. In this segment, every one of these errors is discussed.

4.5. The Incompleteness of the Study Search. Key examinations can be missed during the time spent recovering the investigations. This can influence the overall fulfilment of the

investigation search. Accordingly, to lighten this danger and further ensure that all critical and forthcoming examinations have been covered, the overall pursuit was done on five information bases (see Table 1). This information sources contain countless Journals, Conference, Workshop, and Symposium procedures in this space that are ordered.

The chosen examines in reverse and forward reference looked to ensure that critical examinations are incorporated. Even though we took measures to upgrade the examination search's fulfilment, the investigation can at present experience the missing effects of choice tendency. This is because different libraries, for example, EI Compendex and Citceerx, were not included in this study.

4.6. Bias on Study Selection. Regarding the examination choice cycle, we figured exceptionally clear and exact IC/EC standards to diminish predisposition by specialists. Every scientist can have an alternate comprehension of the IC/EC models; consequently, every individual analyst's investigation choice consequences are conceivable going to contrast. To ease this inclination, we led a pilot determination to ensure that an arrangement between the analysts is accomplished on the overall comprehension of the measures. The conceivable botch of copy examines another danger too. This error may have gradually changed our outcomes. Three potential duplications were recognized and were surveyed entirely to see whether they are a similar report.

Also, to choose an examination, the conclusion is taking by the two scientists who directed the hunting cycle. In this manner, any difference that emerges between the two scientists will be fixed between them through the conversation until a detailed understanding is build up. Moreover, excess specialists will audit the last chosen examines. For this investigation, we just incorporate companion audited examines. Nonetheless, there is a probability that we may miss some essential non-peer-investigated concentrate in this area.

4.7. The Inaccuracy of Data Extraction. In information extraction, the inclination can occur in this cycle and influence the outcomes classification and examination of the last investigations. The researchers evaluate the data extracted in distinct teams, and agreement on the significance of all the data extracted was reached to reduce this threat. Moreover, a final weight of the most senior researcher in the teams was taking into consideration when there is an issue that cannot be resolved between the researchers. Thus, the information things separated were evaluated by two analysts, where contradictions were thought and fixed. These estimates taken to diminish predisposition will help in improving the precision of the removed information things.

5. Conclusion

This paper presented eleven years (2011–2021) summary of the literature on integrating and adopting BIM and IoT integration in the construction industry. From the initial search conducted, 81 studies were selected based on the defined IC and EC and quality assessment criteria. The findings from this study

revealed that the research domain is progressing with stable growth, particularly during the last four years. We see that 77.78% of the selected studies were published in Journals sources, while 22.22% were published proceedings such as Conferences, Symposium, and Workshops. Furthermore, the quality analysis results showed that all the studies have a score greater than 1.40.74% of the selected studies score 6 and 16.04% scores 5.5, which amounts to 56.78% of the total selected paper. This displays the overall quality of the studies selected. With regards to publication sources and publishers, we identified three sources that more visible. These sources are Engineering Construction and Architectural Management, Construction Innovation, and Automation in Construction and were the top contributors with 13, 8, and 5 publications, respectively. We also identified seven publishers, which are Taylor & Francis, with 13 publication sources, followed by IEEE (13), Emerald Insight (12), ACM (4), Elsevier (4), Springer (1), and MDPI (1). Our result also shows that, concerning research focus, 53.95% of the studies selected focused on BIM adoption, while 46.05% focused on BIM and IoT device integration. We further identify 12 contributions. Out of the 12 identified contributions, five were proposed more and conducted by researchers: Investigation, Evaluation, Model, Framework, and System with 32.09%, 16.04%, 16.04%, 8.64%, and 8.64%, respectively. Hence, we identified nine different theories that were adopted from these studies. Some of the most popular theories are innovation diffusion theory (IDT) (S30, S34, S54, and S74), technology acceptance theory (TAM) (S37, S43, and S55), technology-organization-environment (TOE) framework (S44 and S54), BIM maturity model (S72 and 74), and unified theory of acceptance and use of technology (UTAUT) (S19 and S46). Regarding performance measures used, we found 15 (19.74%) studies out of the studies selected that utilized performance measure for evaluation. We further observed that 11 out of the 15 works that utilized performance measure works on BIM and IoT integration. Lastly, this paper shows the research community's interest level in this domain, considering the general consistency in the publication in the last four years. Hence, we anticipate more contributions from both new and veteran researchers in years to come. Furthermore, the challenges and directions identified in this study must be considered by the research community to help tackle the constraints in the area of research.

Data Availability

Data sharing is not applicable to this article as no new data were created or analyzed in this study.

Conflicts of Interest

The authors declare no conflicts of interest.

Acknowledgments

This research was fully funded by Universiti Kebangsaan Malaysia and the Ministry of Higher Education Malaysia for financially supporting this research (FRGS/1/2020/TK0/UKM/02/9).

References

- [1] S. Tang, D. R. Shelden, C. M. Eastman, P. Pishdad-Bozorgi, and X. Gao, "A review of building information modeling (BIM) and the internet of things (IoT) devices integration: present status and future trends," *Automation in Construction*, vol. 101, pp. 127–139, 2019.
- [2] A. H. Hussain, M. K. A. Husain, A. F. Roslano, and F. Fadzilo, "The fourth industrial revolution and organisations' propensity towards building information modelling (BIM) adoption," *Malaysian Construction Research Journal (MCRJ)*, vol. 27, no. 1, 2019.
- [3] S. A. Girinkaya, "A Roadmap for BIM Adoption and Implementation in Developing Countries: The Pakistan Case," *Archnet-IJAR*, vol. 14, no. 1, 2019.
- [4] Z. Ding, J. Zuo, J. Wu, and J. Y. Wang, *Key Factors for the BIM Adoption by Architects: A China Study*, Eng Constr Archit Manag, USA, 2015.
- [5] B. J. Gledson and D. Greenwood, "The adoption of 4D BIM in the UK construction industry: an innovation diffusion approach," *Engineering Construction and Architectural Management*, vol. 24, no. 6, pp. 950–967, 2017.
- [6] V. Singh and J. Holmström, "Needs and technology adoption: observation from BIM experience," *Engineering Construction and Architectural Management*, vol. 22, no. 2, pp. 128–150, 2015.
- [7] K. Ullah, I. Lill, and E. Witt, "An overview of BIM adoption in the construction industry: benefits and barriers," in *Proceedings of the 10th Nordic Conference on Construction Economics and Organization*, pp. 297–303, Bingley, WY, England, May 2019.
- [8] A. H. I. M. F. I. Mohd-Nor, M. M. Tahir, and I. M. S. Usman, "The usage OF building information modelling (BIM)," in *MALAYSIA'S ARCHITECTURE INDUSTRY*, vol. 12, no. 1, pp. 1–20, 2019.
- [9] M. F. I. Mohd-Nor and M. P. Grant, "Building information modelling (BIM) in the malaysian architecture industry," *WSEAS Transactions on Environment and Development*, vol. 10, pp. 264–273, 2014.
- [10] A. I. Che-Ani, M. Harris, M. F. I. Mohd-Nor, and M. Zulhanif, "A review OF building information modelling (BIM)-BASED building condition assessment concept," *MALAYSIAN Constr. Res. J.* vol. 20, no. 3, 85 pages, 2016.
- [11] R. Eadie, M. Browne, H. Odeyinka, C. Mckeown, and S. Mcniff, "A Survey of Current Status of and Perceived Changes Required for BIM Adoption in the UK," *Built Environment Project and Asset Management*, vol. 5, no. 1, pp. 4–21, 2015.
- [12] M. Jacobsson and C. Merschbrock, "BIM coordinators: a review," *Engineering Construction and Architectural Management*, vol. 25, no. 8, pp. 989–1008, 2018.
- [13] B. Abdal Noor and S. Yi, "Review of BIM literature in construction industry and transportation: meta-analysis," *Construction Innovation*, vol. 18, no. 4, pp. 433–452, 2018.
- [14] R. Jin, K. Gidado, P. Ashton, and N. Painting, "Scientometric Analysis of BIM-Based Research in Construction Engineering and Management," *Engineering, Construction and Architectural Management*, vol. 26, no. 8, pp. 1750–1776, 2019.
- [15] A. Al-Yami and M. O. Sanni-Anibire, "BIM in the Saudi Arabian construction industry: state of the art, benefit and barriers," *Int. J. Build. Pathol. Adapt.* vol. 39, no. 1, pp. 33–47, 2019.
- [16] A. M. I. Raouf and S. G. Al-Ghamdi, "Building information modelling and green buildings: challenges and opportunities," *Architectural Engineering and Design Management*, vol. 15, no. 1, pp. 1–28, 2019.
- [17] M. K. Dixit, V. Venkatraj, M. Ostadalimakhmalbaf, F. Pariafsai, and S. Lavy, "Integration of Facility Management and Building Information Modeling (BIM)," *Facilities*, vol. 37, pp. 455–483, 2019.
- [18] T. O. Olawumi and D. W. M. Chan, "An Empirical Survey of the Perceived Bene Fi Ts of Executing BIM and Sustainability Practices in the Built Environment," *Construction Innovation*, vol. 19, no. 5, pp. 321–342, 2019.
- [19] E. Witt and K. Kähkönen, "BIM-enabled Education: A Systematic Literature Review," in *Proceedings of the 10th Nordic Conference on Construction Economics and Organization*, pp. 261–269, Bingley, WY, England, May, 2019.
- [20] T. O. O. Olowa, E. Witt, and I. Lill, "BIM for Construction Education: Initial Findings from a Literature Review," in *Proceedings of the 10th Nordic Conference on Construction Economics and Organization*, pp. 305–313, Bingley, WY, England, May, 2019.
- [21] H. Wang, Y. Pan, and X. Luo, "Integration of BIM and GIS in sustainable built environment: a review and bibliometric analysis," *Automation in Construction*, vol. 103, pp. 41–52, 2019.
- [22] Q. Meng, Y. Zhang, Z. Li, W. Shi, J. Wang, and X. Wang, "A Review of Integrated Applications of BIM and Related Technologies in Whole Building Life Cycle," *Engineering, Construction and Architectural Management*, vol. 27, no. 8, pp. 1647–1677, 2020.
- [23] X. Yin, H. Liu, Y. Chen, and M. Al-Hussein, "Building information modelling for off-site construction: review and future directions," *Automation in Construction*, vol. 101, pp. 72–91, 2019.
- [24] M. Munir, A. Kiviniemi, S. Jones, and S. Finnegan, "BIM business value for asset owners: key issues and challenges," *International Journal of Building Pathology and Adaptation*, vol. 39, no. 1, pp. 135–151, 2020.
- [25] A. H. B. Hashim, N. Safie, H. Sallehuddin, and A. H. D. Hussain, "Building Information Modelling (BIM) and the Internet-Of-Things (IoT): A Systematic Mapping Study," *IEEE Access*, vol. 8, Article ID 155183, 2020.
- [26] M. Muzafar, "Building information modelling to mitigate the health and safety risks associated with the construction industry: a review," *International Journal of Occupational Safety and Ergonomics*, vol. 27, no. 4, pp. 1087–1095, 2020.
- [27] N. u. B. M. Zaid, N. Hamzah, and M. A. Khoiry, "Review building information modelling for infrastructure: benefits for constructor," *Journal of Computational and Theoretical Nanoscience*, vol. 17, no. 2, pp. 620–628, 2020.
- [28] A. I. C. Ani, S. Johar, N. M. Tawil, M. Z. A. Razak, and N. Hamzah, "Building Information Modeling (BIM)-based building condition assessment: a survey of water ponding defect on a flat roof," *Jurnal Teknologi*, vol. 75, no. 9, 2015.
- [29] S. Keele, "Guidelines for performing systematic literature reviews in software engineering," Technical Report, Ver. 2.3 EBSE Technical Report EBSE, sn, 5, 2007.
- [30] H. Arksey and L. O'Malley, "Scoping studies: towards a methodological framework," *International Journal of Social Research Methodology*, vol. 8, no. 1, pp. 19–32, 2005.
- [31] D. Levac, H. Colquhoun, and K. K. O'Brien, "Scoping studies: advancing the methodology," *Implementation Science*, vol. 5, no. 1, pp. 69–9, 2010.

- [32] Y. Xiao and M. Watson, "Guidance on Conducting a Systematic Literature Review," *Journal of Planning Education and Research*, vol. 39, no. 1, 2019.
- [33] I. Ali, I. Ahmedy, A. Gani, M. Talha, M. A. Raza, and M. H. Anisi, "Data collection in sensor-cloud: a systematic literature review," *IEEE Access*, vol. 8, Article ID 184687, 2020.
- [34] K. A. Alam, R. Ahmad, A. Akhuzada, M. H. N. M. Nasir, and S. U. Khan, "Impact analysis and change propagation in service-oriented enterprises: a systematic review," *Information Systems*, vol. 54, pp. 43–73, 2015.
- [35] S. Ouhbi, A. Idri, J. L. Fernández-Alemán, and A. Toval, "Requirements engineering education: a systematic mapping study," *Requirements Engineering*, vol. 20, no. 2, pp. 119–138, 2015.
- [36] A. Zakari, S. P. Lee, K. A. Alam, and R. Ahmad, "Software fault localisation: a systematic mapping study," *IET Software*, vol. 13, no. 1, pp. 60–74, 2019.
- [37] A. Zakari, S. P. Lee, R. Abreu, B. H. Ahmed, and R. A. Rasheed, "Multiple fault localization of software programs: a systematic literature review," *Information and Software Technology*, vol. 124, Article ID 106312, 2020.
- [38] T. No, *Computer science conference rankings core*, *Journal of the Association for Information Science and Technology*, 2015.
- [39] J. Yuan, X. Li, Y. Ke, W. Xu, Z. Xu, and M. Skibniewski, "Developing a building information modeling-based performance management system for public-private partnerships," *Engineering Construction and Architectural Management*, vol. 27, no. 8, pp. 1727–1762, 2020.
- [40] S. Zhang, D. Hou, C. Wang, F. Pan, and L. Yan, "Integrating and managing BIM in 3D web-based GIS for hydraulic and hydropower engineering projects," *Automation in Construction*, vol. 112, Article ID 103114, 2020.
- [41] S. O. Babatunde, D. Ekundayo, A. O. Adekunle, and W. Bello, "Comparative Analysis of Drivers to BIM Adoption Among AEC Firms in Developing Countries," *Journal of Engineering, Design and Technology*, vol. 18, no. 6, pp. 1425–1447, 2020.
- [42] N. Shafiq, M. F. Nurrudin, S. S. S. Gardezi, and A. B. Kamaruzzaman, "Carbon footprint assessment of a typical low rise office building in Malaysia using building information modelling (BIM)," *International Journal of Sustainable Building Technology and Urban Development*, vol. 6, no. 3, pp. 157–172, 2015.
- [43] S. Shrivastava and A. Chini, "Using building information modeling to assess the initial embodied energy of a building," *International Journal of Construction Management*, vol. 12, no. 1, pp. 51–63, 2012.
- [44] C. Z. Li, R. Y. Zhong, F. Xue et al., "Integrating RFID and BIM technologies for mitigating risks and improving schedule performance of prefabricated house construction," *Journal of Cleaner Production*, vol. 165, pp. 1048–1062, 2017.
- [45] W. Xiang and F. Wang, "Research on integration of multi-source BIM models based on GIS platform," in *Proceedings of the 2019 5th International Conference Information Management*, pp. 40–44, England, United Kingdom, March 2019.
- [46] A. Golabchi, M. Akula, and V. Kamat, "Automated Building Information Modeling for Fault Detection and Diagnostics in Commercial HVAC Systems," *Facilities*, vol. 34, pp. 233–246, 2016.
- [47] H. M. F. Shehzad, R. B. Ibrahim, A. F. Yusof, and K. A. M. Khaidzir, "Building information modeling: factors affecting the adoption in the AEC industry," in *Proceedings of the 2019 6th International Conference on Research and Innovation in Information Systems (ICRIIS)*, pp. 1–6, Johor Bahru, Malaysia, December 2019.
- [48] S. Ghosh, S. Negahban, Y. H. Kwak, and M. J. Skibniewski, "Impact of Sustainability on Integration and Interoperability between BIM and ERP-A Governance Framework," in *Proceedings of the First International Technology Management Conference*, pp. 187–193, San Jose, CA, USA, June 2011.
- [49] C. Dore and M. Murphy, "Integration of Historic Building Information Modeling (HBIM) and 3D GIS for recording and managing cultural heritage sites," in *Proceedings of the 2012 18th International Conference on Virtual Systems and Multimedia*, pp. 369–376, Milan, Italy, September 2012.
- [50] N. E. Mustafa, R. M. Salleh, and H. L. B. T. Ariffin, "Experiences of building information modelling (BIM) adoption in various countries," in *Proceedings of the 2017 International Conference on Research and Innovation in Information Systems (ICRIIS)*, pp. 1–7, IEEE, Langkawi, Malaysia, July 2017.
- [51] D. Juan, "The Research to Open BIM-Based Building Information Interoperability Framework," in *Proceedings of the 2013 2nd International Symposium on Instrumentation and Measurement, Sensor Network and Automation (IMSNA)*, pp. 440–443, IEEE, Toronto, ON, Canada, December 2013.
- [52] C. Zhang, J. Chen, X. Sun, and A. Hammad, "Lifecycle evaluation of building sustainability using BIM and RTLS," in *Proceedings of the Winter Simulation Conference 2014*, pp. 3236–3247, Savannah, GA, USA, December 2014.
- [53] L. Wang, Y. He, and Y. Han, "Research on power engineering construction management based on BIM technology," in *Proceedings of the 2018 International Conference on Robots & Intelligent System (ICRIS)*, pp. 107–109, IEEE, Changsha, China, May 2018.
- [54] S. Wang, G. Wainer, V. S. Rajus, and R. Woodbury, "Occupancy analysis using building information modeling and Cell-DEVS simulation," in *Proceedings of the Symposium on Theory of Modeling & Simulation-DEVS Integrative M&S Symposium*, pp. 1–8, San Diego, CA, USA, April 2013.
- [55] A. L. Ahmed and M. Kassem, "A unified BIM adoption taxonomy: conceptual development, empirical validation and application," *Automation in Construction*, vol. 96, pp. 103–127, 2018.
- [56] D. T. Olapade and B. G. Ekemode, "Awareness and utilisation of building information modelling (BIM) for facility management (FM) in a developing economy," *Journal of Facilities Management*, vol. 16, no. 4, pp. 387–395, 2018.
- [57] M. Addy, E. Adinyira, and J. Ayarkwa, "Antecedents of building information modelling adoption among quantity surveyors in Ghana an application of a technology acceptance model," vol. 16, no. 2, pp. 313–326, 2018.
- [58] G. Kelly, N. Dawood, M. Serginson, and S. Lockley, "BIM in facilities management applications: a case study of a large university complex," *Built Environment Proj Asset Manag*, vol. 5, no. 3, 2015.
- [59] S. O. Babatunde, S. Perera, D. Ekundayo, and T. E. Adeleye, "An investigation into BIM-based detailed cost estimating and drivers to the adoption of BIM in quantity surveying practices," *Journal of Financial Management of Property and Construction*, vol. 25, no. 1, pp. 61–81, 2019.
- [60] C. Bueno, L. M. Pereira, and M. M. Fabricio, "Life cycle assessment and environmental-based choices at the early design stages: an application using building information modelling," *Architectural Engineering and Design Management*, vol. 14, no. 5, pp. 332–346, 2018.

- [61] L. Design, C. Boddupalli, E. A. Rezazadeh, A. Sadhu, E. R. Azar, and S. Pattysan, "Improved visualization of infrastructure monitoring data using building information modeling," *Structure and Infrastructure Engineering*, vol. 15, no. 9, pp. 1247–1263, 2019.
- [62] M. Arslan, Z. Riaz, and S. Munawar, "Building Information Modeling (BIM) Enabled Facilities Management Using Hadoop Architecture," in *Proceedings of the 2017 Portland International Conference on Management of Engineering and Technology (PICMET)*, Portland, OR, USA, July 2017.
- [63] B. J. Gledson, "Hybrid project delivery processes observed in constructor BIM innovation adoption," *Construction Innovation*, vol. 16, no. 2, pp. 229–246, 2016.
- [64] S. H. A. Ahmed and S. M. A. Suliman, "A Structure Equation Model of Indicators Driving BIM Adoption in the Bahraini Construction Industry," *Construction Innovation*, vol. 20, no. 1, pp. 61–78, 2019.
- [65] G. Ngowtanasuwan and B. H. W. Hadikusumo, "System dynamics modelling for BIM adoption in Thai architectural and engineering design industry," *Construction Innovation*, vol. 17, no. 4, pp. 457–474, 2017.
- [66] A. Marefat, H. Toosi, and R. Mahmoudi Hasankhanlo, "A BIM approach for construction safety: applications, barriers and solutions," *Engineering Construction and Architectural Management*, vol. 26, no. 9, pp. 1855–1877, 2019.
- [67] X. Zhao and X. Wang, "Risk Paths in BIM Adoption: Empirical Study of China," *Engineering, Construction and Architectural Management*, vol. 25, no. 8, pp. 1170–1187, 2018.
- [68] T. Almuntaser, M. O. Sanni-Anibire, and M. A. Hassanain, "Adoption and implementation of BIM—case study of a Saudi Arabian AEC firm," *International Journal of Managing Projects in Business*, vol. 11, no. 3, pp. 608–624, 2018.
- [69] C. Vidalakis, F. H. Abanda, and A. H. Oti, "BIM adoption and implementation: focusing on SMEs," *Construction Innovation*, vol. 20, no. 1, pp. 128–147, 2020.
- [70] V. Singh, "BIM and Systemic ICT Innovation in AEC," *Constr Innov*, vol. 14, no. 3, pp. 292–306, 2014.
- [71] A. Ahankoob, K. Manley, and B. Abbasnejad, "The role of contractors' building information modelling (BIM) experience in realising the potential values of BIM," *International Journal of Construction Management*, vol. 22, no. 4, pp. 588–599, 2019.
- [72] P. Demian and D. Walters, "The advantages of information management through building information modelling," *Construction Management & Economics*, vol. 32, no. 12, pp. 1153–1165, 2014.
- [73] R. Davies and C. Harty, "Measurement and exploration of individual beliefs about the consequences of building information modelling use," *Construction Management & Economics*, vol. 31, no. 11, pp. 1110–1127, 2013.
- [74] J. Matthews, P. E. D. Love, J. Mewburn, C. Stobaus, and C. Ramanayaka, "Building information modelling in construction: insights from collaboration and change management perspectives," *Production Planning & Control*, vol. 29, no. 3, pp. 202–216, 2018.
- [75] Ø. Mejlænder-Larsen, "Using a change control system and building information modelling to manage change in design," *Architectural Engineering and Design Management*, vol. 13, no. 1, pp. 39–51, 2017.
- [76] J. Korpela, R. Miettinen, T. Salmikivi, and J. Ihalainen, "The challenges and potentials of utilizing building information modelling in facility management: the case of the Center for Properties and Facilities of the University of Helsinki," *Construction Management & Economics*, vol. 33, no. 1, pp. 3–17, 2015.
- [77] C. Tsai, Y. Xiao, H. Chen, Y. Ye, C. Wang, and T. Liang, "Integration of BIM and GIS to Query Management on Pipeline of Building-A Case Study of Dormitory," in *Proceedings of the 2017 International Conference on Applied System Innovation (ICASI)*, pp. 944–947, Sapporo, Japan, May 2017.
- [78] M. A. Tariq, U. Farooq, E. Aamir, and R. Shafaqat, "Exploring adoption of integrated building information modelling and virtual reality," in *Proceedings of the 2019 International Conference on Electrical, Communication, and Computer Engineering (ICECCE)*, pp. 1–6, Swat, Pakistan, July 2019.
- [79] Y. K. Juan, W. Y. Lai, and S. G. Shih, "Building information modeling acceptance and readiness assessment in Taiwanese architectural firms," *Journal of Civil Engineering and Management*, vol. 23, no. 3, pp. 356–367, 2016.
- [80] Y. Chen, Y. Yin, G. J. Browne, and D. Li, "Adoption of building information modeling in Chinese construction industry," *Engineering Construction and Architectural Management*, vol. 26, no. 9, pp. 1878–1898, 2019.
- [81] Y. Hong, A. W. A. Hammad, and A. Akbarnezhad, "BIM Adoption Model for Small and Medium Construction Organisations in Australia," *Engineering, Construction and Architectural Management*, vol. 26, no. 2, pp. 154–183, 2019.
- [82] M. Hilal, T. Maqsood, and A. Abdekhodae, "A hybrid conceptual model for BIM in FM," *Construction Innovation*, vol. 19, no. 4, pp. 531–549, 2019.
- [83] E. O. Oyewole and J. O. Dada, "Training gaps in the adoption of building information modelling by Nigerian construction professionals," *Built Environment Project and Asset Management*, vol. 9, no. 3, pp. 399–411, 2019.
- [84] W. I. Enegbuma, U. G. Aliagha, and K. N. Ali, "Preliminary building information modelling adoption model in Malaysia perspective," vol. 14, no. 4, pp. 408–432, 2014.
- [85] J. Rogers, H.-Y. Chong, and C. Preece, "Adoption of building information modelling technology (BIM)," *Engineering Construction and Architectural Management*, vol. 22, no. 4, pp. 424–445, 2015.
- [86] R. Jin, T. Yang, P. Piroozfar, B. G. Kang, and D. Wanatowski, "Project-based pedagogy in interdisciplinary building design adopting BIM," *Engineering Construction and Architectural Management*, vol. 25, no. 10, pp. 1376–1397, 2018.
- [87] S. O. Babatunde, C. Udejaja, and A. O. Adekunle, "Barriers to BIM implementation and ways forward to improve its adoption in the Nigerian AEC firms," *International Journal of Building Pathology and Adaptation*, vol. 39, no. 1, pp. 48–71, 2020.
- [88] A. B. Saka and D. W. M. Chan, "Profound Barriers to Building Information Modelling (BIM) Adoption in Construction Small and Medium-Sized Enterprises (SMEs)," *Constr Innov*, vol. 20, no. 2, pp. 261–284, 2020.
- [89] E. Park, S. J. Kwon, and J. Han, "Antecedents of the Adoption of Building Information Modeling Technology in Korea," *Eng Constr Archit Manag*, vol. 26, no. 8, pp. 1735–1749, 2019.
- [90] A. Grilo, A. Zutshi, R. Jardim-Goncalves, and A. Steiger-Garcia, "Construction collaborative networks: the case study of a building information modelling-based office building project," *International Journal of Computer Integrated Manufacturing*, vol. 26, no. 1–2, pp. 152–165, 2013.
- [91] I. Kovacic and M. Filzmoser, "Designing and evaluation procedures for interdisciplinary building information

- modelling use—an explorative study,” *Engineering Project Organization Journal*, vol. 5, no. 1, pp. 14–21, 2015.
- [92] A. R. A. Usmani, A. Elshafey, M. Gheisari, C. Chai, E. B. Aminudin, and C. S. Tan, “A scan to as-built building information modeling workflow: a case study in Malaysia,” *Journal of Engineering, Design and Technology*, vol. 18, no. 4, pp. 923–940, 2019.
- [93] A. Gouda, M. Reda, and M. Marzouk, “Automation in Construction BIM and semantic web-based maintenance information for existing buildings,” *Automation in Construction*, vol. 116, Article ID 103209, 2020.
- [94] I. V. Lokshina, M. Greguš, and W. L. Thomas, “Application of integrated building information modeling, IoT and blockchain technologies in system design of a smart building,” *Procedia Computer Science*, vol. 160, pp. 497–502, 2019.
- [95] W. Jeong, J. B. Kim, M. J. Clayton, J. S. Haberl, and W. Yan, “A framework to integrate object-oriented physical modelling with building information modelling for building thermal simulation,” *Journal of Building Performance Simulation*, vol. 9, no. 1, pp. 50–69, 2016.
- [96] J. Louis and K. Rashid, “Utilizing building information models as operating systems for smart homes,” in *Proceedings of the Human-Habitat Heal. Human-Habitat Multimodal Interact. Promot. Heal. Well-Being Internet Things era*, pp. 1–4, New York, NY, USA, October 2018.
- [97] J. Melzner, S. Zhang, J. Teizer, and H.-J. Bargstädt, “A case study on automated safety compliance checking to assist fall protection design and planning in building information models,” *Construction Management & Economics*, vol. 31, no. 6, pp. 661–674, 2013.
- [98] Y. Ren, M. J. Skibniewski, and S. Jiang, “Building information modeling integrated with electronic commerce material procurement and supplier performance management system,” *Journal of Civil Engineering and Management*, vol. 18, no. 5, pp. 642–654, 2012.
- [99] L. Shengyi and W. Jia, “Research on Integrated Application of Virtual Reality Technology Based on BIM,” in *Proceedings of the 2016 Chinese Control and Decision Conference (CCDC)*, pp. 2865–2868, Yinchuan, China, May 2016.
- [100] S. Tang, D. R. Shelden, C. M. Eastman, P. Pishdad-bozorgi, and X. Gao, “BIM assisted Building Automation System information exchange using BACnet and IFC,” *Automation in Construction*, vol. 110, Article ID 103049, 2020.
- [101] O. Davtalab, A. Kazemian, and B. Khoshnevis, “Perspectives on a BIM-integrated software platform for robotic construction through Contour Crafting,” *Automation in Construction*, vol. 89, pp. 13–23, 2018.
- [102] J. Hwang, C. Hong, and H. Choi, “Implementation of Prototype for Interoperability between BIM and GIS Demonstration Paper,” in *Proceedings of the IEEE 7th International Conference on Research Challenges in Information Science (RCIS)*, pp. 3–4, Paris, France, May 2013.
- [103] A.-M. Mahamadu, L. Mahdjoubi, and C. Booth, “Challenges to BIM-cloud integration: implication of security issues on secure collaboration,” in *Proceedings of the 2013 IEEE 5th International Conference on Cloud Computing Technology and Science*, pp. 209–214, Bristol, United Kingdom, December 2013.
- [104] K. Chen, G. Xu, F. Xue, R. Y. Zhong, D. Liu, and W. Lu, “A physical internet-enabled building information modelling system for prefabricated construction,” *International Journal of Computer Integrated Manufacturing*, vol. 31, no. 4–5, pp. 349–361, 2018.
- [105] X. Zhou, J. Zhao, J. Wang et al., “OutDet: an algorithm for extracting the outer surfaces of building information models for integration with geographic information systems,” *International Journal of Geographical Information Science*, vol. 33, no. 7, pp. 1444–1470, 2019.
- [106] A. Ahankoob, K. Manley, C. Hon, and R. Drogemuller, “The impact of building information modelling (BIM) maturity and experience on contractor absorptive capacity,” *Architectural Engineering and Design Management*, vol. 14, no. 5, pp. 363–380, 2018.
- [107] P. Rathnasiri and S. Jayasena, “Green building information modelling technology adoption for existing buildings in Sri Lanka,” *Facilities management perspective” Intelligent Building International*, vol. 14, no. 1, pp. 1–22, 2019.
- [108] K. O. Ayinla and Z. Adamu, “Bridging the Digital divide gap in BIM Technology Adoption,” *Eng Constr Archit Manag*, vol. 25, no. 10, pp. 1398–1416, 2018.
- [109] M. Munir, A. Kiviniemi, and S. W. Jones, “Business value of integrated BIM-based asset management,” *Engineering, Construction and Architectural Management*, vol. 26, no. 6, pp. 1171–1191, 2019.
- [110] Z. A. B. Ismail, “Thermal comfort Practices for Precast concrete Building Construction Projects: Towards BIM and IOT Integration,” *Engineering Construction and Architectural Management*, vol. 29, no. 3, pp. 1504–1521, 2021.
- [111] A. B. A. Altohami, N. A. Haron, and A. H. Ales@Alias, “Investigating approaches of integrating BIM, IoT, and facility management for renovating existing buildings: a review,” *Sustainability*, vol. 13, no. 7, 3930 pages, 2021.
- [112] X. Tan, “Intelligent construction integrated management system based on BIM and Internet of Things,” in *Proceedings of the 2021 6th International Conference on Communication and Electronics Systems (ICCES)*, pp. 604–608, IEEE, Coimbatre, India, July 2021.
- [113] L. Ding, W. Jiang, and C. Zhou, “IoT sensor-based BIM system for smart safety barriers of hazardous energy in petrochemical construction,” *Frontiers of Engineering Management*, vol. 9, pp. 1–15, 2021.
- [114] J. X. Zhou, G. Q. Shen, S. H. Yoon, and X. Jin, “Customization of on-site assembly services by integrating the internet of things and BIM technologies in modular integrated construction,” *Automation in Construction*, vol. 126, pp. 103663–112021, 2021.

Research Article

Simulation of Quantity and Quality of Saq Aquifer Using Artificial Intelligence and Hydraulic Models

Abdul Razzaq Ghumman ¹, **Ghufran Ahmed Pasha** ², **Md. Shafiquzzaman** ¹,
Afaq Ahmad ², **Afzal Ahmed** ², **Riaz Akhtar Khan** ³, and **Rashid Farooq** ⁴

¹Department of Civil Engineering, College of Engineering, Qassim University, Buraidah 51452, Saudi Arabia

²Department of Civil Engineering, University of Engineering and Technology, Taxila 47050, Pakistan

³Department of Civil Engineering, Leads University, Lahore 54792, Pakistan

⁴Department of Civil Engineering, International Islamic University, Islamabad 44000, Pakistan

Correspondence should be addressed to Afaq Ahmad; afaq.ahmad@uettaxila.edu.pk

Received 29 November 2021; Revised 31 March 2022; Accepted 19 April 2022; Published 16 May 2022

Academic Editor: Bangbiao Wu

Copyright © 2022 Abdul Razzaq Ghumman et al. This is an open access article distributed under the Creative Commons Attribution License, which permits unrestricted use, distribution, and reproduction in any medium, provided the original work is properly cited.

Scarcity of water resources is becoming a threatening issue in arid regions like Gulf. Accurate prediction of quantities and quality of groundwater is the first step towards better management of water resources where groundwater is the major source of water supply. Groundwater modelling with respect to its quantity and quality has been performed in this paper using Artificial Neural Networks (ANNs), Adaptive Neurofuzzy Inference System (ANFIS), and hydraulic model MODFLOW. Five types of ANN models with various training functions have been investigated to find the most efficient training function for the prediction of quantity and quality of groundwater, which is an original contribution useful for engineering sector. The results of the hydraulic model, ANFIS, and ANN have been compared. Nash-Sutcliffe Model Efficiency and Mean Square Error have been used for assessing the performance of models. Taylor's Diagram has also been used to compare various models. The part of Saq Aquifer lying in the Qassim Region has been investigated as the study area. Modern tools, including Geographical Information System (GIS) and Digital Elevation Model (DEM) are applied to process the required data for modelling. Climatic, geographical, and quality of groundwater (contaminants) data are obtained from the Ministry of Environment, Water, and Agriculture, Jeddah/Riyadh. ANFIS model is found to be the most efficient for modelling both the quality and quantity of the aquifer. Sensitivity analysis was performed, and then various future scenarios were investigated for sustainable groundwater pumping. The results of the research will be useful for the community and experts working in the field of water resources engineering, planning, and management in arid regions.

1. Introduction

Groundwater resources of the Gulf region are under high stress. These are being depleted at an alarming rate of about 6.8 mm/year in some transboundary aquifers like Saq shared by Iraq, Jordan, and Saudi Arabia. This rapid depletion of groundwater resources (Figure 1) is due to anthropogenic and climatic factors. The rainfall in the region is small, but the extraction rate of groundwater for irrigation and domestic purposes is very high due to phenomenal increase in the population [1, 2]. For sustainable management and development of water resources around the globe, the future predictions of groundwater levels are of utmost importance

[3–6]. The changes in groundwater levels are affected by several factors. The timing, location, and extent of hydrologic responses to human activities or natural events depend on the duration, intensity, and nature of the activities/event affecting groundwater, the subsoil properties, and the interaction of groundwater and surface water. The field surveys or remote sensing data of various aquifer characteristics may provide a theoretical understanding of the groundwater system, but often the measured data is scarce with respect to space and time, and hence the system-understanding remains undefined and inadequate in most cases.

Some awareness of the complex behavior of the groundwater system can be developed through groundwater

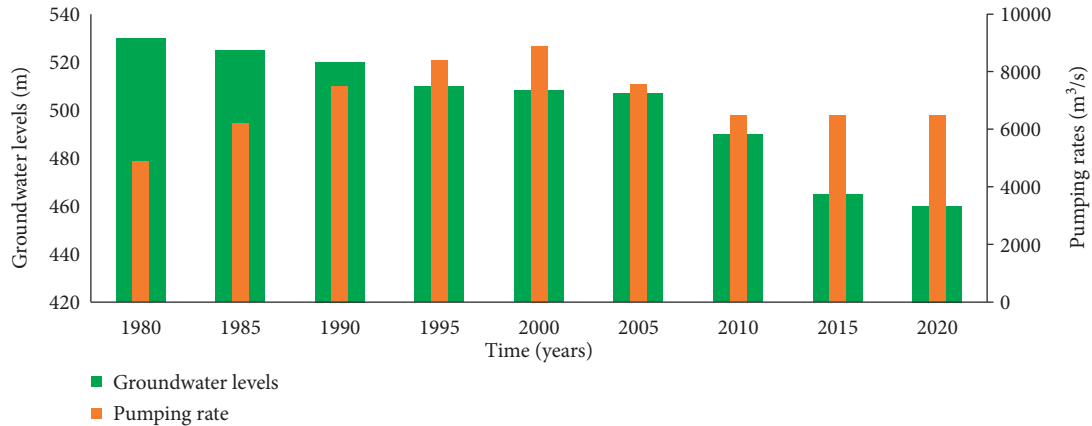


FIGURE 1: Groundwater depletion and pumping rates for Saq Aquifer (Qassim Region).

TABLE 1: Review of data-driven models and hydraulic model MODFLOW.

Characteristics	ANN/ANFIS	Hydraulic model	Remarks
Efforts/costs involved in computation expenses (need high-speed computers and time for computations)	x	About 10 times x	Although the hydraulic models like MODFLOW require computers with relatively large processing speed as compared to the data-driven models like ANN and ANFIS, which require only ordinary-type computers [12], this factor is not considered nowadays as high-speed computers are easily available.
Requirements related to the processing of models and data	x	About 3 times x	Data for only water levels, pumping rates, and concentration of contaminants are required. The data for hydraulic parameters and topography (Digital Elevation Model (DEM)) are required in addition to data for water levels, pumping rates, and concentration of contaminants. The hydraulic model (MODFLOW) requires highly accurate aquifer-parameter values. Furthermore, a mesh of an extraordinary resolution and lower time steps but qualifying the limiting ratio of time step to the nodal distance is required, whereas only a good dataset can be sufficient for data-driven models like ANN and ANFIS [13–15].
Model category	Data-driven (black box/semiblack box)	Distributed (based on laws of physics)	Hydraulic models incorporate physical processes and equations based on laws of physics in predicting groundwater levels and groundwater contamination parameters, whereas ANFIS/ANN, being data-driven models, do not use equations based on laws of physics. These models only use the recorded data for their training, testing, and validation [13–16].
Model prediction biases	x	About 10 times x	There is a wide range of variation in biases in the case of hydraulic model results, whereas the biases are mostly limited to a certain range for data-driven model (ANFIS/ANN) predictions. However, the ANFIS/ANN lack generality [13–16].
Future predictions for a long time	Highly challenging	Much easier once the model is calibrated	After calibration and validation of the hydraulic model, it is very easy to use it for future predictions, whereas very high experience and expertise in definite phenomenon is required for long-time future predictions by ANFIS/ANN [13–16].

models. Once a model is developed and designed properly, it can be used to predict the future behavior of groundwater, which may help in decision-making and exploring the alternative approaches for management, planning, and development of water resources [6–9]. This paper has multiple goals. One of the main goals of this paper is to develop groundwater models for the simulation of water levels of the Saq Aquifer. However, there is no single model which may provide results to the entire satisfaction of the researcher because there is always some degree of uncertainty in model results. Hence a variety of data-driven models based on

Artificial Neural Networks (ANNs), Adaptive Neurofuzzy Inference System (ANFIS), and hydraulic model MODFLOW have been investigated in this research.

The hydraulic models for transboundary aquifers having undefined boundary conditions for specific regions demand very expensive data acquisition schemes. Although this difficulty has been resolved in this paper by using the “general head boundary condition,” there is a need to investigate some other alternative modelling techniques. The data-driven models can be a good alternative for predicting groundwater levels in the vicinity of some crucial areas like

pumping stations [10, 11]. Both types of models, that is, hydraulic and artificial intelligence, are compared in Table 1. Data-driven models are divided into several categories. Khedri et al. [17] compared five different data-driven models for the prediction of groundwater levels. They have investigated the performance of ANN, Adaptive Neurofuzzy Inference System, Fuzzy Logic, Support Vector Regression, and Group Method of Data Handling. According to them, the ANN are the most commonly used efficient method. Majumder and Eldho [18] applied ANN coupled with an optimization technique to model groundwater flow. They have also observed better convergence by ANN combined with optimization. Suprayogi et al. [19] applied ANN to forecast groundwater levels in Meskom, Indonesia. They have observed high values of correlation coefficient having a successful application of ANN for groundwater level forecast for a short time basis. Wunsch et al. [20] have outlined the ability of prediction of groundwater levels by recurrent ANNs using data from 17 groundwater wells within the Upper Rhine Graben, one of the largest groundwater resources in Central Europe. Solgi et al. [21] have investigated the performance of ANN for long- and short-term groundwater level predictions using more than 17 years of the most recent observed data of groundwater levels in San Antonio, Texas, United States of America. In addition to the prediction of groundwater levels, another dimension of groundwater modelling is predicting its quality [9, 22, 23]. Fadipe et al. [24] have studied groundwater quality for the community of Boluwaduro, Ofatedo, Osun State. The concentrations of nitrite, nitrate, iron, and lead have been investigated by training ANN structure to get the best possible output. Al-Adhaileh and Alsaade [25] have studied groundwater quality for various locations of aquifers in India using various types of artificial intelligence methods. A thorough literature survey shows that there are several dimensions of data-driven models which need to be investigated to choose the best possible model for groundwater predictions.

In this paper, the ANN techniques and Adaptive Neurofuzzy Inference System (ANFIS) have been investigated rigorously for the prediction of both the quantity and quality of flow through an aquifer. The areas of research regarding ANN include the selection of architecture of ANN, the study of the impact of activation functions, and the choice of an efficient training algorithm. The ANN may have several types of architectures depending upon the number of hidden layers, the number of neurons in each hidden layer, and the activation function [2, 26]. Working of these models further changes if different types of training functions are used [2, 20]. There are twelve types of training functions that can be used. The performances of three types of ANN models in order to predict groundwater levels have been investigated by Coulibaly et al. [27]. Input delay neural network, recurrent neural network, and generalized radial basis function models have been tested and it was found that recurrent neural networks are the most efficient models for predicting monthly groundwater level fluctuations in the Gondo plain, northwestern Burkina Faso. Two types of architectures of ANN have been applied to study groundwater modelling by

Nordin et al. [28]. Quantities of different effluents in groundwater have been predicted. The model was applied to real data from groundwater in Faisalabad, the largest industrial city of Pakistan. Seven categories of ANN architectures and training algorithms have been applied by Daliakopoulos et al. [29] to forecast monthly groundwater in Messara Valley in Crete, Greece. They observed that the standard feedforward ANN with the Levenberg-Marquardt algorithm provided the best results for forecasts up to 18 months. Yoon et al. [30] applied ANN with the backpropagation algorithm as a training function to forecast groundwater levels in the beach of the coastal town of Mukho, Donghae city, Korea, on a short-term basis. They found some degree of uncertainty in ANN results and suggested that these should always be designed very carefully. Lohani and Krishan [31] also used backpropagation algorithm as training function in ANN to simulate groundwater level changes in Punjab, India districts of Patiala, Faridkot, Ludhiana, and Ferozepur. They found that groundwater levels can be successfully predicted with acceptable accuracy for future six months using ANN-backpropagation algorithm as training function. The process of learning in advanced types of ANN is achieved by the use of a training algorithm which is similar to optimization [22]. The main aim in each iteration of ANN learning/training is to minimize the error between the predicted and observed groundwater levels and concentration of contaminants.

The weights and biases are adjusted in different trials of training in an efficient way to obtain a global minimum with the help of the training algorithm. There are about 12 different training functions for the multilayer perceptron. The ANN will achieve the best performance in the minimum possible computer time if the most efficient training function is used. Performances of only a few out of 12 have been reported in past studies. Hence, in this paper, we have compared the performances of the five most important training functions to simulate the levels and quality of groundwater around pumping stations of Buraydah, Qasim, Saudi Arabia.

There are several parameters/contaminants which need to be investigated for studying the quality of the groundwater. However, the main objective of this paper is to compare the performances of various ANN and ANFIS models, so only a few quality parameters have been chosen to make the comparison visible and comparatively easier. TDS, Fe, and Mn were easily available from recorded data. Therefore, these three contaminants have been selected for the quality study. Another point is worth mentioning here that the available data consists of annual values of concentration and groundwater levels. Hence, the investigation regarding seasonal variability is out of the scope of this paper.

2. Materials and Methods

2.1. Methodological Framework. In this paper, two types of techniques, the hydraulic model MODFLOW and the data-driven models (ANFIS and ANN), have been used to predict the groundwater quality and quantity for the Saq Aquifer. A

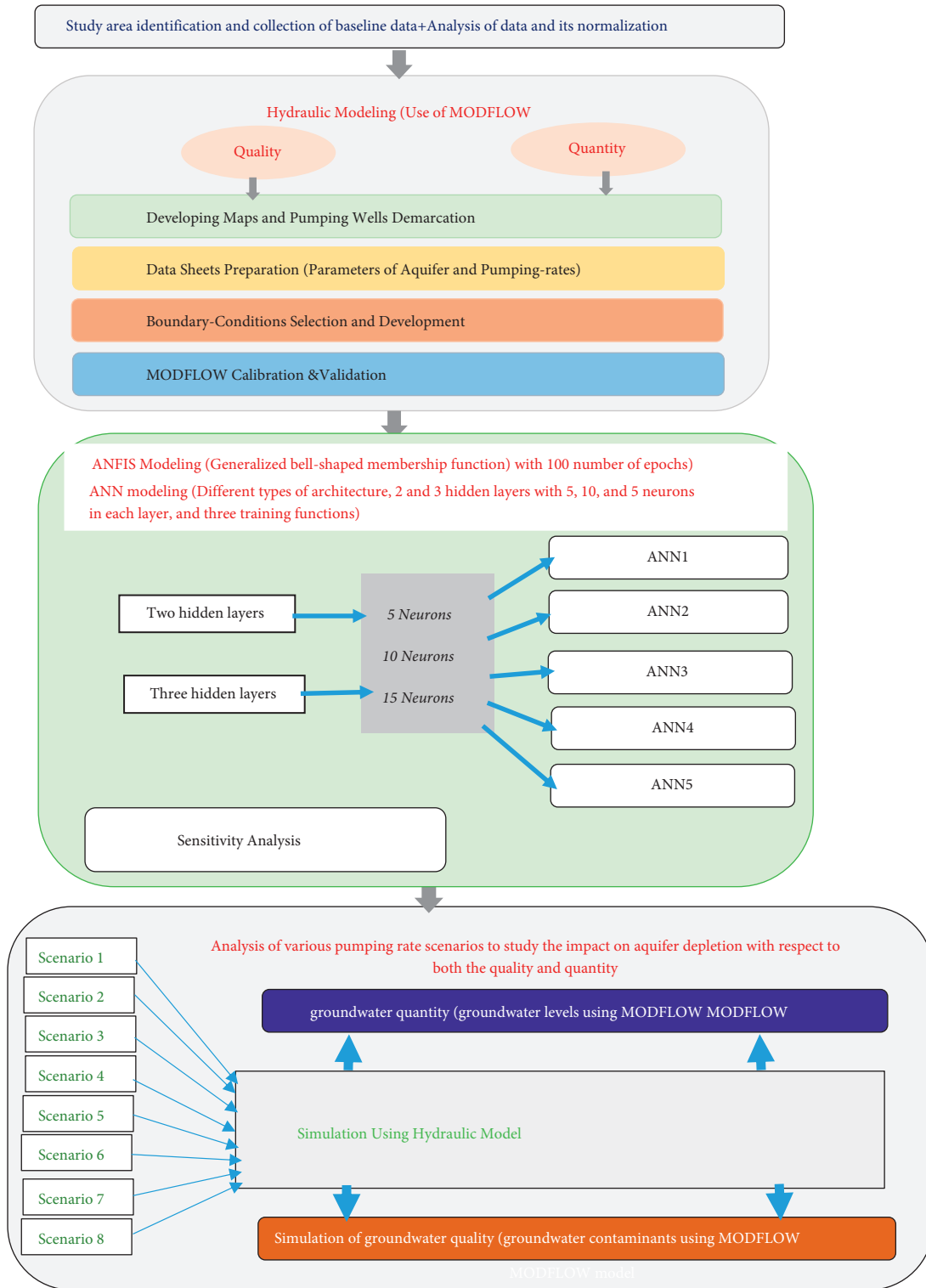


FIGURE 2: Groundwater modelling framework to explore the impacts of pumping on depletion of aquifer.

conceptual comparison of the two techniques is given in Table 1. An overall methodology framework is shown in Figure 2. Three main steps are involved in this research work. The first step comprised data collection, including pumping rates, groundwater levels, well locations, the concentration of contaminants, and parameters of the

aquifer. The data for pumping rates, groundwater levels, and concentration of contaminants have been normalized in the case of ANFIS and ANN models. The second step was to calibrate/train/test/validate as per the requirement of both categories of models (hydraulic/ANFIS and ANN). Part of the data (say 60%) was used for calibration/training, and the

TABLE 2: Future scenarios for pumping rates.

Scenario no.	Description	Scenario no.	Description
1	Assuming a decrease in the pumping rate by 1% yearly	5	Assuming the pumping rate to increase 3% yearly
2	Assuming the present pumping rate to continue during the entire period	6	Assuming the pumping rate to increase 4% yearly
3	Assuming the pumping rate to increase 1% yearly	7	Assuming the pumping rate to increase 5% yearly
4	Assuming the pumping rate to increase 2% yearly	8	Assuming scenario 2 with an artificial recharge case

remaining (40%) was used for validation/testing. It is worth mentioning that calibration and validation were done for both the quantity and quality of groundwater. Hydraulic parameters were adjusted to obtain accurate groundwater levels at certain locations after a certain model runtime as close to the observed groundwater levels as possible. The calibration of the pollutant transport model has mainly been done by adjusting the contaminant transport parameters (dispersion coefficient, etc.) until the observed concentration values were consistent with the model's predicted values. Six wells were processed and used as concentration observation wells with their coordinates and historical records of groundwater levels.

The data were divided into two parts, 60% for calibration and 40% for validation of the hydraulic model, and three parts, 60%, 20%, and 20%, for the training, validation, and testing of ANFIS/ANN models, respectively. A computer program (coding) was prepared in MATLAB to develop ANFIS/ANN models to achieve the required objectives.

Sensitivity analysis of parameters was made to see the impact of various hydraulic and quality parameters on model results. Step three included the application of the chosen model for future predictions of groundwater quality and levels to study the aquifer depletion in both quality and quantity. Due to the phenomenal increase in population and high living standards of people, there is an increasing trend in groundwater use [32]. Eight future scenarios for different pumping rates (as given below) have been tested to investigate the depletion of an aquifer with respect to both quality and quantity. The farthest optimistic scenario, farthest pessimistic scenario, and possible scenarios between the two extremes have been examined as given in Table 2.

2.2. Study Area. The study area included the most important area of Saq Aquifer located in the Qassim Region, as shown in Figure 3. Qassim region is one of the important regions of the Kingdom of Saudi Arabia. It is characterized as an arid region. It has an area of approximately 80,000 km², located between latitudes 25°00' and 27°00' N and longitudes 42°30' and 45°00' E [2, 5]. It has an altitude ranging between 600 and 850 m above sea level. Qassim has a population of nearly 1,423,935 capita as per 2017 records. It is the second-largest agricultural region in Saudi Arabia, and groundwater from the Saq Aquifer is available easily. The region comprises a desert climate, characterized by cold and rainy winter and hot summer with low humidity. The evaporation is nearly

4500 mm per annum on average. The summer temperature is as high as 49°C during the daytime and 36°C during the nighttime. However, the winter temperature may sometimes fall below 0°C. The average annual rainfall in Qassim Region is about 125 mm [2]. The main source of water supply to the region is groundwater extracted mainly from the Saq Aquifer, which is one of the most important aquifers in the Kingdom [5, 33]. It has a very vast outcrop, which spreads over a length of approximately 1200 km only in the Kingdom of Saudi Arabia and joins the border of Jordan as far south as latitude 24°30' N and longitude 45°00' E. The huge aquifer is confined in nature with a thickness varying from 400 m in the southern part to 700 m in its northern part. The part of the aquifer under study has an average thickness of about 500 m [2]. The strata consist of sandstone having medium to coarse size. A few areas comprise sandstone of fine size at local levels. Most of the private and public tube wells are partially penetrating, with 125 m screen and a depth of approximately 650 m [2]. Wadi Al-Rummah is considered a big valley that passes through the Saq area in the Qassim Region. The Saq Aquifer has a high salinity value in the area near Wadi Al-Rummah compared to the area away from Wadi Al-Rummah. Recharge from Wadi, agriculture processes, and effluent from wastewater treatment plants are essential factors that may contribute to its comparatively higher salinity in the surrounding area of Wadi Al-Rummah [5].

2.3. Description of Hydraulic Model (MODFLOW)

2.3.1. Groundwater Levels and Flow Modelling. The groundwater flow modelling is highly complicated [34] as it is governed by partial differential equations as given below [35].

$$\frac{\partial}{\partial x} \left(K_{xx} \frac{\partial h}{\partial x} \right) + \frac{\partial}{\partial y} \left(K_{yy} \frac{\partial h}{\partial y} \right) + \frac{\partial}{\partial z} \left(K_{zz} \frac{\partial h}{\partial z} \right) = S_s \frac{\partial h}{\partial t} - W, \quad (1)$$

where the parameters " K_{xx} ," " K_{yy} ," and " K_{zz} " represent the hydraulic conductivities in the x , y , and z directions, respectively; the groundwater head is expressed by " h "; " S_s " is the parameter called the specific storage of the aquifer; the source/sink is represented by W ; and " t " is time. A denser mesh was created at the locations of wells to model the wells as accurately as possible [36–39].

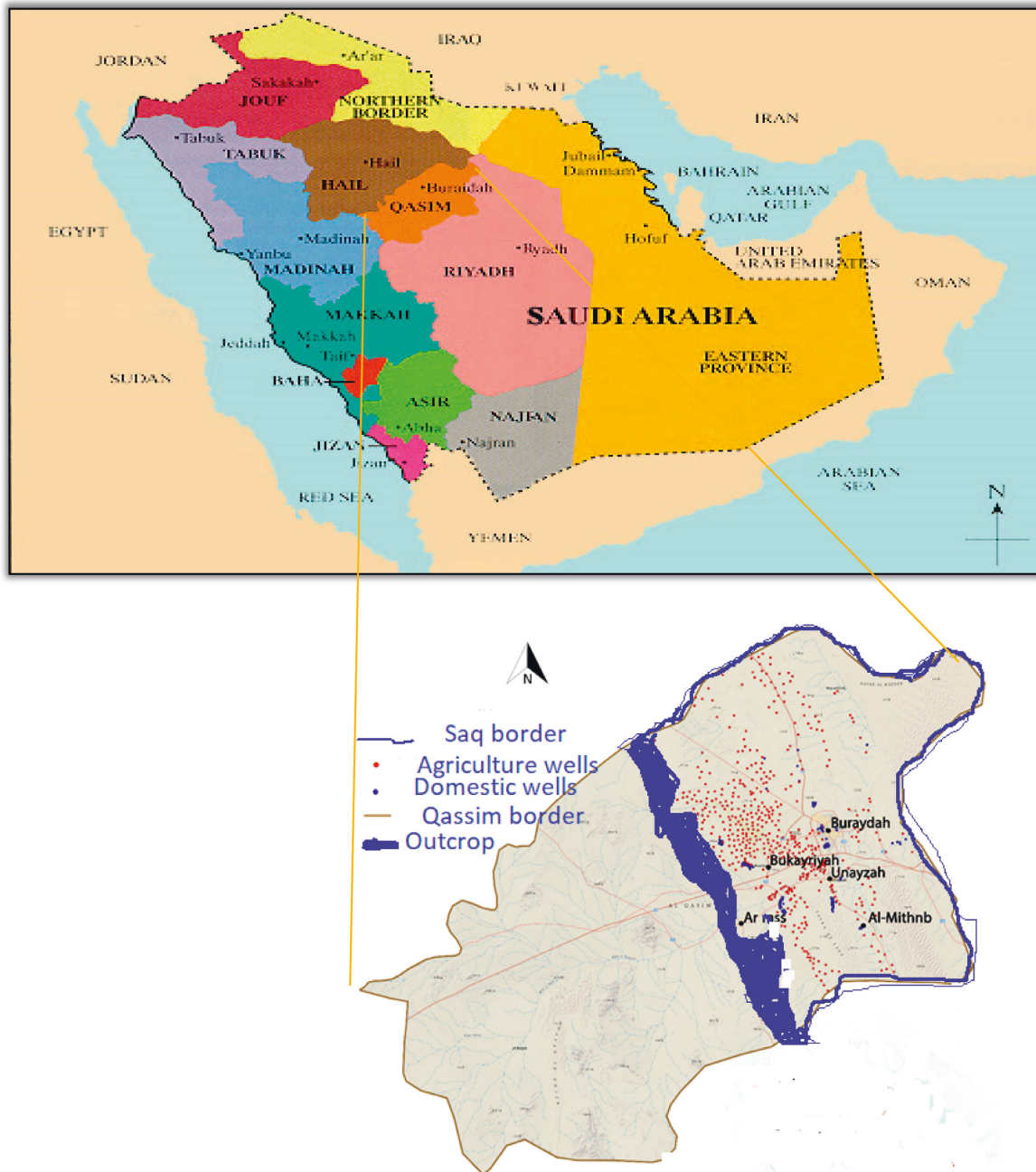


FIGURE 3: Map of the study area showing the locations of pumping wells, Saq in the Qassim Region, and Saq outcrop.

Visual MODFLOW is a commercial graphical user interface. It has unique features in which users have the ability to use Excel files, Surfer grids, GIS, and AutoCAD data as input files instead of the form of text files. Also, the results can be shown in the charts and contour maps. These features help in lowering the execution time and making the analysis of results easier [37–39]. In addition to finite element, there are many finite difference schemes to solve (1), including explicit finite difference and implicit finite difference. The model MODFLOW uses an implicit finite difference scheme to achieve the solution of equation (1). The input and output data for MODFLOW are presented in Table 3. Selection of the mesh size and appropriate boundary conditions is a

highly challenging task in large aquifers like Saq. In this paper, a rectangular type of mesh of $30 \text{ km} \times 20 \text{ km}$ was developed by creating 80 rows and 70 columns; in one case, slightly bigger area was modelled in case of studying the area around Wadi Al-Rumamah. The numbers of columns and rows for the mesh around the pumping wells were significantly increased to determine a highly dense mesh for the prediction of the quantity and quality of groundwater as accurately as possible. The thickness of the aquifer in the vertical direction was taken as approximately 500 m with an impermeable cover of about 628 m above 500 m thick layer of Saq Aquifer [2, 33]. As mentioned above, the pumping wells are partially penetrating with a 125 m long screen.

TABLE 3: Input values of data for MODFLOW.

Required data	Data description/estimation	Adopted values of data
Transmissivity and conductivity	Cooper-Jacob technique applied on pumping test to estimate the hydraulic conductivity of Saq Aquifer in Qassim Region [33, 40]	$T = 0.024$ to $1.62 \text{ m}^2/\text{minute}$, $K_{yy} = K_{xx} = K_{zz} = 2.8 \text{ m/day}$
No. of aquifer layers	Published research papers [2, 33]	Adopted layers = 5, each of 631, 125, 125, 125, and 125 m, respectively
Mesh size	By running model with different mesh sizes and choosing the best	As much dense as possible. It was further made dense around the wells
Pumping rates	As per data collected from the Ministry of Environment, Water, and Agriculture, Saudi Arabia	Public and private tube wells data available from 1980 to 2018
Water levels (a)	As per data collected from the Ministry of Environment, Water, and Agriculture, Saudi Arabia	Public and private tube wells data available from 1980 to 2018
Initial conditions	As per data collected from the Ministry of Environment, Water, and Agriculture, Saudi Arabia	Water levels at the start time of simulations
Boundary conditions	Calibrated assuming general head boundary conditions	Highly challenging work
Storage coefficient	Cooper-Jacob technique applied on pumping test to estimate the hydraulic conductivity of Saq Aquifer in Qassim Region [33, 40]	2.5×10^{-3} to 6.3×10^{-5}
Contaminant concentrations	Recorded values	Recorded data

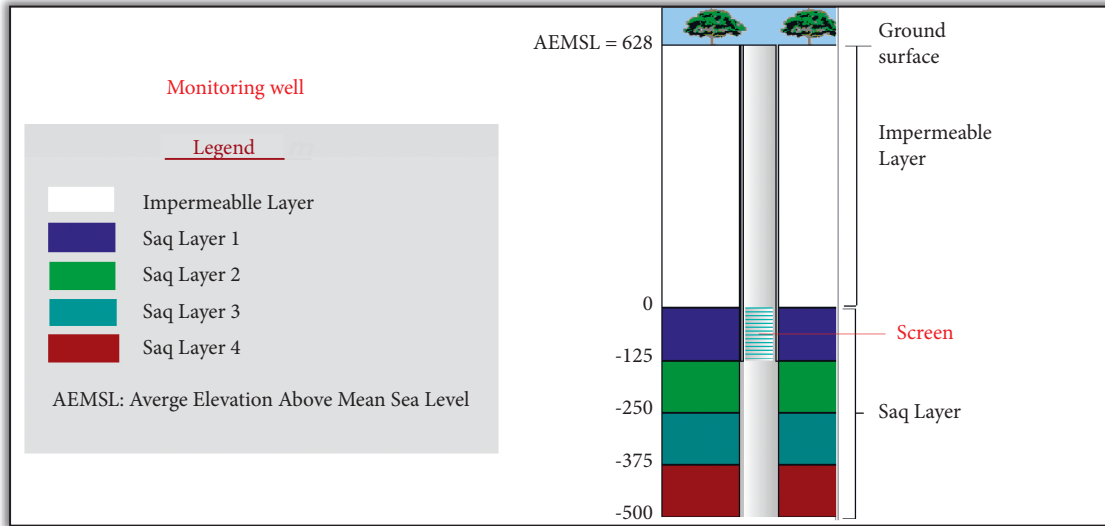


FIGURE 4: Layers of the Saq Aquifer for MODFLOW models (after Almuhaylan et al. [2]).

Therefore, for simulating the effects of well screen accurately, the confined 500 m thick aquifer has been divided into four layers of equal thickness (125 m each). Accordingly, five layers of 631, 125, 125, 125, and 125 m thickness have been adopted (the top 631 m layer being impermeable) (Figure 4).

2.3.2. Quality Modelling. For groundwater quality investigations, the transport and concentration of contaminants are modelled. Hence an additional equation is required for quality modelling on the basis of the transport of contaminants. The equation given below is a partial differential equation for the three-dimensional transport of contaminants in a groundwater flow system [41]:

$$\frac{\partial C}{\partial t} = \frac{\partial}{\partial x_i} \left(D_{ij} \frac{\partial C}{\partial x_j} \right) - \frac{\partial}{\partial x_i} (v_i C) + \frac{q_s}{\theta} C_s + \sum_1^N R_k, \quad (2)$$

where “ C ” is the dissolved concentration of contaminant k in groundwater, “ θ ” is porosity of the subsurface porous medium, “ D_{ij} ” is hydrodynamic dispersion coefficient, “ x_i ” is the distance along the respective Cartesian coordinate axis, “ v_i ” is seepage or linear pore water velocity, “ q_s ” is volumetric flow rate, “ R_k ” is the chemical reaction term, and “ C_s ” is the concentration of the source [41, 42].

There are several techniques to solve (2) combined with equation (1). Finite difference and finite element are the most commonly used techniques. Simultaneous solutions of equations (1) and (2) by numerical methods are used for groundwater quantity and quality modelling, which is a challenging task. Several commercial packages are available for this purpose. MODFLOW is used in this paper to model both the quality and quantity of groundwater.

All the above parameters described under Section 2.3.1 and used in the prediction of groundwater levels were kept the same for contaminant transport simulations (quality

modelling). The constant concentration option has been selected as a transport boundary condition in the Visual MODFLOW. Average values of TDS, Mn, and Fe during 2010 were taken as initial values in the model. To assign initial concentration values, “Assign” from the menu bar of MODFLOW was selected, and the values of initial concentration were added in “Assign Window.” The MT3DMS module of Visual MODFLOW was used to simulate the contaminants transport route and concentration of contaminants in groundwater. This module solves (2) coupled with (1) by finite difference technique. The standard dispersion parameters have been adopted. The option of saturated constant density was chosen. The calibration of the contaminant (TDS, Fe, and Mn) transport model was executed by adjusting the contaminant transport parameters (dispersion coefficient, etc.) until the observed concentration values of TDS, Fe, and Mn were consistent with the predicted values of the model for these contaminants. As described above, the six wells were used as the observation wells for concentration. The coordinates of these wells, concentration of TDS, Fe, and Mn, and historical records of groundwater levels were provided to the model.

2.4. Artificial Intelligence Models. In groundwater modelling, the application of models based on artificial intelligence (AI) is becoming highly popular and is useful in fact [2, 20, 22, 26]. AI techniques have been effectively used in water resources planning/development/management, hydrological processes, water quality predictions, and operation of reservoirs [43–46]. The AI models are gaining importance and expansion in application scope because of their ability to generalize the relationships for a complex phenomenon based on the learning process [47, 48]. However, the use of AI models in the area of specialization of prediction of both groundwater quality and quantity is limited and is still a vital and critical research issue [47–49]. A general layout of AI models is shown in Figures 5(a) and 5(b).

2.4.1. Artificial Neural Network (ANN) Models. In ANN type models, the neurons play a key role in determining the values of output variables comparable to the target values from input variable values. As shown in Figure 5(a), there are mainly three layers: input, hidden, and output layers. An internal-structural procedure is performing the calculations. The hidden layers in an internal-structural procedure, that is, the backbone of the predictions, work as the back-propagation (BP) and the feedforward mechanism for delivering outputs with required precision. The case of multiple hidden layers generates the well-known “Multilayer Perceptron” (MPL). The training function is another important entity of ANN models which are of several types [50]. This paper has used 5 distinct training functions (Table 4). On these bases, the ANN models are termed as ANN1, ANN2, ANN3, ANN4, and ANN5. Both the triple and double hidden layers have been tested. These are represented by the symbol “DL” for the double layer and the symbol “TL” for the triple layer. The hidden layers may have a different number of neurons which need to be fixed for the best

possible results [51–53]. The hit-and-trial method has been used in this research for the selection of the best possible number of neurons. A model is considered to be precise if its predictions are matching to the measured values. In modern techniques of ANN, it is accomplished by combining an effective optimization methodology in which weights are adjusted ANN process to find the highest possible accuracy.

2.4.2. Adaptive Neurofuzzy Inference Systems. An effective optimization subroutine with a hybrid AI model may become a basis for a robust technique for modelling the quality and quantity of groundwater. It is termed as an “Adaptive Neurofuzzy Inference System” (ANFIS). ANFIS can be used to solve a complex nonlinear hydraulic phenomenon with high precision [2, 50]. Figure 5(b) shows the structure of ANFIS, including five layers (Table 5).

2.5. Model Performance Evaluation. The performances of models in this paper are represented by two statistical parameters, the Nash-Sutcliffe Model Efficiency (NSE) and Mean Square Error (MSE). Both parameters are based on some weighted difference between the recorded and simulated values of variables (groundwater levels, TDS, Fe, and Mn). About 38 years (1980–2018) of data for groundwater levels and pumping rates and long records of TDS, Mn, and Fe have been used to evaluate the model performance for different runtime stages (training/calibration, testing, and validation). Many of the previous studies have utilized a similar approach [2, 50, 54].

The Nash-Sutcliffe Model Efficiency (NSE) is given as

$$NSE = 1 - \frac{\sum_{i=1}^n (GWL_i^o - GWL_i^p)^2}{\sum_{i=1}^n (GWL_i^o - GWL_{avg})^2}, \quad (3)$$

where “ $(GWL_i^o$ and $GWL_i^p)$ ” denote the observed and predicted groundwater levels, respectively, for the i^{th} data value and “ n ” is the total number of observed/predicted data points. The NSE values ranging from 0.75 to 1.0 may be termed as “very good,” 0.65 to 0.75 may be taken as “good,” and 0.5 to 0.65 as “satisfactory,” and the values ranging between 0.4 and 0.5 may be expressed as “acceptable” regarding the model’s performance [55, 56].

The Mean Square Error (MSE) is given as

$$MSE = \frac{1}{n} \sum_{i=1}^n (GWL_i^o - GWL_i^p)^2. \quad (4)$$

In the case of quality modelling, GWL will be replaced by the values of TDS or the concentrations of Mn and Fe in (3) and (4).

3. Results and Discussion

3.1. Quantity Modelling

3.1.1. Results of Hydraulic and AI Models. The results of calibration, adjustment of general head boundary condition, and validation are shown in Figures 6(a) and 6(b).

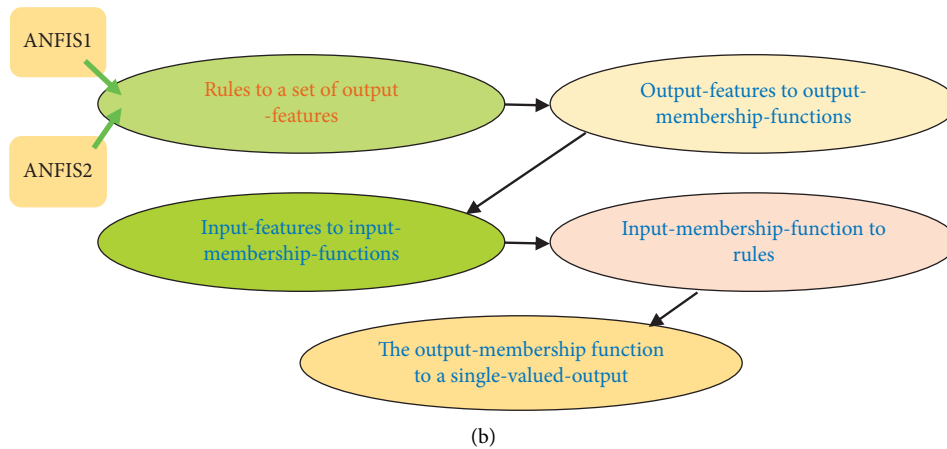
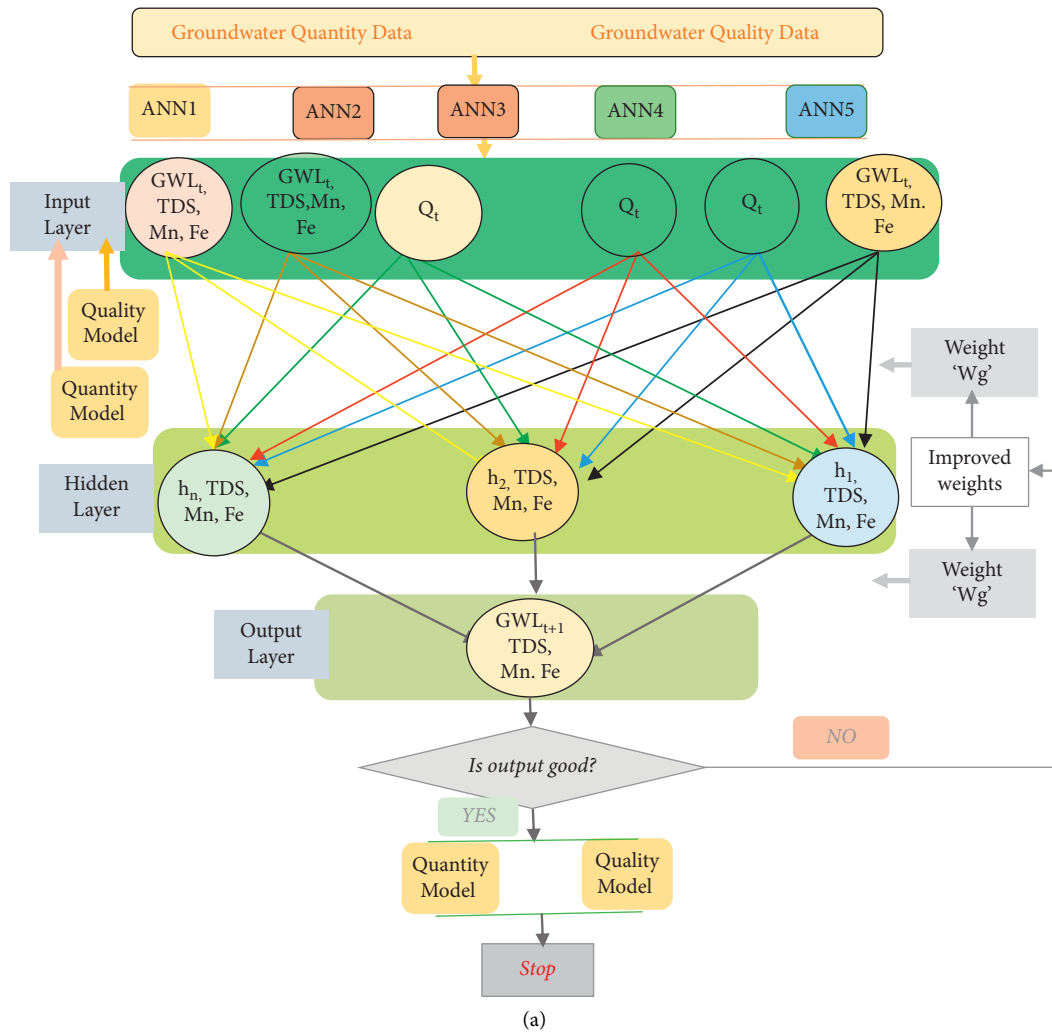


FIGURE 5: AI modelling approach. (a) Flowchart representing the MLP (a feedforward-ANN). (b) Five functional blocks in ANFIS.

TABLE 4: Various training functions used for ANN models.

Model	Description of training function	Function
ANN1	Scaled Conjugate Gradient BP	Trainscg
ANN2	Levenberg-Marquardt BP	Trainlm
ANN3	Bayesian regularization	Trainbr
ANN4	BFGS Quasi-Newton BP	Trainbfg
ANN5	Resilient backpropagation (rprop)	Trainrp

TABLE 5: Structural layers of ANFIS.

Layer no.	Description
1	A fuzzy layer in which every intersection is called an adaptive node. The member functions may be treated as nodal functions like the generalized bell, and Gaussian functions may be used as nodal functions
2	A product layer in which every nodal output represents the firing strength of a rule
3	A normalized layer in which each node expresses the firing strength of a rule in the normalized form
4	A defuzzy layer in which each node represents an adaptive node with a nodal function specifying the influence of the rules in terms of the overall output
5	A total output layer that describes the defuzzified output values

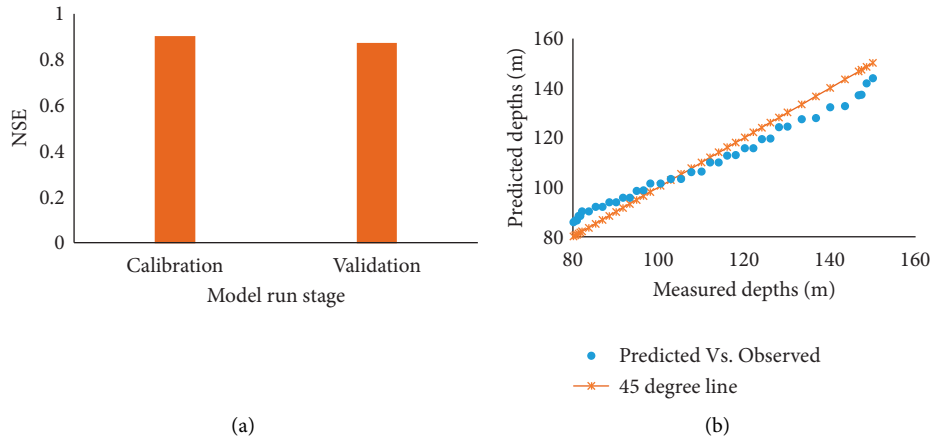


FIGURE 6: MODFLOW results. (a) The values of NSE. (b) Comparison of simulated versus observed groundwater depths and 1 : 1 line (45° line).

Figure 6(a) indicates that a value of NSE equal to 0.9 has been achieved. It is quite a reasonable value. It falls in the range of “very good” as per the conditions stated by previous researchers [55, 56]. The simulated versus recorded graph shown in Figure 6(b) is also close to the 1 : 1 line (the 1 : 1 line represents ideal fitting between the simulated and recorded groundwater levels). The NSE equal to 0.87 has been obtained in validation which advocates that the validation results are also acceptable. As mentioned in Section 2.3, one of the highly challenging and original tasks of this research work is the adjustment of the general head boundary condition for the hydraulic model. The results represented in Figures 6(a) and 6(b) show that this task has been executed plausibly. Some of the simulated groundwater depths have been minutely underestimated, whereas others are slightly overestimated. Previous research works by Lyons et al. [57] and Mohanty et al. [58] support these results. Such results are acceptable in groundwater modelling. There are several reasons for this aspect. Firstly, the selection of the hydraulic parameters of the model, including hydraulic conductivity and specific storage, always contributes to the uncertainty in the model results. Secondly, the quality of data in technologically developing countries is not that excellent to obtain very high efficiencies of a groundwater model. Thirdly, the local grid refinement may have a significant impact on parameter estimates, which can ultimately affect the modelling results. Finally, the accuracy of the results also depends upon how sophisticated the optimization technique that has been used in MODFLOW. In short, it is concluded from

these results that the traditional methods (physical and numerical models) rely on various input values of parameters and the underlying mechanisms are normally too complicated to grasp. Hence the data-driven approaches should also be tested.

The results of ANN are shown in Figures 7(a) and 7(b). The hit-and-trial method was used to find the optimal value of neurons in the case of all 5 ANN models (ANN1, ANN2, ANN3, ANN4, and ANN5). The best performance was noticed for ANNs with 10 hidden neurons in both the two-layer architecture and the three layer architecture. The performance for 5 or 15 neurons was not as good as that for 10 neurons. Within an ANN, a neuron is a mathematical function that models the functioning of a biological neuron. There is a lot of literature on the function of neurons. How the behavior of ANN changes with changing the number of neurons is also a topic of reading. However, engineers are interested in obtaining the best solution of an applied problem. Therefore, the exercise performed in this paper is sufficient for solving the groundwater problem at hand. So, the use of 10 neurons has been adopted in the comparison of ANN for the double layer (DL) and the triple layer (TL). This exercise was done for model ANN1 only. The values of NSE equal to 0.97, 0.81, and 0.92 for training, testing, and validation, respectively, in case of TL have been obtained in comparison to the NSE values of 0.95, 0.94, and 0.96 for training, testing, and validation, respectively, in case of DL. The performance of the model with NSE values ranging from 0.75 to 1.0 may be termed as “very good.” The MSE error is

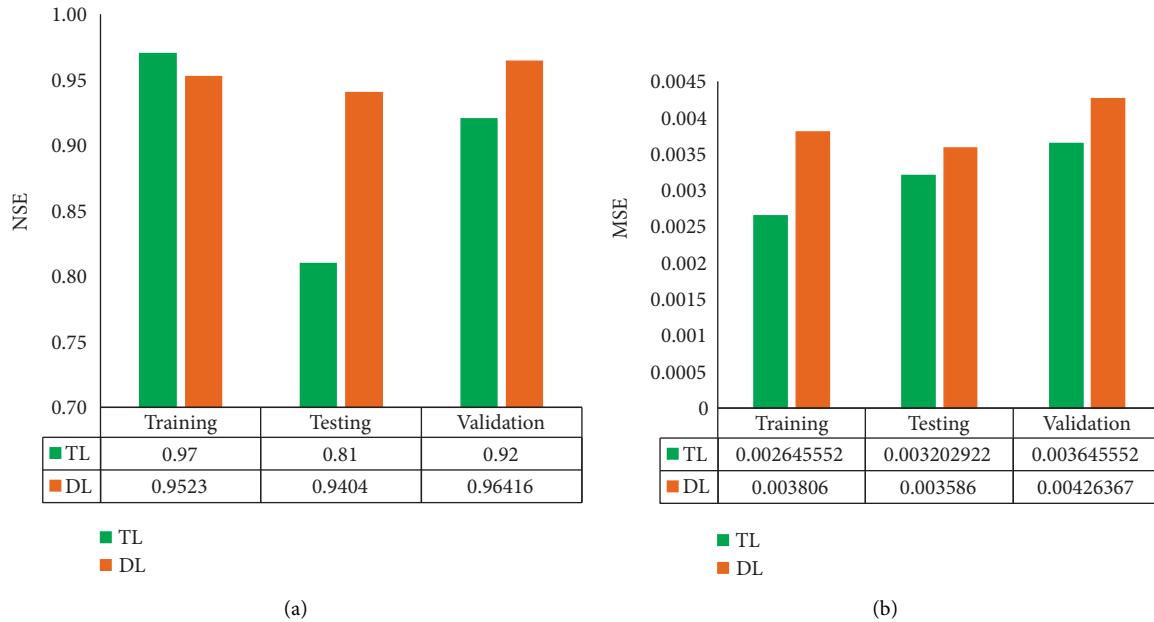


FIGURE 7: ANN1 results. (a) The values of NSE. (b) The values of MSE.

also very small in the range of 0.002 to 0.004. Hence the performances of both models are “very good.” However, the ANN with TL performs comparatively better than the ANN with DL. Deep understanding of the behaviors of ANNs with DL and TL needs a lot of reading of the literature on ANN, but, for engineers working in the field of groundwater hydrology, the results of this part of the paper may be sufficient. Similar results have been reported by Stylianoudaki et al. [50] and Almuhaylan et al. [2]. Hence, for further analysis, the ANNs with 10 neurons and TL have been used.

The performances of five ANN models are shown in Figures 8(a) and 8(b). According to Figure 8(a), the performance of ANN1 (the Scaled Conjugate Gradient training function) is observed to be comparatively better than those of the other ANN models (ANN2: Levenberg-Marquardt training function, ANN3: Bayesian regularization training function, ANN4: BFGS Quasi-Newton BP training function, and ANN5: resilient backpropagation training function). The Scaled Conjugate Gradient is an efficient training algorithm having highly quick convergence with a very high degree of accuracy. Most probably, comparatively better performance of ANN1 may be due to the reason that a highly effective optimization routine has been used in the Scaled Conjugate Gradient for obtaining the best possible global minimum [2, 57, 58]. However, Figure 8(a) shows that the NSE values range from 0.65 to 0.97 for almost all the ANN models. Hence, the overall performance of all the five models can be categorized as “good” to “very good.” The value of Mean Square Error (Figure 8(b)) ranging from 0.02 to 0.03 further strengthens these findings. Quite similar predictions have been reported by the previous research works [2, 17, 50, 59, 60]. However, most of these publications lack in one way or the other covering a wide range of aspects of groundwater flow, which makes the present research a comprehensive study and an original contribution.

Figures 9(a), 9(b), and 9(c) show modelling results regarding the quantity of groundwater by various techniques. Overall values of NSE for training, testing, and validation are shown in these figures. It is observed that the performances of ANN and ANFIS models are comparatively better than that of the hydraulic model (MODFLOW). The values of NSE are noticed to be 0.998 for ANFIS1, 0.997 for ANFIS2, 0.997 for ANN1, 0.995 for ANN2, 0.996 for ANN3, 0.995 for ANN4, and 0.995 for ANN5 to 0.997 for ANN and 0.9 for hydraulic model (Figure 9(a)). The predictions by recent publications also support our simulations [12, 13, 15, 16, 50]. Figures 9(b) and 9(c) further confirm this finding. The simulated versus recorded graph is close to the 1 : 1 line in case of ANN and ANFIS [61–63]. As stated above, the 1 : 1 line represents the best matching between the simulated and recorded groundwater levels. In the case of hydraulic model, the simulated groundwater depths in the beginning have been minutely underestimated, whereas others are slightly overestimated (Figure 9(b)). The reason for this has already been explained in Section 3.1.1.

3.2. Quality Modelling

3.2.1. *Results of Hydraulic and AI Models.* The overall results of ANN, ANFIS, and hydraulic models are compared in Figures 10(a)–10(g). In quality modelling, the performances of the double-layer and triple-layer ANN models are found to be nearly similar. There is not much difference between the NSE values for the DL and TL architecture (visual comparison is made in Figures 10(a) and 10(b), and exact values of NSE can be seen in Tables 6 and 7). The MSE values given in Figures 10(c) and 10(d) also confirm this finding.

Regarding five ANN models, the performance of ANN1 is outstanding. The NSE values are 0.99, 0.756, and 0.859 for TDS, Fe, and Mn, respectively, in the case of TL and 0.989,

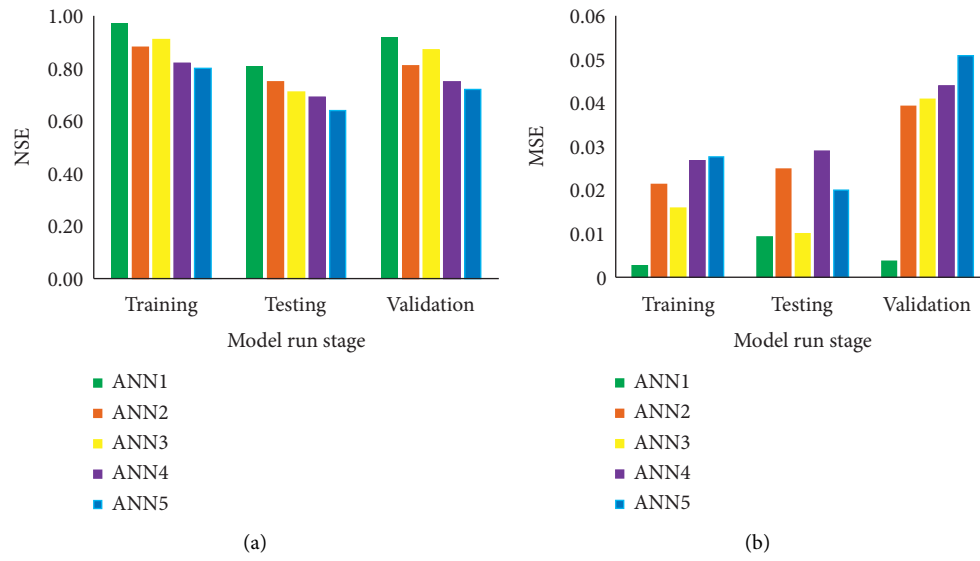
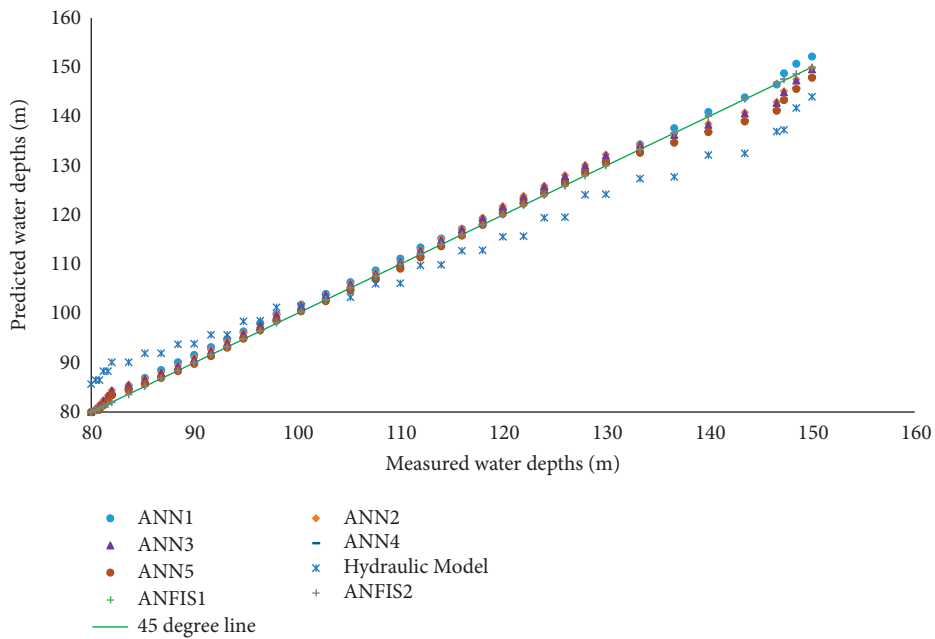
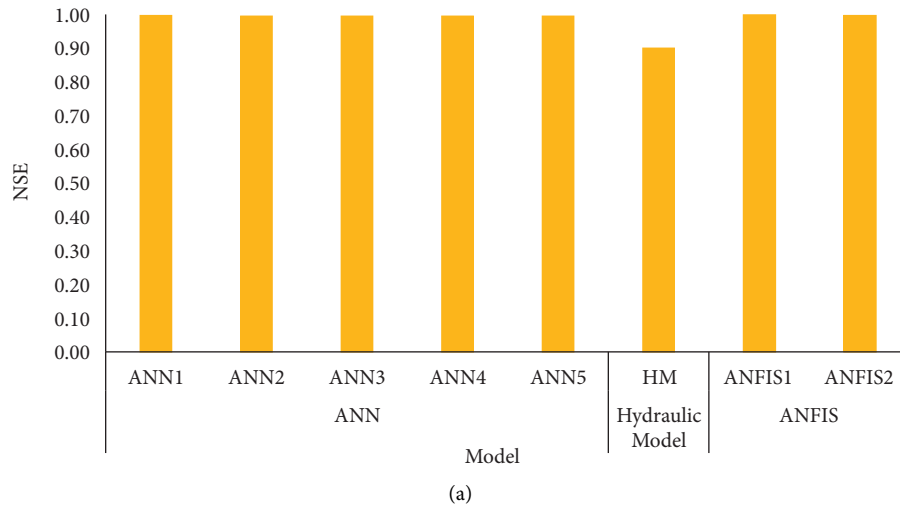


FIGURE 8: ANN model results. (a) The values of NSE. (b) The values of MSE.



(b)
FIGURE 9: Continued.

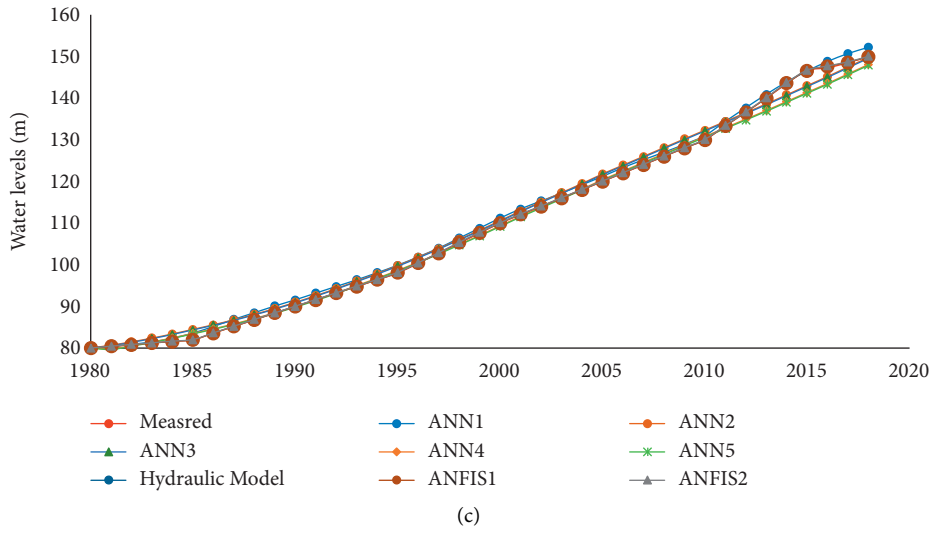


FIGURE 9: Comparison of the ANN, ANFIS, and hydraulic models. (a) Values of NSE. (b) Predicted versus recorded groundwater depths. (c) Comparison between measured and simulated results by various models with respect to time.

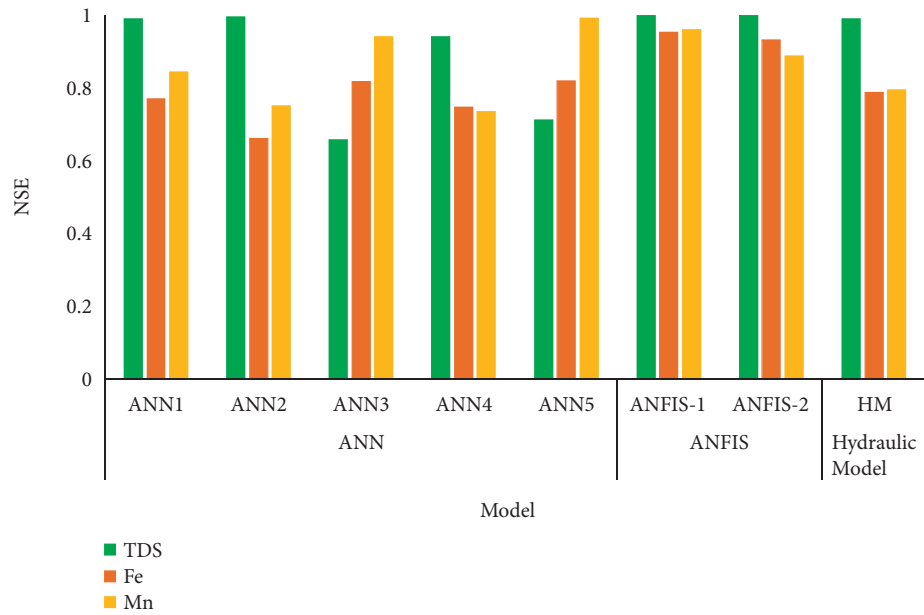
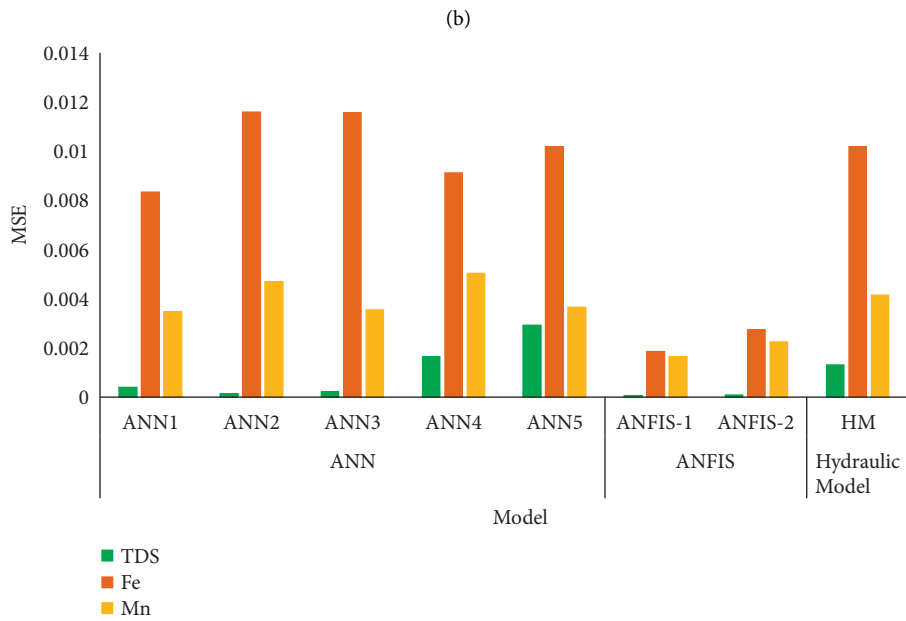
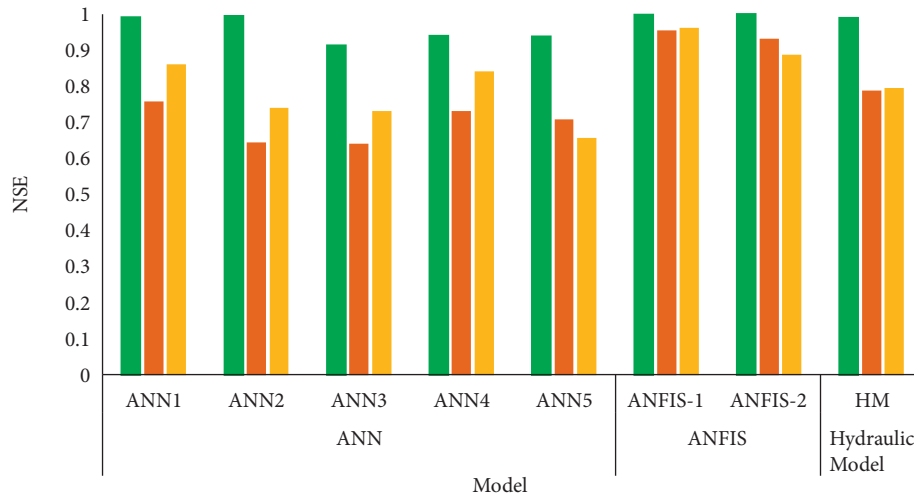
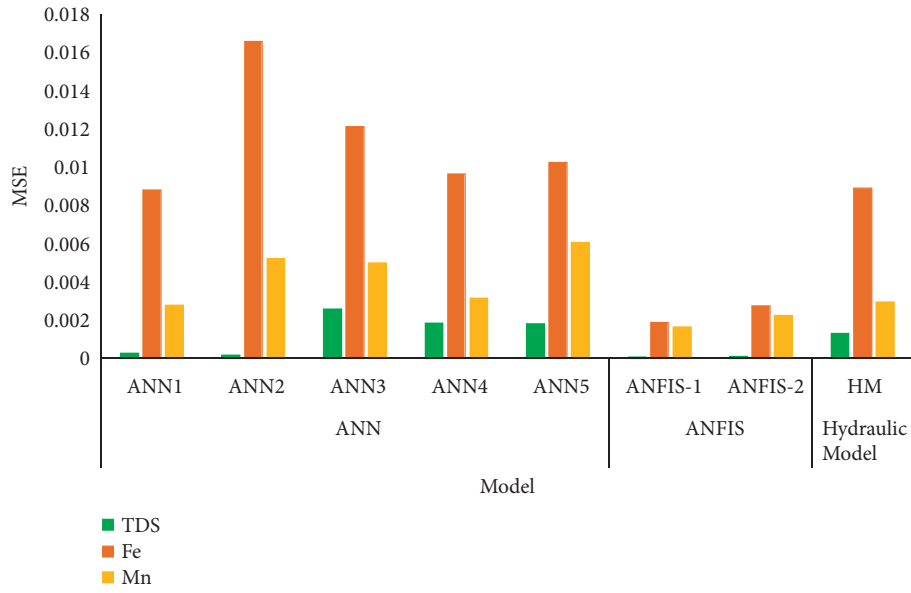


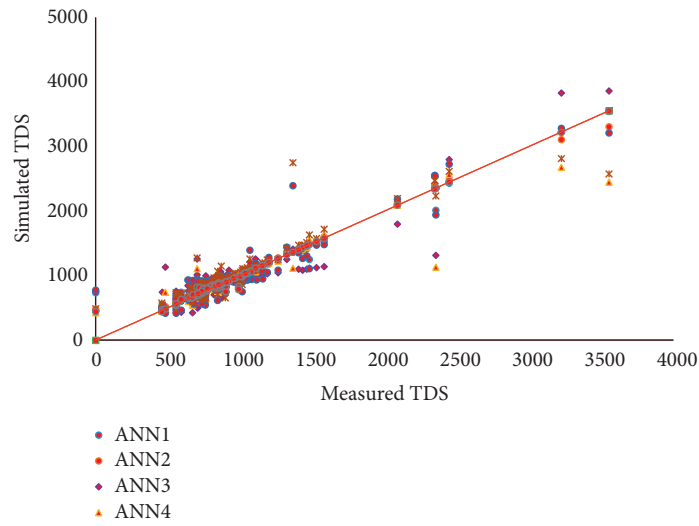
FIGURE 10: Continued.



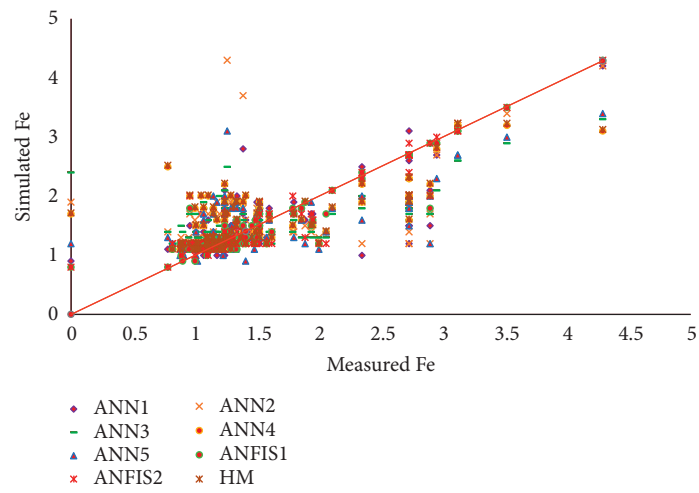
(c)
FIGURE 10: Continued.



(d)



(e)



(f)

FIGURE 10: Continued.

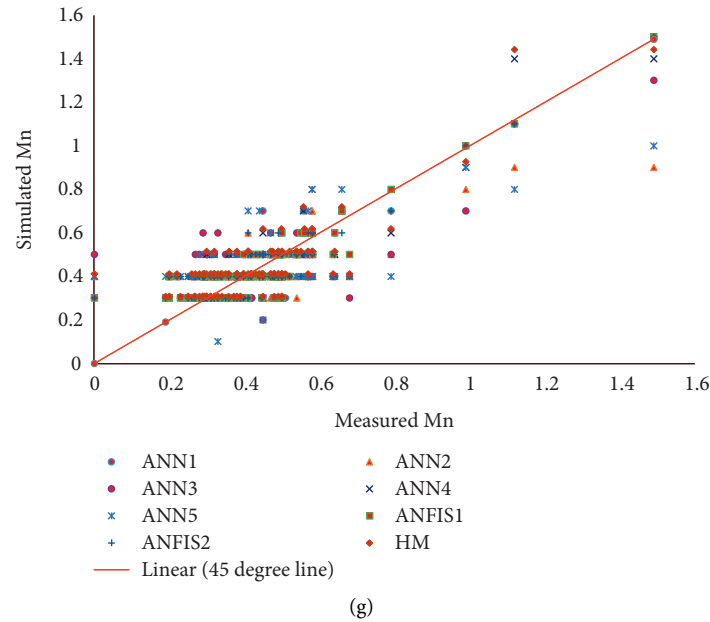


FIGURE 10: Results of the ANN, ANFIS, and hydraulic models. (a) Values of NSE for DL ANN, (b) values of NSE for TL, (c) values of MSE for DL ANN, (d) values of MSE for TL ANN, (e) predicted versus recorded TDS, (f) predicted versus recorded Fe, and (g) predicted versus recorded Mn.

0.769, and 0.843 for TDS, Fe, and Mn, respectively, in the case of DL architecture of model. However, the performances of the other four ANN models are also acceptable (Figures 10(a)–10(g), Figures 11–11(d), and Table 6 and 7). Only five or six values of NSE out of 30 are less than 0.7.

According to Figures 10–10(d), the performances of ANFIS1 and ANFIS 2 are better than that of ANN. The values of NSE range from 0.886 to 0.998, although the performances of ANN and hydraulic models can also be rated as “good” to “excellent.” The values of NSE for ANN1 in the case of TDS, Fe, and Mn are 0.99, 0.756, and 0.859, respectively. The values of NSE for ANN2 in the case of TDS, Fe, and Mn are 0.995, 0.642, and 0.738, respectively; for ANN3, these values are 0.91, 0.638, and 0.729, respectively; for ANN4, these values are 0.939, 0.73, and 0.84; for ANN5 in the case of TDS, Fe, and Mn, these values are 0.937, 0.71, and 0.655 respectively; for ANFIS1 in the case of TDS, Fe, and Mn, these values are 0.998, 0.953, and; for ANFIS2, these values are 0.96, 0.999, 0.93, and 0.887, respectively. However, Figures 10(e)–10(g) and Taylor’s Diagrams (Figures 11(a)–11(d)) show different behavior. Wide range scatters from 1 : 1 line for predicted values indicate that the performances of the models are not that good, as shown by NSE and MSE. Hence the researchers should not always depend upon the NSE and MSE values only to assess the performance of models. In Taylor’s Diagram, the graphs showing predicted versus measured results and some other statistical parameters should also be investigated. This fact is confirmed by Taylor’s Diagram (Figures 11(a)–11(d)). The discrepancy in model results may be due to several reasons. The code selection, impacts of simplifying assumptions in conceptualization, spatial, temporal resolution, and data accuracy are a few parameters that play an important role in determining the reliability and accuracy of the model predictions.

TABLE 6: NSE values for DL and TL ANN Models.

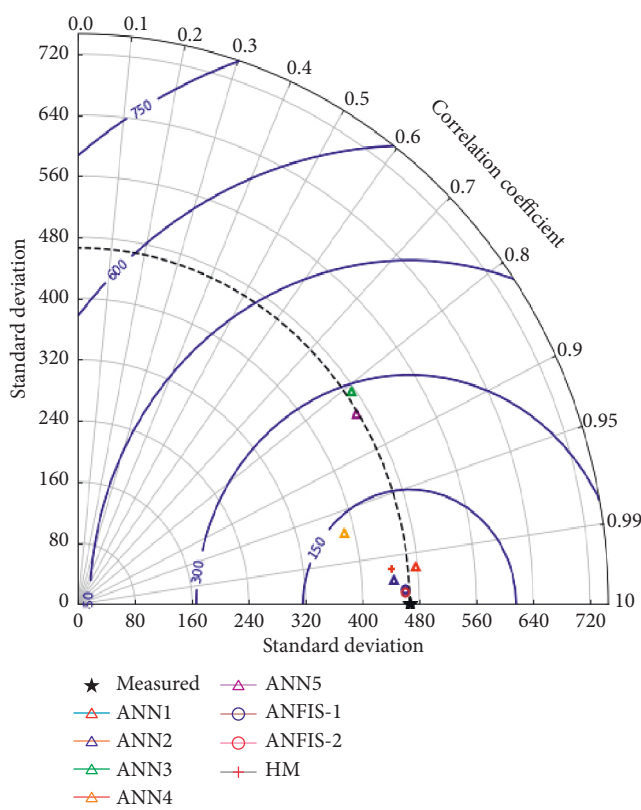
Model	TL NSE values			DL NSE values		
	TDS	Fe	Mn	TDS	Fe	Mn
ANN1	0.99058	0.75591	0.85916	0.98956	0.76975	0.84309
ANN2	0.99473	0.64238	0.73868	0.9949	0.6594	0.75012
ANN3	0.91311	0.6384	0.72918	0.65739	0.81614	0.94077
ANN4	0.93889	0.73029	0.84036	0.94077	0.74665	0.73341
ANN5	0.93736	0.70563	0.65495	0.71182	0.81811	0.99058
ANFIS1	0.99815	0.95308	0.96003	0.99815	0.95308	0.96003
ANFIS2	0.9987	0.93051	0.8866	0.9987	0.93051	0.8866
HM	0.989	0.78665	0.79341	0.989	0.78665	0.79341

The standard deviation values for different parameters are given in Table 8. The maximum concentrations of TDS, Fe, and Mn in the groundwater have been found to be 3553 mg/L, 4.29 mg/L, and 1.49 mg/L, respectively. The corresponding minimum values are 456 mg/L, 0.78 mg/L, and 0.19 mg/L, respectively. The standard deviation and the ranges of minimum and maximum values of TDS and concentrations of Fe and Mn show that there is a large variation in amounts of contaminants. Furthermore, the maximum values of TDS and concentrations of Fe and Mn exceeded the WHO standard limits set for drinking, which are 700 mg/L, 0.3, and 0.1 mg/L, respectively, for TDS, Fe, and Mn. Hence the studied groundwater needs treatment before its use for drinking purposes.

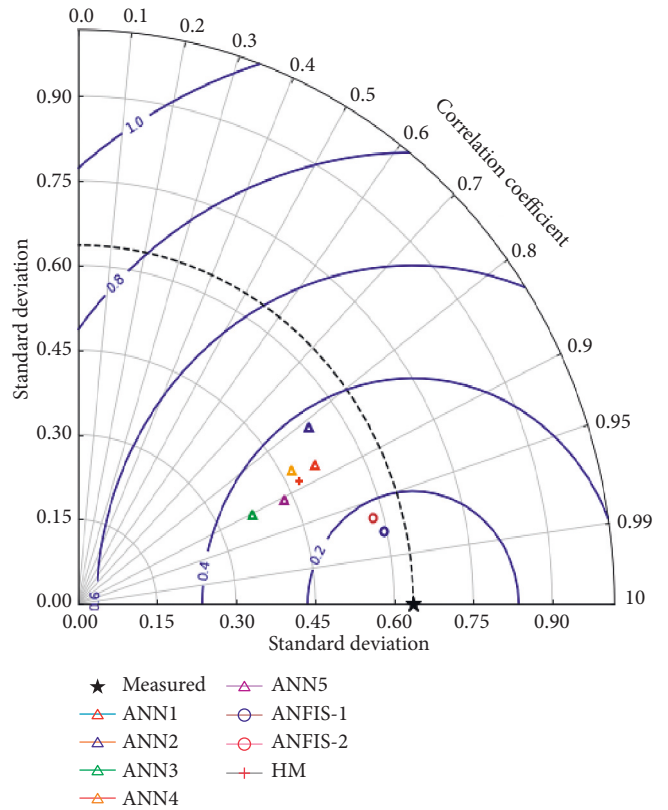
3.3. Results of Sensitivity Analysis. It was found from sensitivity analysis that hydraulic conductivity is the most crucial hydraulic parameter as compared to the other parameters. Any small change in hydraulic conductivity results in significant changes in the predicted groundwater levels.

TABLE 7: MSE values for DL and TL ANN Models.

Model	Quality parameters					
	TL NSE values			DL NSE values		
	TDS	Fe	Mn	TDS	Fe	Mn
ANN1	0.000272	0.008811	0.002763	0.000387	0.008324	0.003474
ANN2	0.000166	0.016562	0.005208	0.000145	0.011591	0.004689
ANN3	0.002585	0.012132	0.004986	0.000213	0.011575	0.003553
ANN4	0.001848	0.009636	0.003139	0.001645	0.009123	0.005025
ANN5	0.001816	0.010232	0.006052	0.002927	0.01019	0.00364
ANFIS1	5.24E-05	1.87E-03	1.64E-03	5.24E-05	1.87E-03	1.64E-03
ANFIS2	9.01E-05	0.00273	0.002249	9.01E-05	0.00273	0.002249
HM	0.001296	0.008911	0.002963	0.001296	0.01019	0.00414



(a)



(b)

FIGURE 11: Continued.

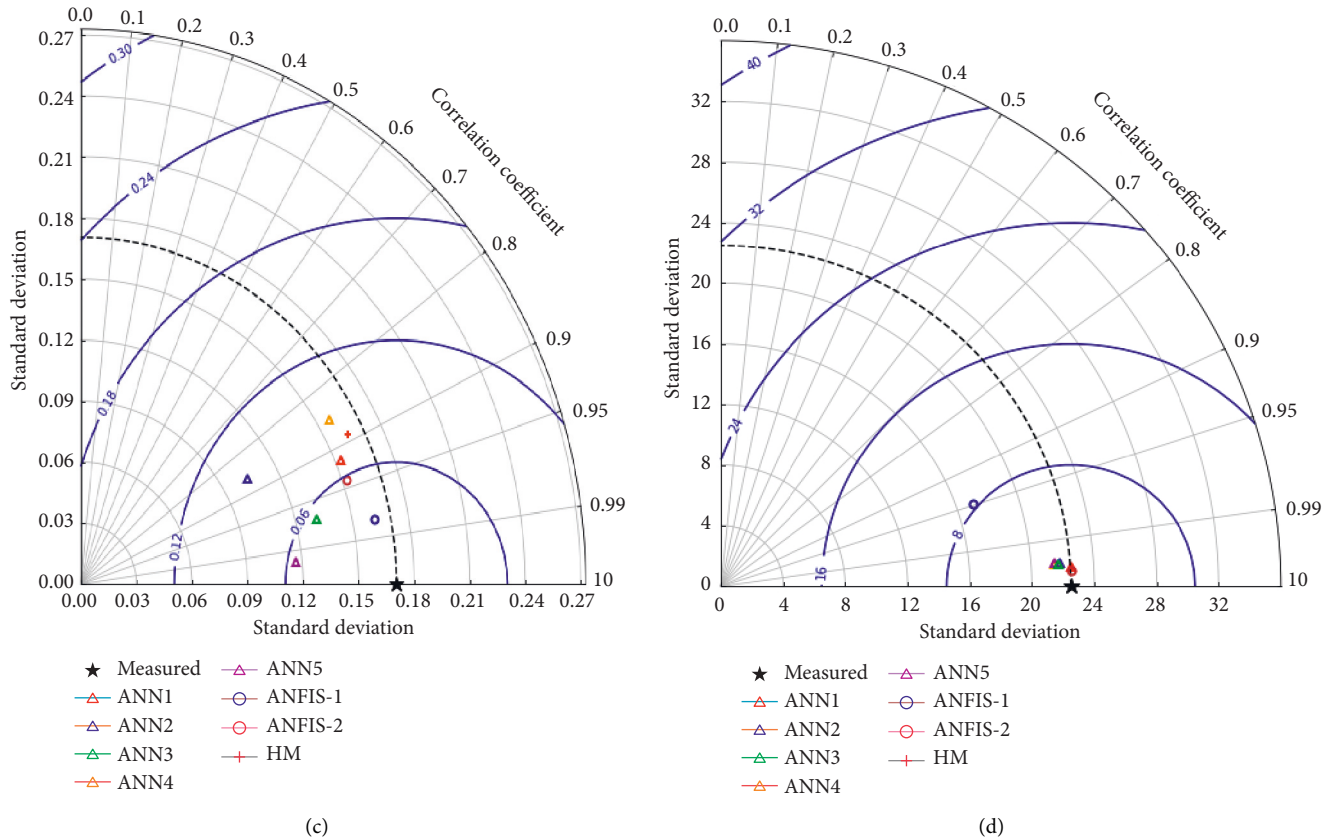


FIGURE 11: Taylor's Diagram showing correlation, standard deviation, and Root Mean Square Error (RMSE, represented by blue contours) for (a) TDS, (b) Fe, (c) Mn, and (d) groundwater levels.

TABLE 8: Standard deviation of data from different sources/models.

Model	TDS	Fe	Mn
Measured	466.3118	0.635919	0.170473
ANN1	447.1221	0.513361	0.153118
ANN2	445.2609	0.538902	0.103719
ANN3	475.0653	0.367694	0.131233
ANN4	385.5242	0.469438	0.157027
ANN5	464.1002	0.432464	0.116558
ANFIS1	459.8986	0.592823	0.161822
ANFIS2	459.3005	0.579713	0.152165
HM	442.9413	0.474132	0.161737

Hence it is the key parameter in the groundwater quantity modelling and must be estimated with very high accuracy either by pumping tests or by using a powerful optimization technique in the calibration of the model.

The sensitivity analysis of contaminant transport model parameters showed that sensitivity from small to large was as follows: hydraulic conductivity, porosity, and dispersion coefficient. The results of sensitivity analysis are quite realistic. The most important parameter in contaminant transport is the dispersion coefficient.

3.4. Future Predictions (8 Scenarios). The future predictions of groundwater depths have been made by MODFLOW for 8 different scenarios, as shown in Figures 12(a) and 12(b). The drawdown values up to the year 2070 with respect to the groundwater levels in 2020 are found to be 52, 70, 82, 90, 105, 118, 135, and 66 for scenarios 1 to 8, respectively (Figure 12(a)). The scenarios have developed with respect to the reference pumping rates in 2020. It is observed that even if the pumping rates are not increased as per increase in the population, the drawdown is very high (70 m). The decrease in pumping rates also results in a drawdown of 52 m. This alarming situation not only threatens the water stress but also warns of a very bad pollution situation (Figure 12(b)). The Saq Aquifer is a confined aquifer. The confining cover has another unconfined aquifer called Qassim Aquifer. It has shallow depths of groundwater which is highly contaminated. Extremely high drawdowns in the Saq Aquifer may cause excessively low pressures in the underlying aquifer, permitting polluted water from overlying Qassim Aquifer to travel downwards. This may cause a severe ecological disaster. Hence adaptation of highly effective sustainable planning, development, and management strategies becomes inevitable.

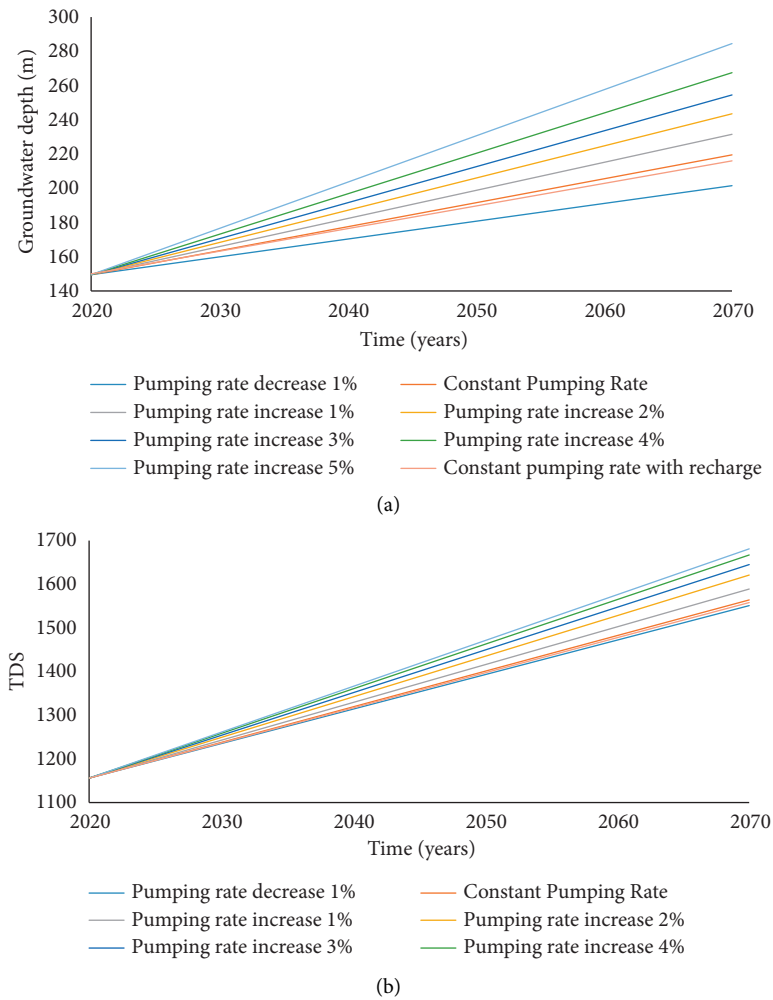


FIGURE 12: Future prediction results of groundwater depths/aquifer depletion for various pumping rate scenarios.

4. Conclusions and Recommendations

The MODFLOW, a well-known hydraulic model, has been applied to forecast the variations in the groundwater quantity and quality of the Saq Aquifer in the Qassim Region. AI models have also efficiently simulated the quantity and quality of groundwater in this aquifer. Different architectures of ANN with triple and double layers having 5, 10, and 15 hidden neurons in every layer have been investigated. Five different categories of training functions are examined in ANN models. Furthermore, two versions of ANFIS have been utilized successfully to predict the depletion of aquifer with respect to both quantity and quality. Three main quality parameters, TDS, Fe, and Mn, have been investigated.

The study concluded that both versions of ANFIS (ANFIS1 and ANFIS2) can efficiently predict groundwater levels and contaminants (TDS, Fe, and Mn) with NSE up to 0.99. The ANN model provides the best results with 10 hidden neurons in each hidden layer. The performance of ANN with the architecture having three layers and 10 neurons in each layer is better than the one with two layers in case of the quality and quantity modelling of

groundwater. The Scaled Conjugate Gradient training function in ANN has comparatively better performance compared to the Levenberg-Marquardt, Bayesian regularization, BFGS Quasi-Newton BP, and resilient back-propagation training functions for predicting groundwater levels and contaminants. The performance of the hydraulic model is good, but, for the given set of data of pumping wells and contaminants, its performance is not as good as that of the ANN or the ANFIS models. However, it is the most robust and reliable model based on the laws of physics. The hydraulic modelling is comparatively more demanding than the ANN and ANFIS models for both the contaminant and flow transport.

There will be extremely excessive drawdowns in groundwater levels of the Saq Aquifer (ranging from 70 to 135 m with respect to the reference water levels in 2020) for various scenarios of pumping rates. Even with the constant rate of pumping without looking at the needs of the increasing population in the region, the drawdown is 70 m for the coming 50 years. The concentrations of contaminants (TDS, Fe, and Mn) are also increasing significantly. There may be a major ecological disaster if preventative actions are not adopted. However, the constant rate of pumping may

result in a comparatively increased life of the Saq Aquifer as compared to the other scenarios of pumping. The drawdown will reduce by 33% over the next 50 years' period compared to the pumping at increased rates to meet the water needs of a growing population. There is a negligible amount of recharge to the Saq Aquifer, which may fade away, causing severe scarcity of water in the future. Thereby, some alternative sources of water should be established to fulfil the goals of the Kingdom's Vision 2030.

The results and models developed in this paper may be very useful in obtaining the pumping rates for an environment-friendly future. For instance, by keeping pumping rates constant (no increase in pumping), there may be a substantial increase in the Saq Aquifer's life. A 33% decrease in drawdown may be accomplished in the coming 50 years by implementing groundwater preservation strategies compared to the situation of uninterrupted increase in pumping rates which otherwise may be necessary to meet the water requirements of the promptly rising population. Results of this research will assist in the planning, development, and management of stressed water resources in the Gulf Region, Saudi Arabia, and the arid regions with analogous water scarcity situations.

An extensive research work to preserve the existing sources and develop new sources of water is recommended. Highly efficient technology, extremely accurate and sufficient data, and demarcation of the location of outcrops are of utmost importance for the study area.

Data Availability

Climatic, geographical, and quality of groundwater (contaminants) data are obtained from the Ministry of Environment, Water, and Agriculture, Jeddah/Riyadh.

Conflicts of Interest

The authors declare that there are no conflicts of interest regarding the publication of this paper.

Authors' Contributions

Abdul Razzaq Ghumman developed the methodology, collected and processed the data, performed simulations, and prepared the manuscript. Ghufran Ahmed Pasha assisted in the preparation of figures and tables, especially Taylor's Diagrams. Md. Shafiquzzaman assisted in ANN simulation. Afaq Ahmed developed the ANN and ANFIS models. Afzal Ahmed was involved in supervising the overall modelling approach, the data collection, and paper writing. Riaz Akhtar Khan and Rashid Farooq helped in MODFLOW simulations and the literature review. All authors have read and agreed to the final version of the manuscript.

Acknowledgments

The authors acknowledge the Ministry of Environment, Water, and Agriculture in Saudi Arabia for data sharing. The authors are thankful to the Deanship of Scientific Research for their Fast Track Publication Program. The authors are

grateful to the Administration of the College of Engineering (Dean and Vice Dean Administration) and the Head of the Civil Engineering Department for their continued support in this research.

References

- [1] O. A. Fallatah, "Groundwater quality patterns and spatio-temporal change in depletion in the regions of the arabian shield and arabian shelf," *Arabian Journal for Science and Engineering*, vol. 45, no. 1, pp. 341–350, 2020.
- [2] M. R. Almuhaylan, A. R. Ghumman, I. S. Al-Salamah et al., "Evaluating the impacts of pumping on aquifer depletion in arid regions using MODFLOW, ANFIS and ANN," *Water*, vol. 12, no. 8, p. 2297, 2020.
- [3] M. Ahmed, "Sustainable management scenarios for northern Africa's fossil aquifer systems," *Journal of Hydrology*, vol. 589, Article ID 125196, 2020.
- [4] Y. Su, B. Guo, Z. Zhou, Y. Zhong, and L. Min, "Spatio-temporal variations in groundwater revealed by GRACE and its driving factors in the huang-huai-hai plain, China," *Sensors*, vol. 20, no. 3, p. 922, 2020.
- [5] J. Mallick, C. K. Singh, M. K. Almesfer, V. P. Singh, and M. Alsubih, "Groundwater Quality Studies in the Kingdom of Saudi Arabia: Prevalent Research and Management Dimensions," *Water (Switzerland)*, vol. 13, 2021.
- [6] P. Li, D. Karunanidhi, T. Subramani, and K. Srinivasamoorthy, "Sources and consequences of groundwater contamination," *Archives of Environmental Contamination and Toxicology*, vol. 80, no. 1, pp. 1–10, 2021.
- [7] C. K. Shuler and K. E. Mariner, "Collaborative groundwater modeling: open-source, cloud-based, applied science at a small-island water utility scale," *Environmental Modelling & Software*, vol. 127, Article ID 104693, 2020.
- [8] R. Barthel, M. Stangefelt, M. Giese, M. Nygren, K. Seftigen, and D. Chen, "Current understanding of groundwater recharge and groundwater drought in Sweden compared to countries with similar geology and climate," *Geografiska Annaler - Series A: Physical Geography*, vol. 103, no. 4, pp. 323–345, 2021.
- [9] N. Shiri and J. Z. M. S. I.-M. V. M. Shiri, "Development of artificial intelligence models for well groundwater quality simulation: different modeling scenarios," *PLoS One*, vol. 16, no. 5, Article ID e0251510, 2021.
- [10] F. B. Banadkooki and M. A. N. F. Y. C. M. H. A. M. A. Ehteram, "Enhancement of groundwater-level prediction using an integrated machine learning model optimized by whale algorithm," *Natural Resources Research*, vol. 29, no. 5, pp. 3233–3252, 2020.
- [11] T. Roshni, M. K. Jha, and J. Drisya, "Neural network modeling for groundwater-level forecasting in coastal aquifers," *Neural Computing & Applications*, vol. 32, no. 16, pp. 12737–12754, 2020.
- [12] C. Chen, W. He, H. Zhou, Y. Xue, and M. Zhu, "A comparative study among machine learning and numerical models for simulating groundwater dynamics in the Heihe River Basin, northwestern China," *Scientific Reports*, vol. 10, no. 1, p. 3904, 2020.
- [13] S. Emamgholizadeh, K. Moslemi, and G. Karami, "Prediction the groundwater level of bastam plain (Iran) by artificial neural network (ANN) and adaptive neuro-fuzzy inference system (ANFIS)," *Water Resources Management*, vol. 28, no. 15, pp. 5433–5446, 2014.

- [14] U. K. Das, P. Roy, and D. K. Ghose, "Modeling water table depth using adaptive Neuro-Fuzzy Inference System," *ISH Journal of Hydraulic Engineering*, vol. 25, no. 3, pp. 291–297, 2019.
- [15] M. Bizhanimanzar, R. Leconte, and M. Nuth, "Catchment-Scale integrated surface water-groundwater hydrologic modelling using conceptual and physically based models: a model comparison study," *Water*, vol. 12, no. 2, p. 363, 2020.
- [16] M. Bizhanimanzar, R. Leconte, and M. Nuth, "Modelling of shallow water table dynamics using conceptual and physically based integrated surface-water-groundwater hydrologic models," *Hydrology and Earth System Sciences*, vol. 23, no. 5, pp. 2245–2260, 2019.
- [17] A. Khedri, N. Kalantari, and M. Vadiati, "Comparison study of artificial intelligence method for short term groundwater level prediction in the northeast Gachsaran unconfined aquifer," *Water Supply*, vol. 20, no. 3, pp. 909–921, 2020.
- [18] P. Majumder and T. I. Eldho, "Artificial neural network and grey wolf optimizer based surrogate simulation-optimization model for groundwater remediation," *Water Resources Management*, vol. 34, no. 2, pp. 763–783, 2020.
- [19] I. Suprayogi, A. Sandhyavetri, N. Anon, J. Anon, W. Anon, and A. Anon, "Groundwater level forecasting model IN tropical peatland using artificial neural network," *International Journal of Civil Engineering & Technology*, vol. 11, no. 2, 2020.
- [20] A. Wunsch, T. Liesch, and S. Broda, "Groundwater level forecasting with artificial neural networks: a comparison of long short-term memory (LSTM), convolutional neural networks (CNNs), and non-linear autoregressive networks with exogenous input (NARX)," *Hydrology and Earth System Sciences*, vol. 25, no. 3, pp. 1671–1687, 2021.
- [21] R. Solgi, H. A. Loáiciga, and M. Kram, "Long short-term memory neural network (LSTM-NN) for aquifer level time series forecasting using in-situ piezometric observations," *Journal of Hydrology*, vol. 601, Article ID 126800, 2021.
- [22] J. Li, W. Lu, and Y. Fan, "Groundwater pollution sources identification based on hybrid homotopy-genetic algorithm and simulation optimization," *Environmental Engineering Science*, vol. 38, no. 8, pp. 777–788, 2021.
- [23] J. Pal and D. Chakrabarty, "Effects of input/output parameters on artificial neural network model efficiency for breakthrough contaminant prediction," *Water Supply*, vol. 21, no. 7, pp. 3614–3628, 2021.
- [24] O. O. Fadipe, L. K. Abidoye, J. O. Adeosun, B. B. Oguntola, O. Adewusi, and T. E. Okeowo, "Simulation of groundwater quality characteristics using artificial neural network," *Nigerian Journal of Technology*, vol. 40, no. 1, pp. 161–167, 2021.
- [25] M. Hmoud Al-Adhaileh and F. Waselallah Alsaade, "Modelling and prediction of water quality by using artificial intelligence," *Sustainability*, vol. 13, no. 8, p. 4259, 2021.
- [26] M. Kulisz, J. Kujawska, B. Przysucha, and W. Cel, "Forecasting water quality index in groundwater using artificial neural network," *Energies*, vol. 14, no. 18, p. 5875, 2021.
- [27] P. Coulibaly, F. Anctil, R. Aravena, and B. Bobée, "Artificial neural network modeling of water table depth fluctuations," *Water Resources Research*, vol. 37, no. 4, pp. 885–896, 2001.
- [28] N. F. Che Nordin, N. S. Mohd, S. Koting, Z. Ismail, M. Sherif, and A. El-Shafie, "Groundwater quality forecasting modelling using artificial intelligence: a review," *Groundwater for Sustainable Development*, vol. 14, Article ID 100643, 2021.
- [29] I. N. Daliakopoulos, P. Coulibaly, and I. K. Tsanis, "Groundwater level forecasting using artificial neural networks," *Journal of Hydrology*, vol. 309, no. 1–4, pp. 229–240, 2005.
- [30] H. Yoon, S.-C. Jun, Y. Hyun, G.-O. Bae, and K.-K. Lee, "A comparative study of artificial neural networks and support vector machines for predicting groundwater levels in a coastal aquifer," *Journal of Hydrology*, vol. 396, no. 1–2, pp. 128–138, 2011.
- [31] L. A. Krishan G, "Groundwater level simulation using artificial neural network in southeast, Punjab, India," *Journal of Geology & Geosciences*, vol. 04, no. 03, 2015.
- [32] F. Gonand, "Impacts of higher energy efficiency on growth and welfare across generations in Saudi Arabia," pp. 1–20, 2016, <https://www.kapsarc.org/wp-content/uploads/2016/10/KS-16-57-DP051A-Impact-of-Higher-Energy-Efficiency-on-Growth-and-Welfare-Across-Generations-in-Saudi-Arabia.pdf>.
- [33] A. M. Al-Omran, A. A. Aly, M. I. Al-Wabel, M. S. Al-Shayaa, A. S. Sallam, and M. E. Nadeem, "Geostatistical methods in evaluating spatial variability of groundwater quality in Al-Kharj Region, Saudi Arabia," *Applied Water Science*, vol. 7, no. 7, pp. 4013–4023, 2017.
- [34] A. Younes, M. Fahs, and P. Ackerer, *Modeling of Flow and Transport in Saturated and Unsaturated Porous Media*, Multidisciplinary Digital Publishing Institute, Basel, Switzerland, 2021.
- [35] L. El Mezouary and B. El Mansouri, "Groundwater flow equation, overview, derivation, and solution," *E3S Web of Conferences*, vol. 314, no. 2–5, p. 04007, 2021.
- [36] A. K. Behera, R. M. Pradhan, S. Kumar, G. J. Chakrapani, and P. Kumar, "Assessment of groundwater flow dynamics using MODFLOW in shallow aquifer system of mahanadi delta (east coast), India," *Water*, vol. 14, no. 4, p. 611, 2022.
- [37] M. R. Namitha, J. S. Devi Krishna, H. Sreelekshmi, and P. Muhammed Ashik, "Ground water flow modelling using visual modflow," *Journal of Pharmacognosy and Phytochemistry*, vol. 8, no. 1, pp. 2710–2714, 2019.
- [38] T. Jafari, A. S. Kiem, S. Javadi, T. Nakamura, and K. Nishida, "Fully integrated numerical simulation of surface water-groundwater interactions using SWAT-MODFLOW with an improved calibration tool," *Journal of Hydrology: Regional Studies*, vol. 35, Article ID 100822, 2021.
- [39] S. Mamo, B. Birhanu, T. Ayenew, and G. Taye, "Three-dimensional groundwater flow modeling to assess the impacts of the increase in abstraction and recharge reduction on the groundwater, groundwater availability and groundwater-surface waters interaction: a case of the rib catchment in the Lake Tana sub-basin of the Upper Blue Nile River, Ethiopia," *Journal of Hydrology: Regional Studies*, vol. 35, Article ID 100831, 2021.
- [40] H. H. Cooper Jr and C. E. Jacob, "A generalized graphical method for evaluating formation constants and summarizing well-field history," *Transactions - American Geophysical Union*, vol. 27, no. 4, pp. 526–534, 1946.
- [41] A. Kamali and M. H. Niksokhan, "Multi-objective optimization for sustainable groundwater management by developing of coupled quantity-quality simulation-optimization model," *Journal of Hydroinformatics*, vol. 19, no. 6, pp. 973–992, 2017.
- [42] E. Jabbari, M. Fathi, and M. Moradi, "Modeling groundwater quality and quantity to manage water resources in the Arak aquifer, Iran," *Arabian Journal of Geosciences*, vol. 13, no. 14, p. 663, 2020.
- [43] C. Mattas, L. Dimitraki, P. Georgiou, and P. Venetsanou, "Use of factor Analysis (FA), artificial neural networks (ANNs), and multiple linear regression (MLR) for electrical

- conductivity prediction in aquifers in the Gallikos river basin, northern Greece,” *Hydrology*, vol. 8, no. 3, p. 127, 2021.
- [44] S. Singha, S. Pasupuleti, S. S. Singha, R. Singh, and S. Kumar, “Prediction of groundwater quality using efficient machine learning technique,” *Chemosphere*, vol. 276, Article ID 130265, 2021.
- [45] R. Raghavendra Kumar, G. Kumar, and R. Gupta, “Assessment of sustainability index for rural water management using ANN,” *Water Supply*, vol. 22, no. 2, pp. 1421–1433, 2021.
- [46] O. Bozorg-Haddad, S. Baghban, and H. A. Loáiciga, “Assessment of global hydro-social indicators in water resources management,” *Scientific Reports*, vol. 11, no. 1, Article ID 17424, 2021.
- [47] M. E. Abd-Elmaboud, H. A. Abdel-Gawad, K. S. El-Alfy, and M. M. Ezzeldin, “Estimation of groundwater recharge using simulation-optimization model and cascade forward ANN at East Nile Delta aquifer, Egypt,” *Journal of Hydrology: Regional Studies*, vol. 34, Article ID 100784, 2021.
- [48] M. M. R. Tabari, T. Azari, and V. Dehghan, “A supervised committee neural network for the determination of aquifer parameters: a case study of Katasbes aquifer in Shiraz plain, Iran,” *Soft Computing*, vol. 25, 2021.
- [49] H.-N. Wu, S.-L. Shen, R.-P. Chen, and A. Zhou, “Three-dimensional numerical modelling on localised leakage in segmental lining of shield tunnels,” *Computers and Geotechnics*, vol. 122, Article ID 103549, 2020.
- [50] C. Stylianoudaki, I. Trichakis, and G. P. Karatzas, “Modeling groundwater nitrate contamination using artificial neural networks,” *Water*, vol. 14, no. 7, p. 1173, 2022.
- [51] K. G. Sheela and S. N. Deepa, “Review on methods to fix number of hidden neurons in neural networks,” *Mathematical Problems in Engineering*, vol. 2013, pp. 1–11, Article ID 425740, 2013.
- [52] F. Arifin, H. Robbani, T. Annisa, and N. N. M. I. Ma’arof, “Variations in the number of layers and the number of neurons in artificial neural networks: case study of pattern recognition,” *Journal of Physics: Conference Series*, vol. 1413, no. 1, Article ID 012016, 2019.
- [53] J. N. Ogunbo, O. A. Alagbe, M. I. Oladapo, and C. Shin, “N-hidden layer artificial neural network architecture computer code: geophysical application example,” *Heliyon*, vol. 6, no. 6, Article ID e04108, 2020.
- [54] H. Afzaal, A. A. Farooque, F. Abbas, B. Acharya, and T. Esau, “Groundwater estimation from major physical hydrology components using artificial neural networks and deep learning,” *Water*, vol. 12, no. 1, p. 5, 2020.
- [55] F. Lin, X. Chen, and H. Yao, “Evaluating the use of Nash-Sutcliffe efficiency coefficient in goodness-of-fit measures for daily runoff simulation with SWAT,” *Journal of Hydrologic Engineering*, vol. 22, no. 11, Article ID 05017023, 2017.
- [56] R. H. McCuen, Z. Knight, and A. G. Cutter, “Evaluation of the Nash-Sutcliffe efficiency index,” *Journal of Hydrologic Engineering*, vol. 11, no. 6, pp. 597–602, 2006.
- [57] R. T. Lyons, R. C. Peralta, and P. Majumder, “Comparing single-objective optimization protocols for calibrating the birds nest aquifer model-A problem having multiple local optima,” *International Journal of Environmental Research and Public Health*, vol. 17, no. 3, p. 853, 2020.
- [58] S. Mohanty, M. K. Jha, A. Kumar, and D. K. Panda, “Comparative evaluation of numerical model and artificial neural network for simulating groundwater flow in Kathajodi-Surua Inter-basin of Odisha, India,” *Journal of Hydrology*, vol. 495, pp. 38–51, 2013.
- [59] N. Djurovic and M. R. V. V. R. E. U. Domazet, “Comparison of groundwater level models based on artificial neural networks and ANFIS,” *The Scientific World Journal*, vol. 2015, pp. 1–13, Article ID 742138, 2015.
- [60] J. Jeong and E. Park, “Comparative applications of data-driven models representing water table fluctuations,” *Journal of Hydrology*, vol. 572, pp. 261–273, 2019.
- [61] A. Ahmad, D. M. Cotsovos, and N. D. Lagaros, “Framework for the development of artificial neural networks for predicting the load carrying capacity of RC members,” *SN Applied Sciences*, vol. 2, no. 4, pp. 1–21, 2020.
- [62] A. Ahmad, V. Plevris, and Q. U. Z. Khan, “Prediction of properties of FRP-confined concrete cylinders based on artificial neural networks,” *Crystals*, vol. 10, no. 9, p. 811, 2020.
- [63] S. Ganguly, A. Ahmed, and F. Wang, “Optimised building energy and indoor microclimatic predictions using knowledge-based system identification in a historical art gallery,” *Neural Computing and Applications*, vol. 32, no. 8, pp. 3349–3366, 2020.

Research Article

Pothole Detection Using Deep Learning: A Real-Time and AI-on-the-Edge Perspective

Muhammad Haroon Asad ¹, Saran Khaliq ¹, Muhammad Haroon Yousaf ^{1,2},
Muhammad Obaid Ullah ³ and Afaq Ahmad ⁴

¹Swarm Robotics Lab, National Centre of Robotics and Automation, Rawalpindi, Pakistan

²Department of Computer Engineering, University of Engineering and Technology Taxila, Taxila, Pakistan

³Department of Electrical Engineering, University of Engineering and Technology Taxila, Taxila, Pakistan

⁴Department of Civil Engineering, University of Engineering and Technology Taxila, Taxila, Pakistan

Correspondence should be addressed to Afaq Ahmad; afaq.ahmad@uettaxila.edu.pk

Received 10 January 2022; Revised 19 February 2022; Accepted 3 March 2022; Published 20 April 2022

Academic Editor: Qian Chen

Copyright © 2022 Muhammad Haroon Asad et al. This is an open access article distributed under the Creative Commons Attribution License, which permits unrestricted use, distribution, and reproduction in any medium, provided the original work is properly cited.

Asphalt pavement distresses are the major concern of underdeveloped and developed nations for the smooth running of daily life commute. Among various pavement failures, numerous research can be found on pothole detection as they are injurious to automobiles and passengers that may turn into an accident. This work is intended to explore the potential of deep learning models and deploy three superlative deep learning models on edge devices for pothole detection. In this work, we have exploited the AI kit (OAK-D) on a single-board computer (Raspberry Pi) as an edge platform for pothole detection. Detailed real-time performance comparison of state-of-the-art deep learning models and object detection frameworks (YOLOv1, YOLOv2, YOLOv3, YOLOv4, Tiny-YOLOv4, YOLOv5, and SSD-mobilenetv2) for pothole detection is presented. The experimentation is performed on an image dataset with pothole in diverse road conditions and illumination variations as well as on real-time video captured through a moving vehicle. The Tiny-YOLOv4, YOLOv4, and YOLOv5 evince the highest mean average precision (mAP) of 80.04%, 85.48%, and 95%, respectively, on the image set, thus proving the strength of the proposed approach for pothole detection and deployed on OAK-D for real-time detection. The study corroborated Tiny-YOLOv4 as the befitted model for real-time pothole detection with 90% detection accuracy and 31.76 FPS.

1. Introduction

Roads are the essential means of transportation for a country to provide commutation facilities nationwide. Road infrastructure enables opportunities to connect people and transport goods to enhance business opportunities, access to jobs, economic growth, and health care system across the country. As first-rated roads contribute to the country's GDP [1], the calamitous infrastructure of roads can become fatal for passengers' safety and vehicles' condition. The roads are usually made up of asphalt pavement and are prone to different structural damages with the passage of time.

The asphalt pavement distresses have been a concern of authorities to avoid unwanted circumstances. These

pavements are vulnerable to scenarios such as traffic load, weather conditions, age, poor material used for construction, and miserable drainage system, exhibiting two major pavement failures such as cracks and potholes. Potholes are essentially the concave-shaped depressions in the road surface that requires attention as they induce awful circumstances such as accidents, unpleasant driving experiences, and malfunctioning of vehicles, as shown in Figure 1. Potholes should be dealt with on a priority basis to minimize their contribution towards unfortunate scenarios. According to the prediction made by WHO (World Health Organization), road accidents will become the fifth leading cause of death in 2030 [3]. The significance of potholes created conspicuous interest for the researchers of the civil



FIGURE 1: Road image having potholes [2].

community. The developing nations use manual inspection methods to recognize the potholes leading to inaccurate estimation as it is highly dependent on individual experience. These manual inspection methods require human interventions that are time consuming and costly. Many technical solutions exist for pothole detection such as scanning based with 3D reconstruction [4–6], vibration sensor based [7–10], thermal imaging [11, 12], and computer vision based [13–15].

A sensor-based network “BusNet” [9] is proposed for the monitoring of road conditions whereas the camera was mounted on the public transport buses. Several sensors and GPS are used which are fast, sensitive, and cost efficient. However, this system is not ideal for every case due to weather conditions that may damage the sensor leading to the performance degradation of the BusNet. Over the last few years, the computer vision and image processing based techniques acquired fame due to the accessibility of cameras which are inexpensive and feasible, and have been proved to be the replacement of old fashioned manual inspection methods for pothole detection. However, the image processing-based pothole detection is still a demanding job because of the irregular pothole textures, pothole structures, road bumps, manholes and shadows, etc. For this problem, different computer-vision based approaches have been studied for pothole detection and classification. In [16], the authors proposed a cost-effective solution for pothole detection and severity estimation based on image processing techniques. As compared to the manual method, their study achieved 88.4% accuracy with the automated method. The proposed system is less time consuming and can be done without the committee; however, the lightweight camera can be used to overcome shadow effects. Zhou et al. [17] proposed a methodology to replace human intervention methods with the image processing techniques based on the discrete wavelet transform for pavement distress detection. Another work [18] proposed discolorations, where potholes are detected based on characteristics such as dark region, globe shape, and rough texture. However, the discolorations may not always be potholes as we have other reasons such as road markings, shadows, wet roads, and manholes. Wang et al. [19] proposed a method in which wavelet energy is assembled via morphological processing initially for pothole detection, and afterward, detected pothole images are segmented using the Markov random field model so that the pothole edge is extracted. This methodology tested and trained over 120 pavement images in MATLAB. The method

has attained an accuracy of 86.7%, with 83.3% precision, and 87.5% recall. The overlap degree between the extracted pothole region and the original pothole region is approximately above 85%, which accounts for 88.6% of the total detected pavement pothole images.

Altogether, machine learning and deep learning techniques have reduced complexity and cost for pothole detection. Arbawa et al. [20] proposed a method for detecting road potholes using the gray-level co-occurrence matrix (GLCM) feature extractor and support vector machine (SVM) as a classifier. They analyzed three features such as contrast, correlation, and dissimilarity. The results have shown that a combination of contrast and dissimilarity features exhibits better results with an accuracy of 92.033% and computing time of 0.0704 seconds per frame. Oche et al. [21] used five binary classification models (Naïve Bayes, Logistic regression, SVM, K-Nearest Neighbors (KNN), and Random Forest Tree) and presented a comparison of various machine learning approaches on data collected through smartphones and car routes. The Random Forest Tree and KNN achieved the highest accuracy of 0.8889 on the test set. To improve the accuracy of the Random Forest Tree, they tuned hyper-parameters and increased accuracy up to 0.9444. The model has shown promising results on different routes and out of sample data. Ping et al. [22] presented techniques based on the combination of machine learning and deep learning models to detect potholes. A pothole detection system uses YOLOv3, HOG, SSD, SVM, and Faster R-CNN, trained on their dataset collected by mounting smartphone on vehicle dashboard. After machine learning and deep learning models trained on each of the mentioned techniques, YOLOv3 outperformed others in detecting potholes and estimating the size of the pothole with an accuracy of 82% on 1,500 images. However, their performance on out-of-sample data is unsatisfactory as they have not tested real-world scenarios. Ye et al. [23] proposed a method for the inspection of road defects and potholes based on two convolutional neural networks, conventional CNN, and prepooling CNN. The model is trained on 96,000 digital pavement images and achieved higher recognition precision of 98.95% with optimized prepooling CNN. They concluded optimized prepooling CNN with higher stability and robustness for real-world scenarios against traditional image processing techniques. K-means and Sobel edge detection algorithms did not detect and localize potholes accurately as CNN did. In [24], three different datasets are used to classify three different road types such as paved, unpaved, and asphalt for the further classification of the pothole in each road type. Finally, the CNN model uses 7,000 images of datasets that are RTK, KITTI, and caRINA for training. Moreover, they proposed an application that notifies pedestrians and drivers of upcoming potholes on the route. YOLOv3 and CNN models were used to detect the potholes and classify road types. Zhang et al. [25] proposed an embedded system integrated with CNN for pavement distress detection using the Montreal Pavement dataset. The model exhibits a true-positive rate for a pothole, patch, marking, crack linear, and crack network as 75.7%, 84.1%, 76.3%, 79.4%, and 83.1%, respectively.

It is crucial to assess the condition of road surfaces for public safety and usability. Hassan et al. [26] provided a

summary and detailed insight of factors that affect the generalizability of any model for automated pavement assessment by investigating some common issues such as the distance of pothole from camera angle and lighting, and variations of images in terms of image size. They used the Kaggle pothole dataset and tested Faster RCNN with inception V2 as a backbone. The model achieved an accuracy of 90% as they performed the first experiment on the negative image. Later, the second experiment is performed on the Cranfield dataset, which results in 80% precision and 92% recall. In the third experiment, images are captured by stereocamera, the model results in 95% precision and 84% recall. The fourth experiment is performed on images collected across Dublin city center in daylight and the model gives precision 78% and 68% recall in normal light, and 78% precision and 73% recall in low light. Kavitha et al. [27] proposed a method for self-driving vehicles and used the YOLO algorithm to detect objects and the training. PASCAL VOC dataset with XML format is collected and then implemented the method on Raspberry pi. Chen et al. [28] proposed a novel location-aware convolutional neural network and trained on a public pothole dataset that consists of 4,026 images as training samples and 1,650 images as test samples. The proposed model is based on 2D-vision techniques and location-aware convolutional networks. CNN networks consist of two main subnetworks; the first localization subnetwork (LCNN) finds as many candidate regions as possible by employing a high recall network model, and the second part-based subnetwork (PCNN) performs classification on the candidates on which the network is expected to focus. The proposed method achieved high precision 95.2% and recall 92.0%. Rani et al. [29] detected potholes and road bumps for an advance driver assistance system (ADAS) using SSD-MobileNet for detection which is trained on their self-made dataset collected from Malaysian roads. The model was able to detect potholes and road bumps with the limitations of accuracy and confidence however they suggested it for real-time detection as FPS (frame per second) was 22. Lately, deep convolutional neural networks (DCNNs) have become well known for problems like object classification [30], object detection, and recognition [31, 32] as they automatically extract the main features from images with basically no interventions. Furthermore, DCNNs have various applications in domains such as natural language processing (NLP) [33] and speech and audio processing (SAP) [34].

The literature shows that the sensor-based pothole detections are vulnerable to weather conditions. Furthermore, the pothole is not detected unless a vehicle or sensor is above the pothole. The sensor-based detection system is prone to failure if potholes contain pebbles or sand. A 3D reconstruction-based system detects potholes with size estimation. This system has a limitation of close-range detection with costly equipment. Sensor-based and 3D reconstruction-based systems are less feasible for real-time applications as they require complex hardware. Vision-based systems that incorporate intelligent and low-cost cameras have gained attention from researchers. These

systems are proven robust and feasible but with limitations of false detection, illumination, and the texture of road potholes. Machine-learning-based systems are the superior version of the above-discussed techniques and require prior knowledge and time to develop a feature extractor for the dedicated problem. Therefore, deep learning techniques are more suitable for pothole detection with edge devices mounted on vehicles.

In this work, our contributions are as follows:

- (i) We have presented a comprehensive experimental and comparative study of whole YOLO family and SSD-Mobilenetv2 on pothole detection in terms of accuracy and speed
- (ii) We have introduced a thorough methodology to deploy custom-trained CNNs on edge devices for pothole detection.
- (iii) We have proposed a real-time and AI-on-the-edge solution for pothole detection using an OAK-D camera on a single-board computer (Raspberry Pi) as host by deploying the top three models based on performance metrics

In further proceedings of this article, we shall discuss in Section 2 our proposed methodology for a real-time pothole detection system. Similarly, Section 3 discusses the experimental results thoroughly. We discussed the conclusion and a few comments on future work in the Section 4 of this article.

2. Proposed Methodology

For a real-time pothole detection system, the block diagram of the proposed methodology is shown in Figure 2. Annotation for each image is performed explicitly after the collection of the dataset. The annotated data are split into training and testing data before passing it to deep learning models such as the YOLO family and SSD for custom model training. The weights obtained after training contribute to model performance evaluation on testing data. The custom weights are then converted into the OpenVino IR format to perform real-time detection on OAK-D and Raspberry pi as host computer. The methodology is discussed in detail in the following sections.

2.1. Dataset Acquisition. The performance and reliability of the models depend upon the dataset used for training. The dataset must contain realistic pothole images. Hence, the latest publicly available pothole image dataset is used [2] that consists of 665 images, with effects of shadows, moving vehicles, and illumination variations that incorporate real-world scenarios around potholes. The dataset images are collected from online sources making noisy and low-quality images. Each image of a dataset contains at least three potholes. So, 8,000 potholes are available in the whole dataset approximately. Some samples from the pothole image dataset are shown in Figure 3.

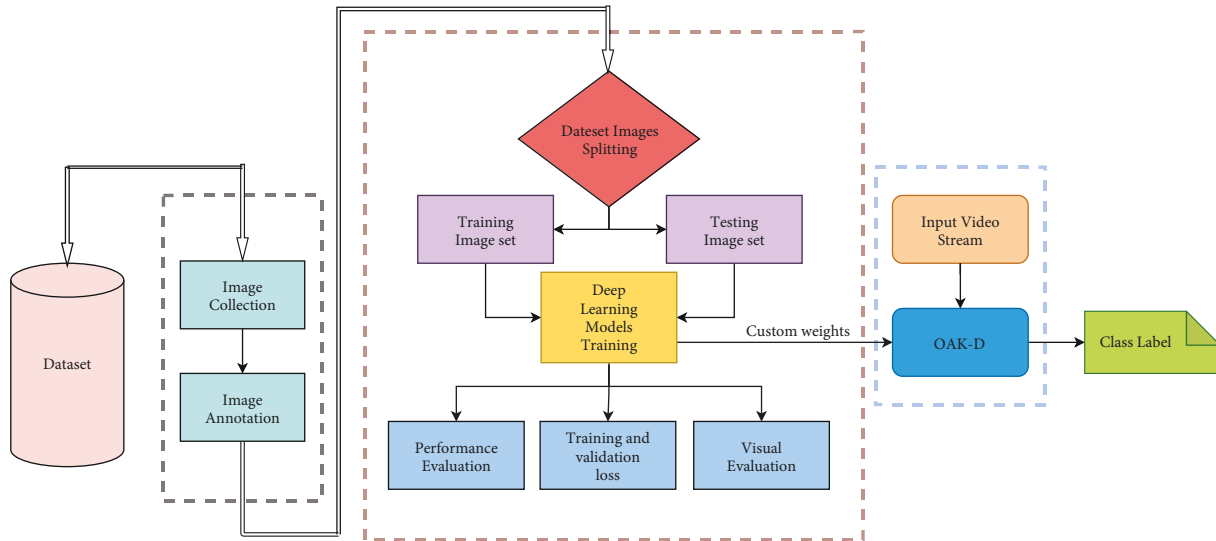


FIGURE 2: Proposed methodology block diagram of real-time pothole detection.



FIGURE 3: Sample of pothole images from the dataset.

2.2. Pothole Detection Using Deep Learning Models. The potholes are considered as the objects to be detected. Deep convolutional neural networks (DCNNs) have proven their abilities for many object detection tasks. These object detectors can be one-stage object detectors or two-stage object detectors. Several object detection models such as region-based convolutional neural network family (R-CNN) [31], YOLO family [35], and SSD family [36], are available in deep learning for training. However, the R-CNN family is computationally expensive result in low latency. Conversely, YOLO and SSD are under study to supplement the

responsiveness issues of the R-CNN family. Hence, we had focused on YOLO and SSD family for this problem.

2.2.1. YOLO Family. YOLO (you only look once) was first introduced in 2016 by Redmon [35]. It divides the input image into $S \times S$ grid cells where each cell is responsible for detecting an object and predicting its bounding box coordinates. Each object bounding box shows the X , Y coordinates, height (h), width (w), and confidence score with the class label. The confidence score is the matching percentage

of the actual labeled object bounding box with the predicted bounding box and tells the accuracy of prediction of the bounding box. It can detect, classify, and localize multiple objects in one step, whereas other algorithms require multiple scanning of an input image. This algorithm was the milestone for real-time object detection known as YOLOv1. YOLOv1 exhibits some limitations when small and cluttered objects are detected. These drawbacks were removed in 2016 and presented as YOLO900 or YOLOv2 [37]. The improved version offered significant features such as better speed, performance, and accuracy. This version included advanced techniques such as batch normalization and anchor boxes. In 2018, “YOLOv3: an incremental improvement,” another improved version was proposed [38] which was even better and stronger than previous versions. Figure 4 shows that YOLOv3 outperforms state-of-the-art detectors such as RetinaNet, SSD, and its variants. It made a significant improvement in terms of speed over other detection models, as shown in Figure 4.

YOLOv4 [39] was developed by Alexey Bochkovskiy, Chien-Yao Wang, and Hong-Yuan Mark Liao on April 23, 2020, claiming up to 10% improvement in mean average precision as well as 12% in frames per second as compared to YOLOv3. In addition, Tiny YOLOv4 is a compressed version of the original YOLOv4 that is simpler and faster real-time object detector [40]. After the YOLOv4 release, a company named “Ultralytics” came up with the YOLOv5 by Glenn Jocher [41]. It is different from previous YOLO releases as its implementation is in the PyTorch framework keeping in mind the v5 is not a fork of the original, unlike Alexey’s repository. They claim it to be extremely lightweight and speedy than the YOLOv4. However, the accuracy is comparatively equal to YOLOv4.

2.2.2. Architectures. YOLOv2 uses Darknet19 composed of 19 convolutional layers, five max-pooling layers, and a softmax layer at the end for assigning class labels. The overall mAP of YOLOv2 increased up to 4% by taking the input image of size 448×448 from 224×224 . In YOLOv2, anchor boxes perform the prediction and localization and are responsible for predicting the bounding box. The fine-grained features of YOLOv2 enhance the quality to detect small objects. YOLOv3 uses logistic regression instead of the softmax layer for predicting class probabilities and objectiveness scores. YOLOv3 can detect objects at different scales using the feature pyramid network (FPN). It uses Darknet-53 deeper than Darknet-19 as it contains 53 convolutional layers of feature extractor comparatively. The standard input image size of YOLOv3 architecture is 416×416 . The YOLOv4 architecture combines three main blocks starting with the CSPDarknet53 as the backbone, following the neck block that adds layers between the head and the backbone CSPDarknet53. A path aggregation network (PANet) is used for feature aggregation to improve the overall accuracy within YOLOv4. It also uses the spatial pyramid pooling (SPP) block to segregate essential features from the backbone. As in YOLOv3, the head performs the detection along with other techniques like bag of freebies and bag of specials

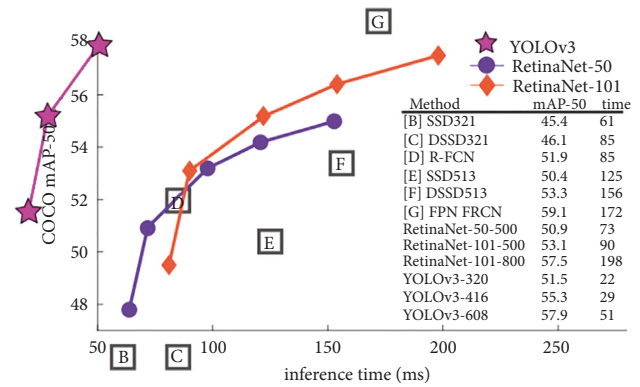


FIGURE 4: Detection model performance as compared to YOLOv3 [38].

which helps in training and minimizing inference time. It takes an input image of resolution 608×608 . On the other hand, Tiny-YOLOv4 takes input images of resolution 416×416 . Experimentation proved YOLOv4 as the best real-time object detector without compromising accuracy and outperformed the efficient detection model, EfficientDET. YOLOv5 is the latest version with the same architecture (backbone, neck, and output block) as YOLOv4 but implemented in a PyTorch framework. YOLOv5 passes 640×640 resolution images to the backbone, and features are extracted using BottleneckCSP. Four models (YOLOv5s, YOLOv5m, YOLOv5l, and YOLOv5x) are created by adjusting the height and the width of BottleneckCSP. YOLOv4 surpassed YOLOv5 in mAP when tested on COCO benchmark despite claiming an improvement of YOLOv4, as shown in Figure 5.

2.2.3. SSD-Mobilenetv2. Mobilenetv2 is a single-shot object detector created using the TensorFlow object detection. API was released by Google researchers in 2018 as an improved version of Mobilenetv1. It generates bounding boxes and class probabilities in a single step. MobileNet is integrated with SSD as designed for mobile and embedded applications. Mobilenetv2 contains two blocks with three layers. The basic building block of Mobilenetv2 is a bottleneck depth-separable convolution with residual block. The second block is for downsizing with the stride of two. Mobilenetv2 is suitable for real-time applications as its speed is high along with shorter inference time but with compromised accuracy. However, Mobilenetv2 is 35% faster than the Mobilenetv1.

2.2.4. AI-on-the-Edge Implementation. We have mentioned that we have opted OAK-D camera on Raspberry Pi for real-time implementation of the proposed approach. To make our OAK-D computational, we need a host computer that has a USB port to plug in OAK-D; for this, we used both windows and raspbian. The next step is to install DepthAI that is a computer vision library provided by Luxonis to get our model running; and after installing DepthAI requirements, we were able to run over a custom model on OAK-D. OAK-D sensor has been chosen because it is a SpatialAI tool,

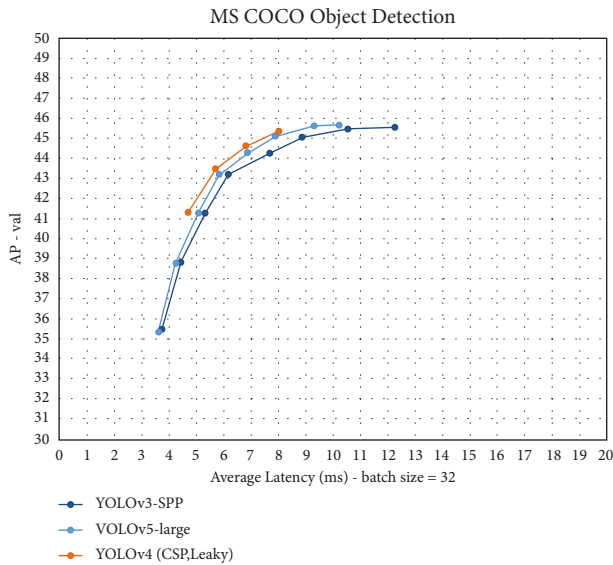


FIGURE 5: Performance of YOLOv5 as compared to other models [42].

capable of running complex neural networks while providing depth through its left and right stereo cameras and detection from the 4K RGB middle camera.

However, the darknet framework is not optimized to run on the Myriad X VPU hardware in Luxonis OAK-D. To run our custom model on OAK-D for real-time detection, we first need to translate our darknet YOLO weights to OpenVino format. We first need to convert to TensorFlow.pb weights and then to OpenVino as we do not have any direct conversion method for darknet weights. After the conversion, we get the.blob file to deploy on the OAK-D kit. For YOLOv5 to deploy on OAK-D, we have converted the YOLOv5 best.pt PyTorch weights to the ONNX framework.xml and.bin file, and the.blob file, respectively. SSD-Mobilenetv2 weights are also converted to OpenVino.blob file by converting TensorFlow.pb to.xml and.bin file to OpenVino IR representation that is.blob file.

3. Experimentation and Results

3.1. Frameworks Used

3.1.1. Darknet Framework. We used YOLOv1, YOLOv2, YOLOv3, YOLOv4, and Tiny-YOLOv4 for training. YOLO is trained using an opensource neural network framework which is fast due to CUDA and C language providing the real-time attribute for our detection.

3.1.2. PyTorch Framework. An opensource deep learning framework reduces the gap between research and practical application. It is used for the training of YOLOv5 as the darknet framework does not support YOLOv5.

3.1.3. TensorFlow Framework. TensorFlow is an opensource deep learning and machine learning framework by Google that provides researchers with a wide range of tools and

libraries for different machine learning and deep learning development and deploy applications. We used the TensorFlow framework for the training of SSD-Mobilenetv2.

3.2. Dataset Annotation. After the collection of a dataset, the next step was to manually annotate them; so, for the annotation, we have used labeling. It is a free graphical image annotation tool that generates labels in YOLO darknet format. For training the YOLO model, the annotations should be in YOLO format as `<object-class> <x> <y> <width> <height>`, where object class is an integer value starting from 0 up to the number of classes defined; in our case, the object class will be 0 as we have only one class, i.e., pothole and the remaining parameters are the coordinates, height, and width of the labeled object bounding box.

The YOLOv5 annotation format is a bit different from the YOLO darknet format, so the conversion is needed here. As YOLOv5 implementation is in PyTorch, its annotation format is `< class_id > < center_x > < center_y > < width > < height >`, where the class id is normalized to 1 from 0 and remaining parameters are same as YOLO darknet.txt annotation format. The other thing needed for dataset preparation is 'data.yaml' file which contains the number of classes, a path to train and validation folder, and lastly the class names. After annotation, the dataset is split into train and test folders with a ratio of 80% for training and 20% for testing. Each folder contained the images corresponding to its annotation.txt file having identical file names.

The SSD-Mobilenetv2 implementation is in the TensorFlow object detection, so the dataset annotations must be converted to the TensorFlowTF record from Darknet txt for custom object training. The annotation format used for this model is a CSV file that contains the filename, width, and height of image, class name, and x_{min} , y_{min} , x_{max} , y_{max} coordinates of the labeled pothole. The dataset split ratio has been kept the same as YOLOv5 and YOLO Darknet. The train and test folder contains the images with the CSV annotation file each. The labelmap.pbtxt for train and test is written which contains the class name and id of the labeled objects in each folder.

3.3. Experimentation Protocols. The training of the YOLO and its variants are carried out on a system having Intel (R) Xeon (R) CPU at 3.0 GHz, RAM of 64 GB, and NVIDIA Titan Xp GPU. The dataset is split into 80% (1,066 images) training of the model and 20% (264 images) for the testing with labels of each image. The files needed for training are obj.names (names of the classes), obj.data (the number of classes), a path to train, test, and a backup folder. The backup folder saves the weights after every 100th iteration. The major file required for training is the configuration file which changes according to the model requirements. In our case, each model is trained for 20,000 max iterations with the batch size of 64 having subdivisions of 32 and a learning rate of 0.001 enclosed in the .cfg configuration file. The filters are set to 18 according to the formula $filter\ size = (class+5) * 3$ where $class = 1$ in a .cfg file. For the training of YOLOv5, same parameters are used.

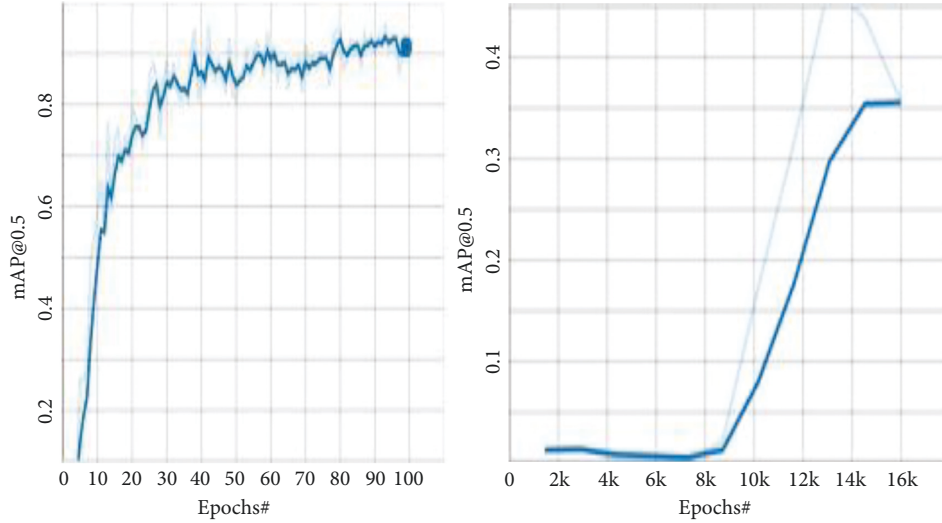


FIGURE 6: Accuracy graphs of (a) YOLOv5 when trained for 100 epochs and (b) SSD-Mobilenetv2 when trained for 16,000 batches.

According to the model and performance, we used pretrained weights from Google. Here, pretrained weights of YOLO v1, v2, v3, v4, v5, and Tiny-YOLOv4 were downloaded for training and used as transfer learning. YOLOv5 has less training time as compared to the rest of the YOLO models as 1 hour max, as shown in Figure 6(a). For the training of SSD-Mobilenetv2, we used 20,000 training steps, 50 evaluation steps, and an initial learning rate of 0.004 for better accuracy in the configuration file. The TensorFlow object detection pretrained model was used for training. The overall training time for SSD-Mobilenetv2 taken was 3-hours 8-min approximately for 20,000 training steps, as shown in Figure 6(b).

3.4. Performance Criteria. The performance of each model has been evaluated with performance metrics (mAP, precision, recall, F1-score, and average inference time per image) for all the trained deep learning models, as shown in equations (1) to (5). By adjusting a threshold and observing the precision and recall values, the model is evaluated. N thresholds are assumed for the precision and recall calculations, with each threshold consisting of a pair of precision (P_n) and recall (R_n) ($n=1, 2, \dots, N$). Average precision (AP) is defined by equation (4), and mean average precision (mAP) defined by (1) is the average of AP of each class. In our case, the AP and mAP will be same as we have only one class. The measure of overlapping area between the predicted bounding box and the ground truth bounding box is compared with the defined threshold called Intersection over Union (IOU). For this work, we have set the threshold to 0.3. Therefore, a prediction is correct if IOU score is greater than or equal to the threshold of 0.3 (30%). The precision, recall, and F1-score of YOLOv2 and YOLOv3 are nearly same, but the mAP@0.5 for YOLOv2 is 81.21% and 83.60%. However, the inference time of YOLOv2 is 33.7 ms which is quite good, as shown in Table 1. YOLOv4 and Tiny-YOLOv4 have achieved mAP@0.5 of 85.48% and 80.04%, respectively, whereas the inference time of Tiny-YOLOv4 is 4.8 ms which is very low as compared to

the pure YOLOv4. YOLOv5 showed the highest mAP@0.5 of 95% with an inference time of 10 ms per image. The inference time of Tiny-YOLOv4 is the lowest to deploy on edge devices such as Raspberry Pi, Google Coral, and NVIDIA Jetson Nano. We found out SSD-Mobilenetv2 can be run for real-time detection but did not perform for our problem as mAP is 47.4% which is not even close to the mAP of the YOLO family. Table 1 presents the overall evaluation parameters of other deep learning models.

$$\text{Precision} = \frac{TP}{TP + FP} \quad (1)$$

$$\text{Recall} = \frac{TP}{TP + FN} \quad (2)$$

$$F1 = \frac{2 * \text{Precision} * \text{Recall}}{\text{Precision} + \text{Recall}} \quad (3)$$

$$AP = \sum_{n=1}^N (R_n - R_{n-1})P_n \quad (4)$$

$$mAP = \frac{1}{N} \sum_{i=1}^N AP_i \quad (5)$$

After looking into the pothole detection result using SSD-Mobilenetv2, we concluded that SSD-Mobilenetv2 does not detect objects that rely upon the appearance of environment like potholes because it does not consider its neighboring pixels, unlike YOLO. YOLO divides an image into grid cells of equal size. Each cell is to detect the object that lies in the center. Furthermore, SSD-Mobilenetv2 fails small pothole detection as our dataset contained small bounding boxes as well.

Figure 7 shows the detection results obtained from each trained model. The red circled pothole is not detected by YOLOv5 and SSD-Mobilenetv2 in Figure 7. In contrast, the YOLOv4 even detected the small potholes, as well as long-distance potholes with a considerable confidence threshold of 0.67, encircled red in Figure 7.

TABLE 1: Performance evaluation of each model on test subset of pothole image dataset (PID)

Model	Precision	Recall	F1-score	mAP@0.5 (%)	Inference time (ms)
SSD-Mobilenetv2	0.42	0.56	0.479	47.4	7
YOLOv1	0.82	0.69	0.74	79.55	340
YOLOv2	0.81	0.76	0.78	81.21	33.7
YOLOv3	0.77	0.78	0.78	83.60	70.57
Tiny-YOLOv4	0.76	0.75	0.76	80.04	4.86
YOLOv4	0.81	0.83	0.82	85.48	52.51
YOLOv5	0.93	0.83	0.87	95.00	10

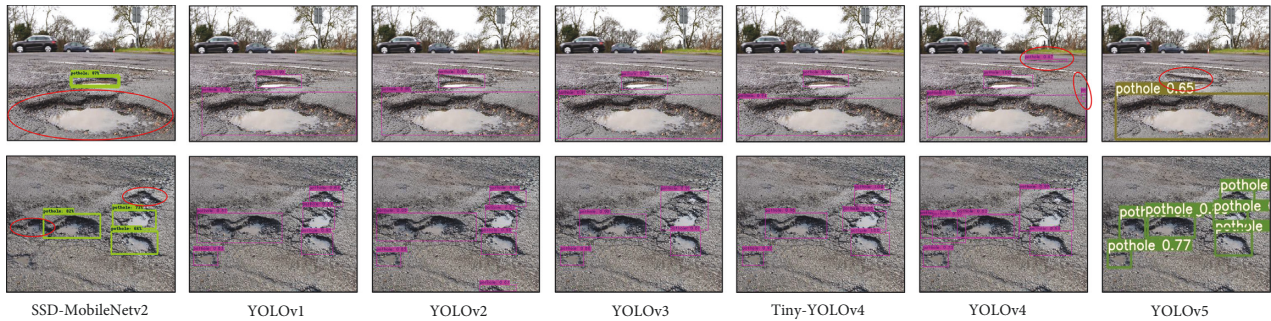


FIGURE 7: Prediction of potholes by YOLO family and SSD-Mobilenetv2.

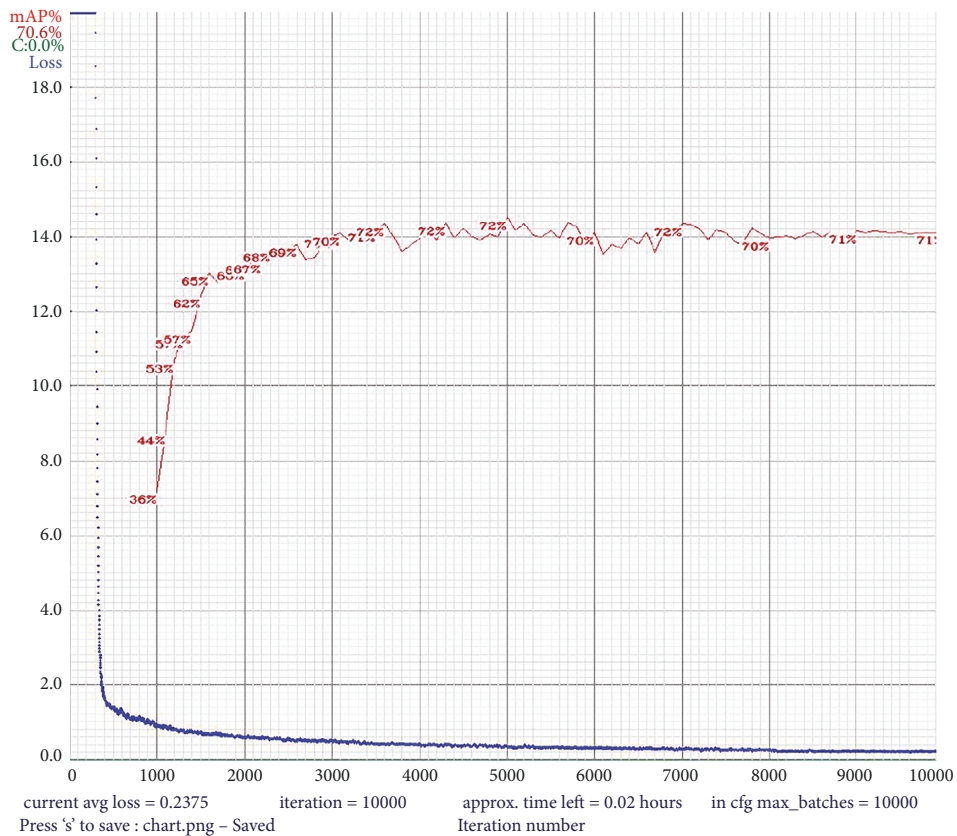


FIGURE 8: Average loss vs. iterations and mAP graph of YOLOv4 when trained for 10,000 iterations.

3.5. Accuracy Graphs. Figure 6(a) shows 95% as the best mean average precision for YOLOv5 for the present case. Similarly, the training loss is nearly equal to zero that is 0.02. Figure 6(b) shows the mAP and the total number of iteration

set. Initially, iteration set to train SSD-Mobilenetv2 was 20000. After the 14,000th iteration, mAP started decreasing and became constant at the 16,000th iteration. Thus, the training is stopped at the 16,000th iteration, with an average

TABLE 2: Qualitative analysis on test images.

Image ID	No. of Labelled potholes	Detected by YOLOv4	Detected by SSD-Mobilenetv2	Detected by YOLOv5	False detection by YOLOv5
a	7	7	3	6	0
b	11	11	0	9	0
c	6	6	1	3	1
d	9	9	3	9	3
e	8	8	1	4	0
Average detection	—	100%	21%	73%	—

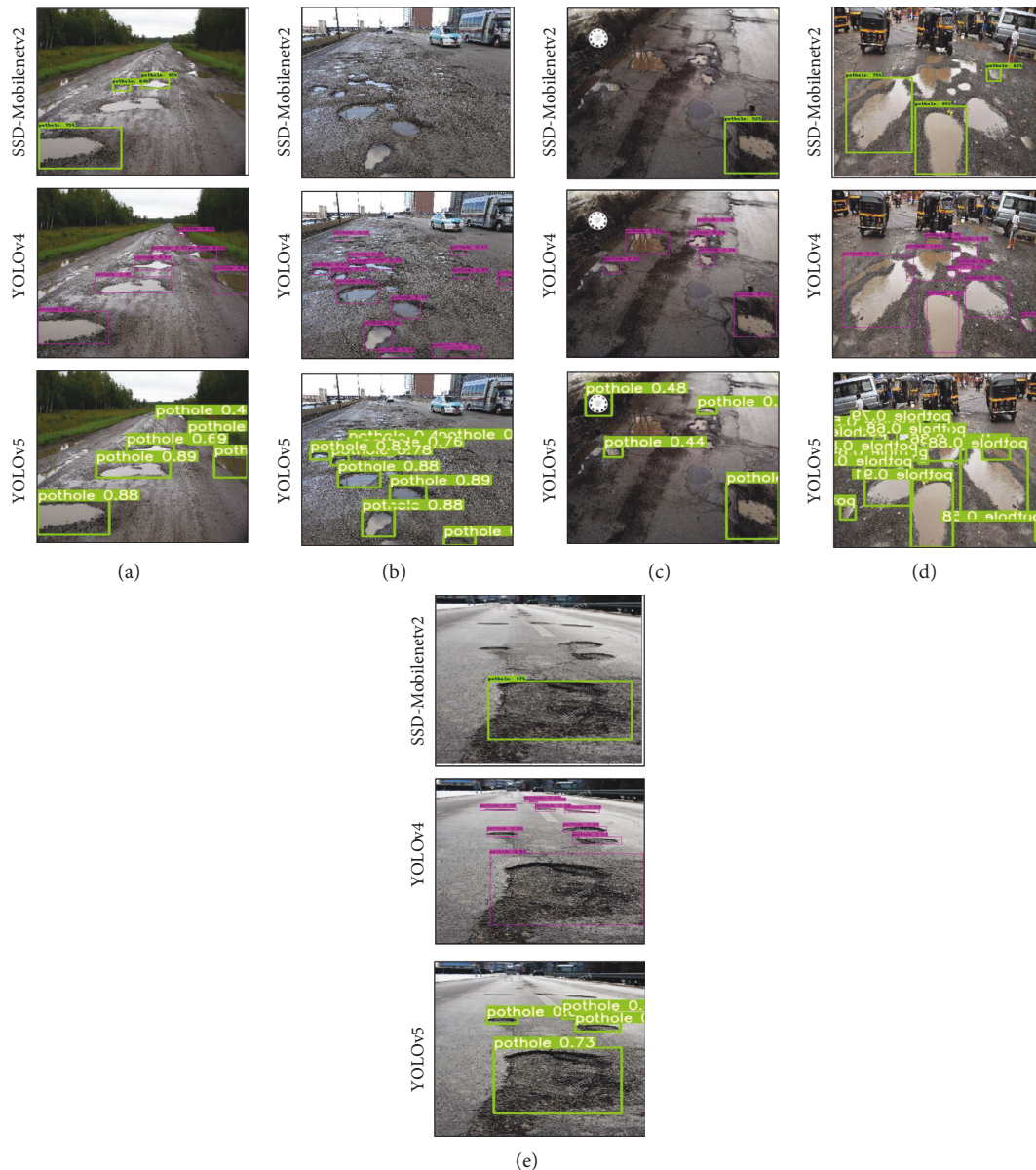


FIGURE 9: Qualitative analysis of SSD-Mobilenetv2, YOLOv5, and YOLOv4 on test images.

loss up to 4.5 at the end of training. Figure 8 shows average loss vs. no. of iterations as well as mAP of Tiny-YOLOv4. The loss and mAP became constant at the 4,000th iteration,

so we continued training for 10,000 iterations. At last, 71% mAP@0.5 has been achieved with an average iteration loss of 0.237.



FIGURE 10: Real-time detection of potholes using OAK-D and Raspberry Pi on different distance ranges.

TABLE 3: Real-time detection performance evaluation of each model.

Model	No. of potholes	Detected Potholes	Accuracy (%)	FPS
SSD-Mobilenetv2	10	4	40	26.65
YOLOv5	10	5	50	18.25
YOLOv2	10	8	80	3.20
YOLOv3	10	9	90	2.39
YOLOv4	10	10	100	1.98
Tiny-YOLOv4	10	9	90	31.76

3.6. *Qualitative Analysis.* Table 2 presents the qualitative analysis of five test images. YOLOv4 performed well as compared to YOLOv5, while SSD-Mobilenetv2 showed unsatisfactory results. As shown in Figure 9 Image ID c, YOLOv5 misclassified objects as potholes and does not detect potholes despite being visible. In Figure 9 Image ID b, SSD-Mobilenetv2 shows no detection of potholes provided many potholes are in the scene. YOLOv5 and SSD-Mobilenetv2 could not detect potholes with long distances from the camera. However, based on these analyses, YOLOv4 performed 100% accurately. The detections done by SSD-Mobilenetv2, YOLOv5, and YOLOv4 are present in Figure 9. Average detection is measured using (2).

$$\text{Average_Detection} = \left(\frac{\text{Detected_Potholes}}{\text{Total_Potholes}} \right) * 100. \quad (6)$$

3.7. *Real-Time Detection of Potholes by Our System.* We have conducted real-time pothole detection using OAK-D and Raspberry Pi on three different locations and distance ranges (Long-Range \cong 10 m, Mid-Range \cong 5 m, Close-Range \cong 2 m). In Figure 10, YOLOv5 and SSD-Mobilenetv2 did not detect the potholes located on the long-distance range and even missed the potholes in mid range and close range. However, Tiny-YOLOv4 detects all the potholes with the highest confidence score up to 96% in all defined distance ranges.

For real-time testing on vehicles, OpenCV AI Kit (OAK-D) has been mounted at the center of the vehicle dashboard to capture the maximum road area possible for better evaluation. However, the speed is constant at 65 km/h throughout the experiment. Raspberry Pi acted as a host computer for OAK-D. The Tiny-Yolov4 detects potholes at a distance of 10 meters from the dashboard with a high FPS of 31.76.

TABLE 4: Comparison with state-of-the-art vs. our results.

Contribution	Dataset	mAP@0.25	mAP@0.5	Inference time (ms)
Omar et al. [43]	Pothole image dataset (PID)	60%	—	—
Shaghouri et al. [44]	Pothole image dataset (PID)	75.53%	—	—
Gajjar et al. [45]	Self + Online collected	—	18.5%	481
Sung-Sik et al. [46]	Pothole image dataset (PID)	—	74.8%	—
Our trained SSD-MobileNetv2	Pothole image dataset (PID)	—	47.4%	7
Our trained YOLOv3	Pothole image dataset (PID)	83.60%	—	70.57
Our trained YOLOv4	Pothole image dataset (PID)	85.48%	—	52.51
Our trained YOLOv5	Pothole image dataset (PID)	—	95%	10

Tiny-YOLOv4 is considered the best model to implement for real-time pothole detection systems as it has maximum FPS with the highest detection accuracy compared to YOLOv2, YOLOv3, and YOLOv4. SSD-MobileNetv2 has shown low performance as it only detects when the confidence threshold is 30% or less having false and no detection. YOLOv5 has 18.25 FPS and misses a large number of potholes during real-time inference. However, it is fruitful for real-time pothole detection systems with high FPS but lower accuracy. The real-time detection results are present in Table 3. The testing is done in a completely unknown environment as we trained our models on the Pothole image Dataset.

3.8. Comparison. We have compared our results with other state-of-the-art techniques, showing that our YOLOv4 trained model has performed better in detection with minimum inference time. Shaghouri et al. [44] used a pothole image dataset with 75.63% mAP using YOLOv4; the trained YOLOv4 has achieved 85.48%, which is 9.85% more accurate; whereas [45] used self-collected dataset and achieved mAP@0.5 of 18.5% with higher inference time using SSD-MobileNetv2. Researchers in [46] used YOLOv5 on the PID and achieved the mAP@0.5 of 74.48% which is in difference of 20.52% as compared to our trained YOLOv5. Table 4 presents the comparison with other state-of-the-art techniques.

4. Conclusion

This work presented the state-of-the-art deep learning models (YOLO family and SSD-MobileNetv2) for real-time pothole detection leading towards the deployment on edge devices. Although, YOLOv5 showed the highest mAP@0.5 of 95% among other models but exhibits misclassification and no detection potholes at long distances. Therefore, we concluded the YOLOv4 as the best-fit pothole detection model for accuracy and Tiny-YOLOv4 as the best-fit pothole detection model for real-time pothole detection with 90% detection accuracy and 31.76 FPS. The proposed approach can help road maintenance authorities to formulate rapid and optimized actions for road infrastructure repairs. A more sophisticated solution with the help of the global position system (GPS) can detect and point out the location of pavement failures. This work can contribute to self-driving applications and the automation industry. This work can further be

extended to detect other pavement distresses, road depressions, classify roads as per quality, and depth estimation of potholes. The accuracy limitations can also be resolved in the future by further modification and extension in the real-time deployment.

Data Availability

The data are available upon request to the author.

Conflicts of Interest

The authors declare no conflicts of interest regarding authorship and publication of this research work.

Acknowledgments

This research work had been carried out at Swarm Robotics Lab under National Center of Robotics (NCRA) which was being funded by Higher Education Commission (HEC), Pakistan. The authors acknowledge the NCRA and HEC for technical and financial support.

References

- [1] C. Ng, T. Law, F. Jakarni, and S. Kulanthayan, "Road infrastructure development and economic growth," in *IOP conference series: materials science and engineering*, vol. 512, no. 1, Article ID 012045, IOP Publishing, 2019.
- [2] S. Rahman, A. Patel, "Pothole Image Dataset. Kaggle, 2020, <https://www.kaggle.com/sachinpatel21/pothole-image-dataset/>.
- [3] W. health, *Statistics*, "Injury Deaths Rise in Rank, 2008, https://www.who.int/violence_injury_prevention/key_facts/VIP_key_fact_3.pdf/.
- [4] K. C. Wang, "Challenges and Feasibility for Comprehensive Automated Survey of Pavement conditions," in *Proceedings of the Applications of Advanced Technologies in Transportation Engineering (2004)*, pp. 531–536, Beijing, China, May 2004.
- [5] K. Chang, J. Chang, and J. Liu, "Detection of pavement distresses using 3d laser scanning technology," in *Proceedings of the Computing in Civil Engineering (2005)*, pp. 1–11, Cancun, Mexico, May 2005.
- [6] Z. Hou, K. C. Wang, and W. Gong, "Experimentation of 3d pavement imaging through stereovision," in *Proceedings of the International Conference on Transportation Engineering 2007*, pp. 376–381, Chengdu, China, July 2007.
- [7] P. Harikrishnan and V. P. Gopi, "Vehicle vibration signal processing for road surface monitoring," *IEEE Sensors Journal*, vol. 17, no. 16, pp. 5192–5197, 2017.

- [8] B. X. Yu and X. Yu, "Vibration-based system for pavement condition evaluation," in *Proceedings of the Applications of Advanced Technology in Transportation*, pp. 183–189, Chicago, IN, USA, August 2006.
- [9] K. De Zoysa, C. Keppitiyagama, G. P. Seneviratne, and W. Shihan, "A public transport system based sensor network for road surface condition monitoring," in *Proceedings of the 2007 Workshop on Networked Systems for Developing Regions*, pp. 1–6, Colombo, Sri Lanka, August 2007.
- [10] J. Eriksson, L. Girod, B. Hull, R. Newton, S. Madden, and H. Balakrishnan, "The pothole patrol: using a mobile sensor network for road surface monitoring," in *Proceedings of the 6th International Conference on Mobile Systems, Applications, and Services*, pp. 29–39, Breckenridge, CO, USA, June 2008.
- [11] A. Glowacz, "Ventilation diagnosis of angle grinder using thermal imaging," *Sensors*, vol. 21, no. 8, p. 2853, 2021.
- [12] —, "Thermographic fault diagnosis of ventilation in blcd motors," *Sensors*, vol. 21, no. 21, p. 7245, 2021.
- [13] C. Koch and I. Brilakis, "Pothole detection in asphalt pavement images," *Advanced Engineering Informatics*, vol. 25, no. 3, pp. 507–515, 2011.
- [14] G. Jog, C. Koch, M. Golparvar-Fard, and I. Brilakis, "Pothole properties measurement through visual 2d recognition and 3d reconstruction," in *Proceedings of the Computing in Civil Engineering (2012)*, pp. 553–560, Clearwater Beach, FL, USA, June 2012.
- [15] L. Huidrom, L. K. Das, and S. Sud, "Method for automated assessment of potholes, cracks and patches from road surface video clips," *Procedia-Social and Behavioral Sciences*, vol. 104, pp. 312–321, 2013.
- [16] I. H. Abbas and M. Q. Ismael, "Automated pavement distress detection using image processing techniques," *Engineering, Technology & Applied Science Research*, vol. 11, no. 5, pp. 7702–7708, 2021.
- [17] J. Zhou, P. S. Huang, and F.-P. Chiang, "Wavelet-based pavement distress detection and evaluation," *Optical Engineering*, vol. 45, no. 2, p. 027007, 2006.
- [18] S. Lee, S. Kim, K. E. An, S.-K. Ryu, and D. Seo, "Image processing-based pothole detecting system for driving environment," in *Proceedings of the 2018 IEEE International Conference on Consumer Electronics (ICCE)*, pp. 1–2, IEEE, Las Vegas, NV, USA, January 2018.
- [19] P. Wang, Y. Hu, Y. Dai, and M. Tian, "Asphalt pavement pothole detection and segmentation based on wavelet energy field," *Mathematical Problems in Engineering*, vol. 2017, 2017.
- [20] Y. K. Arbawa, F. Utaminigrum, and E. Setiawan, "Three combination value of extraction features on glcm for detecting pothole and asphalt road," *Jurnal Teknologi dan Sistem Komputer*, vol. 9, no. 1, pp. 64–69, 2021.
- [21] O. A. Egaji, G. Evans, M. G. Griffiths, and G. Islas, "Real-time machine learning-based approach for pothole detection," *Expert Systems with Applications*, vol. 184, p. 115562, 2021.
- [22] P. Ping, X. Yang, and Z. Gao, "A deep learning approach for street pothole detection," in *Proceedings of the 2020 IEEE Sixth International Conference on Big Data Computing Service and Applications (BigDataService)*, pp. 198–204, IEEE, Oxford, UK, August 2020.
- [23] W. Ye, W. Jiang, Z. Tong, D. Yuan, and J. Xiao, "Convolutional neural network for pothole detection in asphalt pavement," *Road Materials and Pavement Design*, vol. 22, no. 1, pp. 42–58, 2021.
- [24] R. Agrawal, Y. Chhadva, S. Addagarla, and S. Chaudhari, "Road surface classification and subsequent pothole detection using deep learning," in *Proceedings of the 2021 2nd International Conference for Emerging Technology (INCET)*, pp. 1–6, IEEE, Belagavi, India, May 2021.
- [25] C. Zhang, E. Nateghinia, L. F. Miranda-Moreno, and L. Sun, "Pavement distress detection using convolutional neural network (cnn): a case study in montreal, Canada," *International Journal of Transportation Science and Technology*, vol. 1, 2021.
- [26] S. I. Hassan, D. O'Sullivan, and S. McKeever, "Pothole detection under diverse conditions using object detection models," *IMPROVE*, vol. 1, pp. 128–136, 2021.
- [27] R. Kavitha and S. Nivetha, "Pothole and object detection for an autonomous vehicle using yolo," in *Proceedings of the 2021 5th International Conference on Intelligent Computing and Control Systems (ICICCS)*, pp. 1585–1589, IEEE, Madurai, India, May 2021.
- [28] H. Chen, M. Yao, and Q. Gu, "Pothole detection using location-aware convolutional neural networks," *International Journal of Machine Learning and Cybernetics*, vol. 11, no. 4, pp. 899–911, 2020.
- [29] M. Rani, M. Mustafar, N. Ismail, M. Mansor, and Z. Zainuddin, "Road peculiarities detection using deep learning for vehicle vision system IOP Conference Series: materials Science and Engineering," *IOP Publishing*, vol. 1068, no. 1, p. 012001, 2021.
- [30] A. Krizhevsky, I. Sutskever, and G. E. Hinton, "Imagenet classification with deep convolutional neural networks," *Communications of the ACM*, vol. 60, no. 6, pp. 84–90, 2017.
- [31] R. Girshick, J. Donahue, T. Darrell, and J. Malik, "Rich feature hierarchies for accurate object detection and semantic segmentation," in *Proceedings of the IEEE Conference on Computer Vision and Pattern Recognition*, pp. 580–587, San Juan, PR, USA, June 2014.
- [32] S. Antol, A. Agrawal, J. Lu et al., "Vqa: visual question answering," in *Proceedings of the IEEE International Conference on Computer Vision*, pp. 2425–2433, Santiago, Chile, December 2015.
- [33] C. Zhang, Z. Yang, X. He, and L. Deng, "Multimodal intelligence: representation learning, information fusion, and applications," *IEEE Journal of Selected Topics in Signal Processing*, vol. 14, no. 3, pp. 478–493, 2020.
- [34] B. Martinez, P. Ma, S. Petridis, and M. Pantic, "Lipreading using temporal convolutional networks," in *Proceedings of the ICASSP 2020-2020 IEEE International Conference on Acoustics, Speech and Signal Processing (ICASSP)*, pp. 6319–6323, IEEE, Beijing, China, January 2020.
- [35] J. Redmon, S. Divvala, R. Girshick, and A. Farhadi, "You only look once: unified, real-time object detection," in *Proceedings of the IEEE Conference on Computer Vision and Pattern Recognition*, pp. 779–788, Los Alamitos, CA, USA, June 2016.
- [36] W. Liu, D. Anguelov, D. Erhan et al., "Ssd: single shot multibox detector," in *Proceedings of the European Conference on Computer Vision*, pp. 21–37, Springer, Cham, September 2016.
- [37] J. Redmon and A. Farhadi, "Yolo9000: better, faster, stronger," in *Proceedings of the IEEE Conference on Computer Vision and Pattern Recognition*, pp. 7263–7271, Cham, June 2017.
- [38] "Y.3: An Incremental Improvement," 2018, <https://arxiv.org/abs/1804.02767>.

- [39] A. Bochkovskiy, C.-Y. Wang, and H.-Y. M. Liao, *Yolov4: Optimal Speed and Accuracy of Object Detection*, 2020, <https://arxiv.org/abs/2004.10934>.
- [40] Z. Jiang, L. Zhao, S. Li, and Y. Jia, *Real-time Object Detection Method Based on Improved Yolov4-Tiny*, 2020, <https://arxiv.org/abs/2011.04244>.
- [41] A. Malta, M. Mendes, and T. Farinha, "Augmented reality maintenance assistant using yolov5," *Applied Sciences*, vol. 11, no. 11, p. 4758, 2021.
- [42] Roboflow, "Y.5," 2020, <https://models.roboflow.com/object-detection/yolov5>.
- [43] M. Omar and P. Kumar, "Detection of roads potholes using yolov4," in *Proceedings of the 2020 International Conference on Information Science and Communications Technologies (ICISCT)*, pp. 1–6, IEEE, Tashkent, Uzbekistan, November 2020.
- [44] A. A. Shaghouri, R. Alkhatib, and S. Berjaoui, "Real-time pothole detection using deep learning," 2021, <https://arxiv.org/abs/2107.06356>.
- [45] K. Gajjar, T. van Niekerk, T. Wilm, and P. Mercorelli, *Vision-based Deep Learning Algorithm for Detecting Potholes*, 2021.
- [46] S.-S. Park, V.-T. Tran, and D.-E. Lee, "Application of various yolo models for computer vision-based real-time pothole detection," *Applied Sciences*, vol. 11, no. 23, p. 11229, 2021.

Research Article

Optimization of the Operation Rule Curves for Cascade Reservoirs Using the Cuckoo Search Algorithm

Ismail Ara ¹ and Mutlu Yasar ²

¹*Hidrosolar Energy Production Construction and Industry and Trade Co., Denizli, Turkey*

²*Pamukkale University, Department of Civil Engineering, Denizli, Turkey*

Correspondence should be addressed to Mutlu Yasar; mutluyasar@pau.edu.tr

Received 28 August 2021; Revised 10 December 2021; Accepted 14 March 2022; Published 6 April 2022

Academic Editor: Vagelis Plevis

Copyright © 2022 Ismail Ara and Mutlu Yasar. This is an open access article distributed under the Creative Commons Attribution License, which permits unrestricted use, distribution, and reproduction in any medium, provided the original work is properly cited.

Reservoir operation optimization models are based on the hydrological cycle principle. These models determine the inflow and outflow necessary to meet the demands for drinking water, irrigation water, etc. Rather than optimizing each reservoir separately in cascaded reservoir systems, more efficient results are obtained if the reservoirs are optimized as a whole. In this study, the optimal operation rule curves for cascaded reservoirs were obtained by using the cuckoo search algorithm, which is a soft computing method. Both the irrigation and flood control constraints of the Adiguzel and Cindere dams in Denizli (Turkey) were satisfied by utilizing these rule curves, and the total energy production was maximized. In addition, these rule curves considered turbine efficiency, which significantly contributes to published literature. The total energy obtained with the proposed operation rule curves was 14% higher than that currently produced by the Adiguzel and Cindere dams.

1. Introduction

Water and energy are two of the most important needs of society. Fresh water has become considerably more important due to global climate change. It is therefore crucial to use fresh water efficiently and produce maximum energy from it. As in all developing countries, Turkey's need for water and energy increases year by year because the population and level of development increase. Therefore, the water resources available in Turkey must be used optimally and be able to produce more energy every year.

Most of the energy produced in Turkey comes from imported and consumable resources such as oil and natural gas. This causes dependency on external energy resources and increases the unit cost of energy production. Accordingly, sustainable domestic and renewable energy resources with lower unit costs are important for energy production.

Hydroelectric energy is the most important renewable energy source in Turkey and meets 32% of Turkey's total energy needs [1]. Thirty percent of the electrical energy installed power in Turkey consists of hydrological resources.

Approximately 70% of the facilities established on hydrological resources in Turkey consist of storage dams. Therefore, these reservoirs should be used efficiently to meet the energy demand [2].

Various factors, such as inflow, outflow, water elevation, and evaporation, directly affect the operation of reservoirs. Using traditional methods for reservoir operation can lead to failure in meeting some of these demands. Therefore, reservoir operation studies of various optimization techniques aimed at maximizing energy production and economic benefits are important research topics today. Due to the development of computer technology, especially in the last 40 years, various optimization techniques have been developed to manage and operate single- and multireservoir systems. These optimization techniques are comprehensively presented in studies by Yeh [3], Wurbs [4], Chau and Albermani [5], and Labadie [6]. These studies indicated that optimization methods developed using dynamic programming, nonlinear programming, and various soft computing algorithms are suitable for the optimal operation of cascade reservoirs.

Karamouz et al. [7] applied discrete dynamic programming to a multireservoir water resource system in the Gunpowder River basin near Baltimore. The study investigated the operation of reservoir systems using stochastic dynamic programming and Bayesian decision theory.

Li et al. [8] suggested an improved decomposition-coordination optimization method and discrete differential dynamic programming to effectively solve a large-scale hydropower system problem. The proposed method was applied to the long-term optimal dispatch of the large-scale hydropower system in the Yangtze River basin. The method performed effectively, not just for total power generation but also for optimizing the large-scale hydropower system operation.

In a study by Bozorg Haddad et al. [9], two problems with single and cascade reservoirs were selected to demonstrate the applicability and performance of the honey bee mating optimization (HBMO) algorithm in the nonconvex hydropower system design and operation. The problems were solved with both HBMO and gradient-based LINGO 8.0, and their results were compared. HBMO produced feasible and near-optimal solutions for both the single- and multireservoir problems, but LINGO 8.0 did not produce feasible solutions for the multireservoir problem.

Afshar et al. [10] presented an improved HBMO algorithm to obtain optimal operation rules for multireservoir systems. The performance of the proposed model was tested through sensitivity analysis, and its results were compared with a real-coded genetic algorithm for a 60-month single-reservoir operation problem. The improved model was then used to derive the release rule and storage balance functions that set the operational policy for the multireservoir system's water supply and hydropower generation.

Oliveira and Loucks [11] used real-coded genetic algorithms to implement multireservoir operation policies. These genetic algorithms utilize real-value vectors, including the information needed to define both the system release and the individual reservoir storage volume. The proposed algorithm was tested on sample reservoir systems used for water supply and hydropower. Sharif and Wardlaw [12] presented a genetic algorithm approach for optimizing multireservoir systems. The approach was demonstrated by applying it to a reservoir system in Indonesia, considering both the existing development situation in the basin and two future water resource development scenarios. The results obtained with the genetic algorithm were compared with those of discrete differential dynamic programming.

Hinçal et al. [13] investigated the efficiency and effectiveness of the genetic algorithm in optimizing cascade reservoirs. Three reservoirs in the Colorado River Storage Project were optimized to maximize power generation. The results obtained compared real operational data with the effectiveness of the genetic algorithm and showed that it could be used as an alternative to traditional optimization techniques.

Yang et al. [14] proposed several improvement strategies to prevent early convergence of the genetic algorithm in multireservoir optimization problems. The performance of these proposed strategies was tested on the optimal operation of the cascade reservoirs of the Three Gorges Dam.

Meng et al. [15] proposed a new multipurpose cuckoo search algorithm to overcome its existing deficiencies. A multipurpose hydropower plant operation optimization model for the Xiaolangdi and Xixiyuan-cascaded hydropower plants in the Lower Yellow River was constructed and used to validate the effectiveness of these algorithms along with five benchmarking problems.

SeethaRam [16] presented a genetic algorithm optimized rule curve (GA-RC) model for monthly operation of a multipurpose reservoir, which maximizes the hydropower produced while reliably meeting the irrigation demands. Instead of the usual single target storage for each period, the GA-RC model considers three sets of target storage, namely, dry, normal, and wet storage, based on the storage level at the beginning of the period.

Yuan et al. [17] proposed an improved cuckoo algorithm that featured a new neighbor sequence algorithm for global search and a variable neighborhood descent algorithm for local search, and then applied the improved cuckoo algorithm to optimize the characteristics for the operation of cascaded reservoir power generation.

Determining reservoir operation policies and optimizing reservoir operation to use the storage dams efficiently is an important part of planning and managing water resources. For example, to meet irrigation needs, the turbine efficiency is increased by using the same amount of water from a higher head. Much higher electricity production can be achieved by operating the spillway at a minimum level. Many studies in published literature have created optimal rule curves to maximize electricity production. If an optimal operation rule curve specific to each power plant is developed to increase energy production efficiency, the maximum benefit can be achieved without any additional investment [2].

Unfortunately, most of the many hydroelectric production facilities in Turkey are operated without following any optimal operation rules. The Adigüzel and Cindere cascaded dams are operated in this manner. Both the Adiguzel Dam and hydroelectric power plant (HEPP), and the Cindere Dam and hydroelectric power plant on the Büyük Menderes River were therefore selected as the sample study areas.

This study examined reservoir operations to maximize the energy produced by multipurpose cascaded reservoirs while meeting their water demands. The method suggested is based on the cuckoo search algorithm, which is a bio-based metaheuristic alternative to the methods suggested in the above studies.

Adiguzel Dam is inside the borders of Denizli and Usak. It was designed for irrigation, energy production, and flood control. The hydroelectric power plant has a total installed power of 62 MWe and an annual electricity generation potential of 280 GWh.

Cindere Dam is in the southern district of Denizli, downstream from Adiguzel Dam. The Directorate General for State Hydraulic Works (DSI) designed the dam for irrigation and energy production. The Cindere hydroelectric power plant has a total installed capacity of 29.31 MWe and an annual energy production of 88.10 GWh, according to feasibility calculations.

Yasar [2] developed a CS algorithm-based solution to optimize the reservoir's operational system and generate an optimal operation rule curve. The results showed that the CS algorithm improved the system operation, and the energy production would be increased by about 10%. The significant success of the CS algorithm for single-reservoir operation is the main motivation for this study. For this purpose, this study was carried out to test the success of the CS-based optimization model developed by Yasar [2] in operating cascade reservoirs. The study aimed at producing the most energy with the least water consumption within the specified constraints of the multipurpose cascaded reservoirs. The optimization experiments used metaheuristic methods to create reservoir operation rule curves. The average inflow of Adiguzel Dam and average monthly intermediate basin flow between the Adigüzel and Cindere Dams from 1999 to 2017 were used. Basic rules for reservoir operation were determined by considering variables such as the inflow, outflow, water loss, and storage capacity used in the sequential streamflow routing method. In the past 228 months (1999–2017) of flow data from the Adiguzel and Cindere Dams, the cascaded reservoirs were operated using codes and functions written in the MATLAB program primarily using the sequential streamflow routing method.

2. Materials and Methods

In this study, the method used for optimal operation of cascaded reservoirs consisted of three main steps. In the first step, the cascaded reservoirs are operated using the sequential streamflow routing method; in the second step, the optimum turbine flow was determined for maximizing turbine efficiency in reservoir operation, and in the third step, the objective function was optimized using the cuckoo search algorithm by considering all constraints in the cascaded reservoir operation model. After these three steps, the operation rule curves for the cascaded reservoirs were obtained.

2.1. Operating Cascaded Reservoirs with the Sequential Streamflow Routing Method. When planning a reservoir system, the system performance has to meet the existing variable water demands. The purpose of the operation and planning of a reservoir system is to maximize benefits, minimize costs, and meet variable water demands under mass balance equations and other constraints [18].

The reservoir operation is established by calculating the inflow, outflow, and loss using mass balance equations. The first step in establishing how the reservoir operates is to apply the sequential streamflow routing method, using the continuity equation to evaluate the operation of the reservoir's storage system. This method aims at reaching the targeted storage capacity by successive applications throughout the operation period. The sequence-trial streamflow routing method can be applied monthly, daily, or hourly by using the reservoir input-output data and considering the operational purposes of the reservoir. This method is based on the continuity equation given as follows:

$$\Delta V = I - O - L, \quad (1)$$

where ΔV is the change in the volume of the water stored in the reservoir, I is the amount of inflow, O is the amount of outflow, and L is the amount of water lost in the reservoir due to evaporation, leakage, and similar reasons.

This method can be used in storage hydroelectric power plant projects where the head changes, regardless of the flow, although it is quite complex. Weekly or monthly intervals are often used because collecting daily calculations for longer periods is time-consuming [19].

In this study, the operation of the cascaded reservoirs in the system was measured monthly using the sequential streamflow routing method. The reservoir data obtained for each month after operating the cascaded reservoirs were used as the initial reservoir data for the following month. In the sequential streamflow method, the area-volume-elevation values of reservoirs, tailwater channel flow elevation values, and turbine efficiency curve equations were used along with the hydrological data.

The elevation-area-volume curve of a reservoir shows the changes in the reservoir basin and its volume, depending on the water elevation in the reservoir. Land topography directly affects the storage capacity of the reservoir. When operating the cascaded reservoirs in this study, the water elevations and basin area changes corresponding to those for the volume of the reservoirs were determined by the interpolation method, using the existing elevation-area-volume values obtained from the DSI of the Aydin Regional Directorate. The area-volume-elevation values for the Adiguzel and Cindere Dam reservoirs are summarized in Figures 1 and 2, respectively.

One of the most important variables affecting the energy production of hydroelectric power plants is the net head. The head of a hydroelectric power plant is obtained by determining the difference between the water elevation in the reservoir and that in the tailwater channel. Therefore, the water elevation in the tailwater channel directly affects energy production. In this study, to calculate the net head more precisely for the operational optimization of cascaded reservoirs, the water elevation in the tailwater channel was considered based on the turbine flow. Tailwater channel models were created by examining the technical properties of the tailwater channels of both dams and obtaining tailwater rating curves.

The Adiguzel hydroelectric power plant operates between flows of $10 \text{ m}^3/\text{s}$ and $64 \text{ m}^3/\text{s}$, while the Cindere hydroelectric power plant operates between flows of $7.50 \text{ m}^3/\text{s}$ and $70.20 \text{ m}^3/\text{s}$. To optimize reservoir operation, when the turbine water was operated at the relevant flows for each power plant, the water elevations in their tailwater channels were obtained from the tailwater rating curves shown in Figures 3 and 4. The data on the tailwater channel water elevations for the Adiguzel and Cindere hydroelectric power plants were obtained from the Aydin Regional Directorate of State Hydraulic Works in the CD format. The graphs presented in Figures 3 and 4 were obtained with the help of these data.

One of the important variables affecting energy production is turbine efficiency. It varies according to the

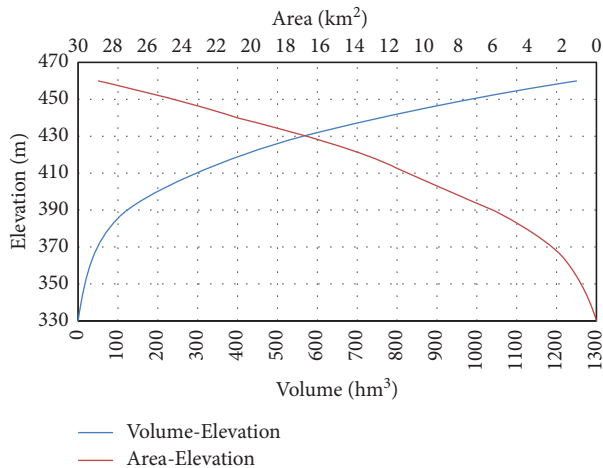


FIGURE 1: Area-volume-elevation curve of Adiguzel Dam.

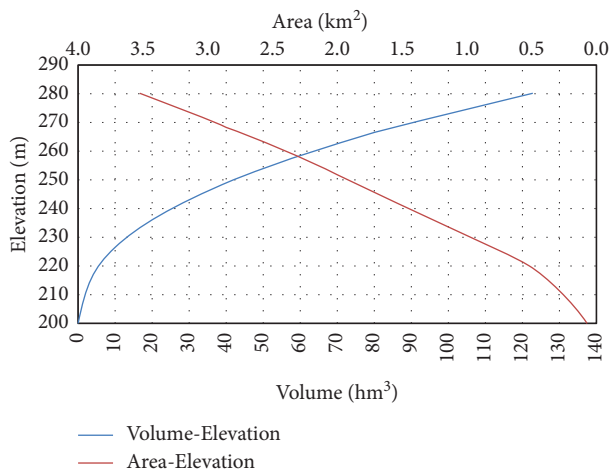


FIGURE 2: Area-volume-elevation curve of Cindere Dam.

turbine flow and turbine type. After achieving the required head and flow in the reservoir, the amount of turbine flow during operation directly affects the energy production.

Technical information about the turbines used in Adiguzel and Cindere Dam hydroelectric power plants was obtained from the DSI Aydın Regional Directorate. Francis-turbines are used in both dams.

While modeling the reservoir operation with the sequential streamflow routing method, the ratio of the monthly turbine flow (Q_t) to the turbine design flow (Q_d) was calculated after distributing the turbine volume. This ratio was used as a function input to obtain the turbine efficiency coefficient as the output of the function. Monthly turbine efficiency coefficients were used in calculating monthly energy production. The turbine efficiency curves of the Adiguzel and Cindere Dams were based on the technical data and calculation reports obtained from the DSI Aydın Regional Directorate. Data on turbine efficiency curves presented in Figures 5 and 6 were not available online. Relevant data were obtained from the State Hydraulic Works in the CD format upon a written request and payment of a fee.

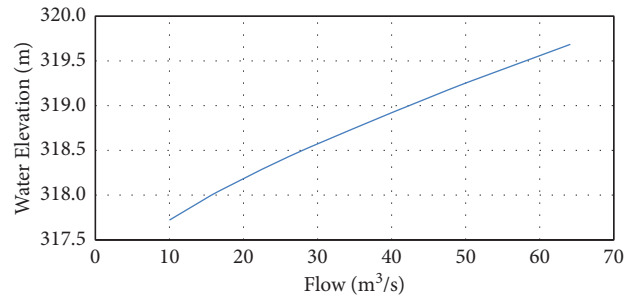


FIGURE 3: HEPP tailwater rating curve of Adiguzel Dam.

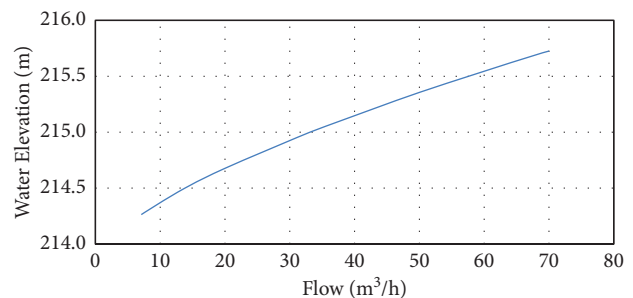


FIGURE 4: HEPP tailwater rating curve of Cindere Dam.

The turbine efficiency curves and equations given in Figures 5 and 6 were considered in the energy production calculations for the reservoir operation optimization studies.

These results were used to create the reservoir operational model with the sequential streamflow routing method. This was the first step in optimizing the reservoir operation to obtain the rule curves. The cascaded reservoirs in this study were operated to meet irrigation demands, which was their primary objective, and then water elevation changes in the tailwater channel and turbine efficiency curves were included in the monthly energy production calculation.

2.2. Calculating Optimum Turbine Flow. In previous studies on the development of operation rule curves, the effect of turbine efficiency on energy production was usually not taken into account in a realistic way. Regardless of the amount of turbine flow, the effect of the efficiency curve on energy production was ignored by taking the turbine efficiency coefficient to be constant. However, in this study, turbine efficiency equations were derived for both power plants to obtain the operation rule curves. The intention was that the turbines should operate with the highest possible efficiency during reservoir operation.

To determine the optimum turbine flow, models were created based on the constraints determined by the number of turbines in each power plant and by turbine design criteria. In optimizing the cascaded reservoir operation to obtain the reservoir operation rule curves, the monthly turbine volume was distributed to the turbines according to these models by considering the turbine efficiency. The model developed to determine the optimum turbine flow had the following constraints:

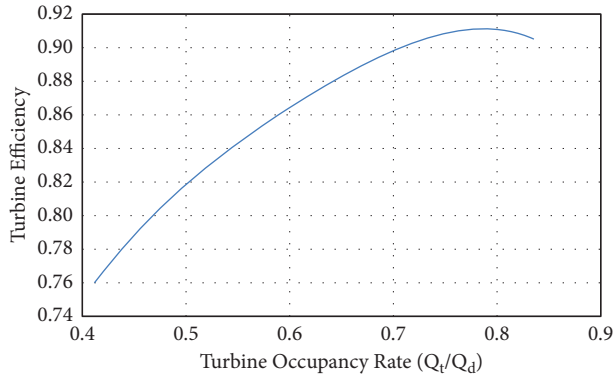


FIGURE 5: HEPP turbine efficiency curve of Adiguzel Dam.

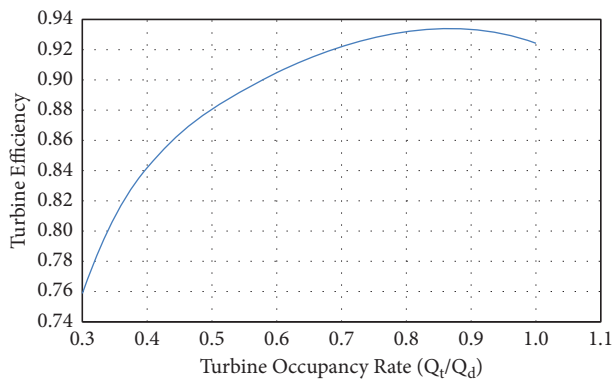


FIGURE 6: HEPP turbine efficiency curve of Cindere Dam.

- (1) If the turbine flow was less than the minimum single turbine flow, the power plant was operated on a stop-and-go principle in the range that generated the highest turbine efficiency and energy. However, the optimum turbine flow to be used was determined by considering the irrigation need. Thus, energy production was carried out during a specific part of the day, not all day. At the same time as meeting the irrigation needs, energy was therefore produced at high efficiency.
- (2) If the turbine flow was between the minimum single turbine flow and the maximum single turbine flow, energy was produced using only one turbine.
- (3) If the turbine flow was greater than the maximum single turbine flow and less than the plant design flow, the turbine flow was sent to the existing turbines equally, and energy was produced in both turbines.

In obtaining the operation rule curves for cascaded reservoirs, maximizing the turbine efficiency coefficient in the reservoir operation optimization achieved results closer to the actual production. Therefore, instead of using a constant turbine efficiency coefficient in the reservoir operation studies, it was necessary to determine a turbine's optimum flow by using the turbine efficiency curves.

2.3. Cuckoo Search Algorithm. The cuckoo search algorithm is a metaheuristic algorithm developed by Xin She Yang and Suash Deb. It is a new generation of optimization algorithm inspired by the brood parasitism and random flights of some cuckoo species [20]. The cuckoo bird is fascinating because of its aggressive brooding strategy and charming voice. The Ani and Guira species of cuckoo lay their eggs in other birds' nests, and they drop the other birds' eggs to increase the likelihood of their own eggs hatching. This parasitic behavior using other birds' (and mostly other species) nests as sites to lay eggs are followed by many other species. The pseudocode in Figure 7 summarizes the main steps of the cuckoo search (CS) algorithm.

Random search is particularly important in metaheuristic algorithms. The cuckoo search algorithm conducts random searches via the Lévy flight process. Lévy flight is a process that includes a series of random sequential steps. Mathematically, there must be two consecutive stages for the Lévy flight to generate random numbers. In the first stage, the steps are created, and in the second stage, a random direction is selected. The following equation is used to generate new solutions for the Lévy flight:

$$x_i^{j+1} = x_i^j + \alpha L(x_i^j - x_{\text{best}}^j), \quad (2)$$

where x_i^j is the current solution, x_i^{j+1} is the next solution, x_{best}^j is the best solution generated up to that step, α is the parameter used to control step size, and L is the step length.

The current solution—the first term of Equation (2)—and the transition probability—the second term of Equation (2)—are the only parameters that the next step in the Markov Chain is dependent on, and it can generally be considered a random walk. Using Lévy flight and random walk together, longer step-sizes investigate the search space more efficiently [21]. One of the most efficient and simplest methods is using the Mantegna algorithm. The L -step size in this algorithm can be calculated by the following equation [21]:

$$L = \frac{u}{|v|^{1/z}}, \quad (3)$$

where z is a parameter that takes values between 1 and 2—assumed to be 1.5 in this study. The terms u and v are calculated through a normal distribution function in the following equation:

$$u = N(0, \sigma_u^2), v = N(0, \sigma_v^2), \quad (4)$$

where σ_u and σ_v are obtained via the formula below:

$$\sigma_u = \left\{ \frac{\Gamma(1+z) \sin(\pi z/2)}{\Gamma[(1+z)/2] z 2^{(z-1)/2}} \right\}^{1/z}, \quad (5)$$

$$\sigma_v = 1,$$

where Γ represents the gamma function.

Although there is a similar random walk in other heuristic algorithms, this walk explores the search space with the cuckoo algorithm more effectively because the Lévy flight achieves longer steps [21]. The Lévy flight produces some

```

Objective Function  $f(x)$ ,  $x = (x_1, x_2, \dots, x_d)^T$ 
Generate initial population of  $n$  host nests  $x_i$ 
While ( $t > \text{MaxGeneration}$ ) or (stopping criteria)
    • Get a cuckoo randomly generated solution by Levy flights and then evaluate its quality/fitness  $F_i$ 
    • Choose a nest among  $n$  (say,  $j$ ) randomly
        If ( $F_i > F_j$ )
            • Replace  $j$  by the new solution
        end
    • A fraction ( $p_a$ ) of worse nests are abandoned and new ones/solutions are built /generated
    • Keep best solution (or nests with quality solutions)
    • Rank the solution and find current best
end while
Postprocess results and visualization

```

FIGURE 7: Pseudo-code of the cuckoo search algorithm.

new solutions that are closer to the best solution, which accelerates the local search. In addition, most of the new solutions are produced far enough from the best solution to eliminate the local minimum problem.

The main drawback of the CS algorithm is that its evolutionary operators may not adequately preserve the diversity of its population during the evolution process, and this may cause it to converge earlier than expected and deliver suboptimal solutions. Many studies have been carried out to eliminate this disadvantage. Abed-alguni [22] introduced an improved variation of CS called island-based CS with polynomial mutation (iCSPM) that adapts two improvements to CS. Abed-alguni [23] proposed a new action-selection method called cuckoo action-selection (CAS) method based on the cuckoo search algorithm. Abed-alguni and Paul [24] experimentally evaluated the performance of the CS algorithm after replacing the Lévy flight method in the original CS algorithm with seven different mutation methods. Abed-alguni et al. [25] introduced a variation of CS called exploratory CS (ECS), which incorporates three modifications to the original CS algorithm to enhance its exploration capabilities. Alawad and Abed-alguni [26] presented a variation of iCSPM (island-based Cuckoo Search with highly disruptive polynomial mutation) called discrete iCSPM with an opposition-based learning strategy (DiCSPM) for scheduling workflows in cloud computing environments based on two objectives: computation and data transmission costs. Salgotra et al. [27] are proposed three modified versions of CS to improve the properties of exploration and exploitation. All these versions employ Cauchy operator to generate the step size instead of Lévy flights to efficiently explore the search space. Moreover, two new concepts, division of population and division of generations, are also introduced in CS so as to balance the exploration and exploitation. Salgotra et al. [28] are proposed a new self-adaptive CS (SACS) algorithm to improve

its performance. The algorithm employs adaptive parameters and hence no parameter tuning is required to be done. Only two parameters exist for monitoring the performance of the CS algorithm: α and p_a . The interval $[0, 1]$ is used to select the step size α : the controller of the random search in Lévy flight. Small-sized optimization problems were reported to be solved successfully with a step size of $\alpha = 0.1$ [29]. An important parameter in the CS algorithm, p_a , represents the fraction of cuckoo eggs discovered by the host birds in the real-life phenomenon. In mathematical applications, the convergence rate of the algorithm was reported not to be strongly affected by this parameter and a value of $p_a = 0.25$ was suggested [30]. In this study, a parameter-free CS algorithm (PFCS) proposed by Karahan et al. [31] was preferred. The parameters of the PFCS algorithm (α , p_a) were selected randomly as shown below:

$$p_a = 0.1 + 0.2 * \text{rand}, \quad (6)$$

$$\alpha = 0.1 + 0.9 * \text{rand}. \quad (7)$$

2.4. Determination of the Optimal Rule Curves for Cascaded Reservoirs Using the Cuckoo Search Algorithm. To obtain the operation rule curves for optimal reservoir operation in the two cascaded dams, the codes written in the MATLAB program for the operation model were based on the constraints of the reservoirs, the operational purposes of the sequential streamflow routing, and the optimum turbine flow steps. The objective function was optimized using the cuckoo search algorithm.

The water elevation in the reservoir was kept at the highest possible level to maximize energy production in the cascaded reservoirs. The target water elevations were determined in the reservoir operations every month, taking the irrigation water demands and other constraints into consideration, and the

reservoirs were kept at these elevations. The amount of water used for energy production each month was determined according to the target water elevation.

In obtaining operation rule curves for cascaded reservoirs, the main decision variable of the problem is their target water elevation. Moreover, the optimum turbine flow and energy production times of the units are the design variables of this problem. The objective function created to solve this optimization problem is given in Equation (3), and the design variables used are briefly explained as follows.

2.5. Objective Function.

$$E_{\max} = \sum_{i=1}^{228} (E_{A,i}^1 + E_{A,i}^2) + \sum_{i=1}^{228} (E_{C,i}^1 + E_{C,i}^2 + E_{C,i}^3), \quad (8)$$

where E_{\max} is the total energy production — which is the objective function to be optimized, i is the number of months of operation, $E_{A,i}^1$ and $E_{A,i}^2$ are the monthly energy outputs of Adiguzel Dam's two turbines, and $E_{C,i}^1$, $E_{C,i}^2$, and $E_{C,i}^3$ are the monthly energy outputs of the Cindere Dam's three turbines.

While optimizing the objective function of the problem, the following were considered the constraints of the problem: the maximum storage volume, the maximum and minimum operation elevations and the reservoir volumes corresponding to these operation elevations, the targeted operation elevations at the end of the period, the minimum and maximum turbine flows, and finally, the flows based on energy production. The constraints of the problem are given in Equations (4)-(10) and explained in detail as follows.

2.6. Constraints.

$$S_{i+1} - S_i = I_i - P_i - E_i - IW_i - NV_i, \quad i = 1, 2, \dots, 228, \quad (9a)$$

$$\text{if } S_{i+1} < 0 \text{ then } S_{i+1} = 0, \quad (9b)$$

$$\text{if } NV_i > V_{TM} \text{ then } S_O = NV_i - V_{TM} \text{ else } S_O = 0, \quad (9c)$$

where S_{i+1} is the storage volume at the end of the period, S_i is the storage volume at the beginning of the period, I_i is the monthly reservoir inflow, P_i is the precipitation in the reservoir basin, E_i is the monthly evaporation in the reservoir basin, IW_i is the monthly amount of irrigation water to be released from the reservoir, and NV_i is the net volume to be released from the reservoir at the end of the period, S_O is the overflow volume at the end of the period, and V_{TM} is the maximum turbine volume:

$$h_{1,\min} \leq h_{1,T} \leq h_{1,\max}, \quad (10)$$

$$h_{2,\min} \leq h_{2,T} \leq h_{2,\max}, \quad (11)$$

$$S_{1,\min} \leq S_{1,T} \leq S_{1,\max}, \quad (12)$$

$$S_{2,\min} \leq S_{2,T} \leq S_{2,\max}, \quad (13)$$

$$Q_{A,\min} \leq Q_{A,1}, Q_{A,2} \leq Q_{A,\max}, \quad (14)$$

$$Q_{C,\min} \leq Q_{C,1}, Q_{C,2}, Q_{C,3} \leq Q_{C,\max}, \quad (15)$$

where $h_{1,\min}$ is the minimum operation elevation of Adiguzel Dam, $h_{1,\max}$ is the maximum operation elevation of Adiguzel Dam, $h_{1,T}$ is the target operation elevation of Adiguzel Dam for the month, $h_{2,\min}$ is the minimum operation elevation of Cindere Dam, $h_{2,\max}$ is the maximum operation elevation of Cindere Dam, $h_{1,T}$ is the target operation elevation of Cindere Dam for the month, $S_{1,\min}$ is the reservoir volume of Adiguzel Dam at its minimum operation elevation, $S_{1,\max}$ is the reservoir volume of Adiguzel Dam at its maximum operation elevation, $S_{1,T}$ is the reservoir volume in Adiguzel Dam at the monthly targeted operation elevation, $S_{2,\min}$ is the reservoir volume in Cindere Dam at its minimum operation elevation, $S_{2,\max}$ is the reservoir volume of Cindere Dam at its maximum operation elevation, $S_{2,T}$ is the reservoir volume in Cindere Dam at the monthly target operation elevation, $Q_{A,\min}$ is the minimum turbine flow in Adiguzel Dam, $Q_{A,\max}$ is the maximum turbine flow in Adiguzel Dam, $Q_{A,1}$, $Q_{A,2}$ are the energy production-based monthly flows for Adiguzel Dam, $Q_{C,\max}$ is the minimum turbine flow in Cindere Dam, $Q_{C,\min}$ is the maximum turbine flow in Cindere Dam, and $Q_{C,1}$, $Q_{C,2}$, $Q_{C,3}$ are energy production-based monthly flows for Cindere Dam.

Considering all these constraints, the objective function is maximized and optimal rule curves were obtained. The following stopping criterion were used to check the convergence of the solutions obtained with successive iterations:

$$|f_{\text{best}} - f_{\text{worst}}| \leq \varepsilon, \quad (16)$$

where ε is a small threshold value ($1E-9$), and f_{best} and f_{worst} denote the best and the worst convergence values in the objective function.

3. Results and Discussions

This study demonstrated that the water resources available in Turkey can be used more efficiently and more energy can be produced merely by creating new operational policies in Turkey's existing hydropower storage plants. Unlike other studies conducted in this cascaded reservoir operation study, an optimum turbine flow concept was used. As can be seen from the turbine efficiency curves shown in Figures 5 and 6, the optimum flow is the one that provides an approximately 90% turbine occupancy rate. To determine the optimum turbine flow, models were created using the constraints specified in Section 2.3 according to the number of turbines and turbine design criteria in each power plant. In the cascaded reservoir operation optimization study carried out to develop the reservoir operation rule curves, the monthly turbine volume was distributed among the turbines according to these models by considering the turbine efficiency.

To maximize the total energy production, the sequential streamflow routing method was applied, the objective function created by considering the constraints of each

cascaded reservoir was optimized by the cuckoo search algorithm in the MATLAB program, and the elevations of the reservoir operation rule curves were obtained.

As a result of determining the best reservoir operation policy for each dam, reservoir operation rule curves showing the optimum reservoir operation elevations for each period were obtained.

Tables 1 and 2 with Figures 8 and 9 show the operation elevations currently used and those proposed in this study of the Adiguzel Dam and the Cindere Dam, respectively. Since the current operating levels of Adiguzel Dam and Cindere Dam cannot be obtained online, they were obtained from the Aydın Regional Directorate of State Hydraulic Works in the CD format.

As a result of the optimization study, the proposed operation elevations for Adiguzel Dam are higher than the existing operation elevations in Table 1. Therefore, more energy can be produced without increasing water consumption with the proposed operation elevation. This possibility reveals the importance of reservoir operation policy.

Figure 8 compares the existing operation rule curve with the operation rule curve obtained for the Adiguzel Dam achieved by optimizing the cascaded reservoir operation with the outlined method.

The optimized operation elevations proposed for the Cindere Dam are generally slightly higher than its existing operation elevations, as seen in Table 2. Energy production can be increased by obtaining more head with the proposed operation elevations.

Figure 9 compares the existing operation rule curve with the operation rule curve obtained for the Cindere Dam as a result of optimizing cascaded reservoir operation. As can be seen from Figures 8 and 9, the existing operation elevations are lower than those of the operation rule curves obtained by the optimization study. In addition to contributing to energy production, this allows cascaded reservoirs to have more volume in potential dry periods, thus eliminating the possibility that cascaded reservoirs do not meet the irrigation demands in those periods.

Adiguzel Dam, with an active volume of 821 million cubic meters, is the main storage dam of the cascaded dam system optimized in this study. With the optimization results, Adiguzel Dam operation elevations were increased by approximately 17 m in some months. This increased the cascaded dam system's active storage amount and eliminated the risk that irrigation demands cannot be met during dry periods.

According to the information provided by the DSI Aydın Directorate, Adiguzel Dam achieved 2171.07 GWh of energy production between 1999 and 2017, while Cindere Dam produced 378.97 GWh of energy between 2012 and 2017. In comparison, 2550.04 GWh of energy was produced by these two dams with existing operational policies.

If Adigüzel and Cindere Dams had been operated according to the rule curves obtained by this study, the energy that would have been produced annually as a result of the optimized reservoir operation of the cascaded dams is shown in Tables 3 and 4, respectively.

TABLE 1: Existing and proposed operation elevations for the Adigüzel Dam in meters.

Month	Existing operation elevations	Proposed operation elevations
October	435.30	449.29
November	435.30	452.03
December	435.30	450.44
January	437.25	447.47
February	440.44	448.42
March	443.55	451.92
April	446.10	453.25
May	447.96	453.25
June	448.61	453.25
July	447.20	453.25
August	441.91	445.91
September	435.83	446.96

TABLE 2: Existing and proposed operation elevations for the Cindere Dam in meters.

Month	Existing operation elevations	Proposed operation elevations
October	266.22	265.55
November	266.30	266.13
December	266.30	267.00
January	266.46	267.00
February	266.46	267.00
March	266.46	267.00
April	266.39	267.00
May	266.50	267.00
June	266.30	267.00
July	266.11	267.00
August	266.11	267.00
September	266.11	266.40

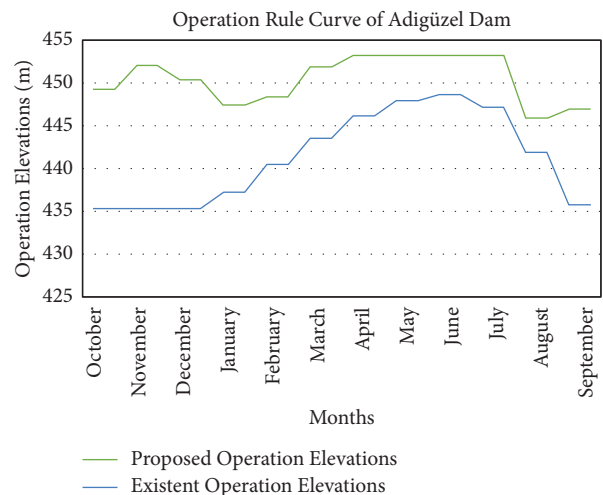


FIGURE 8: Comparison of the existent and proposed monthly operation elevations for the Adiguzel Dam.

The current cumulative energy production of the Adiguzel and Cindere Dams, and the cumulative energy production obtained with the optimal rule curve are

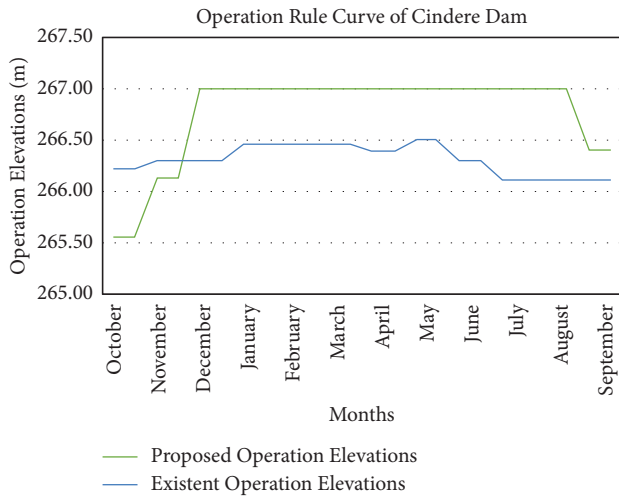


FIGURE 9: Comparison of existent and proposed monthly operation elevations of the Cindere Dam.

TABLE 3: Potential energy production achieved by the Adiguzel Dam optimization.

Year	Energy production (GWh)
1999	102.40
2000	125.21
2001	113.75
2002	122.13
2003	196.67
2004	171.27
2005	132.21
2006	111.09
2007	112.81
2008	101.47
2009	112.58
2010	201.38
2011	170.49
2012	219.03
2013	173.23
2014	113.29
2015	148.01
2016	166.49
2017	101.98
TOTAL	2695.46

TABLE 4: Potential energy production achieved by the Cindere Dam optimization.

Year	Energy production (GWh)
2012	91.44
2013	72.22
2014	48.11
2015	62.91
2016	69.69
2017	55.18
TOTAL	399.54

presented in Figures 10 and 11. These data can be accessed from the website <http://www.enerjiatlas.com> [26]. Adiguzel Dam could have produced 2695.46 GWh of energy

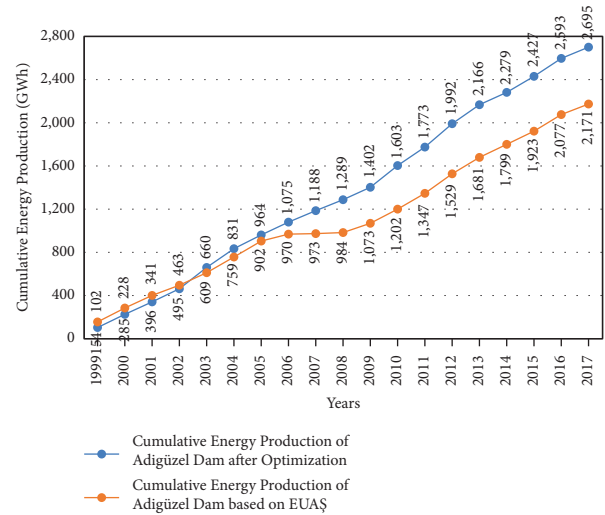


FIGURE 10: Comparison of the existing and proposed cumulative energy production by the Adiguzel Dam.

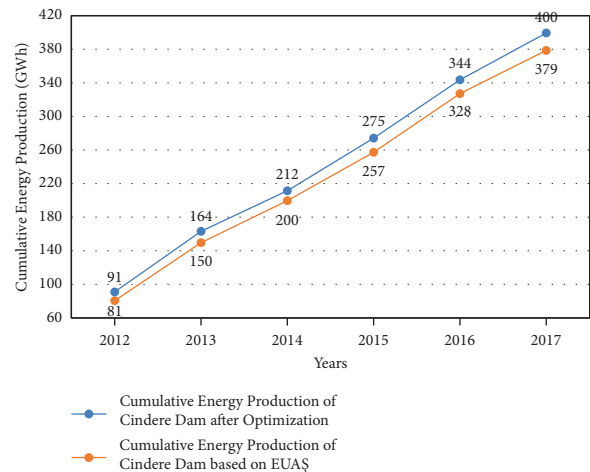


FIGURE 11: Comparison of the existing and proposed cumulative energy production by the Cindere Dam.

between 1999 and 2017, and the Cindere Dam could have produced 399.54 GWh of energy between 2012 and 2017. If they had been operated according to the proposed rule curves, 3095.01 GWh of energy would have been produced by the Adiguzel and Cindere Dams together. All water demands would have been met, and 544.97 GWh more energy would have been produced. This excess energy, potentially produced due to optimization, increases the total energy production of both dams by approximately 18%. Thus, the operational policies developed within the scope of this study confirmed that multipurpose cascaded dams could maximize energy production to meet the primary demands for drinking water, irrigation, and flood control.

Considering the efficient use of existing water resources and the contribution of hydroelectric energy production to the national economy, 544.97 GWh of excess energy would provide a surplus value of approximately USD39.8 million at

a unit price of USD0.073/kWh. It is obvious that by merely by changing the operational policies — without making any extra investment — these cascaded dams can produce more energy and thus contribute more to the national economy.

4. Conclusions

This study was performed not only to optimize the efficiency of freshwater use, which has become more significant due to global climate change, but also to increase the efficiency of hydroelectric power plants and reduce the carbon emissions that are known to be the main driving force behind climate change.

When evaluating the results of this study, operating cascaded dams established on large rivers based on the operation rule curves obtained by more advanced methods instead of storage dams meets all irrigation demands and significantly increases energy production.

Since the results of this study performed on a sample study area make a significant contribution to the national economy, performing this study on all technically appropriate storage hydroelectric power plants in Turkey would add significant value to the national economy.

Moreover, applying the proposals in this study would enable more efficient use of the existing water resources in periods when the water resources and rivers in Turkey are suffering from drought.

Further studies, which were not considered within the scope of the study but may be beneficial, are summarized as follows:

- (1) After obtaining the rule curves, the operation studies should be refreshed by adding the actual monthly data to obtain more up-to-date rule curves.
- (2) This study examined the reservoir operations of two storage dams on the main Büyük Menderes River. The facilities located on the tributaries of the river were not considered. The study can be repeated for all storage facilities in the basin.
- (3) The future operation of reservoirs can be predicted by considering climate change scenarios.
- (4) This study can be repeated using other optimization algorithms.

Data Availability

Relevant data can be obtained from the authors upon request.

Conflicts of Interest

The authors declare no conflicts of interest.

Authors' Contributions

I.A. and M.Y. conceptualized the study; I.A. and M.Y. helped the methodology; I.A. provided software; I.A. and M.Y. validated the study; I.A. and M.Y. did formal analysis; I.A.

investigated the study; I.A. and M.Y. curated the study; I.A. visualized the study; and M.Y. supervised the study.

Supplementary Materials

The provided supplementary materials include the following: Supplementary File S1 (energy productions and operation elevations of Adiguzel and Cindere Dams) related to Tables 1-2 and Figures 8-9, Supplementary File S2 (tail water rating curve of Adiguzel Dam) related to Figure 3, Supplementary File S3 (tail water rating curve of Cindere Dam) related to Figure 4, Supplementary File S4 (turbine efficiency curve of Adiguzel Dam) related to Figure 5, and Supplementary File S5 (turbine efficiency curve of Cindere Dam) related to Figure 6. (*Supplementary Materials*)

References

- [1] Turkish Electricity, "Turkish electricity transmission corporation (TEIAS)," *Installed Power Report of Turkey by Energy Sources*, vol. 6, 2021.
- [2] M. Yasar, "Optimization of reservoir operation using cuckoo search algorithm: example of adiguzel dam, Denizli, Turkey," *Mathematical Problems in Engineering*, vol. 2016, pp. 1-7, 2016.
- [3] W. W.-G. Yeh, "Reservoir management and operations models: a state-of-the-art review," *Water Resources Research*, vol. 21, no. 12, pp. 1797-1818, Article ID 1316038, 1985.
- [4] R. A. Wurbs, "Reservoir-system simulation and optimization models," *Journal of Water Resources Planning and Management*, vol. 119, no. 4, pp. 455-472, 1993.
- [5] K. W. Chau and F. Albermani, "Knowledge-based system on optimum design of liquid retaining structures with genetic algorithms," *Journal of Structural Engineering*, vol. 129, no. 10, pp. 1312-1321, 2003.
- [6] J. W. Labadie, "Optimal operation of multireservoir systems: state-of-the-art review," *Journal of Water Resources Planning and Management*, vol. 130, no. 2, pp. 93-111, 2004.
- [7] M. Karamouz, M. H. Houck, and J. W. Delleur, "Optimization and simulation of multiple reservoir systems," *Journal of Water Resources Planning and Management*, vol. 118, no. 1, pp. 71-81, 1992.
- [8] C. Li, J. Zhou, S. Ouyang, X. Ding, and L. Chen, "Improved decomposition-coordination and discrete differential dynamic programming for optimization of large-scale hydro-power system," *Energy Conversion and Management*, vol. 84, pp. 363-373, 2014.
- [9] O. Bozorg Haddad, A. Afshar, and M. A. Mariño, "Design-operation of multi-hydropower reservoirs: HBMO approach," *Water Resources Management*, vol. 22, no. 12, pp. 1709-1722, 2008.
- [10] A. Afshar, M. Shafii, and O. B. Haddad, "Optimizing multi-reservoir operation rules: an improved HBMO approach," *Journal of Hydroinformatics*, vol. 13, no. 1, pp. 121-139, 2011.
- [11] R. Oliveira and D. P. Loucks, "Operating rules for multi-reservoir systems," *Water Resources Research*, vol. 33, no. 4, pp. 839-852, 1997.
- [12] M. Sharif and R. Wardlaw, "Multireservoir systems optimization using genetic algorithms: case study," *Journal of Computing in Civil Engineering*, vol. 14, no. 4, pp. 255-263, 2000.

- [13] O. Hinçal, A. B. Altan-Sakarya, and A. M. Ger, "Optimization of multireservoir systems by genetic algorithm," *Water Resources Management*, vol. 25, pp. 1465–1487, 2011.
- [14] K. Yang, J. Zheng, M. Yang, R. Zhou, and G. Liu, "Adaptive genetic algorithm for daily optimal operation of cascade reservoirs and its improvement strategy," *Water Resources Management*, vol. 27, no. 12, pp. 4209–4235, 2013.
- [15] X. Meng, J. Chang, X. Wang, and Y. Wang, "Multi-objective hydropower station operation using an improved cuckoo search algorithm," *Energy*, vol. 168, pp. 425–439, 2019.
- [16] K. V. SeethaRam, "Three level rule curve for optimum operation of a multipurpose reservoir using genetic algorithms," *Water Resources Management*, vol. 35, no. 1, pp. 353–368, 2021.
- [17] W. Yuan, M. Liu, M. Liu, F. Wan, and F. Wang, "The application of improved cuckoo search in cascade reservoir power generation optimized operation," *Revista Internacional de Contaminación Ambiental*, vol. 35, no. 1, pp. 123–131, 2019.
- [18] D. Rani and M. M. Moreira, "Simulation-optimization modeling: a survey and potential application in reservoir systems operation," *Water Resources Management*, vol. 24, no. 6, pp. 1107–1138, 2010.
- [19] U. S. Army, "Corps of engineers(USACE)," *Hydro*, vol. 6, 1967.
- [20] X. Yang, S. Deb, and A. C. B. Behaviour, "Cuckoo search via Lévy flights," in *Proceedings of the 2009 World Congress on Nature & Biologically Inspired Computing (NaBIC)*, pp. 210–214, Coimbatore, India, December 2009.
- [21] X. Yang, *Nature-Inspired Metaheuristic Algorithms*, Luniver Press, Bristol, UK, Second Edi edition, 2010.
- [22] B. H. Abed-alguni, "Island-based cuckoo search with highly disruptive polynomial mutation," *International Journal of Artificial Intelligence*, vol. 17, pp. 57–82, 2019.
- [23] B. H. Abed-alguni, "Action-selection method for reinforcement learning based on cuckoo search algorithm," *Arabian Journal for Science and Engineering*, vol. 43, no. 12, pp. 6771–6785, 2018.
- [24] B. H. Abed-Alguni and D. J. Paul, "Hybridizing the cuckoo search algorithm with different mutation operators for numerical optimization problems," *Journal of Intelligent Systems*, vol. 29, no. 1, pp. 1043–1062, 2018.
- [25] B. H. Abed-alguni, N. A. Alawad, M. Barhoush, and R. Hammad, "Exploratory cuckoo search for solving single-objective optimization problems," *Soft Computing*, vol. 25, no. 15, pp. 10167–10180, 2021.
- [26] N. A. Alawad and B. H. Abed-alguni, "Discrete island-based cuckoo search with highly disruptive polynomial mutation and opposition-based learning strategy for scheduling of workflow applications in cloud environments," *Arabian Journal for Science and Engineering*, vol. 46, no. 4, pp. 3213–3233, 2021.
- [27] R. Salgotra, U. Singh, and S. Saha, "New cuckoo search algorithms with enhanced exploration and exploitation properties," *Expert Systems with Applications*, vol. 95, pp. 384–420, 2018.
- [28] R. Salgotra, U. Singh, S. Saha, and A. H. Gandomi, "Self adaptive cuckoo search: analysis and experimentation," *Swarm and Evolutionary Computation*, vol. 60, Article ID 100751, 2021.
- [29] S. Walton, O. Hassan, K. Morgan, and M. R. Brown, "Modified cuckoo search: a new gradient free optimisation algorithm," *Chaos, Solitons & Fractals*, vol. 44, no. 9, pp. 710–718, 2011.
- [30] X. S. Yang and S. Deb, "Engineering optimisation by cuckoo search," *International Journal of Mathematical Modelling and Numerical Optimisation*, vol. 1, no. 4, pp. 330–343, 2010.
- [31] H. Karahan, G. Gurarslan, and Z. W. Geem, "A new nonlinear Muskingum flood routing model incorporating lateral flow," *Engineering Optimization*, vol. 47, no. 6, pp. 737–749, 2015.

Research Article

Machine Learning-Based Model in Predicting the Plate-End Debonding of FRP-Strengthened RC Beams in Flexure

Tianyu Hu  and Guibing Li 

School of Management Science and Engineering, Shandong Technology and Business University, Yantai, Shandong 264005, China

Correspondence should be addressed to Tianyu Hu; 1459430123@qq.com

Received 22 November 2021; Revised 8 February 2022; Accepted 2 March 2022; Published 24 March 2022

Academic Editor: AFAQ AHMAD

Copyright © 2022 Tianyu Hu and Guibing Li. This is an open access article distributed under the Creative Commons Attribution License, which permits unrestricted use, distribution, and reproduction in any medium, provided the original work is properly cited.

Reinforced concrete (RC) beams strengthened with fiber reinforced polymers (FRPs) are structurally complex and prone to plate-end (PE) debonding. In this study, considering the extremely complicated nonlinear relationship between the PE debonding and the parameters, machine learning algorithms, namely, linear regression, ridge regression, decision tree, random forest, and neural network improved by sparrow search algorithm, are established to predict the PE debonding of RC beams strengthened with FRP. The results of reliability evaluation and parameter analysis reveal that ACI, CNR, fib-1, fib-2, and TR55-2 are a little conservative; AS and TR55-1 have the problem of overestimating the shear force; the accuracy and robustness of the SSA-BP model developed in this paper are good; the stirrup reinforcement has the greatest effect on PE debonding; and each parameter shows a complex nonlinear relationship with the shear force when PE debonding occurs.

1. Introduction

The lightweight, high strength, and high corrosion resistance of fiber reinforced polymers (FRPs) make it widely used in the repair and rehabilitation of existing concrete structures [1]. Nevertheless, a large number of experimental studies have demonstrated that external FRP improves the load carrying capacity of RC beams, but due to the linear elasticity characteristics of the material itself, debonding failure often occurs after strengthening, which greatly limits its use in practical applications [2–8]. There are two main types of debonding failure in FRP-strengthened RC beams in flexure: plate-end (PE) debonding and intermediate crack (IC) debonding. For beams with small shear span, since the bending moment is minor at this time, the beam is mainly subjected to shear force and PE debonding is very likely to occur. Concrete cover separation and plate-end interfacial debonding are the two modes of PE debonding. Generally, plate-end interfacial debonding occurs merely when the width of the FRP sheet is much smaller than the width of the strengthened beam. Therefore, concrete cover separation is the more common mode of PE debonding. When the

terminal of FRP is close to the support, the concrete cover separation is mainly caused by the shear crack at the end of FRP. As the load increases, the shear cracks develop to cause vertical and horizontal displacement in the concrete beam and thus generate interfacial shear stress and normal stresses. With the increase in stress, the concrete cover will separate when the crack reaches the horizontal plane of the tensile reinforcement [9, 10]. When the terminal of FRP is far away from the support, the inclined cracks are generated in the shear area, and when the inclined cracks reach the level of the tensile reinforcement, the cracks spread in the horizontal direction and lead to the splitting of the concrete cover [11, 12]. In order to solve the problem of limiting the use of FRP due to PE debonding, end anchoring is usually used to prevent it. And, in order to better design the end-anchoring system, it is necessary to first determine the shear force when PE debonding occurs.

Researchers and codes have developed different computational models for PE debonding of FRP-strengthened RC beam based on the shear force of the concrete beam and the debonding strain of FRP. Most of these models are based on shear strength of the beams or based on fracture

mechanics. Oehlers developed a strength model based on the shear force and bending moment acting at the plate end in 1992 [9]. Jansze proposed a plate-end debonding strength model, which was originally developed for steel-plated beams in 1997. The proposed model considered the occurrence of PE debonding failure at the onset of shear cracking in RC beams [13]. Ahmed and van Germert modified the model of Jansze considering the differences between FRP and steel properties and the effect of shear reinforcement in 1999 [14]. Smith and Teng proposed a model that is based on the concrete shear strength only in 2002 [15]. A theoretical model based on truss analogy was proposed by Colotti and others in 2004 to predict the failure mode and ultimate capacity of FRP-strengthened RC beams [16]. Yao and Teng and Teng and Yao conducted experimental and analytical investigations on FRP-strengthened beams in 2007, thus modifying the moment shear interaction expression proposed by Oehlers [17, 18]. The fib Bulletin 14 (fib, 2001) presented the model proposed by Blaschko which is based on the concrete shear strength of the beam. The Technical Report 55 (TR55) of the Concrete Society (2012), ACI 440.2R (ACI, 2017), and Australian Standard AS 5100.8 (Standards Australia, 2017b) recommended an upper limit for the acting shear force at the plate-end region to avoid PE debonding. El-sayed and others proposed a model which is based on the concrete shear strength of the beams considering main parameters known to affect the opening of the shear cracks and consequently affect PE debonding in 2021 [19]. Nevertheless, due to the complex structure of FRP-strengthened RC beams and the nonlinear relationship between PE debonding and parameters, most of the above models suffer from low computational accuracy and poor robustness. Therefore, it is especially important to establish a more precise nonlinear mapping relationship between PE debonding and each parameter.

Given the large number of parameters that affect the PE debonding, this study uses several machine learning algorithms, namely, linear regression, ridge regression, decision tree, random forest, and neural network optimized by the sparrow search algorithm to develop several intelligent prediction models for PE debonding of FRP-strengthened RC beams and then select the best prediction model from it. Based on the best model obtained, the robustness of the model and the codes are assessed and the parameters affecting PE debonding are analyzed too.

2. Parameter Identification and Data Collection

2.1. Parameter Identification. Based on relevant codes and experimental studies [13–24], concrete strength (f_c), location of FRP cut-off point (L_{ua}/a), tensile strength of tensile reinforcement (f_y), tensile strength of stirrup reinforcement (f_{yv}), stirrup reinforcement ratio (ρ_{sv}), tensile strength of FRP (f_{fu}), FRP stiffness (E_{ftf}), and the ratio of FRP width to the width of the strengthened beam (b_f/b) are selected as input parameters for predicting PE debonding in this study. For the convenience of establishing the model, the above parameters are denoted as X_1 , X_2 , X_3 , X_4 , X_5 , X_6 , X_7 , and

X_8 , respectively, and the shear force is taken as the output of models and denoted as V .

2.2. Criteria for Collection Analysis of Parameters

- (1) PE debonding occurred in all strengthened beams [6–8, 17, 25–52].
- (2) The FRP sheets are not prestressed and the end of the strengthened beams is not anchored.
- (3) The geometric and material properties of the strengthened beams, FRP, and reinforcement are clear.
- (4) The range of parameter variation is large and basically covers the case of general beams. The range of the variation of each parameter is shown in Figure 1.

From Figure 1, we can get that the maximum interval of f_c is 30 MPa–40 MPa, accounting for 49%, and merely 6% of the f_c is more than 60 MPa, indicating that the f_c is mostly at plain level; the maximum interval of the L_{ua}/a is 0.8–1.0, accounting for 64%, while other intervals account for less; the design value of f_{yv} is mainly distributed from 250 MPa to 510 MPa, accounting for 69%, and only 6% of the strength is over 570 MPa, indicating that the f_{yv} is mostly at ordinary level, and high-strength reinforcement accounts for a relatively small percentage; the maximum interval of ρ_{sv} is 0.6–0.9, accounting for 38%, and the distribution of each range is more uniform; the maximum interval of f_{fu} is 3000 MPa–4000 MPa, accounting for 54%, and the tensile strength above 4000 MPa accounts for only 9%; the maximum interval of the f_y is 350 MPa–510 MPa, accounting for 51%, but the percentage of tensile strength over 510 MPa is 49%, indicating that a larger portion of tensile reinforcement in the collected specimens is high-strength reinforcement; the maximum interval of E_{ftf} is from 75 MPa to 125 MPa, accounting for 40%, and only 8% above 225 MPa; the maximum interval of the b_f/b is > 0.9 , accounting for 37%, and the distribution of each interval is relatively uniform. In addition, some of the parameters differed significantly across intervals, which would result in machine learning models having smaller prediction errors in intervals with more data than in intervals with less data.

3. Machine Learning Models

This part uses several machine learning algorithms, namely, linear regression, ridge regression, decision tree, random forest, and neural network optimized by sparrow search algorithm to develop several intelligent prediction models for PE debonding of FRP-strengthened RC beams. The data are used from [6–8, 17, 25–52], where the percentages of training set, validation set, and testing set are 60%, 20%, and 20%, respectively.

To further analyze the prediction accuracy and generalization ability of each model, the average absolute error (MAE) and goodness-of-fit (R^2) of the training set, the validation set, and the testing set of the models are calculated and given in Figure 2.

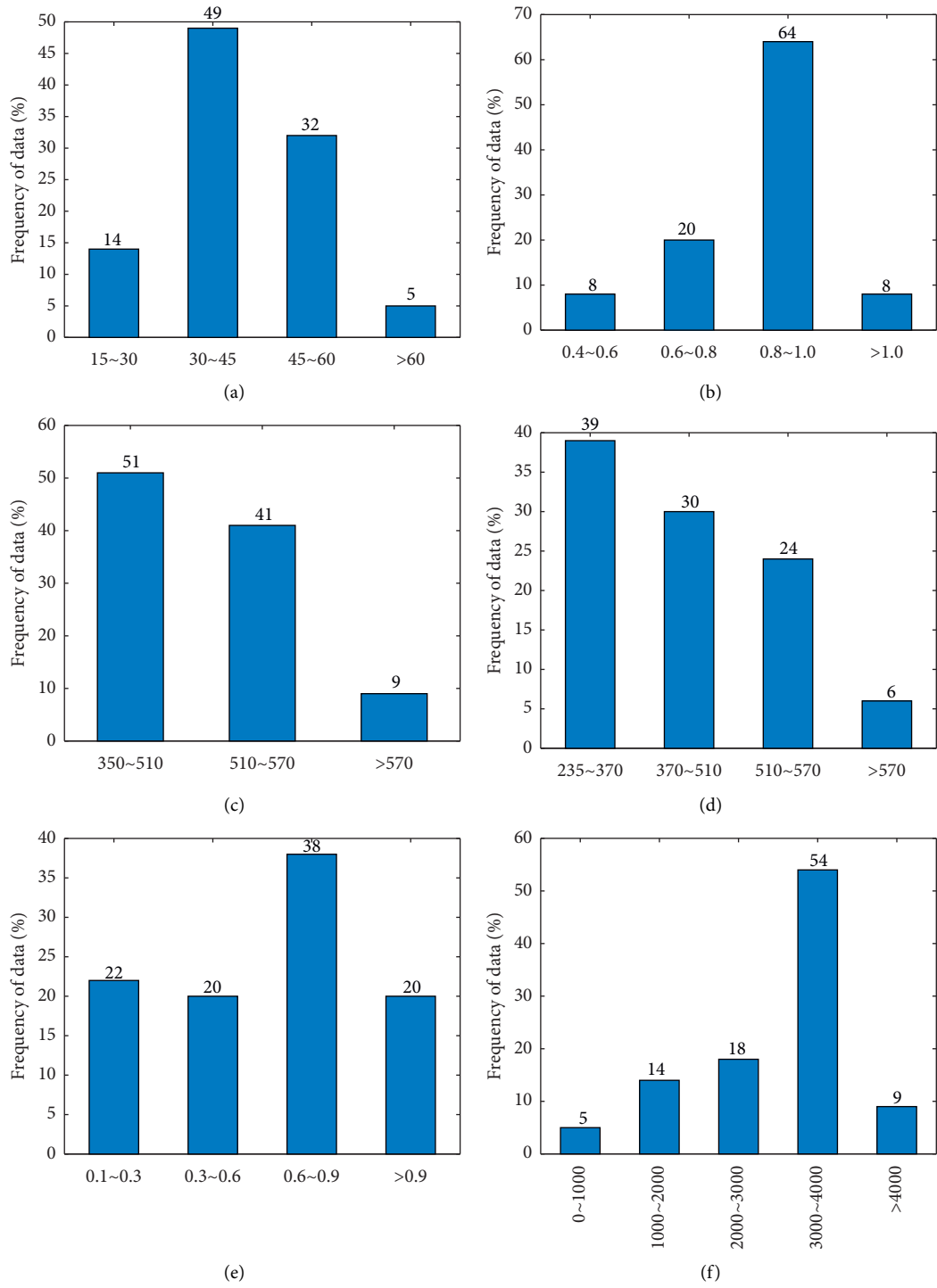


FIGURE 1: Continued.

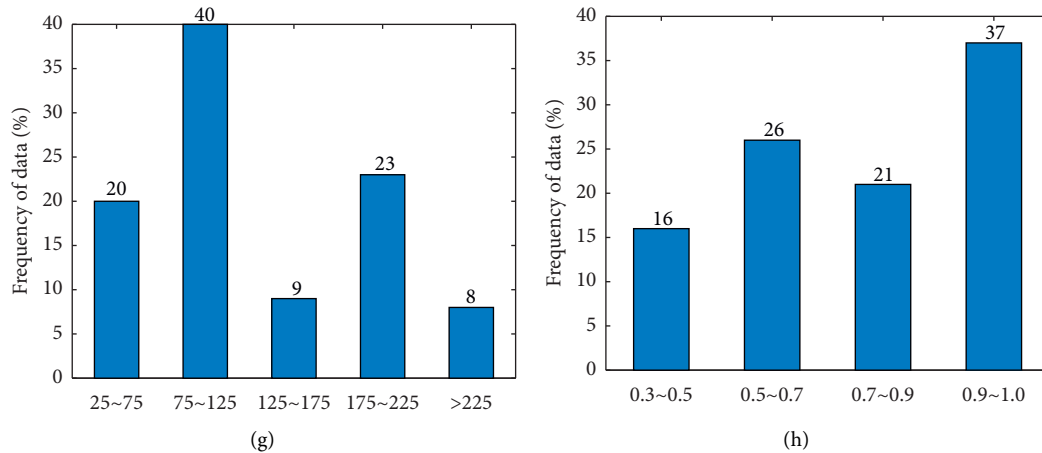


FIGURE 1: Range of the parameters. (a) f_c /MPa. (b) L_{ua}/a . (c) f_y /MPa. (d) f_{yv} /MPa. (e) ρ_{sv} . (f) f_{fu} /MPa. (g) E_{ftf} /GPa.mm. (h) b_f/b .

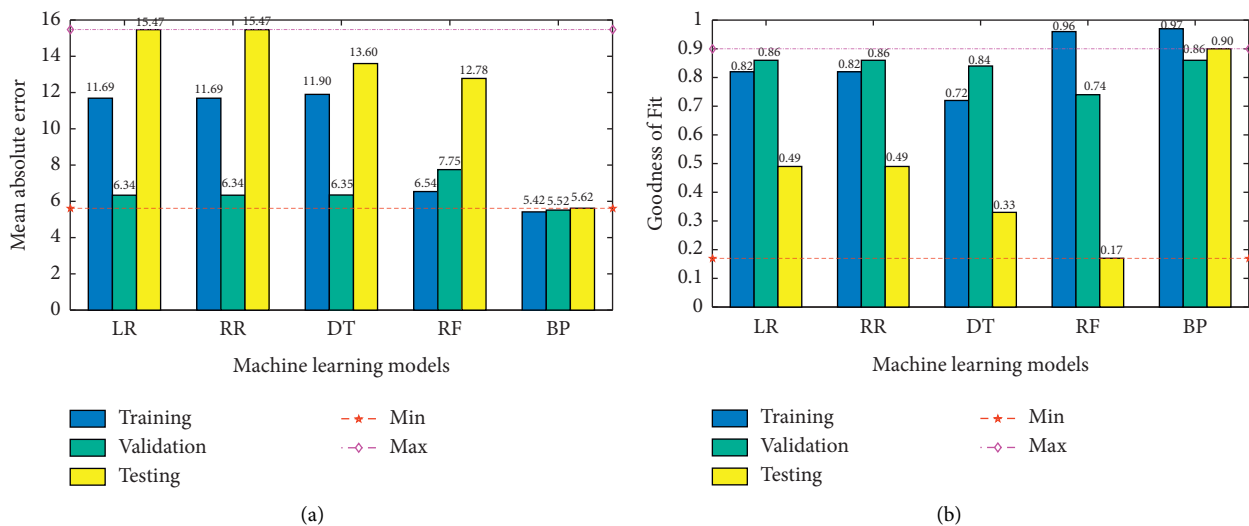


FIGURE 2: Performance of the models. (a) MAE. (b) R2.

From Figure 2, the MAE and the R2 of linear regression, ridge regression, decision tree, and random forest differ greatly in the training set, the validation set, and the testing set, indicating that the generalization ability of these models is poor, while the MAE of BP neural network is 5.42, 5.52, and 5.62 in the training set, the validation set, and the testing set, respectively, which is not only the smallest but also the most average among all machine learning algorithms. Also, the R2 of the training set, the validation set, and the testing set of the BP neural network is 0.97, 0.86, and 0.90, respectively, which is the highest among all machine learning models. In summary, the BP neural network model not only has the highest prediction accuracy but also has excellent generalization ability.

4. Reliability Evaluation of the Code

To further illustrate the precision and robustness of the SSA-BP, this section compares it with several international codes

[13–17]. The codes and their expressions are shown in Table 1, and the comparison between the calculated and actual values of SSA-BP and the codes is shown in Figure 3.

It can be visualized from Figure 3 that the calculated values of SSA-BP are basically within 15% above and below the true value and are significantly superior to the calculated values given by each code. The calculated values of ACI and fib-1 are basically below 15% of the true value, indicating that these two codes are too conservative; while AS and TR55-1 have a larger portion of calculated values above 15% of the true value, which takes the risk of overestimating the shear strength in the event of PE debonding. The quantitative evaluation of the performance of BP and each code is shown in Table 2.

As can be seen from Table 2, the coefficient of variation of the neural network is merely 20.3%, which is better than the calculated values of each code. The coefficients of variation of CNR and fib-1 and TR55-2 are smaller, but their conservative estimates account for 79%, 80%, and 95%,

TABLE 1: Codes and their expressions.

Codes	Calculation formula
ACI440.2 R	$V_{db,end} < 0.67V_c$
AS 5100.8	$V_{db,end} < 0.67V_u$
Fib-1	$V_{db,end} < 0.15f_{ck}^{1/3}bd$
Fib-2	$\varepsilon_{fd} = \begin{cases} \alpha_1 c_1 k_c k_b \sqrt{f_{ct}/n_{frp} E_{frp} t_{frp}} & l_b \geq l_{b,max} \\ \alpha_1 c_1 k_c k_b \sqrt{f_{ct}/n_{frp} E_{frp} t_{frp}} \cdot (l_b/l_{b,max}) (2 - l_b/l_{b,max}) & l_b < l_{b,max} \end{cases}$ $l_{b,max} = \sqrt{(n_{frp} E_{frp} t_{frp}) / (c_2 f_{ct})}$ $k_b = 1.06 \sqrt{(2b_{frp}/b) / (1 + b_{frp}/400)} \geq 1$ $b_{frp}/b \geq 0.33$
TR55-1	$V_{db,end} < 0.67V_{rd}$
TR55-2	$\varepsilon_{fd} = \begin{cases} 0.5k_b \sqrt{f_{ct}/n_{frp} E_{frp} t_{frp}} & l_b \geq l_{b,max} \\ 0.5k_b \sqrt{f_{ct}/n_{frp} E_{frp} t_{frp}} \cdot (l_b/l_{b,max}) (2 - l_b/l_{b,max}) & l_b < l_{b,max} \end{cases}$ $l_{b,max} = 0.7 \sqrt{n_{frp} E_{frp} t_{frp} / f_{ct}}$
CNR	$\varepsilon_{fd} = \begin{cases} 1/\gamma_{f,d} \sqrt{2\Gamma_{Fd}/n_{frp} E_{frp} t_{frp}} & l_b \geq l_{b,max} \\ 1/\gamma_{f,d} \sqrt{2\Gamma_{Fd}/n_{frp} E_{frp} t_{frp}} \cdot (l_b/l_{b,max}) & l_b < l_{b,max} \end{cases}$ $\Gamma_{Fd} = k_b k_G \sqrt{f'_c f_{ct}}$ $k_b = \begin{cases} \sqrt{(2 - b_{frp}/b) / (1 + b_{frp}/b)} \geq 1 & b_{frp}/b \geq 0.25 \\ 1.18 & b_{frp}/b < 0.25 \end{cases}$ $l_{b,max} = \min \left\{ (1/\gamma_{R,d} f_{bd}) \sqrt{\pi^2 E_{frp} t_{frp} \Gamma_{Fd} / 2}, 200\text{mm} \right\}$ $f_{bd} = 2\Gamma_{Fd} / S_u$

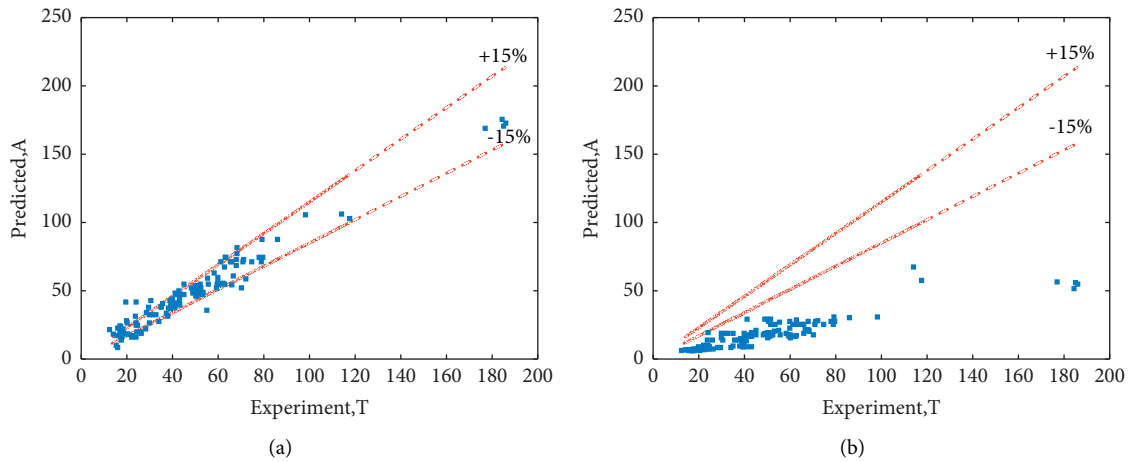


FIGURE 3: Continued.

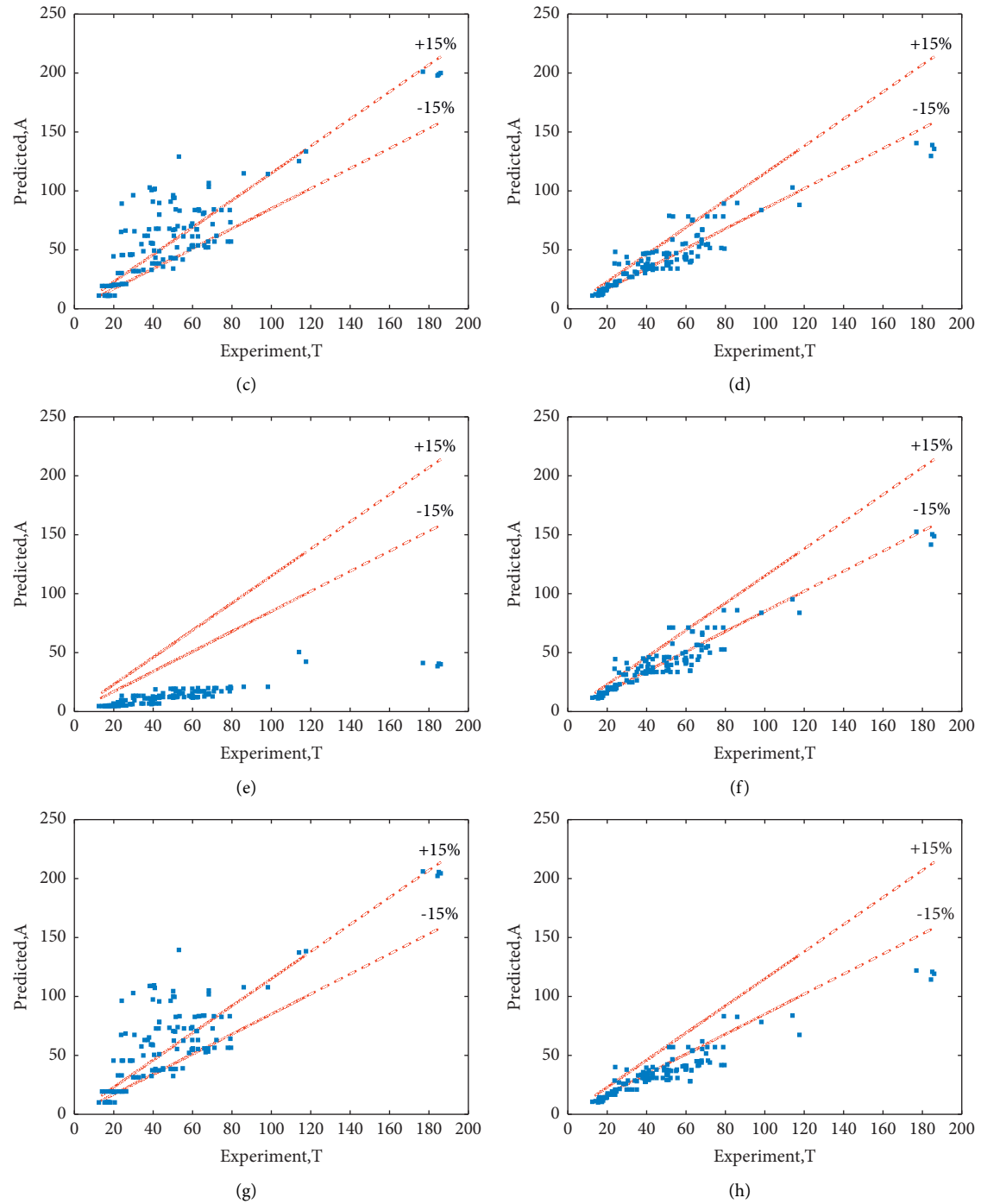


FIGURE 3: Comparison of the calculated values and real values. (a) SSA-BP. (b) ACI. (c) AS. (d) CNR. (e) fib-1. (f) fib-2. (g) TR55-1. (h) TR55-2.

TABLE 2: Performance of the models.

Models	Evaluation indicators		
	Coefficient of variation (%)	Conservative (%)	Nonconservative (%)
SSA-BP	20.3	52	48
ACI	26.6	100	0
AS	44.5	38	63
CNR	23.4	79	21
Fib-1	25.1	100	0
Fib-2	21.2	80	20
TR55-1	48.3	39	61
TR55-2	20.5	95	5

TABLE 3: Weights and biases between connection layers.

	Hidden layer							Output
	H(1:1)	H(1:2)	H(1:3)	H(1:4)	H(1:5)	H(1:6)	H(1:7)	V
Bias	.743	.529	2.692	.061	-1.476	.038	.776	
X1	.022	1.514	.906	.179	.279	.443	-.473	
X2	-.095	-.656	-.243	.438	.662	-.188	-1.296	
X3	-.348	.946	-.998	-.395	.900	-.240	.362	
X4	-.037	.765	-.727	.350	-.142	-.096	-1.060	
X5	-.006	.782	1.731	.816	-.139	.281	-.277	
X6	-.681	-.587	-.845	-.428	-.135	-.695	.584	
X7	.272	1.773	-.444	.053	.583	-.030	1.619	
X8	1.225	.077	-.300	.169	.669	.940	.993	
Bias								1.115
H(1:1)								-1.425
H(1:2)								.381
H(1:3)								-2.224
H(1:4)								.511
H(1:5)								-1.377
H(1:6)								1.147
H(1:7)								.736

respectively, which are a little conservative compared with 50% for SSA-BP.

5. Parametric Study

5.1. Analysis of the Importance of Parameters. In Matlab software, by inputting the 'net.iw', the 'net.lw', and the 'net.b', the weights and biases of the neural network can be obtained. See Table 3 for details.

After getting the weights and biases between layers, we can get the transfer functions through the code 'TransferFcn' in Matlab. The transfer functions are shown in equation (1) and (2).

$$y_i = f \cdot \left(\sum_i w_{ij}x_i + \phi_j \right) = \frac{2}{1 + e^{-2(\sum_i w_{ij}x_i + \phi_j)}} - 1. \quad (1)$$

$$y_i = f \cdot \left(\sum_i w_{ij}x_i + \phi_j \right) = \sum_i w_{ij}x_i + \phi_j. \quad (2)$$

The weights and biases obtained in Table 1 were substituted into (1) and (2) and subsequently normalize the calculated value obtained to get the importance of each parameter on PE debonding, as shown in Figure 4.

As can be seen from Figure 4, the importance of each parameter is $X5 > X7 > X2 > X1 > X8 > X4 > X3 > X6$ in order; that is, the ρ_{sv} has the greatest effect on the PE debonding, and the ffu, fy, and fyv have less effect on it.

5.2. Sensitivity Analysis of Parameters. Based on the effects of each parameter on PE debonding obtained in section 5.1, the ffu, which has the least effect on PE debonding, is selected as the grouping variable for the sensitivity analysis of each parameter, and four grades of 200, 1200, 2200, and 3200 are taken based on its distribution in section 2.1. When studying the sensitivity of a single variable to PE debonding, the other variables are averaged based on the statistics in section 1.2.

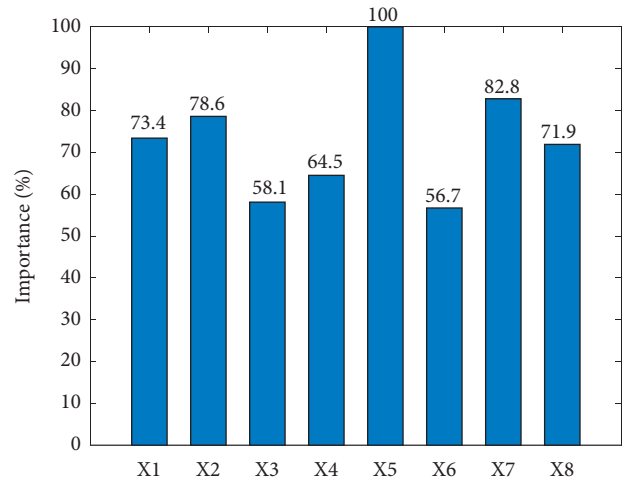


FIGURE 4: Importance of each parameter.

The sensitivity of each parameter to the shear strength is shown in Figure 5.

From Figure 5, we can get that (a) when the ffu is in the first two grades, the shear strength tends to increase and subsequently decrease with the increase in fc. When it is in the last two grades, the shear strength tends to increase, subsequently decrease, and then increase as the fc increases; (b) for the Lua/a, the shear strength increases and subsequently decreases with the increase in the Lua/a, regardless of the grade of ffu; (c) regarding the ρ_{sv} , no matter which grade the ffu is at, as the ρ_{sv} increases, the shear strength first decreases, then increases, and then decreases; (d) for the fyv, there are three patterns when the ffu is in different grades, namely, when the ffu is in two grades of 200 and 1200, the shear strength is inversely proportional to the increase in fyv; when the ffu is in grade 2200, the shear strength tends to decrease and subsequently increase with the increase in fyv; when the ffu is in grade 3200, the shear strength is proportional to the fyv; (e) for Eftf and bf/b, as they increase, the

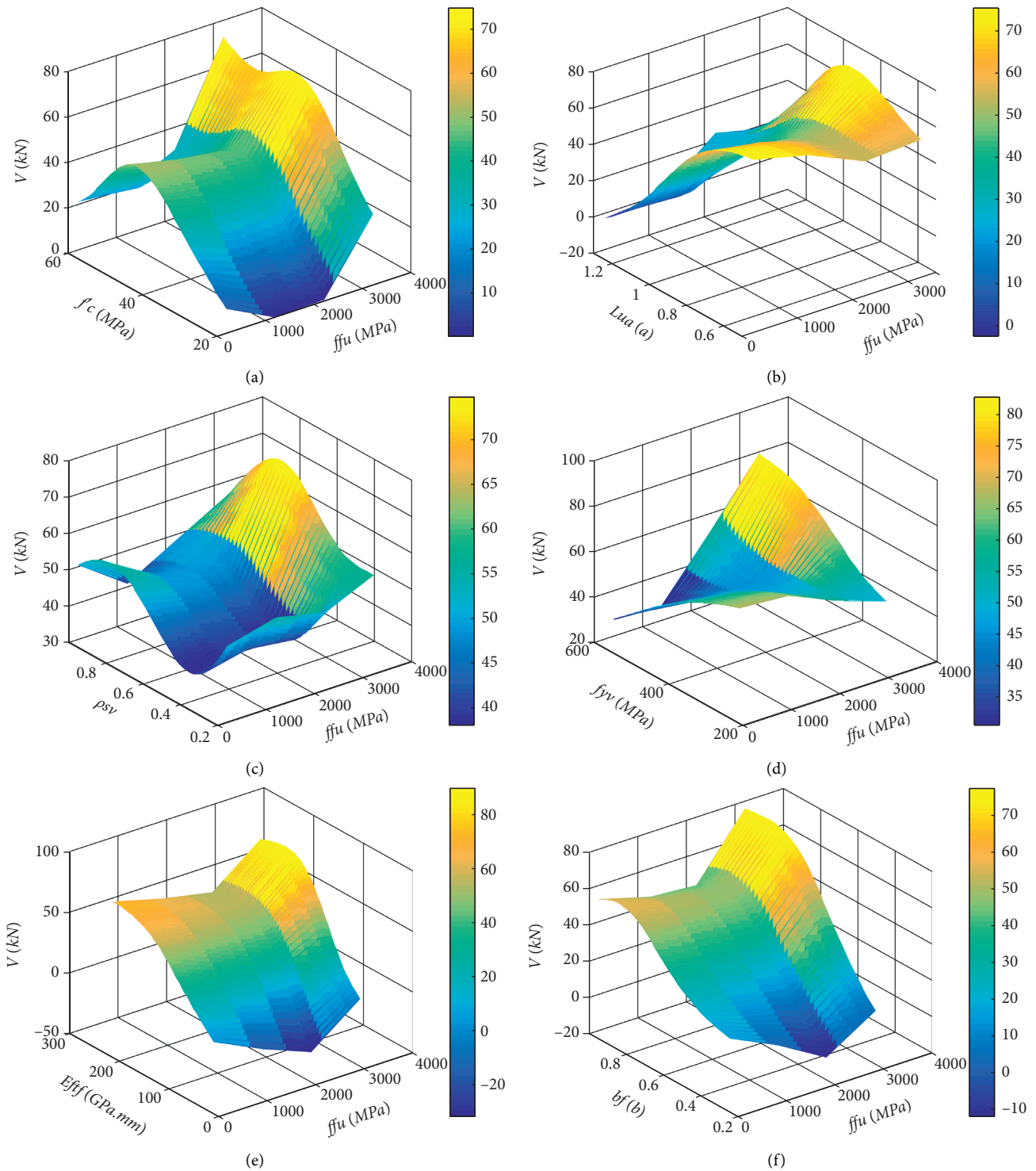


FIGURE 5: Sensitivity of each parameter.

shear strength basically increases and subsequently decreases, but when the E_{ftf} and bf/b are larger, the shear strength decreases not significantly.

In summary, there is a complex nonlinear relationship between the shear force at PE debonding and each parameter. In the future, the effect of different parameters on PE debonding under different conditions

needs to be considered when performing the end anchorage system.

6. Conclusion

In this study, a machine learning approach was used to synthesize the effects of various parameters on the PE

debonding of FRP-strengthened RC beams in flexure, and the resulting models were evaluated against several codes. The following conclusions can be drawn:

- (1) ACI, CNR, fib-1, fib-2, and TR55-2 are too conservative, which have 100%, 80%, 100%, 79%, and 95% values below the experimental values, respectively. AS and TR55-1 had 63% and 61% values above the experimental values, respectively, potentially overestimating the shear force in the case of PE debonding. The coefficient of variation, conservative, and nonconservative values of SSA-BP is 20.3%, 52%, and 48%, respectively, and its robustness and prediction accuracy are superior to the above codes.
- (2) ρ_{sv} , Eftf, and Lua/a have more influence on the shear force at PE debonding, while f_y and f_{fu} have less influence on the shear force. Moreover, there are complex nonlinear relationships between each parameters and the shear force, and the effect of different parameters on PE debonding under different conditions needs to be considered when performing the system of end anchorage in the future.
- (3) There are two problems with the model built in this paper: on the one hand, the uneven distribution of parameters in the dataset on which the model is built leads to the prediction accuracy of the model to be improved, and on the other hand, the model is complicated by considering too many parameters. In the future, more data need to be collected and the parameters in the model need to be streamlined.

Notation

f_c :	Compressive strength of concrete
ρ_{sv} :	Stirrup reinforcement ratio
f_y :	Tensile strength of tensile reinforcement
f_{yv} :	Tensile strength of stirrup reinforcement
Eftf:	FRP stiffness
bf/b:	The ratio of sheet width to beam width
Lua/a :	The ratio of anchorage length to shear span
f_{fu} :	Tensile strength of FRP
fct:	Tensile strength of concrete
Vdb,	Factored shear force at the FRP plate end
end:	
Vc:	The shear capacity of concrete alone calculated according to ACI 318 (ACI Committee 318, 2014)
Vu:	The nominal shear strength of the concrete section including concrete and steel stirrups, calculated in accordance with AS 5100.5 (2017)
fck:	The characteristic strength of concrete calculated according to BS EN 1992-1-1 (2004)
Vrd:	The shear strength of the beam section calculated in accordance with Section 6.2.3 of BS EN 1992-1-1 (2004)
lb, max:	The maximum anchorage length
Ifd:	The design value of the specific fracture energy of the FRP-concrete interface.

Data Availability

The data for the study were collected from articles by different researchers and have been marked in the article.

Conflicts of Interest

The authors declare that there are no conflicts of interest.

References

- [1] R. Kotynia, E. Oller, A. Marí, and M. Kaszubska, "Efficiency of shear strengthening of RC beams with externally bonded FRP materials - state-of-the-art in the experimental tests," *Composite Structures*, vol. 267, Article ID 113891, 2021.
- [2] R. Bakay, E. Y. Sayed-Ahmed, and N. G. Shrive, "Interfacial debonding failure for reinforced concrete beams strengthened with carbon-fibre-reinforced polymer strips," *Canadian Journal of Civil Engineering*, vol. 36, no. 1, pp. 103–121, 2009.
- [3] F. Ceroni, M. Pecce, S. Matthys, and L. Taerwe, "Debonding strength and anchorage devices for reinforced concrete elements strengthened with FRP sheets," *Composites Part B: Engineering*, vol. 39, no. 3, pp. 429–441, 2008.
- [4] J. Pan, C. K. Y. Leung, and M. Luo, "Effect of multiple secondary cracks on FRP debonding from the substrate of reinforced concrete beams," *Construction and Building Materials*, vol. 24, no. 12, pp. 2507–2516, 2010.
- [5] M. A. Al-Saawani, A. K. El-Sayed, and A. I. Al-Negheimish, "Assessment of plate-end debonding design provisions for RC beams strengthened with FRP," *Latin American Journal of Solids and Structures*, vol. 17, 2020.
- [6] M. A. Al-Saawani, A. K. El-Sayed, and A. I. Al-Negheimish, "Effect of basic design parameters on IC debonding of CFRP-strengthened shallow RC beams," *Journal of Reinforced Plastics and Composites*, vol. 34, no. 18, pp. 1526–1539, 2015.
- [7] P. J. Fanning and O. Kelly, "Ultimate response of RC beams strengthened with CFRP plates," *Journal of Composites for Construction*, vol. 5, no. 2, pp. 122–127, 2001.
- [8] D. M. Nguyen, T. K. Chan, and H. K. Cheong, "Brittle failure and bond development length of CFRP-concrete beams," *Journal of Composites for Construction*, vol. 5, no. 1, pp. 12–17, 2001.
- [9] D. J. Oehlers, "Reinforced concrete beams with plates glued to their soffits," *Journal of Structural Engineering*, vol. 118, no. 8, pp. 2023–2038, 1992.
- [10] S. S. Zhang and J. G. Teng, "End cover separation in RC beams strengthened in flexure with bonded FRP reinforcement: simplified finite element approach," *Materials and Structures*, vol. 49, no. 6, pp. 2223–2236, 2016.
- [11] M. Achintha and C. J. Burgoyne, "Fracture mechanics of plate debonding: validation against experiment," *Construction and Building Materials*, vol. 25, no. 6, pp. 2961–2971, 2011.
- [12] P. M. M. Achintha and C. J. Burgoyne, "Fracture mechanics of plate debonding," *Journal of Composites for Construction*, vol. 12, no. 4, pp. 396–404, 2008.
- [13] W. Jansze, *Strengthening of RC members in bending by externally bonded steel plates*, PhD thesis, Delft University of Technology, South Holland, Netherlands, 1997.
- [14] O. Ahmed and D. Van Gemert, "Effect of longitudinal carbon fiber reinforced plastic laminates on shear capacity of reinforced concrete beams," in *Proceedings of the 4th International Symposium on Fiber Reinforced Polymer Reinforcement for Reinforced Concrete Structures*, Maryland, MD, USA, 1999.

- [15] S. T. Smith and J. G. Teng, "FRP-strengthened RC beams. II: assessment of debonding strength models," *Engineering Structures*, vol. 24, no. 4, pp. 397–417, 2002.
- [16] V. Colotti, G. Spadea, and R. N. Swamy, "Structural model to predict the failure behavior of plated reinforced concrete beams," *Journal of Composites for Construction*, vol. 8, pp. 104–122, 2004.
- [17] J. Yao and J. G. Teng, "Plate end debonding in FRP-plated RC beams-I: Experiments," *Engineering Structures*, vol. 29, no. 10, pp. 2457–2471, 2007.
- [18] J. G. Teng and J. Yao, "Plate end debonding in FRP-plated RC beams-II: strength model," *Engineering Structures*, vol. 29, no. 10, pp. 2472–2486, 2007.
- [19] A. K. El-Sayed, M. A. Al-Saawani, and A. I. Al-Negheimish, "Empirical shear based model for predicting plate end debonding in frp strengthened rc beams," *Journal of Civil Engineering and Management*, vol. 27, no. 2, pp. 117–138, 2021.
- [20] International Federation for Structural Concrete (fib), Externally bonded FRP reinforcement for RC structures. Technical Report, Task Group 9.3, Bulletin No. 14, Lausanne, Switzerland, 2001.
- [21] Concrete Society, "Design guidance for strengthening concrete structures using fibre composite materials," Technical Report No. 55, Crowthorne, London, UK, 2012.
- [22] American Concrete Institute, "Guide for the design and construction of externally bonded FRP systems for strengthening concrete structures," Farmington Hills, Michigan, MI, USA, ACI 440.2R, 2017.
- [23] Standards Australia, "Bridge design, Part 8: rehabilitation and strengthening of existing bridges," SA1 Global Limited, Australia, AS 5100.8, 2017.
- [24] National Research Council, "Guide for the design and construction of externally bonded FRP systems for strengthening existing structures," CNR-DT 200 R1, Rome, Italy, 2013.
- [25] P. A. Ritchie, D. A. Thomas, L. W. Lu, and G. M. Connelly, "External reinforcement of concrete beams using fibre reinforced plastics," *ACI Structural Journal*, vol. 88, no. 4, pp. 490–500, 1991.
- [26] R. J. Quantrill, L. C. Hollaway, and A. M. Thorne, "Experimental and analytical investigation of FRP strengthened beam response: Part I," *Magazine of Concrete Research*, vol. 48, no. 177, pp. 331–342, 1996.
- [27] M. Arduini, A. Di Tommaso, and A. Nanni, "Brittle failure in FRP plate and sheet bonded beams," *ACI Structural Journal*, vol. 94, no. 4, pp. 363–370, 1997.
- [28] H. N. Garden, L. C. Hollaway, and A. M. Thorne, "A preliminary evaluation of carbon fibre reinforced polymer plates for strengthening reinforced concrete members," *Proceedings of the Institution of Civil Engineers - Structures and Buildings*, vol. 122, no. 2, pp. 127–142, 1997.
- [29] H. N. Garden, R. J. Quantrill, L. C. Hollaway, A. M. Thorne, and G. A. R. Parke, "An experimental study of the anchorage length of carbon fibre composite plates used to strengthen reinforced concrete beams," *Construction and Building Materials*, vol. 12, no. 4, pp. 203–219, 1998.
- [30] A. J. Beber, A. C. Filho, and J. L. Campagnolo, "Flexural strengthening of R/C beams with CFRP sheets," in *Proceedings of the 8th International Conference on Advanced Composites for Concrete Repair*, London, UK, 1999.
- [31] E. David, C. Djelal, E. Ragneau, and F. B. Bodin, "Use of FRP to strengthen and repair RC beams: experimental study and numerical simulations," in *Proceedings of the 8th International Conference on Advanced Composites for Concrete Repair*, London, UK, 1999.
- [32] K. M. Hau, "Experiments on concrete beams strengthened by bonding fibre reinforced plastic sheets," MSc in Civil Engineering thesis, The Hong Kong Polytechnic University, Hong Kong, China, 1999.
- [33] G. Tumialan, P. Serra, A. Nanni, and A. Belarbi, "Concrete cover delamination in reinforced concrete beams strengthened with carbon fiber reinforced polymer sheets," in *Proceedings of the 4th International Symposium on Fiber Reinforced Polymer Reinforcement for Reinforced Concrete Structures*, pp. 725–735, Maryland, MA, USA, 1999.
- [34] O. A. F. Ahmed, *Strengthening of R. C. beams by means of externally bonded CFRP laminates: improved model for plate-end shear*, PhD Thesis, Department of Civil Engineering, Catholic University of Leuven, Catholic, Belgium, 2000.
- [35] S. Matthys, *Structural behavior and design of concrete beams strengthened with externally bonded FRP reinforcement*, PhD thesis, Ghent University, Ghent, Belgium, 2000.
- [36] B. Gao, W. Leung, C. Cheung, J. K. Kim, and C. K. Y. Leung, "Effects of adhesive properties on strengthening of concrete beams with composite strips," in *Proceedings of the International Conference on FRP composites in Civil Engineering*, pp. 423–432, Elsevier, 2001.
- [37] M. Maalej and Y. Bian, "Interfacial shear stress concentration in FRP-strengthened beams," *Composite Structures*, vol. 54, no. 4, pp. 417–426, 2001.
- [38] H. Rahimi and A. Hutchinson, "Concrete beams strengthened with externally bonded FRP plates," *Journal of Composites for Construction*, vol. 5, no. 1, pp. 44–56, 2001.
- [39] S. T. Smith and J. G. Teng, "Shear-bending interaction in debonding failures of FRP-plated RC beams," *Advances in Structural Engineering*, vol. 6, no. 3, pp. 183–199, 2003.
- [40] M. Valcuende, J. Benlloch, and C. J. Parra, "Ductility of reinforced concrete beams strengthened with CFRP strips and fabric," in *Proceedings of the 6th International Symposium on FRP Reinforcement for Concrete Structures*, pp. 337–346, 2003.
- [41] S. F. Breña and B. M. Macri, "Effect of carbon-fiber-reinforced polymer laminate configuration on the behavior of strengthened reinforced concrete beams," *Journal of Composites for Construction*, vol. 8, no. 3, pp. 229–240, 2004.
- [42] B. Gao, J. K. Kim, and C. K. Y. Leung, "Taper ended FRP strips bonded to RC beams: experiments and FEM analysis," in *Proceedings of the 2nd International Conference on FRP in Civil Engineering*, pp. 399–405, 2004.
- [43] B. Gao, J.-K. Kim, and C. K. Y. Leung, "Experimental study on RC beams with FRP strips bonded with rubber modified resins," *Composites Science and Technology*, vol. 64, no. 16, pp. 2557–2564, 2004.
- [44] N. F. Grace and S. B. Singh, "Durability evaluation of carbon fiber-reinforced polymer strengthened concrete beams: experimental study and design," *ACI Structural Journal*, vol. 102, no. 1, pp. 40–48, 2005.
- [45] H. B. Pham and R. Al-Mahaidi, "Prediction models for debonding failure loads of carbon fiber reinforced polymer retrofitted reinforced concrete beams," *Journal of Composites for Construction*, vol. 10, no. 1, pp. 48–59, 2006.
- [46] O. Benjeddou, M. B. Ouezdou, and A. Bedday, "Damaged RC beams repaired by bonding of CFRP laminates," *Construction and Building Materials*, vol. 21, no. 6, pp. 1301–1310, 2007.
- [47] M. R. Esfahani, M. R. Kianoush, and A. R. Tajari, "Flexural behaviour of reinforced concrete beams strengthened by CFRP sheets," *Engineering Structures*, vol. 29, no. 10, pp. 2428–2444, 2007.

- [48] F. Ceroni, "Experimental performances of RC beams strengthened with FRP materials," *Construction and Building Materials*, vol. 24, no. 9, pp. 1547–1559, 2010.
- [49] A. K. Al-Tamimi, R. Hawileh, and J. Abdalla, "Effects of ratio of CFRP plate length to shear span and end anchorage on flexural behavior of SCC RC beams," *Journal of Composites for Construction*, vol. 15, no. 6, pp. 908–919, 2011.
- [50] A. Sadrmomtazi, H. Rasmi Atigh, and J. Sobhan, "Experimental and analytical investigation on bond performance of the interfacial debonding in flexural strengthened RC beams with CFRP sheets at tensile face," *Asian Journal of Civil Engineering (BHRC)*, vol. 15, no. 3, pp. 391–410, 2014.
- [51] A. Hasnat, M. Islam, and A. Amin, "Enhancing the debonding strain limit for CFRP-strengthened RC beams using U-clamps: identification of design parameters," *Journal of Composites for Construction*, vol. 20, no. 1, Article ID 04015039, 2016.
- [52] T. Skuturna and J. Valivonis, "Experimental study on the effect of anchorage systems on RC beams strengthened using FRP," *Composites Part B: Engineering*, vol. 91, pp. 283–290, 2016.

Research Article

An Improved Model to Calculate Pullback Force of Trenchless Horizontal Directional Drilling Pipeline

Xiao-qiang Liang,^{1,2,3} Da Hu ,^{1,2,3} Yong-suo Li ,¹ Xian Yang,⁴ Lei Jiang,⁵
and Yun-yi Zhang ^{1,2,3}

¹Hunan Engineering Research Center of Structural Safety and Disaster Prevention for Urban Underground Infrastructure, Hunan City University, Yiyang 413000, China

²School of Civil Engineering, Hunan City University, Yiyang 413000, China

³Key Laboratory of Metallogenic Prediction of Nonferrous Metals and Geological Environment Monitoring, Ministry of Education, Central South University, Changsha 410083, China

⁴School of Resource, Environment and Safety Engineering, Hunan University of Science and Technology, Xiangtan, Hunan 411201, China

⁵Changsha Metro Group Co., Ltd., Changsha 410007, China

Correspondence should be addressed to Da Hu; huda@hncu.edu.cn

Received 6 August 2021; Revised 23 December 2021; Accepted 3 January 2022; Published 20 January 2022

Academic Editor: Afaq Ahmad

Copyright © 2022 Xiao-qiang Liang et al. This is an open access article distributed under the Creative Commons Attribution License, which permits unrestricted use, distribution, and reproduction in any medium, provided the original work is properly cited.

In the pullback operation of horizontal directional drilling pipeline crossing, the existing calculation and prediction models of pullback force are relatively simple. Each pullback force maze greatly simplifies the wellbore trajectory and fails to make a detailed analysis of the pipeline stress and external resistance when the pipeline is pulled back in each characteristic trajectory area. The factors considered are relatively simple. Therefore, it is necessary to improve the calculation method of pullback force. This paper aims to establish an improved model, enhancing the earth pressure calculation method of unloading arch and winch calculation method, and carries out an example calculation of the improved formula. Therefore, it is necessary to study the pullback process of horizontal directional drilling pipeline. Firstly, this paper analyzes the calculation method of pullback force in horizontal directional drilling; studies the calculation formula and principle of common pullback force through examples; obtains the advantages, disadvantages, and applicable scope of different formulas; and improves the calculation model of pullback force and step resistance. The numerical simulation of the step crossing process is carried out, and the variation law of local stress and strain of the pipeline and relevant conclusions are obtained. The results show that the estimates of the winch calculation method are close to the actual pullback load of the project. The earth pressure calculation method of the unloading arch and the winch calculation method are improved, and a more stable and reliable calculation formula is obtained, which provides more valuable calculation data for the actual project. In the process of pullback, the pipeline will encounter step resistance after passing through the soft and hard staggered stratum, which will suddenly increase the increment of pipeline pullback force and lead to engineering accidents. If the pullback load suddenly increases and then decreases, it may encounter similar pipeline collision accidents. At the same time, emergency measures can be taken to prevent the crossing accident and ensure the safe pullback of the pipeline.

1. Introduction

With the continuous development of the social economy, people's awareness of civilization and environmental protection is becoming stronger and stronger, and the requirements for a living environment are also higher [1]. In

order to reduce the environmental protection problems caused by excavation when laying underground pipelines, new technology is urgently needed to meet the needs of people. Horizontal directional drilling (HDD) is to drill a pilot hole of a calibre size according to the horizontal directional drilling rig's design line and crossing curve. Then,

the drill bit is changed to a larger reamer to perform more than one pullback reaming process. When the hole diameter meets the design requirements, the full-length pipeline is finally towed back and laid. Furthermore, most of the long-distance crossing projects adopt the dual-drilling rig docking method for pilot hole construction [2–4]. As a new construction technology, HDD technology includes high construction precision, fast speed, and negligible environmental impact. Therefore, HDD technology has gradually received more and more attention [5]. HDD technology is a large-scale project combining multiple technologies, equipment, and disciplines. All aspects of the construction are linked together, and problems in one of the links will increase the cost of the project or affect the progress of the whole project [6]. HDD technology was first used in oil drilling and gradually combined with infrastructure construction and water well industry. Nowadays, it is widely used in the construction of oil and gas, municipal pipelines, etc. [7]. At present, HDD technology is also commonly used in ground source heat pump and gas layer drilling, and the application effect is good [8]. Compared with other nonexcavation pipeline technologies, HDD technology has more advantages, such as low construction cost, high efficiency, and minor surface disturbance. As a result, it has received more and more attention and has achieved better social and economic benefits [9]. As a branch of trenchless construction technology, horizontal directional drilling crossing technology has not been used in pipeline construction for a long time, but with the unremitting efforts of the majority of scientific researchers and engineers, it has made great progress since it was introduced into China in the 1970s. The construction of ground obstacles such as buildings is being widely used, and remarkable achievements have been made. Because of the outstanding advantages and mature technology of horizontal directional drilling, its application scope is expanding. Nowadays, it is used not only in the field of non-open-ended pipeline laying, but also in the fields of geology, metallurgy, petroleum, etc., and it is used in special underground space occasions like exploration and resource development of two underground sites. At present, the research on horizontal directional drilling technology has reached a certain extent. It can not only develop small- and medium-sized drilling machines produced abroad, but also expand the application field of this technology. Now, directional drilling technology not only has been applied to the laying of pipelines under complex conditions, but also can be applied to exploration and information collection in underground dangerous areas, such as laying military optical cables crossing busy roads or rivers, and automatic collection of soil data in the tunnel area after underground nuclear test. The research of horizontal directional drilling involves the research of various fields, including the research of pipeline back drag force calculation and the research of pipeline step crossing and the local stress deformation of the pipeline during the process of back drag.

Nowadays, China is in a rapid development stage, and there are more and more large-scale infrastructure projects, which will significantly promote the wide application of HDD technology. Simultaneously, the development of

orientation, machinery, and computer technology also provides theoretical support for the application of HDD [10, 11]. In 2010, Chehab and Moore also put forward the mathematical method for calculating the pullback force. They considered the winch effect and the development of the pipeline. Many domestic scholars have also studied the calculation method of pullback force. For example, Hu Shilei put forward a new calculation model of separation in 2012. He not only considered the pipe bending, but also split the bending, considered the situation of pipes under different bending types and strengths, and gave calculation formulas, respectively. Through example verification, the value of pullback force calculated by the new method is more accurate [12]. At present, there is a lack of basic research on the design value of horizontal directional drilling hole/pipe diameter ratio at home and abroad for a long time, and engineering practice depends on some empirical data with a large value range for a long time. Some studies have proposed the calculation method of the bending strength of the curve section, and it is considered that the reasonable limit bending strength of the hole body can be determined only by analyzing and comparing four aspects of the limit bending strength, namely, the limit bending strength of the hole body through which the bottom hole dynamic drilling tool passes smoothly, the limit bending strength of the hole body for safe operation of the drill string, the limit bending strength of the hole body for safe operation of the pipeline, and the limit bending strength of the hole body with the lowest deviation cost per degree [13]. The pipe diameter ratio is the ratio of the diameter of the guide hole to the diameter of the pullback pipe. According to the proposed pullback load prediction method, some scholars analyzed the influence of pipe diameter ratio on the pullback load. When the value is less than 1.5, the change of pipe diameter ratio has a great impact on the pullback load, and when the value is greater than 1.7, the change of pipe diameter ratio has little impact on the calculation results of pullback load [5]. It can be seen that the pipe diameter ratio has an important influence on the pullback load. Therefore, this study analyzes the calculation method of the pullback force of horizontal directional drilling, aiming to improve the calculation models of the backdrop force and the resistance of the step crossing via a case study. To facilitate full understanding of the HDD mechanism, numerical simulation of the step hole crossing is performed. Our research helps to ensure that the directional crossing process can adjust the construction process in time according to the actual situation of the site construction, avoid crossing accidents, and effectively reduce the construction cost and risk.

2. Establishment of an Improved Model to Calculate Pullback Force of HDD

2.1. Calculation and Analysis of Pullback Force in HDD. The pullback force of HDD is complex and consists of knowledge in many disciplines, such as geotechnical, material, fluid, and other mechanics. Among these, the most crucial factor is the cross-sectional size when pulling back the drill. To complete the pipeline crossing smoothly, all the

resistance in the pulling back process needs to be overcome. There are basically four methods to calculate the HDD's pullback force based on the GB50423 standard, the unloading arch earth pressure, the net buoyancy, and the winch effect [14]. Among these calculations, the GB50423 standard provides a straightforward model, mainly considering the buoyancy of the pipeline in the drilling, as shown in the following equation:

$$F_p = \pi L f g \left[\frac{D_2}{4} \rho_m - \rho_s (D - \delta) \right] \times 10^3 + k_v g \pi D L. \quad (1)$$

In (1), F_p is the pulling force of the drilling rig with the unit of N; L is the length of the pipeline with the unit of m ; ρ_m is the mud density with the unit of kg/m^3 ; f is the friction factor, being between 0.2 and 0.5; g is the acceleration of gravity with the unit of m/s^2 ; D is the outer diameter of the pipeline with the unit of m ; δ is the thick wall of the pipeline with the unit of m ; and k_v is the viscosity coefficient, being between 0.01 and 0.05. Note that 1.2~2.5 times of the calculation result of the formula is the final calculation result of the drilling rig. Nonetheless, (1) is an idealized model without full consideration of all influential factors.

The 2nd method is to obtain the unloading arch's earth pressure, which mainly analyzes the influence of the unloading arch above the pipeline on the pipeline's total pullback load, without considering the mud buoyancy inside the borehole. This calculation is given in the following equation:

$$T_{\max} = [2P(1 + K_\alpha) + P_0] f_e L. \quad (2)$$

In (2), T_{\max} is the maximum drag force with the unit of kN; P is the earth pressure per unit length with the unit of kN; K_α is the earth pressure factor, taking 0.3; P_0 is the

gravity per unit pipe with the unit of kN/m; f_e is the friction factor between the pipe and the borehole, being between 0.1 and 0.35; L is the total length of the pipe with the unit of m ; g is the gravity acceleration with the unit of m/s^2 ; and k_v is the viscosity coefficient [0.01–0.05]. Considering the drilling quality factors, the geotechnical thickness h (unit: m) and the vertical earth pressure (unit: kN/m) of the pipe top are shown as follows:

$$h = \frac{D_e [1 + tg(\pi/4 - \phi/2)]}{2f_{kp}}, \quad (3)$$

$$P_v = \frac{v_e D_0 h}{\lambda} = \frac{v_e D_0 D_e [1 + tg(\pi/4 - \phi/2)]}{2f_{kp} \lambda}. \quad (4)$$

In (3) and (4), D_e is the borehole size with the unit of m ; λ is the borehole mass coefficient, being between 20 and 35; ϕ is the rock and soil internal friction angle: $\phi = \arctg f_{kp}$; f_{kp} is the rock and soil coefficient, being 0.3; v_e is the rock and soil bulk density with the unit of kN/m^3 ; D_0 is the outer pipe diameter with the unit of m ; and h is the top rock and soil height with the unit of m . Safe pullback during construction usually means to reduce the friction force between the pipe and the hole wall and to keep the size ratio of the borehole and the pipe between 1.2 and 1.6, so the lateral earth pressure P_k (unit: kN/m) is calculated during the pulling back process, as follows:

$$P_h = P_v t g^2 \left(\frac{\pi}{4} + \frac{\pi}{2} \right). \quad (5)$$

Substituting (3) into (5) and $P = P_v + P_h$ into (2), we have

$$T_{\max} = f_e L \left\{ 2(1 + K_\alpha) \left[\frac{v_e D_0 D_e [1 + tg(\pi/4 - \phi/2)]}{2f_{kp} \lambda} + P_v t g^2 (\pi/4 + \pi/2) \right] + P_0 \right\}. \quad (6)$$

Although the earth pressure calculation of the unloading arch is relatively safe, the calculation process is complex and needs to meet too many conditions.

The 3rd method is to obtain the net buoyancy, which considers the influence of gravity and mud buoyancy on the pipeline, as shown in the following equation:

$$T_{\max} = |P_0 - P_f| f_m L. \quad (7)$$

In (7), P_0 is the weight per unit length of pipe with the unit of kN/m; P_f is the buoyancy in the drilling hole per unit length of pipe with the unit of kN/m; and f_m is the comprehensive friction factor, being between 0.5 and 0.8. If we neglect the thickness and weight of the outer coating of the rigid pipe, we can obtain

$$|P_0 - P_f| = \frac{\pi}{4} |4(D_0 - \delta)\delta\gamma_s - D_0^2\gamma_m|. \quad (8)$$

In (8), δ is the wall thickness of the crossing pipe with the unit of m ; γ_s is the weight of steel, usually 78.5 kN/m^3 ; and γ_m is the volume weight of slurry soil mixture in the hole, usually 11 to 12 kN/m^3 . By substituting (8) into (7), the maximum pullback force of the net buoyancy calculation is obtained as follows:

$$T_{\max} = \frac{\pi}{4} |4(D_0 - \delta)\delta\gamma_s - D_0^2\gamma_m| f_m L. \quad (9)$$

However, the above calculation is still idealized, as the winch effect caused by the bending section at both ends is not considered, so the range of the friction coefficient is broad. Therefore, the 4th method considering the winch effect is developed, mainly regarding the pipeline as a flexible steel cable wound on the huge drum, so the pullback force (unit: kN) of the horizontal pipeline is calculated from the ground surface.

$$F_s = \mu P_B L. \quad (10)$$

In (10), μ is the friction factor of the fluid between the pipe and the ground or in the borehole; P_B is the weight of the unit pipe length on the ground or the net buoyancy in the borehole with the unit of kN/m. If the radius of the bending section reaches a particularly large value, the calculation of the pullback force T_C (unit: kN) of the vertical section or the horizontal section of the pipeline when considering the winch effect is shown in the following equation:

$$T_C = e^{\mu\theta} (\mu P_B L). \quad (11)$$

In (11), θ is the pipe wrap angle and μ is the friction factor between mud and pipe. Considering the resistance caused by the mud during the pipeline backhauling, the backhauling head is regarded as the base point, and the following equation can be derived from (10) and (11).

$$\begin{cases} F_A = e^{\mu\alpha} (\mu_\alpha P_0 (L_1 + L_2 + L_3 + L_4)), \\ F_B = e^{\mu\alpha} (F_A + T_h + \mu_b |P_0 - P_f| L_2 - (P_0 - P_f) H_1 - e^{\mu\alpha} (\mu_\alpha P_0 L_2)), \\ F_C = F_B + T_h + \mu_b |P_0 - P_f| L_3 - e^{(\mu_\alpha + \mu_b)\alpha} (\mu_\alpha P_0 L_3), \\ F_D = e^{\mu\alpha\beta} (F_C + T_h + \mu_b |P_0 - P_f| L_4 + (P_0 - P_f) H_2 - e^{(\mu_\alpha + \mu_b)\alpha} (\mu_\alpha P_0 L_4)). \end{cases} \quad (12)$$

In (12), $T_h = \pi/8\rho(D_e^2 - D_0^2)$, $|P_0 - P_f| = \pi/4g|4(D_0 - \delta)\delta\gamma_s - D_0^2\gamma_m|$. F_A , F_B , F_C , and F_D , respectively, represent the pullback forces when the pipeline is pulled back to the entry point A, the end bending point B, the end bending point C, and the exit point D; P represents the mud pressure with the unit of kN/m³; T_h represents the movement resistance: $T_h = \pi/8q(D_e^2 - D_0^2)$, with the unit of kN; L_1 , L_2 , L_3 , and L_4 , respectively, represent the additional length of the pipeline, the horizontal pullback length from A to B, the length from B to C in the middle horizontal section, and the horizontal pullback length from C to D, with the unit of all these lengths being m ; μ_α and μ_b represent friction factors of the ground section (0.2–0.3) and the hole (0.15–0.25); H_1 and H_2 , respectively, represent the maximum buried depths of the ground end and the excavation end; and α and β , respectively, represent the entry angle and exit angle.

It can be seen from the above equation that $F_D > F_C > F_B > F_A$ indicating that when the pipe is pulled into the expanded borehole, the pullback force increases slowly. Finally, when it is pulled to point D, the force reaches the maximum, agreeing with the actual situation.

2.2. Case Studies. The calculation example of pullback force conducts the case study. First, the engineering parameters are determined according to the actual situation of the project. According to ASTM regulations (0.12–0.2) and the existing construction properties, the friction coefficient between the ground and the pipeline is set to be 0.15, the mud viscosity resistance is 0.25, and the friction coefficient in the borehole is 0.25 [15]. This study mainly analyzes three engineering cases: AA, BB, and CC, respectively. Due to the limited space in this paper, only the calculation process of AA is introduced in detail. AA is refined oil pipeline project, as shown in Figure 1.

The total length of AA crossing line of the project is 1984 m. The length of the downward horizontal section, ground bending area, middle horizontal section, ground bending section, and upward horizontal section is 256 m, 80 m, 1.283 m, 70 m, and 295 m, respectively. The outer diameter D_0 of the pipeline used is 0.61 m, the wall thickness d is 0.127 m, and the reaming diameter D_e is 0.65 m. The entry angle α and the excavation angle β are 16° and 14°, respectively, and the crossing depth $H_1 = H_2 = 73.5$ m.

According to the formula of the pullback force of the drilling rig, the above data are substituted into (1) to get $F_p = 823.6$ kN. Considering that the pullback force of the drilling rig is twice F_p in this study, $F = F_p \times 2 = 1647.2$ kN. Furthermore, by the method of unloading the arch soil pressure, the data is substituted into (6), so $T_{\max} = 2261$ kN, where $f_e = 0.25$, $D_0 = 0.61$ m, $D_e = 0.65$ m, $L = 1984$ m, $v_e = 24$ kN/m, $K_\alpha = 0.3$, $f_{ip} = 0.8$, $\lambda = 40$, $P_0 = 1.949$ kN/m. Moreover, through the net buoyancy method, the data is substituted into (9) to obtain $T_{\max} = 3544$ kN, where $f_m = 0.65$, $r_m = 11.5$, $D_0 = 0.61$ m, $\delta = 0.127$ m, $\gamma_s = 78$ kN, $\gamma_m = 11$ kN/m³, $L = 1984$ m. Finally, by substituting the data into (12) according to winch effect, the maximum pullback force $T_{\max} = 718$ kN, where $\mu_\alpha = 0.15$, $\mu_b = 0.25$, $r_m = 11.5$, $\alpha = 14^\circ$, $\beta = 16^\circ$, $L_1 = 14.4$ m, $L_2 = 287$ m, $L_3 = 1356$ m, $L_4 = 317$ m. Similarly, the pullback forces of the other two projects could be obtained. All these forces, together with the corresponding measured pullback forces, are listed and compared in Table 1.

It can be shown from Table 1 that the pullback force is the result of various factors: different geological conditions and equations result in different deviations in estimation. Therefore, the calculation method should be determined according to the specific geological conditions. It is interesting to see that among the above four methods, the winch calculation method gives the closest estimate of the force compared to the actual one.

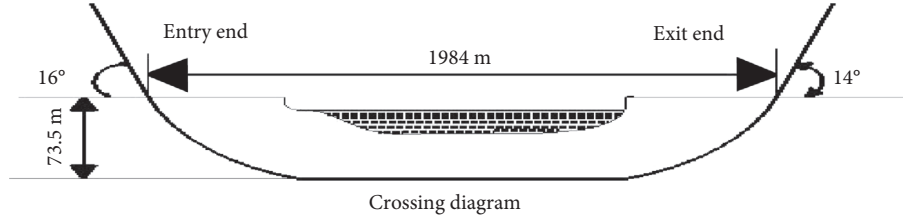


FIGURE 1: Cross section of product oil pipeline crossing project.

TABLE 1: Comparison of pullback forces in three cases.

Calculation method	Engineering		
	AA	BB	CC
Unloading arch earth pressure method (kN)	2261	1221	923
Winch calculation method (kN)	718	693	997
Actual pullback force (kN)	810	997	681

2.3. *Establishment of an Improved Model for Pullback Force Calculation.* In directional drilling engineering, drilling cuttings are flushed away by mud, improving the stability of hole wall [16]. Therefore, the method that considers the

effect of mud on the buoyancy is supposed to be more suitable for the pullback force calculation. Therefore, (2) about the method of unloading arch earth pressure is improved as follows:

$$T_{\max} = [2P(1 + K_{\alpha}) + (P_0 - P_f)]f_e L. \quad (13)$$

By substituting $P_v = v_e D_0 h / \lambda = v_e D_0 D_e [1 + tg(\pi/4 - \phi/2)] / 2f_{kp}\lambda$, $P_h = P_v tg^2(\pi/4 - \pi/2)$, and $P = P_v + P_h$ into (13), the optimized equation based on unloading arch soil and net buoyancy is

$$T_{\max} = f_e L \left\{ \frac{v_e D_0 D_e [1 + tg(\pi/4 - \phi/2)] [1 + tg^2(\pi/4 + \phi/2)] (1 + k_{\alpha})}{f_{kp}\lambda} + (P_0 - P_f) \right\}. \quad (14)$$

This is the improved calculation formula based on unloading arch soil and net buoyancy calculation method. In addition, considering the correlation between parameters and that some parameters change little, (14) can be simplified to the equations below, being straightforward for practical purposes:

$$T_{\max} = f_e L (4D_0 D_e + (P_0 - P_f)), \quad (15)$$

$$|P_0 - P_f| = \frac{\pi}{4} |4(D_0 - \delta)\delta\gamma_s - D_0^2\gamma_m|. \quad (16)$$

On the other hand, as shown previously, the calculation based on winch effect consideration gives best estimate of the force (see Table 1). Nevertheless, it can be seen from (12) that the winch calculation method is unreasonable both in the equation and the actual working condition. In fact, it can be seen from the calculation results and the actual engineering that the influence of the mud flow resistance on the back drag force of the pipeline is very small, so the calculation of

this force has little practical significance. In the estimation stage of the pullback force, its size can be ignored completely, which has little influence on the calculation results. In addition, the earth pressure on the top of the pipe is also considered in the formula, but this method is too rough and far from the actual working condition. The calculation method of earth pressure above the pipe top in the earth pressure calculation method of unloading arch introduced above is relatively mature in the theory of soil mechanics. So, this method can be applied in the winch calculation to calculate the earth pressure above the pipe top. According to the unloading arch earth pressure method,

$$F = 2P(1 + K_{\alpha})f_e L. \quad (17)$$

Among them, $P = P_v + P_h$, $h = D_e [1 + tg(\pi/4 - \phi/2)] / 2f_{kp}$, $P_v = v_e D_0 h / \lambda = v_e D_0 D_e (\pi/4 - \phi/2) / 2f_{kp}\lambda$, and $P_h = P_v tg^2(\pi/4 - \phi/2)$. After substituting (17), the following equation is obtained.

$$F = \frac{v_e D_0 D_e [1 + tg(\pi/4 - \phi/2)] [1 + tg^2(\pi/4 - \phi/2)] (1 + K_{\alpha}) f_e L}{f_{kp}\lambda}. \quad (18)$$

Considering that there is a certain internal relationship between some parameters and that some parameters change little, (18) can be simplified to the following equation:

$$F = 4f_e L D_0 D_e. \quad (19)$$

Therefore, the improved calculation method is shown as follows:

$$\begin{cases} T_B = e^{\mu_a \alpha} \left(T_A + \mu_b |P_0 - P_f| L_2 + 4D_0 D_e \mu_b L_2 - e^{\mu_a \alpha} (\mu_a P_0 L_2) \right), \\ T_C = e^{\mu_b \alpha} \left(T_B + \mu_b |P_0 - P_f| L_3 + 4D_0 D_e \mu_b L_3 - e^{(\mu_a + \mu_b) \alpha} (\mu_a P_0 L_3) \right), \\ T_D = e^{\mu_b \alpha} \left(T_C + \mu_b |P_0 - P_f| L_4 + 4D_0 D_e \mu_b L_4 - e^{(\mu_a + \mu_b) \alpha} (\mu_a P_0 L_4) \right). \end{cases} \quad (20)$$

T_B is the pullback force (kN) when the pipe is pulled back to the final bending point B at the end of entering soil, T_C is the pullback force (kN) when the pipe is pulled back to the bending point C at the earth end, and T_D is the pullback force when the pipe is pulled back to the excavation point d (kN). The improved equation is applied to calculate the AA, BB, and CC of the project. The calculation results are shown in Table 2. Compared with Table 1, it can be seen that the improved model has more stability and regularity. The improved calculation results are larger than the actual pullback force, more regular, more in line with the actual situation, and consistent with the actual working conditions.

3. Numerical Simulation of Pipeline Step Crossing

3.1. Establishment of a Calculation Model for Step Crossing Resistance. At present, China is in the climax of the development of horizontal directional crossing technology. In many cases, the calculation of pipeline pullback force depends on the empirical value, which is greatly affected by human subjective factors, and the theoretical level is far from meeting the needs of practical engineering. Therefore, it is particularly important to analyze the characteristics of pipeline in the process of crossing, especially the study of pullback load. The back drag load is affected by many factors. At present, the research at home and abroad mainly focuses on the geological conditions, trajectory curvature, mud properties, pipeline materials, and ratio of pipe diameter to hole diameter (hole/pipe ratio) but little on special construction conditions. In order to further improve the pipeline crossing theory, based on the case study of stepped hole crossing project, this section analyzes the influence of step set parameters on pipeline pullback force and pipeline mechanical properties.

The formation of the step is mainly due to the fact that the rock is not cleaned by the cutter when the hole is reamed. The two ends of the reamer have different forces when they pass through the junction of soft and hard formations, which will cause the size of the reaming steps to be different. At present, the most commonly used technology for horizontal directional drilling is back drag reaming. Therefore, when the force on both ends of the reamer is uneven, the influence of different step size on the pullback force is also different [17]. With the occurrence of steps, the actual track of drilling normally differs significantly from the theory.

In order to facilitate the construction of the model, this study assumes that the borehole is stable and that the design is entirely consistent with the actual borehole trajectory. The lithologic soil is rigid support, which will not deform and shift; in addition, the pulling back pipe has uniformity. When the hole wall is intact, the influencing track factors include the friction force f between the hole wall and the

pipeline, the pullback force (rig pull force) T , the step resistance f_t , buoyancy F , and gravity G . T can be approximately regarded as follows:

$$T = f + f_t + T_w. \quad (21)$$

Since the length of the pipe is much longer than the step length, the contact area of the pipeline passing through the steps is almost unchanged, so f can be ignored and the main influencing factor is f_t . The main force between the steps and the pipeline can be regarded as G , F , and T , where the resultant force of G and F are shown in the following equation:

$$F_1 = \frac{\pi}{4} \left[(D^2 - d^2) \rho_1 - D^2 \rho_2 \right] \cdot g \cdot L. \quad (22)$$

In (22), D and d are the inner and outer diameters of the pipeline with the unit of m ; ρ_1 and ρ_2 are the density of the pipeline and mud with the unit of kg/m^3 ; and g is the acceleration of gravity, i.e., $g = 9.8 \text{ m/s}^2$. If the pipeline always keeps balance when crossing the steps, the stress of the pipeline is shown in Figure 2.

According to the force balance principle, the horizontal and vertical calculation methods are shown as follows:

$$T = N \cdot \cos \beta + \mu N \cos \alpha + T_w, \quad (23)$$

$$F = G + \mu N \sin \beta - N \cdot \cos \alpha. \quad (24)$$

Therefore, the step resistance f_t of the front section of the pipeline can be obtained by substituting (21) into (24), as shown in the following:

$$f_t = \frac{\pi}{4} \cdot \frac{1 + \mu}{1 - \mu} \tan \alpha \cdot \left[(D^2 - d^2) \rho_1 - D^2 \rho_2 \right] \cdot g. \quad (25)$$

In (25), the step resistance is positively proportional to a and L . Among them, the height and curvature of the step are closely related to α , so it is crucial to consider the influence of the step with different curvatures and heights on the pullback force. Let $\cos = h/r$ and h denote the height of the contact point; thus, the calculation of f_t is as follows:

$$f_t = \frac{\pi}{4} \cdot \frac{1 + \mu}{1 - \mu} \sqrt{\frac{h^2}{r^2 - h^2}} \left[(D^2 - d^2) \rho_1 - D^2 \rho_2 \right] \cdot g \cdot L. \quad (26)$$

3.2. Numerical Simulation of Pipeline Crossing with Steps. The rotation of the pipeline during back-pulling is not considered. A symmetrical model is built to reduce the computational expense, and a symmetrical constraint is imposed on the symmetrical plane to avoid rigid body displacement. The model is composed of a pipeline and

TABLE 2: Table of calculation results after improvement.

Computing method	Engineering		
	AA	BB	CC
Unloading arch earth pressure method (kN)	1566	1218	695
Winch calculation method (kN)	857	1271	997
Actual pullback force (kN)	695	716	681

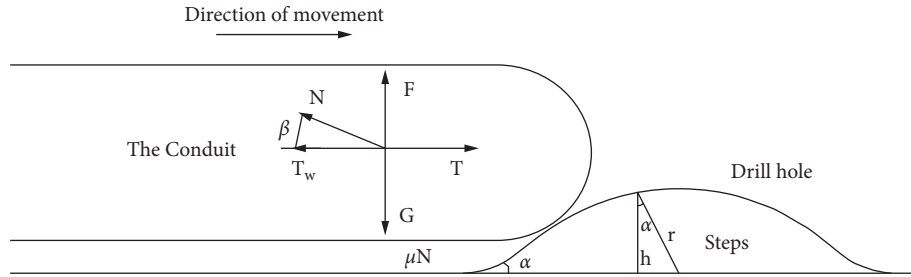


FIGURE 2: Stress analysis of pipeline crossing steps.

geotechnical (with a step) model. When the step height is determined, the higher the contact point between the pipe and the step, the greater the step resistance. When the step height and the contact point height are constant, the step resistance decreases with the increase of step curvature. The above theoretical analysis results lay a theoretical foundation for the simulation results of stepped hole crossing in the later paper and are mutually verified with the simulation results in this paper. The rock length L is 20 m, the height H is 2 m, and the step height h is 0.1 m–0.4 m. The curvature radius r of step and joint is 0.75 m, the radius R is 0.65 m, and the wall thickness d and inner diameter R of the pipe are 0.02 m and 0.49 m. The pipeline material is X-65, the density in the elastic-plastic constitutive relation is 7800 kg/m³, the elastic modulus is 2.1e11 Pa, and the Poisson ratio is 0.3. The stress-strain data of pipeline in the plastic stage are shown in Table 3.

Drucker–Prager model is applied to the geotechnical plastic model, which is suitable for friction materials such as geotechnical materials [18]. The density, Young’s modulus, and Poisson’s ratio of geotechnical elastic parameters are 2700 kg/m³, 4.13e10 Pa, and 0.22 respectively; the friction angle β , strain rate K , and expansion angle f of D-P constitutive model parameters are 44°, 0.8, and 38°, respectively; and the corresponding plastic variables of yield stress in rock hardening parameters under 37.93 MPa, 38.2 MPa, and 38.4 MPa are 0, 0.005, and 0.08, respectively. The analysis step of stepped hole crossing and the contact attributes between hole wall and pipe are set as follows: analysis step (static general analysis step), contact surface (pipe indication), contact type (surface contact), tangential contact (penalty function), normal contact (linear contact), target surface (hole wall), and friction coefficient (0.2).

The simplified model for the step hole crossing is shown in Figure 3(a), including pipeline and geotechnical models (including the step). The boundary conditions and constraints are set for the model. The model is divided into two grids: structured and unstructured. The results include

TABLE 3: Stress-strain data of pipeline in plastic stage.

True stress (MPa)	Plastic strain	True stress (MPa)	Plastic strain
418	0	882	0.25
500	0.01	908	0.35
605	0.02	921	0.45
695	0.056	932	0.55
780	0.095	955	0.65
829	0.15	\	\

12076 grids, and the steps are locally encrypted, so much finer meshes are assigned. C3D10 M and C3D8R are used for tetrahedron and hexahedral grid units, respectively, as shown in Figure 3(b).

The model is verified by the engineering pullback load data in [19]. Figure 4(a) shows the recorded results of the engineering load, and Figure 4(b) shows the calculation results of the stepped hole crossing model. Comparing the two figures, we find that the trend of the change curve is basically the same, which reflects the accuracy of the calculation model proposed in this study. Ashkan et al. used the national standard formula to calculate the maximum pullback force, verified the friction coefficient and viscous force coefficient in the national standard, and gave a relatively certain value. The checking calculation of the actual project is basically consistent with the pullback results and can be used as the subsequent pullback force calculation [20]. However, compared with the checking calculation model proposed by Ashkan et al., the calculation model proposed in this study has higher accuracy.

For the borehole with a specific diameter, the step may have limit curvature radius or limit height, causing excessive pushing stress applied on the pipeline. The stress might exceed the yield strength of the pipe or cause so large back-pulling load that exceeds the maximum tensile force capacity of the drilling machine. Therefore, the limit curvature radius and limit height of the step must be considered for safe back-pulling of the pipeline. Therefore, we first analyze the

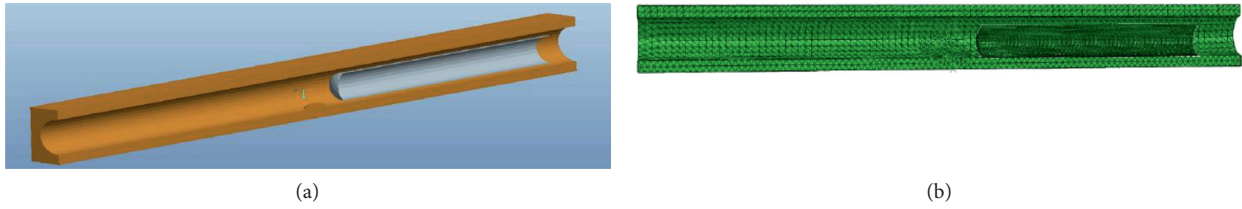


FIGURE 3: Simplified model and meshing diagram of stepped hole crossing.

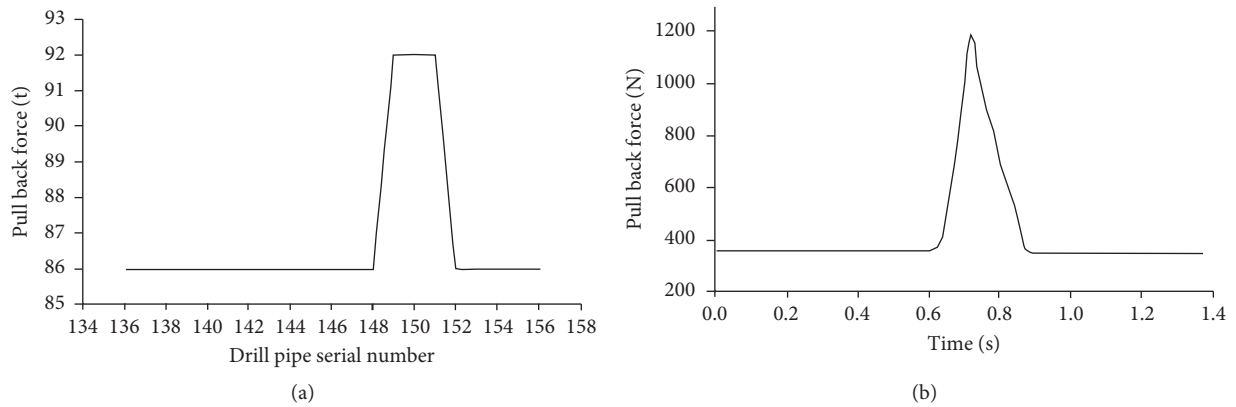


FIGURE 4: Comparison of engineering value and calculation result.

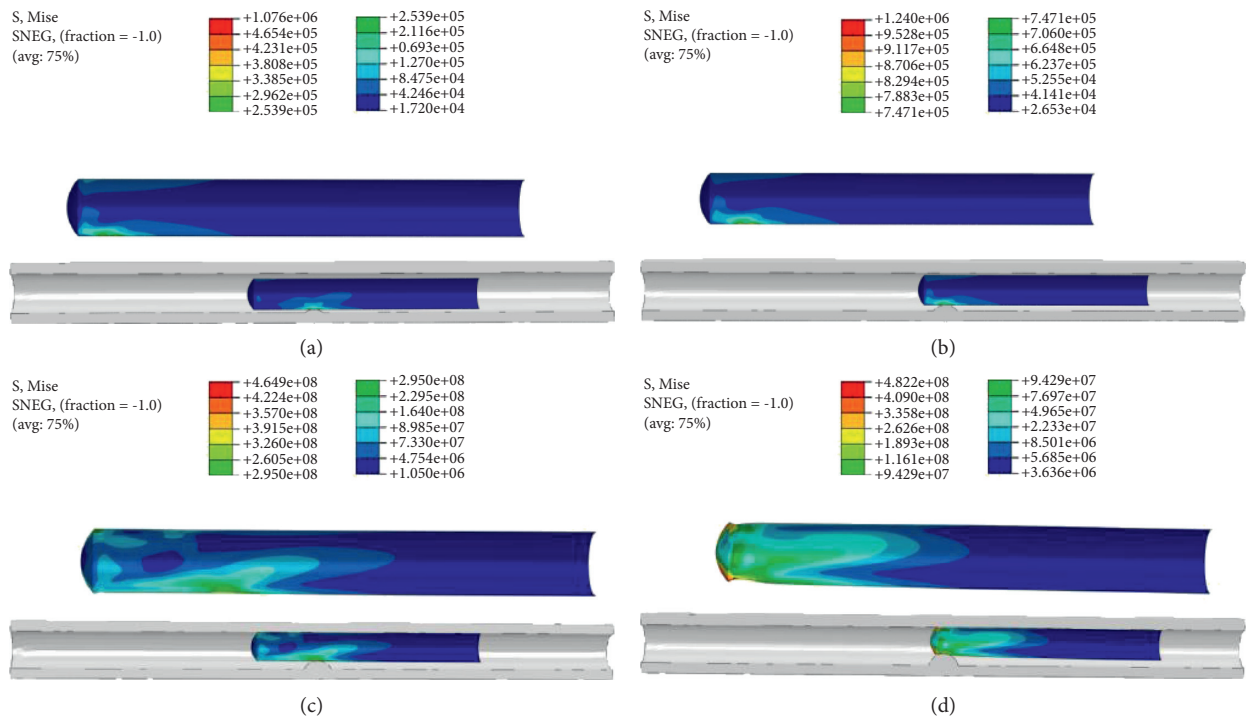


FIGURE 5: Contact stress distribution in borehole at different step heights.

influence of the step height on the pullback force by setting a constant curvature r of 0.5 m while changing the heights between 0.1 m and 0.4 m. The obtained Mises stress distribution is shown in Figure 5.

It can be seen from Figure 5 that when the height of the step increases, the contact stress of the pipe will gradually increase after the pipe hits the step. When the step height is 0.3 m, once hitting happens, the resulting contact stress is up

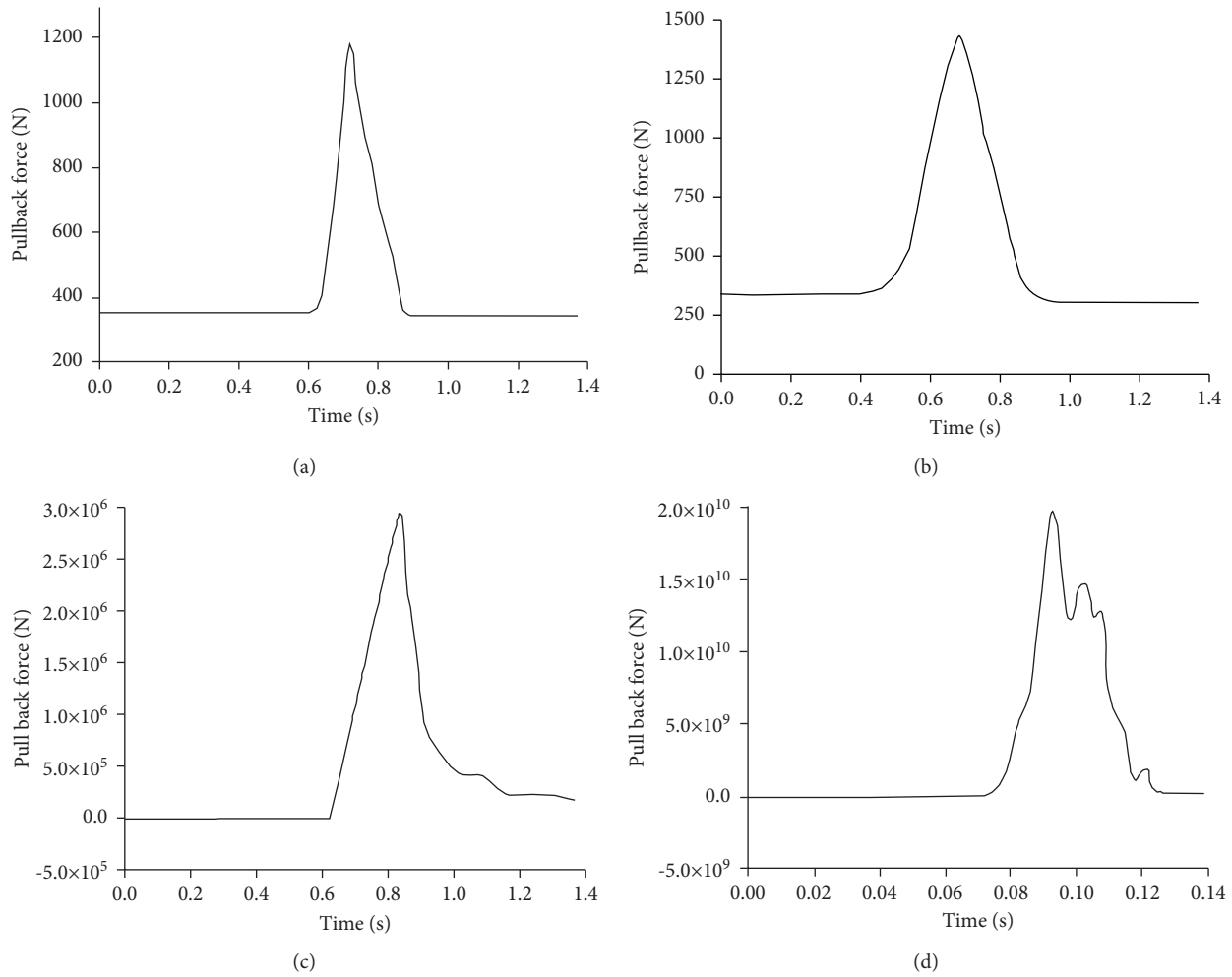


FIGURE 6: Change curve of pullback force.

to 4.65×10^8 Pa, higher than the yield stress (4.2×10^8 Pa) of the pipeline, so the plastic strain occurs. When the step height is 0.4 m, the plastic strain occurs after the pipe hits the step, causing the pipeline damage. Figure 6 shows the relationship between the height of the step and the pullback force. It can be seen from the figure that the back drag force of the pipe increases suddenly after it just enters the step, and the back drag force after the pipe head passes through the step will decrease rapidly.

The relationship between the maximum contact stress, pullback force, and step height is shown in Figure 7. It can be seen from Figure 7 that with the increase of the step height, the pullback force and the maximum contact stress become larger. For example, when the height is 0.3 m, the stress on the pipeline is higher than the yield limit, resulting in the deformation and damage to the pipeline. In addition, when the height is greater than 0.2 m, the pullback force increases rapidly. Furthermore, when the height is 0.4 m, the pullback force will be higher than the maximum tensile capacity of the current drilling rig.

When the height of the step is 0.2 m, the stress distribution of the pipeline under the curvature radius of 1 m, 0.8 m, and 0.5 m is shown in Figure 8. It can be seen from

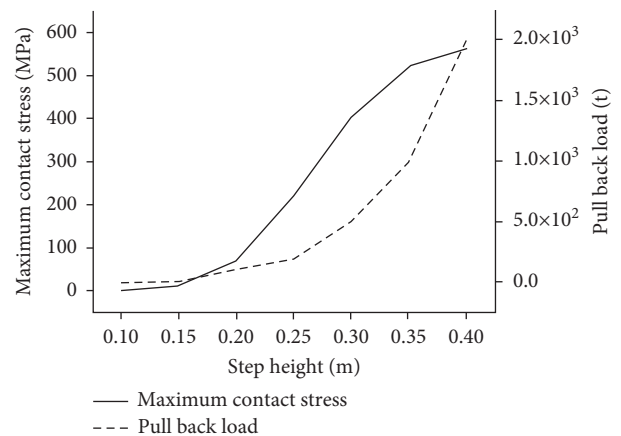


FIGURE 7: Relationship between step height, pullback force, and contact stress.

the figure that there is a minor effect of the step's curvature change on the pipe stress. The corresponding pullback forces are also presented in Figures 9(a) to 9(c), which show high level of similarities under the three curvatures.

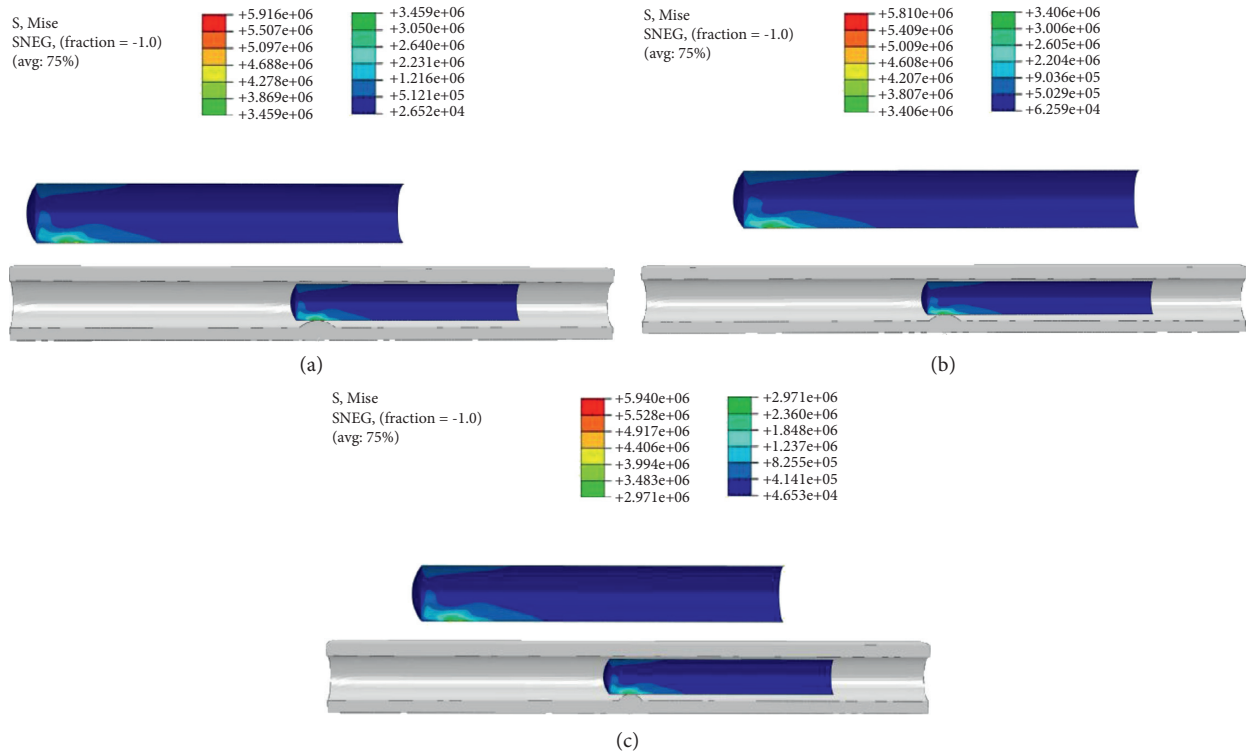


FIGURE 8: Stress diagram under different radius of curvature.

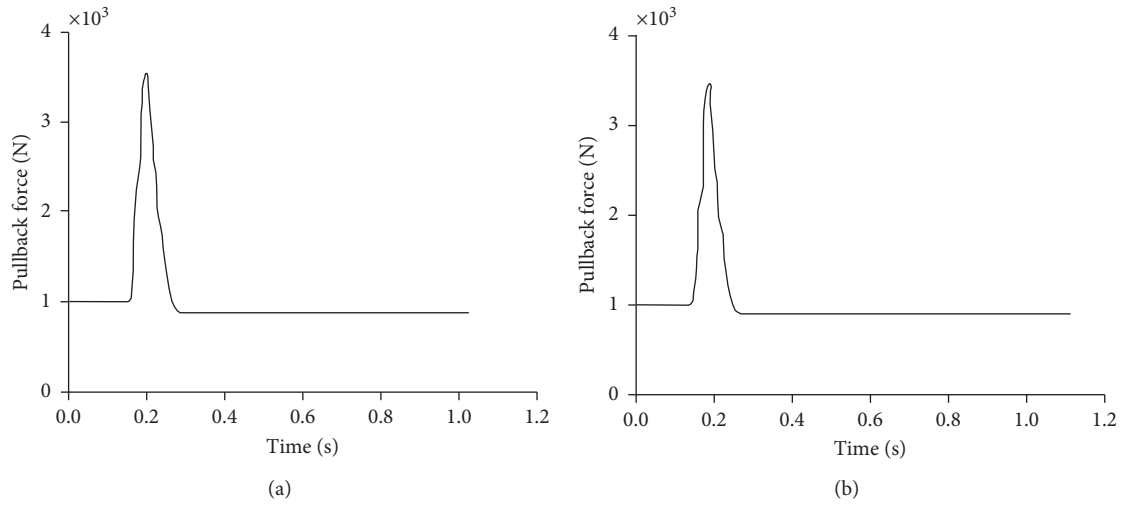


FIGURE 9: Continued.

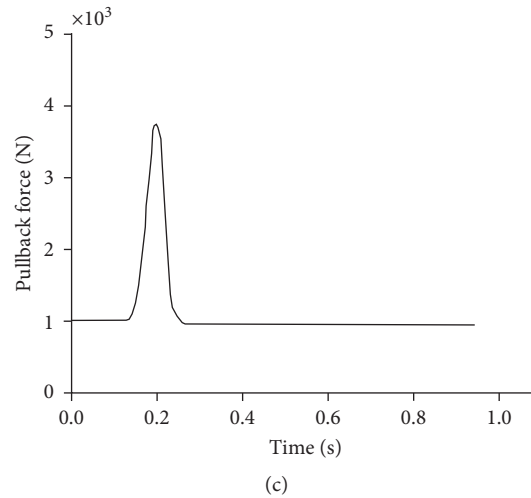


FIGURE 9: Variation curves of pullback forces under different radiuses of curvature.

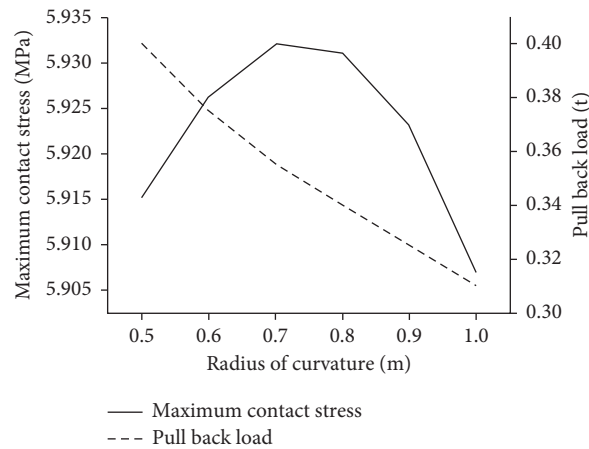


FIGURE 10: Relationship between curvature radius, pullback force, and contact stress.

The relationship between the maximum contact stress, pullback force, and curvature radius of the steps is shown in Figure 10. It shows that for a given step height, the curvature radius is inversely proportional to the step resistance, while the contact stress increases first and then decreases. Nevertheless, such changes in contact stress are minor and can be ignored.

4. Conclusion

With the rapid development of the economy and the enhancement of people's awareness of environmental protection, the traditional pipeline laying and excavation technology has long been unable to meet people's needs. Horizontal directional drilling technology has developed rapidly with its advantages of environmental protection, small disturbance, and high efficiency, but its theoretical level is far from meeting the needs of practical engineering, and it needs to be determined according to experience in many cases. Due to the influence of human subjective factors, it is necessary to study the backhauling process of horizontal directional drilling pipeline. This study adopts

analytical analysis and numerical simulation to study the pullback force of the trenchless horizontal directional drilling (HDD) pipeline. The results show the following:

- (1) When the step height is 0.3 m, the contact stress (4.65×10^8 Pa) is higher than the yield stress (4.2×10^8 Pa), leading to the plastic strain; when the step height is 0.4 m, the plastic strain damage to the pipeline occurs.
- (2) When the pipe just enters the step, the pullback force increases suddenly and then decreases rapidly after the pipe head passes the step; with the increase of the step height, the plastic strain damage occurs. When the height is higher than 0.2 m, the pullback force increases rapidly.
- (3) When the height is 0.4 m, the pullback force will be higher than the maximum pulling force provided by the current drilling rig. Moreover, when the step height is 0.2 m, the influence of step curvature on pipeline stress is small, and the change of pullback force is almost the same under three curvatures.

- (4) When the step height remains unchanged, the curvature radius is inversely proportional to the step resistance, while the contact stress increases first and then decreases with a minor change. During the pullback process, the pipeline will encounter step resistance through the soft and hard staggered stratum, which will suddenly increase the increment of pipeline pullback force and lead to engineering accidents.

At present, the research on pipeline pullback force at home and abroad is mainly focused on the overall level, and there is less research on local areas. Through the common working conditions in the pullback process, the stress state and the change trend of pullback force during pipeline crossing steps are analyzed. If the pullback load suddenly increases and then decreases, it may encounter similar pipeline collision accidents. At the same time, emergency measures can be taken to prevent the crossing accident and ensure the safe pullback of the pipeline.

Due to the limited time and capacity, although the winch effect is considered, the influence of pipe bending on pullback load is not analyzed in this paper. There is no corresponding formula for crossing a variety of strata in complex sections. Although there are many calculation models at present, the calculation results deviate greatly from the actual values. In this paper, there is little research on complex formation, and the understanding of related drilling tools needs to be further deepened. In the future work, we should continue to carry out research in this regard.

Data Availability

All data generated or analyzed during this study are included within this article.

Conflicts of Interest

The authors declare no conflicts of interest.

Authors' Contributions

X. L. analyzed the calculation results and wrote the article; D. H. processed the data; Y. L. and Y. Z. provided the information of the construction site; L. J. and X. Y. offered useful suggestions for the preparation and writing of the paper.

Acknowledgments

This research was funded by the National Natural Science Foundation of China (No. 51678226), the Natural Science Foundation of Hunan (Nos. 2021JJ50147, 2021JJ30078, and 2019JJ50030), the Scientific Research Project of Education Department of Hunan Province (No. 19C0358), and the Science and Technology Innovation Project of Yiyang City (Nos. 2020YR02 and 2019YR02).

References

- [1] L. Cai and M. A. Polak, "A theoretical solution to predict pulling forces in horizontal directional drilling installations," *Tunnelling and Underground Space Technology*, vol. 83, pp. 313–323, 2019.
- [2] M. Rabiei, Y. Yi, and A. Bayat, "Simple methods for fluidic drag estimation during pipe installation via HDD," *Tunnelling and Underground Space Technology*, vol. 76, pp. 172–176, 2018.
- [3] R. Carpenter, "HDD market growing, but challenges abound," *Underground Construction*, vol. 73, no. 6, pp. 16–25, 2018.
- [4] B. Shu and B. Ma, "The return of drilling fluid in large diameter horizontal directional drilling boreholes - science-direct," *Tunnelling & Underground Space Technology Incorporating Trenchless Technology Research*, vol. 52, pp. 1–11, 2016.
- [5] A. Faghih, Y. Yi, A. Bayat, and M. Osbak, "Efficient drilling in horizontal directional drilling by implementing the concept of specific energy," *Geomechanics and Geoengineering*, vol. 12, no. 3, pp. 201–206, 2017.
- [6] G. Ehm, "The changing pipeline industry," *Pipes and Pipelines International*, no. 27, pp. 20–22, 2016.
- [7] M. S. Mohd Norizam, H. Nuzul Azam, S. Helmi Zulhaidi, A. A. Aziz, and A. Nadzrol Fadzilah, "Literature review of the benefits and obstacle of horizontal directional drilling," *IOP Conference Series: Materials Science and Engineering*, vol. 271, Article ID 012094, 2017.
- [8] C. Schmermund, "2016 Large directional drilling rig census," *Pipeline and Gas Journal*, vol. 243, no. 10, pp. 64–68, 2016.
- [9] J. Griffin, "Mud motor for mid-range HDD rigs," *Underground Construction*, vol. 74, no. 1, p. 32, 2019.
- [10] L. Cai, G. Xu, M. A. Polak, and M. Knight, "Horizontal directional drilling pulling forces prediction methods – a critical review," *Tunnelling and Underground Space Technology*, vol. 69, pp. 85–93, 2017.
- [11] X. Zhu and Q. Yi, "Research and application of reaming subsidence control in horizontal directional drilling," *Tunnelling and Underground Space Technology*, vol. 75, pp. 1–10, 2018.
- [12] A. G. Chehab and I. D. Moore, "Parametric study examining the short and long term response of HDPE pipes when installed by horizontal directional drilling," *Tunnelling and Underground Space Technology*, vol. 25, no. 6, pp. 782–794, 2010.
- [13] J. Griffin, "Solving a puzzling project," *Underground Construction*, vol. 74, no. 1, pp. 30–31, 2019.
- [14] X. Guangli, L. Cai, R. Ji, and Z. Wang, "Numerical simulation of pipe-soil interaction during pulling back phase in horizontal directional drilling installations," *Tunnelling and Underground Space Technology*, vol. 76, pp. 194–201, 2018.
- [15] S. Pinghe, M. Dingqiang, T. A. Samuel, C. Han, and Z. Pengfei, "Laboratory study of fluid properties owing to cutting intrusions during horizontal directional drilling," *Underground Space*, vol. 5, no. 1, pp. 20–29, 2020.
- [16] J. Wang, X. Liu, and S. Wang, "Application of directional drilling forward pushing process to crossing mountain with large drop," *Gas & Heat*, vol. 37, no. 7, pp. 67–70, 2017.
- [17] M. Mohammadi, J. G. Dai, Y. F. Wu, and Y. L. Bai, "Development of extended Drucker-Prager model for non-uniform FRP-confined concrete based on triaxial tests," *Construction and Building Materials*, vol. 224, no. 10, pp. 1–18, 2019.

- [18] E. M. Hossain, *Fundamentals of Drilling Engineering (Multiple Choice Questions And Workout Examples For Beginners And Engineers) || Horizontal And Directional Drilling*, Wiley, Hoboken, NJ, USA, 2016.
- [19] J. Raclavský, "Theoretical problems of pipe inserting by making use of the method of horizontal directional drilling," *Acta Montanistica Slovaca*, vol. 13, pp. 156–160, 2008.
- [20] F. Ashkan and Anup, "Study on parameters of pipeline construction pullback force in horizontal directional drilling," *Trenchless technology*, no. 1, pp. 11–14, 2016.

Research Article

Classical and Bayesian Estimation of the Inverse Weibull Distribution: Using Progressive Type-I Censoring Scheme

Ali Algarni,¹ Mohammed Elgarhy ,² Abdullah M Almarashi,¹ Aisha Fayomi,¹ and Ahmed R El-Saeed³

¹Statistics Department, Faculty of Science, King AbdulAziz University, Jeddah 21 551, Saudi Arabia

²The Higher Institute of Commercial Sciences, Al Mahalla Al Kubra, Algarbia 31 951, Egypt

³Department of Basic Sciences, Obour High Institute for Management & Informatics, Cairo, Egypt

Correspondence should be addressed to Mohammed Elgarhy; m_elgarhy85@sva.edu.eg

Received 4 October 2021; Revised 4 November 2021; Accepted 20 November 2021; Published 29 December 2021

Academic Editor: AFAQ AHMAD

Copyright © 2021 Ali Algarni et al. This is an open access article distributed under the Creative Commons Attribution License, which permits unrestricted use, distribution, and reproduction in any medium, provided the original work is properly cited.

The challenge of estimating the parameters for the inverse Weibull (IW) distribution employing progressive censoring Type-I (PCTI) will be addressed in this study using Bayesian and non-Bayesian procedures. To address the issue of censoring time selection, quantiles from the IW lifetime distribution will be implemented as censoring time points for PCTI. Focusing on the censoring schemes, maximum likelihood estimators (MLEs) and asymptotic confidence intervals (ACI) for unknown parameters are constructed. Under the squared error (SEr) loss function, Bayes estimates (BEs) and concomitant maximum posterior density credible interval estimations are also produced. The BEs are assessed using two methods: Lindley's approximation (LiA) technique and the Metropolis-Hasting (MH) algorithm utilizing Markov Chain Monte Carlo (MCMC). The theoretical implications of MLEs and BEs for specified schemes of PCTI samples are shown via a simulation study to compare the performance of the different suggested estimators. Finally, application of two real data sets will be employed.

1. Introduction

Keller and Kamath [1] were the ones to propose the IW model as a sustainable idea for describing the deterioration of structural devices in diesel engines. The IW distribution gives an excellent match to various real data sets, according to [2]. In the perspective of a mechanical system's load-strength relationship, Calabria and Pulcini [3] gave an essential explanation of this distribution. The IW distribution, which was created to explain failures of structural devices influenced by degradation phenomena, plays a critical part in reliability engineering and lifetime testing. It has been looked into from a variety of angles. On the basis of the PC type-II data set, Musleh and Helu [4] used both conventional and Bayesian estimation techniques to estimate parameters from the IW distribution. Singh *et al.* [5] evaluated simulated hazards of

several estimators, with a focus on the Bayesian approach. De Gusmao *et al.* [6] and Elbatal and Muhammed [7] focused their efforts on its comprehensive versions research, which included both generalized and exponentiated generalized IW distributions.

The distribution of IW has been studied from many angles. Khan *et al.* [8] visually and quantitatively depicted several aspects of this distribution, including mean (M), variance (V), kurtosis, and skewness. Erto [9] calculated the IW distribution using a fresh prior distribution, taking into account the shape parameter's range and the predicted value of a quantile (Q) of the sampling distribution. Sultan *et al.* [10] go into great depth on how to include two IW distributions into a hybrid model. The IW distribution's density function (pdf), cumulative function (cdf), and Q function (Q_f) are shown as follows:

$$f(x) = \gamma \lambda x^{-(\gamma+1)} \exp\left(\frac{-\lambda}{x^\gamma}\right), x > 0, \gamma, \lambda > 0, \quad (1)$$

$$F(x) = \exp\left(\frac{-\lambda}{x^\gamma}\right), x > 0, \gamma, \lambda > 0,$$

$$Q(u) = \sqrt[\gamma]{\frac{\lambda}{\ln(1/u)}}. \quad (2)$$

Note that when $\gamma = 1$ and $\gamma = 2$ the IW model reduces to inverted exponential (IE) inverted Rayleigh (IR) models.

Censored data arises in real-life testing trials when the experiments, which include the lifetime of test units, must be stopped before acquiring complete observation. For a variety of reasons, including time constraints and cost minimization, the censoring method is frequent and inescapable in practice. Various types of censorship have been explored in depth, with Type-I and Type-II censoring being the most prevalent. In comparison to classic censoring designs, a generalized type of censoring known as PC schemes has recently garnered substantial attention in the works as a result of its efficient use of available resources. PCTI is one of these PC schemes. When a certain number of lifetime test units are continually eliminated from the test at the conclusion of each of the post periods of time, this pattern is seen [11].

Assume there are n units in a life testing experiment. Assume that X_1, X_2, \dots, X_n indicate the lifetime of all these n units drawn from a population. The equivalent ordered lifetimes recorded from the life test are denoted by $x_{(1)} < x_{(2)} < \dots < x_{(n)}$. Eventually R_i items are omitted from the surviving items at the predetermined period of censoring T_{q_i} in accordance with q_i^{th} Qs, $i = 1, 2, \dots, m$, where m denotes the number of testing stages, $T_{q_i} > T_{q_{i-1}}$ and $n = r + \sum_{i=1}^m R_i$. The values T_{q_i} must be established beforehand:

- (1) According on the experimenter's prior knowledge and expertise with the items on test [12].
- (2) The Qs of lifetimes distribution, q_i th, which may be constructed using the given formula

$$P(X \leq T_{q_i}) = q_i \Rightarrow T_{q_i} = F^{-1}(q_i) \quad i = 1, 2, \dots, m. \quad (3)$$

In these situations, R_i, T_{q_i} , and n are preset and constant, whereas l_i is the number of surviving objects at a given point in time T_{q_i} and $r = \sum_{i=1}^m l_i$ are random variables. The LL function is indicated by

$$\ell(\theta) \propto \prod_{i=1}^r f(x_{(i)}; \theta) \prod_{j=1}^m \left(1 - F(T_{(q_j)}; \theta)\right)^{R_j}, \quad (4)$$

where $x_{(i)}$ is the observed lifetime of the i th order statistic [13]. Figure 1 describes this scheme of censoring [14].

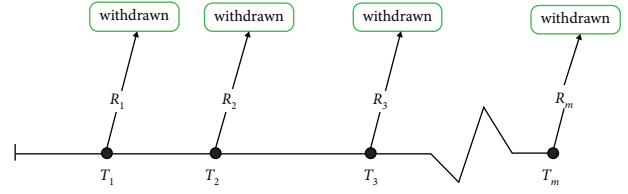


FIGURE 1: PCTI scheme.

One can observe that complete samples and also Type-I censoring scheme can be considered as special cases of this scheme of censoring.

Cohen [13] introduced PCTI scheme for the Weibull distribution. Mahmoud et al. [15] derived the MLEs and the BEs for the parameters of the generalized IE model under PCTI. There are two closely related papers for the PCTI. The first one was the MLEs and ACI estimates for the unknown parameters of the generalized IE model under the idea that there are two types of failures [16]. The MLEs and BEs for the unknown parameters of the generalized IE model [17] were the second.

The purpose of this paper is to look at the PCTI scheme when the lifetimes have their own IW model. We use two distinct techniques to drive the MLEs and BEs and derive the ACI of these different parameters: MCMC and Lindley Approximation. We look at a simulation outcome and a real data set to see how the various models perform in practice. The following is how the remaining of the article is structured: The MLE and confidence intervals are discussed in Section 2. In Section 3, the Metropolis-Hasting (MH) algorithm and LiA are used to explore the Bayesian estimation technique, fully accrediting the gamma distribution as a prior distribution for unknown parameters. A simulated outcome and a real data set are utilized to demonstrate the theoretical conclusions in Section 5. Finally, there are some final observations and a summary.

2. Estimation Using Method of Maximum Likelihood

According on the PCTI method, for the unknown parameters of the IW distribution, the MLE technique of estimate is examined in this section. This is how the PCTI system can be put into practice:

- (i) Suppose a random sample of n units with the next lifetime IW (γ, λ) distribution to the test in a real-life experiment.
- (ii) Prefix m censoring time points T_{q_1}, \dots, T_{q_m} , at which fixed number R_1, \dots, R_{m-1} of surviving items are randomly omitted from the test. The censoring times T_{q_j} are chosen corresponding to $P(X \leq T_{q_j}) = q_j$, where X follows IW (γ, λ) distribution and q_j^{th} is the Qs ($j = 1, 2, \dots, m$) of the chosen lifetime distribution.
- (iii) The life test terminates at or before a prespecified time T_{q_m} .

Therefore, one can obtain PCTI samples $x = (x_{(1)}, x_{(2)}, \dots, x_{(r)})$ that indicate the reported lifetime of r units under that same censoring procedure.

By applying equation (1) of IW distribution in equation (4) of LL function under PCTI, the connected LL function of γ and λ given the PCTI data, x , may be interpreted as

$$\ell(\gamma, \lambda) \propto (\gamma\lambda)^r \prod_{i=1}^r \left(x_i^{-(\gamma+1)} \exp\left(\frac{-\lambda}{x_i^\gamma}\right) \right) \prod_{j=1}^m \left(1 - \exp\left(\frac{-\lambda}{T_{q_j}^\gamma}\right) \right)^{R_j}. \quad (5)$$

Take logarithm of $\ell(\gamma, \lambda)$ to obtain log-LL \mathcal{L} as

$$\begin{aligned} \mathcal{L} \propto r \ln \gamma + r \ln \lambda - (\gamma + 1) \sum_{i=1}^r \ln x_i - \lambda \sum_{i=1}^r x_i^{-\gamma} \\ + \sum_{j=1}^m R_j \ln \left[1 - \exp\left(\frac{-\lambda}{T_{q_j}^\gamma}\right) \right]. \end{aligned} \quad (6)$$

First partial derivatives of log-LL function \mathcal{L} in terms of γ and λ are computed as follows:

$$\frac{\partial \mathcal{L}}{\partial \gamma} = \frac{r}{\gamma} - \sum_{i=1}^r \ln x_i + \lambda \sum_{i=1}^r x_i^{-\gamma} \ln x_i - \sum_{j=1}^m \frac{\lambda R_j \ln T_{q_j}}{A_j}, \quad (7)$$

$$\frac{\partial \mathcal{L}}{\partial \lambda} = \frac{r}{\lambda} - \sum_{i=1}^r x_i^{-\gamma} + \sum_{j=1}^m \frac{R_j}{A_j}, \quad (8)$$

where $A_j = T_{q_j}^\gamma [\exp(\lambda/T_{q_j}^\gamma) - 1]$.

Equating $(\partial \mathcal{L}/\partial \gamma)|_{\gamma=\hat{\gamma}}$ and $(\partial \mathcal{L}/\partial \lambda)|_{\lambda=\hat{\lambda}}$ to 0, then the numerical solution of the above two equations for $\hat{\gamma}$ and $\hat{\lambda}$ is the MLEs of γ and λ .

The approximate variance-covariance (V-C) matrix of the MLEs of γ and λ is

$$I(\gamma, \lambda) = \begin{bmatrix} -E\left(\frac{\partial^2 \mathcal{L}}{\partial \gamma^2}\right) & -E\left(\frac{\partial^2 \mathcal{L}}{\partial \gamma \partial \lambda}\right) \\ -E\left(\frac{\partial^2 \mathcal{L}}{\partial \lambda \partial \gamma}\right) & -E\left(\frac{\partial^2 \mathcal{L}}{\partial \lambda^2}\right) \end{bmatrix}, \quad (9)$$

where

$$\frac{\partial^2 \mathcal{L}}{\partial \gamma^2} = \frac{-r}{\gamma^2} - \lambda \sum_{i=1}^r x_i^{-\gamma} (\ln x_i)^2 - \sum_{j=1}^m \frac{\lambda R_j C_j \ln T_{q_j}}{A_j^2}, \quad (10)$$

$$\frac{\partial^2 \mathcal{L}}{\partial \lambda^2} = \frac{-r}{\lambda^2} - \sum_{j=1}^m \frac{B_j R_j}{A_j^2},$$

$$\frac{\partial^2 \mathcal{L}}{\partial \gamma \partial \lambda} = \sum_{i=1}^r x_i^{-\gamma} \ln x_i - \sum_{j=1}^m \frac{R_j C_j}{A_j^2}, \quad (11)$$

where $B_j = (\partial A_j / \partial \lambda) = \exp(\lambda/T_{q_j}^\gamma)$ and $C_j = (\partial A_j / \partial \gamma) = \ln T_{q_j} [A_j - \lambda B_j]$. Paper [18] came to the conclusion that the approximation V-C matrix might be constructed by

substituting anticipated values with their MLEs. The estimated sample information matrix will now be generated as

$$I(\hat{\gamma}, \hat{\lambda}) = - \begin{bmatrix} \frac{\partial^2 \mathcal{L}}{\partial \gamma^2} & \frac{\partial^2 \mathcal{L}}{\partial \gamma \partial \lambda} \\ \frac{\partial^2 \mathcal{L}}{\partial \lambda \partial \gamma} & \frac{\partial^2 \mathcal{L}}{\partial \lambda^2} \end{bmatrix}, \quad (12)$$

and hence the approximate V-C matrix of $\hat{\gamma}$ and $\hat{\lambda}$ will be

$$\begin{bmatrix} \sigma_{11} & \sigma_{12} \\ \sigma_{21} & \sigma_{22} \end{bmatrix} = - \begin{bmatrix} \frac{\partial^2 \mathcal{L}}{\partial \gamma^2} & \frac{\partial^2 \mathcal{L}}{\partial \gamma \partial \lambda} \\ \frac{\partial^2 \mathcal{L}}{\partial \lambda \partial \gamma} & \frac{\partial^2 \mathcal{L}}{\partial \lambda^2} \end{bmatrix}_{\gamma=\hat{\gamma}, \lambda=\hat{\lambda}}^{-1}. \quad (13)$$

Focused on the empirical distribution of the MLE of the parameters, CIs for the unknown parameters γ and λ will be computed. It is established from the empirical distribution of the MLE of the parameters that

$$(\hat{\gamma}, \hat{\lambda}) - (\gamma, \lambda) \longrightarrow N_2(0, I^{-1}(\hat{\gamma}, \hat{\lambda})), \quad (14)$$

where $N_2(\cdot)$ is bivariate normal distribution and $I(\cdot)$ is the Fisher information matrix which is defined in equation (12).

Considering specific regularity constraints, the two-sided $100(1 - \alpha)\%$, $0 < \alpha < 1$, ACIs for the unknown parameters γ and λ can be obtained as $\hat{\gamma} \pm Z_{\alpha/2} \sqrt{\sigma_{11}}$ and $\hat{\lambda} \pm Z_{\alpha/2} \sqrt{\sigma_{22}}$, where σ_{11} and σ_{22} are the asymptotic Vs of the MLEs of γ and λ , respectively; here $Z_{\alpha/2}$ is the upper $\alpha/2^{\text{th}}$ percentile of the standard normal distribution.

3. Bayesian Estimation

In this part, we will look at how to use Bayesian estimation to estimate the unknown parameters of an IW distribution using a PCTI method. The SEr loss function will be used for Bayesian parameter estimation. It is possible to use separate gamma priors for both parameters of the IW distribution γ and λ with pdfs

$$\pi_1(\gamma) \propto \gamma^{a_1-1} \exp(-b_1\gamma), \gamma > 0, a_1 > 0, b_1 > 0, \quad (15)$$

$$\pi_2(\lambda) \propto \lambda^{a_2-1} \exp(-b_2\lambda), \lambda > 0, a_2 > 0, b_2 > 0, \quad (16)$$

The hyperparameters a_1, b_1, a_2, b_2 are used to represent past knowledge of the unknown parameters in this situation. The joint prior (JP) for γ and λ is as follows:

$$\pi(\gamma, \lambda) \propto \gamma^{a_1-1} \lambda^{a_2-1} \exp(-b_1\gamma - b_2\lambda). \quad (17)$$

Hyperparameter elicitation: the informative priors (IPs) will be used to elicit the hyperparameters. The above IPs will indeed be deduced from the MLEs for (γ, λ) by equating the M and V of $(\hat{\gamma}^j, \hat{\lambda}^j)$ with both the M and V of the regarded priors (Gamma priors), where $j = 1, 2, \dots, k$ and k is the number of observations from the IW distribution that are

available. Thus, on equating M and V of $(\hat{\gamma}^j, \hat{\lambda}^j)$ with the M and V of gamma priors, we acquire (29)

$$\frac{1}{k} \sum_{j=1}^k \hat{\gamma}^j = \frac{a_1}{b_1} \text{ and } \frac{1}{k-1} \sum_{j=1}^k \left(\hat{\gamma}^j - \frac{1}{k} \sum_{j=1}^k \hat{\gamma}^j \right)^2 = \frac{a_1}{b_1^2},$$

$$\frac{1}{k} \sum_{j=1}^k \hat{\lambda}^j = \frac{a_2}{b_2} \text{ and } \frac{1}{k-1} \sum_{j=1}^k \left(\hat{\lambda}^j - \frac{1}{k} \sum_{j=1}^k \hat{\lambda}^j \right)^2 = \frac{a_2}{b_2^2}. \tag{18}$$

The calculated hyperparameters may now be expressed as after solving the preceding two equations

$$a_1 = \frac{(1/k \sum_{j=1}^k \hat{\gamma}^j)^2}{1/k - 1 \sum_{j=1}^k (\hat{\gamma}^j - 1/k \sum_{j=1}^k \hat{\gamma}^j)^2} \text{ and } b_1 = \frac{1/k \sum_{j=1}^k \hat{\gamma}^j}{1/k - 1 \sum_{j=1}^k (\hat{\gamma}^j - 1/k \sum_{j=1}^k \hat{\gamma}^j)^2},$$

$$a_2 = \frac{(1/k \sum_{j=1}^k \hat{\lambda}^j)^2}{1/k - 1 \sum_{j=1}^k (\hat{\lambda}^j - 1/k \sum_{j=1}^k \hat{\lambda}^j)^2} \text{ and } b_2 = \frac{1/k \sum_{j=1}^k \hat{\lambda}^j}{1/k - 1 \sum_{j=1}^k (\hat{\lambda}^j - 1/k \sum_{j=1}^k \hat{\lambda}^j)^2}. \tag{19}$$

According to the observed data, the appropriate posterior density (PD) $x = (x_{(1)}, x_{(2)}, \dots, x_{(r)})$ can indeed be expressed as

$$\pi(\gamma, \lambda | x) = \frac{\pi(\gamma, \lambda)L(\gamma, \lambda)}{\int_0^\infty \int_0^\infty \pi(\gamma, \lambda)L(\gamma, \lambda)d\gamma d\lambda}. \tag{20}$$

The PD function is denoted by the symbol

$$\pi(\gamma, \lambda | x) = K^{-1} \left[\gamma^{r+a_1-1} \lambda^{r+a_2-1} \exp(-b_1\gamma - b_2\lambda) \prod_{i=1}^r \left(x_i^{-(\gamma+1)} \exp\left(\frac{-\lambda}{x_i^\gamma}\right) \right) \prod_{j=1}^m \left(1 - \exp\left(\frac{-\lambda}{T_{q_j}^\gamma}\right) \right)^{R_j} \right], \tag{21}$$

where

$$K = \int_0^\infty \int_0^\infty \gamma^{r+a_1-1} \lambda^{r+a_2-1} \exp(-b_1\gamma - b_2\lambda) \prod_{i=1}^r \left(x_i^{-(\gamma+1)} \exp\left(\frac{-\lambda}{x_i^\gamma}\right) \right) \prod_{j=1}^m \left(1 - \exp\left(\frac{-\lambda}{T_{q_j}^\gamma}\right) \right)^{R_j} d\gamma d\lambda. \tag{22}$$

As a result, the PD may be rewritten as follows:

$$\pi(\gamma, \lambda | x) \propto \gamma^{r+a_1-1} \lambda^{r+a_2-1} \exp(-b_1\gamma - b_2\lambda) \prod_{i=1}^r \left(x_i^{-(\gamma+1)} \exp\left(\frac{-\lambda}{x_i^\gamma}\right) \right) \prod_{j=1}^m \left(1 - \exp\left(\frac{-\lambda}{T_{q_j}^\gamma}\right) \right)^{R_j}. \tag{23}$$

Under the SER, the Bayes estimator of any function, such as $g(\gamma, \lambda)$, is provided by

$$\bar{g}(\gamma, \lambda) = \int_0^\infty \int_0^\infty g(\gamma, \lambda)\pi(\gamma, \lambda | x)d\gamma d\lambda. \tag{24}$$

Consequently, equation (24) cannot be calculated for general $g(\gamma, \lambda)$. As a result, we recommend using the most widely used approximate BEs of γ and λ MCMC.

3.1. Lindley's Approximation. Lindley proposed an approximation to compute the ratio of integrals of the form in equation (25) for the specified priors on γ and λ and under the SER loss function. Consider the ratio $L(X)$

$$L(X) = \frac{\int_{(\gamma, \lambda)} g(\gamma, \lambda) \exp[\mathcal{L}(\gamma, \lambda) + \rho(\gamma, \lambda)] d(\gamma, \lambda)}{\int_{(\gamma, \lambda)} \exp[\mathcal{L}(\gamma, \lambda) + \rho(\gamma, \lambda)] d(\gamma, \lambda)}, \tag{25}$$

where $g(\gamma, \lambda)$ is function of γ and λ only and $\mathcal{L}(\gamma, \lambda)$ is the log-LL given in (5) and $\rho(\gamma, \lambda)$ is the log-JP distribution. Using the approach developed by [19], the ratio $L(X)$ can be expressed as

$$\begin{aligned} L(X) = & \hat{g}(\gamma, \lambda) + \frac{1}{2} \left[(\hat{g}_{\gamma\gamma} + 2\hat{g}_{\gamma\hat{\rho}_\gamma})\hat{\sigma}_{\gamma\gamma} + (\hat{g}_{\lambda\gamma} + 2\hat{g}_{\lambda\hat{\rho}_\gamma})\hat{\sigma}_{\lambda\gamma} \right. \\ & + (\hat{g}_{\gamma\lambda} + 2\hat{g}_{\gamma\hat{\rho}_\lambda})\hat{\sigma}_{\gamma\lambda} + (\hat{g}_{\lambda\lambda} + 2\hat{g}_{\lambda\hat{\rho}_\lambda})\hat{\sigma}_{\lambda\lambda} \left. \right] \\ & + \frac{1}{2} \left[(\hat{g}_{\gamma\gamma}\hat{\sigma}_{\gamma\gamma} + \hat{g}_{\lambda\lambda}\hat{\sigma}_{\lambda\lambda}) (\hat{\mathcal{L}}_{\gamma\gamma\gamma}\hat{\sigma}_{\gamma\gamma} + \hat{\mathcal{L}}_{\gamma\lambda\gamma}\hat{\sigma}_{\gamma\lambda} + \hat{\mathcal{L}}_{\lambda\gamma\gamma}\hat{\sigma}_{\lambda\gamma} \right. \\ & + \hat{\mathcal{L}}_{\lambda\lambda\gamma}\hat{\sigma}_{\lambda\lambda}) + (\hat{g}_{\gamma\gamma}\hat{\sigma}_{\lambda\gamma} + \hat{g}_{\lambda\lambda}\hat{\sigma}_{\lambda\lambda}) (\hat{\mathcal{L}}_{\lambda\gamma\gamma}\hat{\sigma}_{\gamma\gamma} + \hat{\mathcal{L}}_{\gamma\lambda\lambda}\hat{\sigma}_{\gamma\lambda} \hat{\mathcal{L}}_{\lambda\gamma\lambda} \\ & \left. + \hat{\sigma}_{\lambda\gamma} + \hat{\mathcal{L}}_{\lambda\lambda\lambda}\hat{\sigma}_{\lambda\lambda}) \right], \end{aligned} \quad (26)$$

where

$$\begin{aligned} \hat{g}_i = \frac{\partial g(\gamma, \lambda)}{\partial i} \Big|_{\gamma=\hat{\gamma}, \lambda=\hat{\lambda}}, \quad \hat{g}_{ij} = \frac{\partial^2 g(\gamma, \lambda)}{\partial i \partial j} \Big|_{\gamma=\hat{\gamma}, \lambda=\hat{\lambda}}, \quad \hat{\rho}_i = \frac{\partial \rho(\gamma, \lambda)}{\partial i} \Big|_{\gamma=\hat{\gamma}, \lambda=\hat{\lambda}}, \\ \hat{\mathcal{L}}_{ij} = \frac{\partial^2 \mathcal{L}(\gamma, \lambda)}{\partial i \partial j} \Big|_{\gamma=\hat{\gamma}, \lambda=\hat{\lambda}}, \quad \hat{\mathcal{L}}_{ijk} = \frac{\partial^3 \mathcal{L}(\gamma, \lambda)}{\partial i \partial j \partial k} \Big|_{\gamma=\hat{\gamma}, \lambda=\hat{\lambda}}, \quad \hat{\sigma} = -\frac{1}{\hat{\mathcal{L}}} \Big|_{\gamma=\hat{\gamma}, \lambda=\hat{\lambda}}. \end{aligned} \quad (27)$$

Partial derivatives of \mathcal{L} in equations (7)–(11) are also

$$\begin{aligned} \mathcal{L}_{\gamma\gamma\gamma} &= \frac{2r}{\gamma^3} + \lambda \sum_{i=1}^r x_i^{-\gamma} (\ln x_i)^3 - \sum_{j=1}^m \lambda R_j \ln T_{q_j} (K_j A_j - 2C_j^v) A_j^3, \\ \mathcal{L}_{\lambda\lambda\lambda} &= \frac{2r}{\lambda^3} - \sum_{j=1}^m R_j (D_j A_j - 2B_j^2) A_j^3, \\ \mathcal{L}_{\gamma\lambda\gamma} &= -\sum_{i=1}^r x_i^{-\gamma} (\ln x_i)^2 - \sum_{j=1}^m R_j (K_j A_j - 2C_j^2) A_j^3, \end{aligned} \quad (28)$$

$$\mathcal{L}_{\gamma\lambda\lambda} = -\sum_{j=1}^m \frac{E_j R_j (A_j - 2B_j)}{A_j^3}, \quad (29)$$

where $D_j = (\partial B_j / \partial \lambda) = T_{q_j}^{-\gamma} B_j$, $E_j = (\partial B_j / \partial \gamma) = -\lambda T_{q_j}^{-\gamma} \ln T_{q_j} B_j$, $F_j = (\partial C_j / \partial \lambda) = -\lambda D_j \ln T_{q_j}$, and $K_j = (\partial C_j / \partial \gamma) = \ln T_{q_j} [B_j - \lambda E_j]$.

The log-JP is given as

$$\begin{aligned} \rho(\gamma, \lambda) = \log[\pi(\gamma, \lambda)] = C + (a_1 - 1) \log \gamma \\ + (a_2 - 1) \lambda - b_1 \gamma - b_2 \lambda. \end{aligned} \quad (30)$$

Thus, the partial derivatives of log-JP distribution are

$$\rho_\gamma = \frac{\partial \rho(\gamma, \lambda)}{\partial \gamma} = \frac{a_1 - 1}{\gamma} - b_1, \quad (31)$$

$$\rho_\lambda = \frac{\partial \rho(\gamma, \lambda)}{\partial \lambda} = \frac{a_2 - 1}{\lambda} - b_2. \quad (32)$$

Under the SEr function, the BE of γ is already provided as

$$\begin{aligned} g(\gamma, \lambda) = \gamma \Rightarrow g_\gamma = 1, g_\lambda = g_{\gamma\gamma} = g_{\gamma\lambda} = g_{\lambda\gamma} = g_{\lambda\lambda} \\ = 0 \text{ and } \mathcal{L}_{\gamma\lambda\lambda} = 0. \end{aligned} \quad (33)$$

By substituting equations (7)–(11), (18)–(33) in (26), the estimates of γ and λ can be written as $\hat{\gamma}_{\text{Lindley}}$ and $\hat{\lambda}_{\text{Lindley}}$.

3.2. Metropolis–Hasting Algorithm. We need to specify IW model and beginning values for the unknown parameters γ and λ to run the MH method for the IW distribution. We explore a bivariate normal distribution for the proposal distribution, that is, $q((\gamma', \lambda') | (\gamma, \lambda)) = N_2((\gamma, \lambda), S_{\gamma, \lambda})$. We may get negative observations, which are undesirable, if $S_{\gamma, \lambda}$ represents the variance-covariance matrix. We use the MLE for γ and λ to determine the starting values, that is, $(\gamma^{(0)}, \lambda^{(0)}) = (\hat{\gamma}, \hat{\lambda})$. The selection of $S_{\gamma, \lambda}$ is examined to be the asymptotic V-C matrix $I^{-1}(\hat{\gamma}, \hat{\lambda})$, where $I(\cdot)$ is the Fisher information matrix. It is worth mentioning that the choice of $S_{\gamma, \lambda}$ is critical in the MH Algorithm 1, since the acceptance rate is determined by it. The following steps are followed used by the MH method to draw a sample from the PD given by equation (24) supplied in the following manner.

$$\begin{cases} \text{If } u \leq \beta & \text{set } \theta^{(i)} = \theta' \\ \text{otherwise} & \text{set } \theta^{(i)} = \theta. \end{cases} \quad (34)$$

Eventually, using the PD's random samples of size M , part of the initial samples can indeed be eliminated (burn-in), and the remaining samples can be used to produce BEs. Extra precisely equation (24) can be estimated as

$$\tilde{g}_{\text{MH}}(\gamma, \lambda) = \frac{1}{M - I_B} \sum_{i=I_B}^M g(\gamma_i, \lambda_i), \quad (35)$$

where I_B is the total number of burn-in samples.

3.3. Highest Posterior Density (HPD). We use the samples generated from the proposed MH method in the preceding subsection to create HPD intervals for the unknown parameters γ and λ of the IW distribution under PCTI. Consider the following scenario: $\gamma^{(\delta)}$ and $\lambda^{(\delta)}$ are the δ th Q of γ and λ , respectively, that is,

$$(\gamma^{(\delta)}, \lambda^{(\delta)}) = \inf\{(\gamma, \lambda) : \Pi((\gamma, \lambda) | x) \geq \delta\}, \quad (36)$$

where $0 < \delta < 1$ and $\Pi(\cdot)$ is the posterior distribution function of γ and λ . It is worth noting that, for specific γ^* and λ^* , a simulation accurate estimator of $\pi((\gamma, \lambda) | x)$ may be calculated as

$$\Pi((\gamma^*, \lambda^*) | x) = \frac{1}{M - I_B} \sum_{i=I_B}^M I_{(\gamma, \lambda) \leq (\gamma^*, \lambda^*)}. \quad (37)$$

Here $I_{(\gamma, \lambda) \leq (\gamma^*, \lambda^*)}$ is the indicator function. Then the appropriate estimate is computed as

First Step Put initial value of θ as $\theta^{(0)} = (\tilde{\gamma}, \tilde{\lambda})$.
Second Step For $i = 1, 2, \dots, M$ the necessary phases should be repeated:
 2.1: Set $\theta = \theta^{(i-1)}$.
 2.2: Create a new value for the candidate parameter δ from $N_2(\ln \theta, S_\theta)$.
 2.3: Set $\theta' = \exp(\delta)$.
 2.4: Compute $\beta = (\pi(\theta' | x) / \pi(\theta | x))$, where $\pi(\cdot)$ is the PD.
 2.5: Construct a sample u from the uniform $U(0, 1)$ model
 2.6: Accept or deny the new request according to θ'

ALGORITHM 1: Algorithm of MCMC.

$$\hat{\Pi}((\gamma^*, \lambda^*) | x) = \begin{cases} 0 & \text{if } (\gamma^*, \lambda^*) < (\gamma_{(l_B)}, \lambda_{(l_B)}) \\ \sum_{j=l_B}^i \omega_j & \text{if } (\gamma_{(i)}, \lambda_{(i)}) < (\gamma^*, \lambda^*) < (\gamma_{(i+1)}, \lambda_{(i+1)}) \\ 1 & \text{if } (\gamma^*, \lambda^*) > (\gamma_{(M)}, \lambda_{(M)}) \end{cases} \quad (38)$$

where $\omega_j = (1/M - l_B)$ and $(\gamma_{(j)}, \lambda_{(j)})$ are the ordered values of (γ_j, λ_j) . Now, for $i = l_B, \dots, M$, $(\gamma^{(\delta)}, \lambda^{(\delta)})$ can be approximated by

$$(\tilde{\gamma}^{(\delta)}, \tilde{\lambda}^{(\delta)}) = \begin{cases} (\gamma_{(l_B)}, \lambda_{(l_B)}) & \text{if } \delta = 0 \\ (\gamma_{(i)}, \lambda_{(i)}) & \text{if } \sum_{j=l_B}^{i-1} \omega_j < \delta < \sum_{j=l_B}^i \omega_j \end{cases} \quad (39)$$

Let us now compute a $100(1 - \delta)\%$ HPD credible interval for γ and λ

$$\begin{aligned} \text{HPD}_j^\gamma &= (\tilde{\gamma}^{(j/M)}, \tilde{\gamma}^{(j+(1-\delta)M/M)}) \text{ and } \text{HPD}_j^\lambda \\ &= (\tilde{\lambda}^{(j/M)}, \tilde{\lambda}^{(j+(1-\delta)M/M)}) \end{aligned} \quad (40)$$

for $j = l_B, \dots, [\delta M]$; here $[a]$ represents the biggest integer that is less than or equal to a . Then select HPD_j from among all HPD_j 's with the shortest width.

4. Simulation Study and Real Data Application

4.1. Simulation Study. In this part, we use a Monte Carlo simulation study to evaluate the performance of estimation approaches, namely, MLE and Bayesian estimation using MCMC and Lindley's approximation, for the IW distribution using a PCTI scheme. We create 1000 data sets from the IW distribution for the MLEs under the next assumptions:

- (1) Two initial values are IW ($\gamma = 2, \lambda = 1.5$) and IW ($\gamma = 1, \lambda = 2$)
- (2) Sample sizes are $n = 25, 50, 100$
- (3) Number of stages of PCTI is $m = 3, 4, 5$
- (4) Censoring time T_{q_j} is calculated on the basis for the identified q_j^{th} Qs from IW (2, 1.5) and IW (1, 2):
 - (a) At $m = 3$ and $q_j = (10\%, 40\%, 70\%)$

- (b) At $m = 4$ and $q_j = (10\%, 30\%, 50\%, 70\%)$
- (c) At $m = 5$ and $q_j = (10\%, 25\%, 40\%, 55\%, 70\%)$

- (5) Omitted items R_j are proposed based on a fraction of sample size n where the number of removed items in each stage of censoring can be computed from

$$R_j = \lceil \frac{f\%n}{m-1} \rceil, f = 0\%, 25\%, 50\%. \quad (41)$$

Thus, the proposed schemes of removing items can be

Scheme I ($f = 0\%$): $R_1 = R_2 = \dots = R_{m-1} = 0$,

Scheme II ($f = 25\%$): $R_1 = R_2 = \dots = R_{m-1} = \lceil 25\%n/m - 1 \rceil$

Scheme III ($f = 50\%$): $R_1 = R_2 = \dots = R_{m-1} = \lceil 50\%n/m - 1 \rceil$,

When $R_m = n - (\sum_{j=1}^{m-1} R_j + r)$ and r is the number of failure items and $\lceil \cdot \rceil$ is the ceiling function. It is indicated that scheme I represents Type-I censoring scheme where $R_m = n - r$.

We construct MLEs and related 95% asymptotic CIs premised on the data that is generated. When constructing MLEs, the initial estimate values are assumed to be the same as the real parameter values.

Under the informative prior (IP), we calculate BEs using the MH algorithm for Bayesian estimation. Thus, we have the following.

- (i) As previous samples for the gamma prior, we produce 1000 complete samples of size 60 each from the IW (2, 1.5) and IW (1, 2) distributions, and then obtain the hyperparameter values accordingly: $a_1 = 22.74, b_1 = 14.20, a_2 = 9.65, b_2 = 4.29$.

To compute the desired estimations, the aforementioned IP values are entered in. We use the MLEs as starting guess values, as well as the related V-C matrix S_θ of $(\ln(\hat{\lambda}), \ln(\hat{\alpha}))$ when using the MH algorithm. Finally, we eliminated 2000

burn-in samples from the total of 10,000 samples generated by the PD and then used [20] approach to get BEs and HPD interval estimations.

Tables 1–6 show the average estimates for both techniques. In addition, the first row displays average estimates (AVEs) and interval estimates (IEs), while the second row displays related mean square errors (MSEs) and average lengths (ALs) with coverage probabilities (CPrs). It can be seen from the table of values that, depending on MSEs, larger values of n result in better estimates. It is also worth noting that MLEs outperform Lindley BEs and that the performance of BEs produced using MCMC outperforms Bayes estimates obtained via LiA. It is also worth noting that MCMC's ALs and related CPrs for HPD intervals outperform LiA. Furthermore, when the units are eliminated at an early stage in scheme II and scheme III, MSEs and ALs of related interval estimations are typically smaller.

4.2. Real Data Application. Two real data set are investigated for illustration and also to examine the statistical performance of the MLEs and BEs for the IW distribution under different PCTI censoring schemes.

4.2.1. Data Set I. The accompanying basic data set corresponds to an unfiltered data set. The data collection includes 34 observations of vinyl chloride data from [21], which indicates cleanup gradient ground–water monitoring wells in mg/L.

We begin by determining if the IW distribution is appropriate for studying this data set. To assess the quality of fit, we provide the MLEs of the parameters as well as the value of the Kolmogorov–Smirnov (KS) test statistic. The estimated KS and p -value for the IW distribution are 0.1161 and 0.7496, respectively, where $\hat{\gamma} = 0.8431$ and $\hat{\lambda} = 0.7121$, which indicate that this distribution can be considered as an adequate model for the given data set.

From the raw data, one may construct, for example, three PCTI censored samples with $m = 3, 4, 5$ stages at time censoring T_{q_j} matching to the chosen q_j^{th} , Qs, where $j = 1, \dots, m$. The sequences of deleted elements are presented for three fractions of eliminating $f = 0\%, 25\%, 50\%$ of total sample size ($n = 34$). Table 7 describes these patterns of removal process.

Here, $(1^{*4}, 0)$ indicates, for example, that the censoring scheme used is $(1, 1, 1, 1, 0)$

In Table 8, the MLEs of the parameters γ and λ , as well as their related standard error and ACI at suggested schemes for PCTI samples in the provided real data set, have been computed.

Additionally, BEs were computed using the MH algorithm under the noninformative prior, i.e., $a_1 = b_1 = a_2 = b_2 = 0$. It is said while using the MH method to generate samples from the posterior distribution, starting values of (γ, λ) are regarded as $(\gamma^{(0)}, \lambda^{(0)}) = (\hat{\gamma}, \hat{\lambda})$ and $\hat{\gamma}, \hat{\lambda}$ are the MLEs of the parameters γ, λ . Afterwards, 2000 burn-in samples were eliminated from the overall 10 000 samples generated by the PD, and BEs and HPD intervals were

produced. BEs based on LiA have been calculated based on the MLEs.

The convergence of MCMC estimate is in the case of PCTI scheme III for the data set I where the percentage of removal is $f = 50\%$. The BEs utilizing MCMC are converged through three subgraphs, as shown in Figure 2: scatter plot, histogram, and cumulative mean of the 10 000 estimates.

4.2.2. Data Set II. A real data set of the carbonation depth of pier of a reinforced concrete girder bridge was analyzed under progressive Type-I censoring scheme [22]. The data set represents 27 measurements which are

2.0, 2.1, 2.2, 2.3, 2.3, 2.3, 2.4, 2.5, 2.6, 2.7, 2.8, 2.9, 3.0, 3.2, 3.2, 3.3, 3.3, 3.3, 3.4, 3.4, 3.4, 3.5, 3.5, 3.6, 3.7, 3.8, 3.9.

First, we check whether the IW distribution is suitable for analyzing this data set. Also, we provide the MLEs of the parameters as well as the value of the Kolmogorov–Smirnov (KS) test statistic. The estimated KS and p -value for the IW distribution are 0.2074 and 0.1957, respectively, where $\hat{\gamma} = 5.2000$ and $\hat{\lambda} = 157.8003$, which indicate that this distribution can be considered as an adequate model for the given data set.

Two different PCTI censored samples are assumed for the given data set with $m = 3, 5$ stages at time censoring T_{q_j} matching to the chosen q_j^{th} , Qs, where $j = 1, \dots, m$. Table 9 describes the patterns of removing elements for three fractions of eliminating $f = 0\%, 25\%, 50\%$ of total sample size ($n = 27$).

In Table 10, the MLEs of the parameters γ and λ , as well as their related ACI estimations and ACI at suggested schemes for PCTI samples in the provided real data set, have been computed.

As in data set I, BEs were computed using the MH algorithm under the noninformative prior. The starting values of (γ, λ) are regarded as $(\gamma^{(0)}, \lambda^{(0)}) = (\hat{\gamma}, \hat{\lambda})$. Finally, 2000 burn-in samples were eliminated from the overall 10 000 samples generated by the PD, and BEs and HPD intervals were produced. BEs based on LiA have been calculated based on the MLEs as a prior estimates.

Figure 3 illustrates the convergence of MCMC estimate in the case of PCTI scheme II for the real data set II where the percentage of removal is $f = 50\%$. The BEs utilizing MCMC are converged through three subgraphs, as shown in scatter plot, histogram, and cumulative mean of the 10 000 estimates.

5. Summary and Conclusion

We investigated the topic of IW distribution estimation and prediction under PCTI from both classical and Bayesian perspectives in this work. For the unknown parameters of the IW distribution, we calculated maximum likelihood estimates and associated asymptotic confidence intervals. Then, using informative priors, we produced Bayes estimates and the related HPD interval estimates. In addition, when an informative prior is taken into account, a discussion of how to pick the values of hyperparameters in Bayesian estimation is examined based on historical samples. The simulation

TABLE 1: Numerical results of AVEs, ACIs, MSErs, ALs, and CPrs (in %) for $\gamma = 2$ and $\lambda = 1.5$ under number of stages $m = 3$.

$f\%$	n	Parm.	MLLE		Bayesian: MCMC		Bayesian: Lindley
			AVE MSEr	ACI AL/CPr	AVE MSEr	HPD AL/CPr	AVE MSEr
0	25	γ	2.102	(1.344, 2.861)	2.078	(1.348, 2.827)	2.062
			0.159	1.517/96.60	0.155	1.479/96.60	0.278
		λ	1.590	(0.952, 2.228)	1.579	(1.003, 2.329)	1.504
			0.148	1.276/94.10	0.142	1.326/96.10	0.387
	50	γ	2.053	(1.536, 2.570)	2.040	(1.536, 2.584)	2.042
			0.078	1.034/95.30	0.077	1.048/96.10	0.102
		λ	1.541	(1.109, 1.972)	1.535	(1.137, 2.022)	1.522
			0.054	0.863/95.40	0.053	0.885/97.00	0.090
	100	γ	2.029	(1.669, 2.389)	2.023	(1.655, 2.363)	2.026
			0.034	0.720/96.50	0.034	0.708/96.20	0.040
		λ	1.513	(1.214, 1.811)	1.510	(1.207, 1.807)	1.507
			0.024	0.597/96.60	0.024	0.600/96.80	0.032
25	25	γ	2.149	(1.328, 2.970)	2.123	(1.383, 3.074)	2.105
			0.216	1.642/95.50	0.211	1.691/97.30	0.367
		λ	1.586	(0.937, 2.235)	1.577	(1.005, 2.320)	1.442
			0.140	1.298/95.10	0.134	1.315/97.00	0.691
	50	γ	2.065	(1.509, 2.621)	2.051	(1.572, 2.679)	2.053
			0.085	1.112/96.00	0.084	1.107/97.90	0.118
		λ	1.545	(1.103, 1.987)	1.541	(1.159, 2.027)	1.523
			0.057	0.884/95.20	0.056	0.868/97.00	0.104
	100	γ	2.028	(1.647, 2.408)	2.021	(1.648, 2.414)	2.023
			0.039	0.761/96.40	0.039	0.766/96.80	0.047
		λ	1.522	(1.217, 1.828)	1.520	(1.192, 1.833)	1.517
			0.027	0.611/95.90	0.026	0.641/96.20	0.037
50	25	γ	2.167	(1.274, 3.059)	2.136	(1.274, 3.055)	2.091
			0.266	1.785/95.70	0.256	1.780/96.00	0.471
		λ	1.578	(0.914, 2.243)	1.573	(0.922, 2.322)	1.298
			0.153	1.328/94.30	0.149	1.399/96.20	2.160
	50	γ	2.071	(1.481, 2.660)	2.055	(1.506, 2.650)	2.054
			0.097	1.179/96.80	0.095	1.144/97.10	0.136
		λ	1.541	(1.092, 1.990)	1.538	(1.112, 2.013)	1.505
			0.057	0.898/96.10	0.056	0.901/96.80	0.137
	100	γ	2.047	(1.642, 2.452)	2.040	(1.630, 2.450)	2.044
			0.046	0.810/96.10	0.046	0.820/96.50	0.055
		λ	1.518	(1.208, 1.828)	1.516	(1.206, 1.825)	1.510
			0.026	0.620/96.80	0.026	0.619/96.80	0.039

Note: Parm.: parameter, AV: average, and ACI: asymptotic confidence interval.

TABLE 2: Numerical results of AVEs, ACIs, MSErs, ALs, and CPrs (in %) for $\gamma = 2$ and $\lambda = 1.5$ under number of stages $m = 4$.

$f\%$	n	Parm.	MLLE		Bayesian: MCMC		Bayesian: Lindley
			AVE MSEr	ACI AL/CPr	AVE MSEr	HPD AL/CPr	AVE MSEr
0	25	γ	2.110	(1.349, 2.871)	2.086	(1.315, 2.841)	2.107
			0.168	1.522/96.10	0.164	1.526/96.20	0.313
		λ	1.605	(0.960, 2.249)	1.593	(0.906, 2.295)	1.497
			0.153	1.289/93.60	0.148	1.389/95.30	2.667
	50	γ	2.057	(1.539, 2.576)	2.045	(1.516, 2.563)	2.048
			0.077	1.036/96.00	0.076	1.047/96.00	0.101
		λ	1.536	(1.106, 1.966)	1.530	(1.100, 1.974)	1.515
			0.055	0.860/95.60	0.053	0.874/95.90	0.091
	100	γ	2.025	(1.666, 2.385)	2.019	(1.688, 2.363)	2.031
			0.032	0.719/97.30	0.032	0.675/97.00	0.039
		λ	1.513	(1.215, 1.812)	1.510	(1.243, 1.823)	1.501
			0.023	0.596/96.90	0.023	0.580/98.00	0.033

TABLE 2: Continued.

$f\%$	n	Parm.	MLLE		Bayesian: MCMC		Bayesian: Lindley
			AVE MSEr	ACI AL/CPr	AVE MSEr	HPD AL/CPr	AVE MSEr
25	25	γ	2.158	(1.308, 3.007)	2.127	(1.267, 3.025)	2.102
			0.245	1.699/95.10	0.237	1.758/96.00	0.427
		λ	1.586	(0.931, 2.242)	1.578	(0.917, 2.249)	1.385
			0.169	1.311/95.50	0.169	1.331/96.10	1.224
	50	γ	2.083	(1.520, 2.645)	2.069	(1.566, 2.702)	2.072
			0.096	1.125/95.80	0.094	1.136/97.70	0.131
		λ	1.552	(1.109, 1.995)	1.548	(1.125, 2.068)	1.529
			0.061	0.886/94.70	0.059	0.943/97.10	0.113
	100	γ	2.032	(1.650, 2.413)	2.025	(1.607, 2.409)	2.033
			0.042	0.763/96.00	0.042	0.802/96.30	0.046
		λ	1.517	(1.213, 1.821)	1.515	(1.218, 1.810)	1.523
			0.028	0.608/96.60	0.027	0.592/96.30	0.037
50	25	γ	2.175	(1.271, 3.078)	2.141	(1.369, 2.995)	2.108
			0.239	1.807/96.60	0.227	1.626/96.30	0.425
		λ	1.576	(0.917, 2.234)	1.571	(0.928, 2.283)	1.298
			0.140	1.317/94.80	0.136	1.354/96.20	1.758
	50	γ	2.071	(1.481, 2.659)	2.054	(1.518, 2.643)	2.055
			0.090	1.178/96.70	0.088	1.125/96.60	0.128
		λ	1.527	(1.085, 1.970)	1.524	(1.143, 1.965)	1.491
			0.053	0.884/96.80	0.052	0.821/97.00	0.120
	100	γ	2.030	(1.622, 2.437)	2.022	(1.604, 2.408)	2.031
			0.047	0.815/97.00	0.047	0.804/96.50	0.056
		λ	1.522	(1.212, 1.833)	1.521	(1.222, 1.864)	1.519
			0.029	0.621/95.80	0.028	0.642/97.20	0.039

Note: Parm.: parameter, AV: average, and ACI: asymptotic confidence interval.

TABLE 3: Numerical results of AVEs, ACIs, MSErs, ALs, and CPrs (in %) for $\gamma = 2$ and $\lambda = 1.5$ under number of stages $m = 5$.

$f\%$	n	Parm.	MLLE		Bayesian: MCMC		Bayesian: Lindley
			AVE MSEr	ACI AL/CPr	AVE MSEr	HPD AL/CPr	AVE MSEr
0	25	γ	2.110	(1.352, 2.869)	2.086	(1.412, 2.891)	2.072
			0.158	1.517/96.30	0.154	1.479/97.30	0.265
		λ	1.600	(0.958, 2.241)	1.588	(0.946, 2.310)	1.501
			0.151	1.283/94.40	0.144	1.364/95.90	0.575
	50	γ	2.070	(1.550, 2.590)	2.058	(1.560, 2.586)	2.062
			0.079	1.040/96.20	0.077	1.026/96.70	0.104
		λ	1.529	(1.101, 1.956)	1.522	(1.141, 1.993)	1.505
			0.051	0.855/96.20	0.049	0.852/97.90	0.092
	100	γ	2.024	(1.664, 2.383)	2.017	(1.698, 2.415)	2.020
			0.034	0.719/96.10	0.033	0.717/97.50	0.039
		λ	1.521	(1.221, 1.821)	1.518	(1.217, 1.827)	1.516
			0.025	0.600/95.80	0.025	0.610/96.60	0.032
25	25	γ	2.156	(1.275, 3.038)	2.124	(1.331, 3.074)	2.099
			0.228	1.763/95.50	0.218	1.743/96.50	0.412
		λ	1.596	(0.930, 2.261)	1.590	(0.931, 2.268)	1.412
			0.206	1.331/94.70	0.211	1.337/95.60	0.936
	50	γ	2.070	(1.498, 2.642)	2.055	(1.541, 2.668)	2.057
			0.093	1.144/96.10	0.090	1.127/97.00	0.127
		λ	1.542	(1.100, 1.983)	1.537	(1.105, 1.977)	1.512
			0.055	0.883/96.60	0.054	0.872/96.70	0.119
	100	γ	2.034	(1.645, 2.423)	2.026	(1.662, 2.427)	2.030
			0.040	0.778/96.30	0.040	0.765/96.80	0.047
		λ	1.523	(1.217, 1.828)	1.521	(1.245, 1.840)	1.517
			0.025	0.611/97.10	0.024	0.595/97.70	0.035

TABLE 3: Continued.

$f\%$	n	Parm.	MLLE		Bayesian: MCMC		Bayesian: Lindley
			AVE MSEr	ACI AL/CPr	AVE MSEr	HPD AL/CPr	AVE MSEr
50	25	γ	2.178	(1.217, 3.139)	2.138	(1.311, 3.250)	2.076
			0.309	1.922/94.40	0.295	1.939/97.00	0.575
		λ	1.594	(0.915, 2.272)	1.590	(0.876, 2.263)	1.242
			0.193	1.357/95.60	0.190	1.387/95.70	3.589
	50	γ	2.101	(1.477, 2.724)	2.082	(1.504, 2.775)	2.084
			0.119	1.247/95.70	0.115	1.271/97.40	0.166
		λ	1.541	(1.091, 1.992)	1.539	(1.041, 2.019)	1.493
			0.064	0.901/94.80	0.063	0.978/95.80	0.175
	100	γ	2.034	(1.615, 2.452)	2.025	(1.637, 2.471)	2.028
			0.048	0.836/96.20	0.047	0.833/97.30	0.058
		λ	1.516	(1.206, 1.827)	1.515	(1.228, 1.851)	1.506
			0.027	0.621/96.10	0.027	0.622/97.20	0.043

Note: Parm.: parameter, AV: average, and ACI: asymptotic confidence interval.

TABLE 4: Numerical results of AVEs, ACIs, MSErs, ALs, and CPrs (in %) for $\gamma = 1$ and $\lambda = 2$ under number of stages $m = 3$.

$f\%$	n	Parm.	MLLE		Bayesian: MCMC		Bayesian: Lindley
			AVE MSEr	ACI AL/CPr	AVE MSEr	HPD AL/CPr	AVE MSEr
0	25	γ	1.072	(0.688, 1.456)	1.060	(0.644, 1.455)	1.013
			0.051	0.768/95.20	0.050	0.811/95.60	0.323
		λ	2.166	(1.251, 3.081)	2.148	(1.285, 3.286)	2.155
			0.359	1.830/93.80	0.356	2.001/95.70	0.365
	50	γ	1.037	(0.776, 1.299)	1.031	(0.764, 1.288)	1.023
			0.021	0.523/96.20	0.020	0.524/96.00	0.062
		λ	2.086	(1.480, 2.692)	2.075	(1.502, 2.736)	2.082
			0.131	1.212/94.60	0.128	1.234/96.10	0.132
	100	γ	1.011	(0.830, 1.190)	1.007	(0.852, 1.202)	1.002
			0.009	0.360/96.90	0.008	0.350/98.20	0.016
		λ	2.025	(1.615, 2.436)	2.021	(1.614, 2.436)	2.025
			0.046	0.821/95.80	0.046	0.822/96.10	0.047
25	25	γ	1.074	(0.663, 1.485)	1.061	(0.692, 1.483)	1.011
			0.052	0.822/96.10	0.053	0.791/96.70	0.386
		λ	2.156	(1.236, 3.077)	2.150	(1.387, 3.158)	2.142
			0.356	1.841/95.10	0.357	1.771/96.60	0.363
	50	γ	1.042	(0.762, 1.322)	1.035	(0.760, 1.310)	1.025
			0.022	0.560/96.90	0.021	0.550/96.90	0.079
		λ	2.090	(1.476, 2.703)	2.081	(1.491, 2.813)	2.085
			0.130	1.227/94.30	0.127	1.322/97.10	0.133
	100	γ	1.013	(0.820, 1.199)	1.006	(0.831, 1.193)	0.999
			0.010	0.379/96.50	0.009	0.362/96.60	0.019
		λ	2.029	(1.615, 2.443)	2.024	(1.608, 2.435)	2.028
			0.046	0.828/96.50	0.045	0.827/96.60	0.047
50	25	γ	1.086	(0.637, 1.535)	1.071	(0.657, 1.649)	0.964
			0.071	0.898/94.10	0.070	0.992/97.00	0.756
		λ	2.153	(1.225, 3.082)	2.140	(1.316, 3.179)	2.132
			0.303	1.857/95.00	0.301	1.863/96.20	0.322
	50	γ	1.034	(0.739, 1.329)	1.026	(0.744, 1.339)	0.994
			0.025	0.590/95.80	0.025	0.595/96.90	0.122
		λ	2.078	(1.464, 2.693)	2.070	(1.446, 2.738)	2.072
			0.127	1.229/95.20	0.124	1.292/96.30	0.132
	100	γ	1.014	(0.813, 1.215)	1.010	(0.814, 1.211)	1.002
			0.010	0.402/96.90	0.010	0.397/96.70	0.024
		λ	2.036	(1.616, 2.455)	2.031	(1.594, 2.455)	2.034
			0.054	0.839/95.30	0.053	0.861/95.40	0.055

Note: Parm.: parameter, AV average, and ACI asymptotic confidence interval.

TABLE 5: Numerical results of AVEs, ACIs, MSERs, ALs, and CPrs (in %) for $\gamma = 1$ and $\lambda = 2$ under number of stages $m = 4$.

$f\%$	n	Parm.	MLLE		Bayesian: MCMC		Bayesian: Lindley
			AVE MSEr	ACI AL/CPr	AVE MSEr	HPD AL/CPr	AVE MSEr
0	25	γ	1.074	(0.690, 1.458)	1.061	(0.683, 1.436)	1.036
			0.046	0.768/96.10	0.044	0.753/95.80	0.264
		λ	2.161	(1.251, 3.071)	2.141	(1.326, 3.224)	2.149
			0.326	1.820/94.00	0.317	1.898/96.20	0.333
	50	γ	1.027	(0.768, 1.285)	1.020	(0.762, 1.274)	1.005
			0.018	0.517/96.80	0.018	0.512/96.70	0.059
		λ	2.075	(1.473, 2.676)	2.064	(1.526, 2.738)	2.071
			0.116	1.203/95.00	0.113	1.212/96.50	0.117
	100	γ	1.016	(0.835, 1.196)	1.013	(0.835, 1.182)	1.010
			0.008	0.361/96.60	0.007	0.347/96.30	0.015
		λ	2.027	(1.616, 2.437)	2.021	(1.633, 2.465)	2.025
			0.048	0.821/95.60	0.047	0.832/96.90	0.048
25	25	γ	1.089	(0.661, 1.516)	1.074	(0.674, 1.538)	1.032
			0.060	0.855/94.90	0.057	0.864/96.10	0.475
		λ	2.166	(1.241, 3.091)	2.150	(1.359, 3.343)	2.145
			0.334	1.850/94.10	0.328	1.984/97.10	0.351
	50	γ	1.036	(0.756, 1.316)	1.029	(0.744, 1.310)	1.012
			0.022	0.560/95.90	0.021	0.566/96.40	0.083
		λ	2.070	(1.465, 2.675)	2.060	(1.498, 2.777)	2.064
			0.118	1.210/94.70	0.115	1.279/96.60	0.121
	100	γ	1.015	(0.824, 1.206)	1.011	(0.832, 1.238)	1.005
			0.011	0.382/95.60	0.010	0.406/97.60	0.022
		λ	2.038	(1.622, 2.455)	2.034	(1.608, 2.441)	2.037
			0.051	0.833/95.90	0.050	0.833/96.00	0.052
50	25	γ	1.083	(0.630, 1.536)	1.066	(0.630, 1.523)	0.976
			0.066	0.906/95.60	0.063	0.893/96.00	0.741
		λ	2.173	(1.232, 3.113)	2.159	(1.288, 3.363)	2.148
			0.383	1.881/93.70	0.381	2.075/95.80	0.396
	50	γ	1.040	(0.744, 1.336)	1.031	(0.742, 1.348)	1.010
			0.026	0.592/95.80	0.025	0.606/97.20	0.110
		λ	2.066	(1.459, 2.673)	2.057	(1.498, 2.721)	2.060
			0.110	1.214/95.00	0.108	1.224/96.10	0.115
	100	γ	1.019	(0.814, 1.223)	1.014	(0.806, 1.216)	1.009
			0.011	0.409/96.60	0.012	0.410/96.60	0.025
		λ	2.030	(1.613, 2.447)	2.025	(1.646, 2.510)	2.028
			0.051	0.834/95.10	0.054	0.864/97.60	0.053

Note: Parm.: parameter, AV: average, and ACI: asymptotic confidence interval.

TABLE 6: Numerical results of AVEs, ACIs, MSERs, ALs, and CPrs (in %) for $\gamma = 1$ and $\lambda = 2$ under number of stages $m = 5$.

$f\%$	n	Parm.	MLLE		Bayesian: MCMC		Bayesian: Lindley
			AVE MSEr	ACI AL/CPr	AVE MSEr	HPD AL/CPr	AVE MSEr
0	25	γ	1.054	(0.675, 1.432)	1.042	(0.695, 1.435)	0.952
			0.042	0.757/95.90	0.041	0.740/97.00	0.836
		λ	2.170	(1.259, 3.080)	2.151	(1.409, 3.194)	2.164
			0.271	1.821/94.60	0.262	1.785/96.80	0.280
	50	γ	1.027	(0.768, 1.287)	1.021	(0.760, 1.295)	1.005
			0.019	0.519/95.30	0.019	0.535/96.20	0.061
		λ	2.072	(1.471, 2.673)	2.063	(1.492, 2.710)	2.070
			0.117	1.202/94.60	0.115	1.218/96.20	0.120
	100	γ	1.017	(0.836, 1.197)	1.014	(0.842, 1.196)	1.011
			0.009	0.361/96.90	0.008	0.353/97.20	0.016
		λ	2.048	(1.632, 2.464)	2.043	(1.640, 2.456)	2.047
			0.049	0.831/96.80	0.048	0.815/96.80	0.049

TABLE 6: Continued.

f%	n	Parm.	MLLE		Bayesian: MCMC		Bayesian: Lindley
			AVE MSEr	ACI AL/CPr	AVE MSEr	HPD AL/CPr	AVE MSEr
25	25	γ	1.092	(0.648, 1.537)	1.077	(0.687, 1.621)	1.002
			0.071	(0.889/93.10)	0.068	(0.934/97.00)	0.677
		λ	2.171	(1.240, 3.103)	2.157	(1.299, 3.244)	2.149
			0.345	(1.863/93.70)	0.342	(1.945/96.10)	0.363
	50	γ	1.041	(0.753, 1.328)	1.033	(0.757, 1.357)	1.018
			0.024	(0.575/95.50)	0.023	(0.600/97.00)	0.093
		λ	2.089	(1.477, 2.702)	2.079	(1.472, 2.729)	2.085
			0.117	(1.225/95.30)	0.114	(1.257/96.30)	0.120
	100	γ	1.019	(0.824, 1.214)	1.015	(0.831, 1.207)	1.012
			0.010	(0.390/96.80)	0.009	(0.376/96.60)	0.020
		λ	2.036	(1.620, 2.452)	2.032	(1.617, 2.486)	2.035
			0.051	(0.832/95.50)	0.051	(0.869/96.60)	0.052
50	25	γ	1.112	(0.622, 1.602)	1.092	(0.665, 1.701)	1.009
			0.091	(0.980/93.90)	0.085	(1.036/96.80)	0.951
		λ	2.188	(1.233, 3.144)	2.177	(1.319, 3.410)	2.154
			0.410	(1.911/93.40)	0.415	(2.091/96.50)	0.430
	50	γ	1.052	(0.740, 1.365)	1.043	(0.740, 1.369)	1.030
			0.031	(0.625/95.30)	0.030	(0.629/95.90)	0.126
		λ	2.079	(1.466, 2.693)	2.071	(1.509, 2.775)	2.071
			0.120	(1.227/94.80)	0.118	(1.266/96.60)	0.125
	100	γ	1.024	(0.813, 1.234)	1.019	(0.797, 1.231)	1.014
			0.013	(0.421/96.30)	0.012	(0.434/96.60)	0.030
		λ	2.043	(1.623, 2.464)	2.039	(1.612, 2.480)	2.041
			0.056	(0.841/95.30)	0.055	(0.868/96.60)	0.057

Note: Parm.: parameter, AV: average, and ACI: asymptotic confidence interval.

TABLE 7: Removal patterns of units under different censoring schemes for data set I.

Scheme	m	q_j (%)	T_{q_j}	R_i
I	3	(10, 40, 70)	(0.26, 0.90, 2.31)	$f_{0\%}: R = (0^{*2}, R_m)$ $f_{25\%}: R = (3^{*2}, R_m)$ $f_{50\%}: R = (5^{*2}, R_m)$
II	4	(10, 30, 50, 70)	(0.26, 0.59, 1.15, 2.31)	$f_{0\%}: R = (0^{*3}, R_m)$ $f_{25\%}: R = (2^{*3}, R_m)$ $f_{50\%}: R = (4^{*3}, R_m)$
III	5	(10, 25, 40, 55, 70)	(0.26, 0.50, 0.90, 1.251, 2.31)	$f_{0\%}: R = (0^{*4}, R_m)$ $f_{25\%}: R = (2^{*4}, R_m)$ $f_{50\%}: R = (3^{*4}, R_m)$

TABLE 8: MLL, Bayesian, and St.E and ACI based on the PCTI under various censoring schemes for data set I.

Sch.	f%	Parm.	MLL			MCMC			Lindley
			Estimate	St.E	ACI	Estimate	St.E	HPD	Estimate
I	0	γ	0.4720	0.0952	(0.2854, 1.1864)	0.6417	0.0165	(0.4024, 0.9145)	0.7053
		λ	1.7210	0.2727	(0.6586, 2.2556)	1.0312	0.0555	(0.5647, 1.4825)	1.7534
	25	γ	0.5186	0.1131	(0.2968, 1.0013)	0.6151	0.0216	(0.3353, 0.8893)	0.8423
		λ	1.5560	0.2830	(0.7405, 2.1107)	1.0192	0.0671	(0.5144, 1.5035)	1.6146
	50	γ	0.4557	0.1157	(0.2289, 1.0803)	0.5234	0.0198	(0.2898, 0.8476)	0.9699
		λ	1.7423	0.3377	(0.6825, 2.4043)	1.2496	0.0945	(0.6814, 1.8303)	1.8185

TABLE 8: Continued.

Sch.	f%	Parm.	MLL			MCMC			Lindley Estimate
			Estimate	St.E	ACI	Estimate	St.E	HPD	
II	0	γ	0.5406	0.1072	(0.3304, 0.9283)	0.6486	0.0166	(0.4117, 0.9216)	0.7447
		λ	1.4382	0.2601	(0.7507, 1.9482)	1.0257	0.0545	(0.5853, 1.4701)	1.4749
	25	γ	0.6203	0.1207	(0.3838, 0.8324)	0.7199	0.0203	(0.4393, 0.9876)	0.8450
		λ	1.3309	0.2543	(0.8569, 1.8294)	0.9202	0.0493	(0.5122, 1.3606)	1.3860
	50	γ	0.5892	0.1442	(0.3065, 0.7183)	0.5459	0.0247	(0.2531, 0.8646)	0.9890
		λ	1.3319	0.3130	(0.8720, 1.9455)	1.1908	0.0990	(0.6207, 1.8487)	1.4416
III	0	γ	0.5406	0.1072	(0.3304, 0.9283)	0.6427	0.0176	(0.3972, 0.9138)	0.7527
		λ	1.4382	0.2601	(0.7507, 1.9482)	1.0185	0.0561	(0.5831, 1.4811)	1.3028
	25	γ	0.6217	0.1417	(0.3439, 0.6541)	0.6094	0.0211	(0.3299, 0.8943)	0.9460
		λ	1.1831	0.2698	(0.8994, 1.7120)	1.0463	0.0623	(0.5815, 1.5315)	1.2913
	50	γ	0.6971	0.1528	(0.3976, 0.5897)	0.6977	0.0288	(0.3841, 1.0246)	1.0644
		λ	1.1005	0.2606	(0.9966, 1.6114)	0.9170	0.0671	(0.4681, 1.4697)	1.2497

Note: ACI: asymptotic confidence interval, Parm.: parameter, Schs.: scheme, and St.E: standard error.

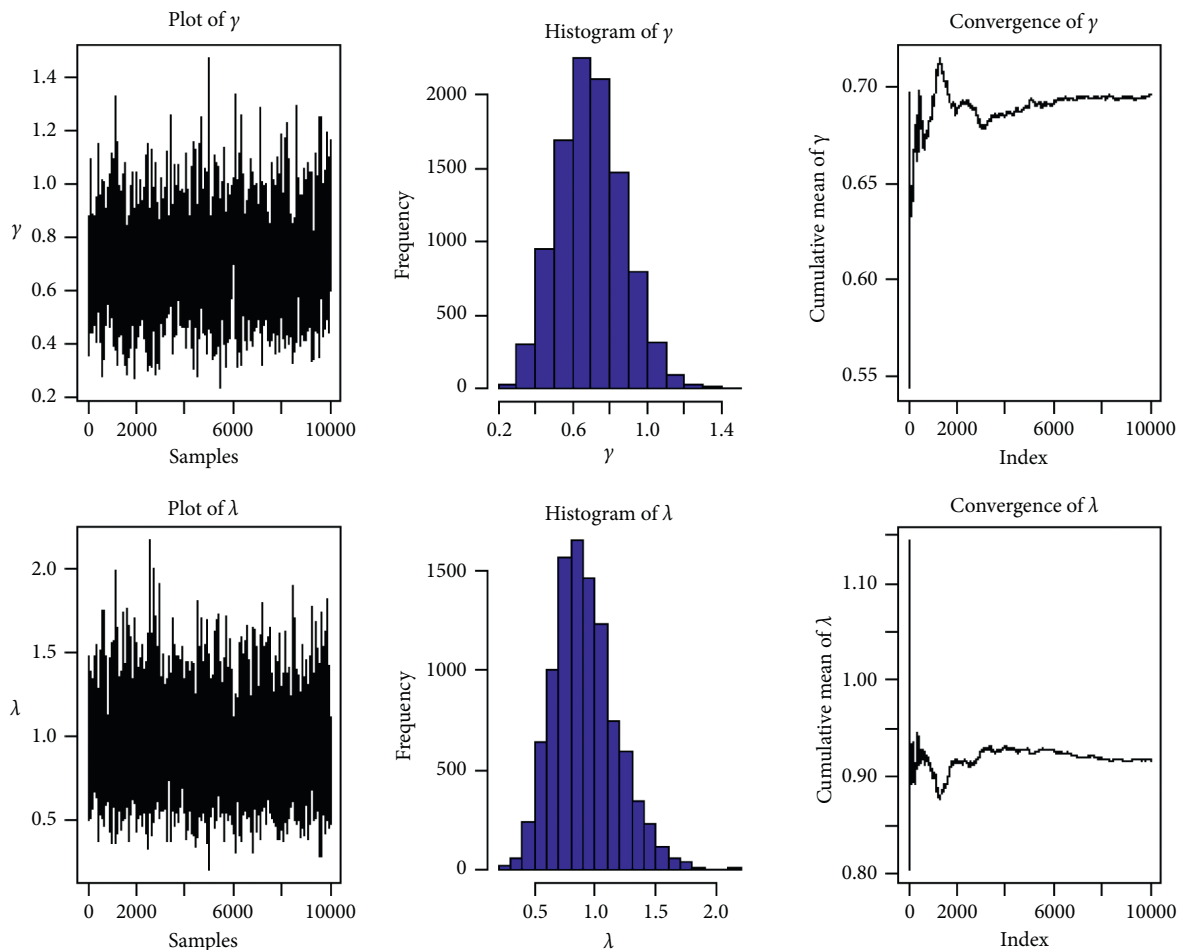


FIGURE 2: Convergence of MCMC estimates for γ and λ implementing the MH method for data set I under PCTI $m = 5$ and $f = 50\%$.

outcomes demonstrate that MLEs informative Bayes estimates using Lindley approximation perform better than both MLEs and informative prior using Lindley approximation and that estimates under informative prior using MCMC perform better than both MLEs and informative

prior using Lindley approximation. We used Bayesian estimation with the squared error loss function for future work, but other loss functions can also be used. In addition, the current approach may be extended to the construction of an optimum progressive censoring, as well as alternative

TABLE 9: Removal patterns of units under different censoring schemes for data set II.

Scheme	m	q_j (%)	T_{q_j}	R_i
I	3	(10, 40, 70)	(2.26, 2.84, 3.40)	$f_{0\%}: R = (0^{*2}, R_m)$ $f_{25\%}: R = (3^{*2}, R_m)$ $f_{50\%}: R = (5^{*2}, R_m)$
II	5	(10, 25, 40, 55, 70)	(2.26, 2.45, 2.84, 3.23, 3.40)	$f_{0\%}: R = (0^{*4}, R_m)$ $f_{25\%}: R = (2^{*4}, R_m)$ $f_{50\%}: R = (3^{*4}, R_m)$

TABLE 10: MLL, Bayesian, and St.E and ACI based on the PCTI under various censoring schemes for data set II.

Sch.	$f\%$	Parm.	MLL			MCMC			Lindley Estimate
			Estimate	St.E	ACI	Estimate	St.E	HPD	
I	0	γ	2.9651	0.6477	(1.6130, 5.6993)	2.9660	$9.34 \times 10^{(-5)}$	(2.9464, 2.9853)	2.9793
		λ	27.0113	1.7130	(23.3172, 33.3233)	27.0115	$1.01 \times 10^{(-4)}$	(26.9920, 27.0312)	27.0107
	25	γ	3.5567	0.8081	(2.0791, 6.0904)	3.5572	$9.72 \times 10^{(-5)}$	(3.5382, 3.5767)	3.5741
		λ	44.8461	3.3430	(24.0343, 64.6019)	44.8460	$1.02 \times 10^{(-4)}$	(44.8270, 44.8656)	44.8457
	50	γ	3.2201	0.9133	(1.5435, 7.6124)	3.2204	$9.93 \times 10^{(-5)}$	(3.2016, 3.2404)	3.2475
		λ	35.1225	4.9036	(23.8966, 46.6325)	35.1224	$1.06 \times 10^{(-4)}$	(35.1022, 35.1414)	35.1216
II	0	γ	3.5062	0.7624	(3.0917, 7.3792)	3.5068	$9.83 \times 10^{(-5)}$	(3.48812, 3.5276)	3.5222
		λ	38.4492	2.7722	(23.9207, 53.5191)	38.4491	$1.02 \times 10^{(-4)}$	(38.4290, 38.4685)	38.4487
	25	γ	4.6583	1.0922	(2.9813, 10.7054)	4.6585	$9.88 \times 10^{(-5)}$	(4.6387, 4.6772)	4.6790
		λ	59.4018	9.4702	(28.3353, 78.0982)	59.4020	$1.06 \times 10^{(-4)}$	(29.3828, 80.4223)	59.4016
	50	γ	3.9068	1.1731	(2.0377, 12.2449)	3.9066	$9.97 \times 10^{(-5)}$	(3.8868, 3.9259)	3.9306
		λ	48.4916	13.8929	(18.7758, 74.7383)	48.4915	$1.09 \times 10^{(-4)}$	(48.4720, 48.5111)	48.4911

Note: ACI: asymptotic confidence interval, Parm.: parameter, Schs.: scheme, and St.E: standard error.

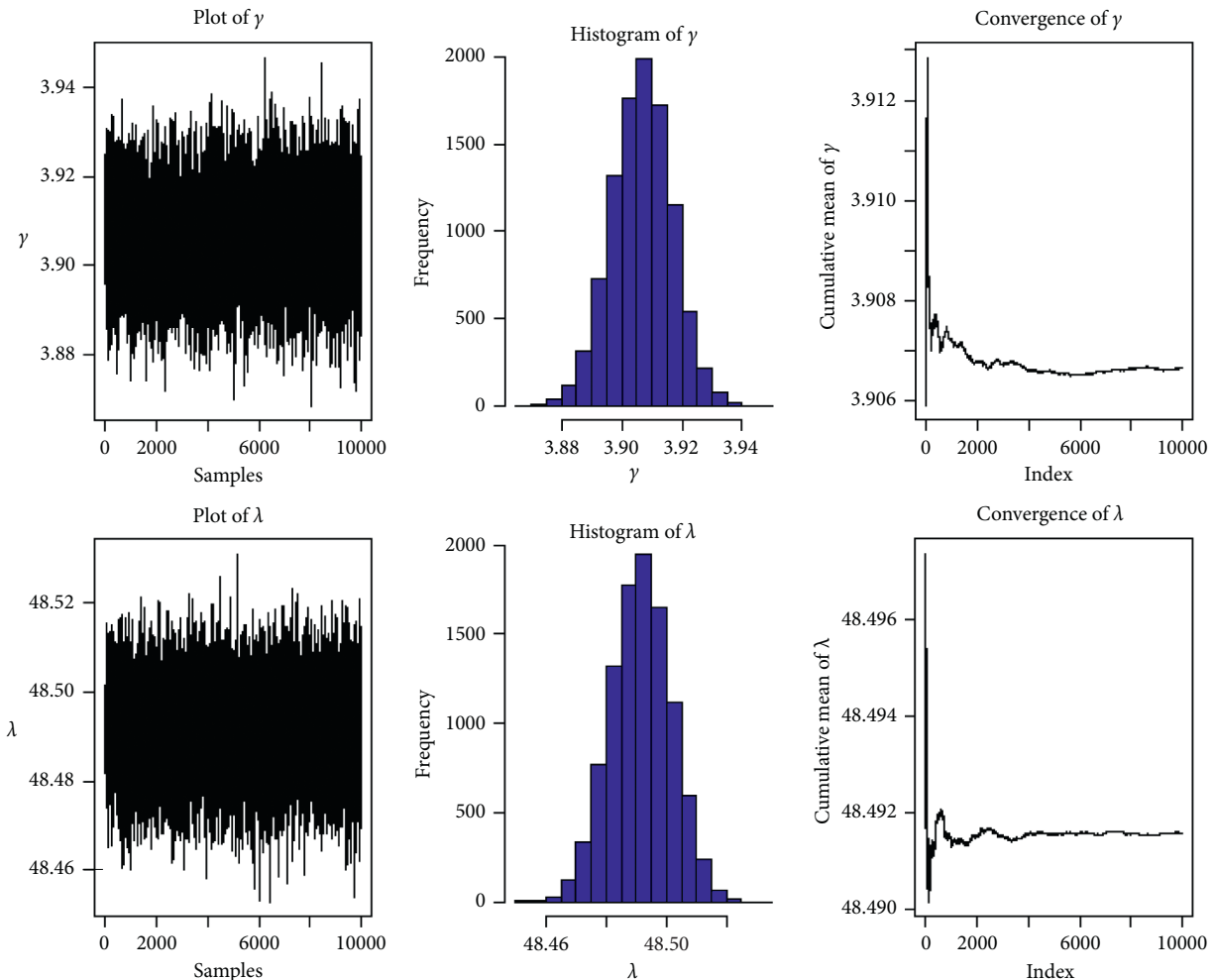


FIGURE 3: Convergence of MCMC estimates for γ and λ implementing the MH method for the data set II under PCTI $m = 5$ and $f = 50\%$.

censoring methods. Neutrosophic statistics can be an extended work on area of progressive censoring schemes under the assumed distribution and PCTTI.

Data Availability

Interested parties can reach out to the author in order to receive a numerical data set used to perform the research described in the study.

Conflicts of Interest

The authors declare that there are no conflicts of interest.

Acknowledgments

The Deanship of Scientific Research (DSR), King Abdul-Aziz University, Jeddah, 299, supported this work, under Grant no. KEP-PhD-75-130-42. The authors, 300 therefore, gratefully acknowledge the DSR technical and financial support.

References

- [1] A. Z. Keller and A. R. R. Kamath, "Alternate reliability models for mechanical systems," *ESA Reliab Maintainab*, pp. 411–415, 1982.
- [2] P. Erto, "Genesis, properties and identification of the inverse Weibull lifetime model," *Statistics and Applications*, vol. 1, pp. 117–128, 1989.
- [3] R. Calabria and G. Pulcini, "Bayes 2-sample prediction for the inverse Weibull distribution," *Communications in Statistics - Theory and Methods*, vol. 23, no. 6, pp. 1811–1824, 1994.
- [4] R. M. Musleh and A. Helu, "Estimation of the inverse Weibull distribution based on progressively censored data: comparative study," *Reliability Engineering & System Safety*, vol. 131, pp. 216–227, 2014.
- [5] S. K. Singh, U. Singh, and D. Kumar, "Bayesian estimation of parameters of inverse Weibull distribution," *Journal of Applied Statistics*, vol. 40, no. 7, pp. 1597–1607, 2013.
- [6] F. R. S. de Gusmão, E. M. M. Ortega, and G. M. Cordeiro, "The generalized inverse Weibull distribution," *Statistical Papers*, vol. 52, no. 3, pp. 591–619, 2011.
- [7] I. Elbatal and H. Z. Muhammed, "Exponentiated generalized inverse Weibull distribution," *Applied Mathematical Sciences*, vol. 8, pp. 1597–1607, 2014.
- [8] M. S. Khan, G. R. Pasha, and A. H. Pasha, "Theoretical analysis of inverse weibull distribution," *WSEAS Transactions on Mathematics*, vol. 7, pp. 30–38, 2008.
- [9] P. Erto, "New practical Bayes estimators for the 2-parameter weibull distribution," *IEEE Transactions on Reliability*, vol. 31, pp. 194–197, 2009.
- [10] K. S. Sultan, M. A. Ismail, and A. S. Al-Moisheer, "Mixture of two inverse Weibull distributions: properties and estimation," *Computational Statistics & Data Analysis*, vol. 51, no. 11, pp. 5377–5387, 2007.
- [11] N. Balakrishnan, D. Han, and G. Iliopoulos, "Exact inference for progressively type-I censored exponential failure data," *Metrika*, vol. 73, no. 3, pp. 335–358, 2011.
- [12] U. Balasooriya and C.-K. Low, "Competing causes of failure and reliability tests for Weibull lifetimes under type I progressive censoring," *IEEE Transactions on Reliability*, vol. 53, no. 1, pp. 29–36, 2004.
- [13] A. C. Cohen, "Progressively censored samples in life testing," *Technometrics*, vol. 5, no. 3, pp. 327–339, 1963.
- [14] N. Balakrishnan and E. Cramer, *The Art of Progressive Censoring: Applications to Reliability and Quality*, Springer, New York, NY, USA, 2010.
- [15] R. M. Mahmoud, H. Z. Muhammed, and A. R. El-Saeed, "Inference for generalized inverted exponential distribution under progressive Type-I censoring scheme in presence of competing risks model," *Sankhya A: The Indian Journal of Statistics*, vol. 134, p. 1, 2021, <https://doi.org/10.1007/s13171-020-00227-y>.
- [16] R. M. Mahmoud, H. Z. Muhammed, and A. R. El-Saeed, "Analysis of progressively Type-I censored data in competing risks models with generalized inverted exponential distribution," *Journal of Statistics Applications & Probability*, vol. 9, pp. 109–117, 2020.
- [17] M. R. Mahmoud, H. Z. Muhammed, A. R. El-Saeed, and A. D. Abdellatif, "Estimation of parameters of the GIE distribution under progressive Type-I censoring," *Journal of Statistical Theory and Applications*, vol. 20, no. 2, pp. 380–394, 2021.
- [18] A. C. Cohen, "Maximum likelihood estimation in the weibull distribution based on complete and on censored samples," *Technometrics*, vol. 7, no. 4, pp. 579–588, 1965.
- [19] D. V. Lindley, "Fiducial distributions and Bayes' theorem," *Journal of the Royal Statistical Society: Series B*, vol. 20, no. 1, pp. 102–107, 1958.
- [20] M.-H. Chen and Q.-M. Shao, "Monte Carlo estimation of bayesian credible and HPD intervals," *Journal of Computational & Graphical Statistics*, vol. 8, no. 1, pp. 69–92, 1999.
- [21] D. K. Bhaumik, K. Kapur, and R. D. Gibbons, "Testing parameters of a gamma distribution for small samples," *Technometrics*, vol. 51, pp. 26–334, 2009.
- [22] X. Guan, D. T. Niu, and J. B. Wang, "Carbonation service life prediction of coal boardwalks bridges based on durability testing," *Journal of Xi'an University of Architecture and Technology*, vol. 47, pp. 71–76, 2015.

Research Article

Early Warning for the Construction Safety Risk of Bridge Projects Using a RS-SSA-LSSVM Model

Gang Li ¹, Ruijiang Ran ², Jun Fang ², Hao Peng ¹ and Shengmin Wang ³

¹School of Architectural Engineering, Xinyang Vocational and Technical College, Xinyang 464000, China

²School of Civil Engineering and Architecture, Wuhan University of Technology, Wuhan 430070, China

³School of Safety Science and Emergency Management, Wuhan University of Technology, Wuhan 430070, China

Correspondence should be addressed to Shengmin Wang; wsm910429@whut.edu.cn

Received 31 August 2021; Revised 1 October 2021; Accepted 23 October 2021; Published 5 November 2021

Academic Editor: Afaq Ahmad

Copyright © 2021 Gang Li et al. This is an open access article distributed under the Creative Commons Attribution License, which permits unrestricted use, distribution, and reproduction in any medium, provided the original work is properly cited.

Bridge engineering is an important component of the transportation system, and early warnings of construction safety risks are crucial for bridge engineering construction safety. To solve the challenges faced by early warnings risk and the low early warning accuracy in bridge construction safety, this study proposed a new early-warning model for bridge construction safety risk. The proposed model integrates a rough set (RS), the sparrow search algorithm (SSA), and the least squares support vector machine (LSSVM). In particular, the initial early warning factors of bridge construction safety risk from five factors (men, machines, methods, materials, and environment) were selected, and the RS was used to reduce the attributes of 20 initial early warning factors to obtain the optimized early warning factor set. This overcame the problem of multiple early warning factors and reduced the complexity of the subsequent prediction model. Then, the LSSVM with the strongest nonlinear modelling ability was selected to build the bridge construction early-warning model and adopted the SSA to optimize the LSSVM parameter combination, improving the early warning accuracy. The Longlingshan Project in Wuhan and the Shihe Bridge Project in Xinyang, China, were then selected as case studies for empirical research. Results demonstrated a significant improvement in the performance of the early-warning model following the removal of redundancy or interference factors via the RS. Compared with the standard LSSVM, Back Propagation Neural Network and other traditional early-warning models, the proposed model exhibited higher computational efficiency and a better early warning performance. The research presented in this article has important theoretical and practical significance for the improvement of the early warning management of bridge construction safety risks.

1. Introduction

Developing countries such as China are currently implementing large-scale bridge projects [1]. However, these projects require large project investment, complex technology, and extensive contents and are typically established in poor construction environments. This results in extremely high construction safety, with an enhanced probability of serious accidents. In recent years, bridge construction safety accidents (e.g., the impact of the cofferdam, the collapse of floating cranes, and flooding) have been a common occurrence [2]. The early warning of construction safety risk generally involves the monitoring, evaluation, and prediction of factors corresponding to construction safety risk, with the aims of predicting future risks, determining the

potential time range of risks, and measuring the strength of risks and their damage degree. Such a system aids decision-makers in taking appropriate risk control measures [3]. Therefore, the systematic identification, estimation, and early warning control of bridge construction safety risks can effectively reduce construction safety risks and achieve the management goals of bridges while complying with safety regulations.

Numerous scholars have performed in-depth studies on the early warning of risk in many fields. To effectively reduce the financial risks of non-life-insurance enterprises, Yan et al. [4] constructed a financial risk early-warning model. Zhang [5] developed a safety risk early-warning model of the food industry chain, revealing that introducing early warning theory into the field of food safety risk can

effectively improve the level of risk management. In order to reduce the loss of ship collision, Cheng et al. [6] introduced risk early warning theory into ship collision risk management. Based on climatology, disaster science, and environmental science, Zhang et al. [7] determined that the risk early warning theory should be introduced into the early management of the drought disaster risk of crops such as corn. Sattlee et al. [8] integrated risk early warning theory into the reliability analysis of geological disasters to effectively reduce the losses caused by landslides and falling rocks. Great achievements have been made in the theory of early warning risk, but the research results on early warning of bridge construction safety risk are rarely reported. The early warning of risk denotes the prediction or classification of the target value of research objects. Scholars have adopted various research methods to build risk early-warning models across different fields of research. Ding [9] comprehensively combined the analytic hierarchy process (AHP) and the fuzzy comprehensive evaluation method to construct the risk early-warning model of financial enterprises. However, the fuzzy comprehensive evaluation is a linear weighted evaluation method and cannot effectively reflect the elevated influence of all evaluation indicators. Nonlinear characteristics are also unable to meet the requirements of practical evaluations. The AHP is associated with several disadvantages, such as strong subjectivity and the sensitivity to extreme expert opinions. Based on the strong self-learning ability and nonlinear processing of artificial neural networks (ANNs), Yan et al. [10] constructed an early-warning model of human resource management risk based on the back propagation neural network (BPNN). However, the application of the BPNN in early warning risk research results in several shortcomings, including overfitting, slow convergence, and easy to fall into a local minimum. Wang et al. [11] employed the grey model (GM) to construct an early warning safety risk model of a railway service system. Although the GM is simple to operate, it requires that variables satisfy the multivariate normal distribution, which is difficult to meet in practical applications. Chen and Zhang [12] used the logistic regression model to construct a logistics-based early warning risk management system for the default risk of cultural creative crowdfunding projects. However, the calculation of the logistic regression model is approximate and thus has several shortcomings, such as complex calculations and low prediction accuracy.

The least square support vector machine (LSSVM) inherits the structural risk concept and kernel mapping concept of the standard support vector machine (SVM). Starting from the loss function of machine learning, two norms are used in the objective function of the optimization problem in the LSSVM, and equality constraint is used instead of inequality constraint in SVM standard algorithm, which makes the solution of optimization problem of LSSVM method become a set of linear equations obtained by Kuhn–Tucker condition. The LSSVM trains the SVM by solving the transformed linear equations, which greatly improves the training efficiency of the SVM [13]. In recent years, the LSSVM has been widely used in data prediction, data classification, and other research fields. Zhao et al. [13]

used the LSSVM to effectively diagnose aircraft engine faults. Ahmadi et al. [14] successfully simulated the vaporization enthalpies of pure hydrocarbons and petroleum fractions via the LSSVM. Statistical results determined the LSSVM-predicted average relative deviation and R^2 of the vaporization enthalpies as 0.51% and 0.9998, respectively, indicating the high prediction accuracy of the LSSVM. To improve the prediction accuracy of the cotton fabric K/S value, Yu et al. [15] combined particle swarm optimization (PSO) with the LSSVM to construct a new prediction model. In order to overcome the low early warning accuracy, in the current study, the LSSVM is employed to build an early-warning model of bridge construction safety risk.

Despite its strong robustness and generalization ability, the LSSVM cannot simplify the dimensions of information space. For high dimensions or large training samples, the LSSVM often faces problems, such as dimension disaster, and an increase in time consumption due to the limited memory capacity or complex network structure. The rough set (RS) does not require any prior knowledge and removes redundant data without affecting the classification accuracy. It is widely used in the fields of attribute sets [16] and key indicator screening. Introducing the RS into the LSSVM can effectively determine key attributes and reduce the adverse effects of redundancy and multicollinearity among various input variables on prediction accuracy. Therefore, when developing the proposed early-warning model based on the LSSVM, the RS is introduced to solve the problem of multiple early warning factors.

As a new machine learning method, the prediction accuracy and computational performance of the LSSVM depend on the reasonable selection of regularization and kernel width parameters. In the development of a landslide displacement prediction model for rainfall, Zhu et al. [17] employed the genetic algorithm (GA) to determine the LSSVM optimal parameters. However, the GA is associated with several bottlenecks, including complex coding, a slow calculation speed, and easy premature convergence [18]. To improve the accuracy of the LSSVM in predicting concrete strength, Xue [19] optimized the calculation parameters via PSO. However, the PSO is also prone to premature convergence (particularly when dealing with complex multimodal search problems) and has a poor local optimization ability [14].

The sparrow search algorithm (SSA) is a new swarm intelligence optimization approach that was inspired by the foraging and antipredation behaviours of sparrows [20]. When predicting the deboning strain of fibre reinforced polymer reinforced concrete, Li et al. [21] employed the SSA to optimize the initial weight and threshold of the BPNN. Empirical results revealed that the SSA-optimized BPNN surpassed the traditional version in terms of prediction accuracy and robustness. Liu and Rodriguez [22] used the SSA to accurately solve the problem of sustainable energy optimization in residential engineering, a complex and multiobjective nonlinear optimization problem. Wumaier et al. [23] adopted the SSA to optimize the SVM parameter combination, and based on wind turbine fault diagnosis data, the SSA-SVM was clearly superior to GA-SVM and

PSO-SVM in terms of computing performance. Therefore, the SSA in the proposed method was adopted to determine the LSSVM optimal parameter for efficient computing performance.

Based on the above analysis and review of the relevant literature, a hybrid early-warning model of bridge construction safety risk was developed based on the RS, SSA, and LSSVM. The contributions and innovations of this article are as follows. (1) At present, researches on the early warning of risk mainly focuses on the financial risk, the food safety, the disaster risk, or other fields. In this study, early warning for the construction safety risk of bridge projects was studied, and a detailed case study was made. This provided new insights for early warning and management of bridge construction project. (2) From five aspects (men, machines, materials, methods, and environment), the index system of early warning for construction safety risk of bridge projects was constructed completely, which provided reference and foundation for similar researches. (3) In this study, a novel early-warning model based on the RS, SSA, and LSSVM was constructed, which not only effectively solved the problem of multiple risk early warning factors but also overcame the problem of low precision of traditional early warning methods.

The remaining sections of this article are arranged as follows. In Section 2, the early warning indicator system of bridge construction safety risk and the early-warning model are constructed. In Section 3, the Longlingshan Bridge Project in Wuhan and the Shihe Bridge Project in Xinyang, China, are used to perform the empirical research. Section 4 analyses the computational performance of the early-warning model proposed in this study, whereas Section 5 summarizes the main conclusions and limitations of this study.

2. Materials and Methods

2.1. Establishment of an Early-Warning Indicator System for Bridge Construction Safety Risk

2.1.1. Preliminary Selection of Early-Warning Indicators for Bridge Construction Safety Risks. Risk early warning mainly includes three parts: identification, division, and prediction of risk levels. The early-warning management system of construction safety risk in a bridge project plays a key role in scientifically creating an early warning indicator system for safety risk. Referring to the underlying reasons of risk loss during bridge construction, the early warning indicators of bridge construction safety risk was screened from five aspects (men, machines, materials, methods and environment; 4M1E) [24, 25], as described in the following.

(1) *Men.* This includes all participants in the bridge construction process. The construction and management of bridge engineering is generally performed by employees, and thus, their safety has a great influence on bridge construction safety. The illegal operation of workers is a common instigator of construction safety accidents [2]. In general, the more workers violating regulations, the greater the

possibility of construction safety accidents and the more serious the consequences. Therefore, the more skilled workers, the lower the safety risks. The safety skills of project managers also play a key role in the daily risk management of construction safety. The stronger the safety skills of project managers, the more effective the daily risk management is. When safety accidents occur, project managers with a good emergency handling ability can effectively reduce secondary accidents and losses caused by safety accidents.

(2) *Machines.* This includes all machinery and equipment used in the construction project. The safety state of machinery in bridge construction projects is a key influencing factor of construction safety. Mechanical quality, mechanical installation, mechanical operation, and mechanical operation failure are generally the most important factors affecting the safety status of objects in bridge construction [3].

(3) *Materials.* This includes all materials employed in the bridge construction process. The quality and management problems of materials will consequently result in the quality and safety problems of the whole bridge construction. The most important building materials for bridge construction are concrete and steel, which are the main stress parts of the bridge structure, and they have obvious influence on the structural performance. When the structural performance of bridges is insufficient, safety accidents such as local collapse are easy to occur. Therefore, the qualification rate of these two building materials has a great influence on the construction safety and engineering quality. In addition, related management problems (e.g., stacking and random inspection of materials) may also result in bridge construction safety accidents [2, 24].

(4) *Methods.* This denotes the overall management process of bridge construction. Method indicators related to construction safety include all rules and regulations, technical requirements, organization and management, and construction methods. Combined with the construction technology and characteristics of bridge engineering, the most important indicators are the monitoring and calculation methods, as well as technical disclosure. Furthermore, a large number of new technologies and processes are often used in bridge construction; thus, the proportion of new construction schemes also has a significant impact on construction safety [25]. In general, the greater the proportion of new construction schemes and the less mature the technology, the greater the risk of construction safety.

(5) *Environment.* This denotes the natural environment and social environment during bridge construction. The characteristics of bridge construction sites and technology and economy lead to a complex construction environment, and there are many natural and social factors that affect bridge construction. Natural disasters, such as earthquakes, typhoons, and rainstorms, will seriously affect construction safety. In bridge construction, the wind has a great influence on bridge construction safety [3]. The social environment of bridge construction mainly refers to the sustainability and socioeconomic stability of engineering projects.

Table 1 provides details of the five early warning indicators. Here, the qualitative indicator refers to the data obtained by expert investigations, whereas the quantitative indicator is obtained by field investigations, consulting design data, or calculations based on national standards. The benefit indicator increases with the bridge construction safety risk level, whereas the opposite is true for the cost indicator.

2.1.2. Threshold Value of Early Warning Bridge Construction Safety Risk. The early-warning threshold of bridge construction safety risk is divided into a general indicator early-warning threshold and a subindicator early-warning threshold. In the actual construction process, rapidly obtaining quantitative data of risk indicators proves to be a difficult task, particularly as indicators related to early warnings still rely on the observation and subjective judgment of site managers. Therefore, a qualitative and quantitative combination, with a qualitative expert determination, method was adopted to judge the warning situation of early warning indicators. Table 2 reports the division of each indicator and the corresponding descriptions.

The warning degree division of each secondary indicator comprehensively considers the related specifications, such as the Load Code for the Building Structure Design (GB 50009-2012), the Specifications for Long-Span Highway Bridge Construction Surveys (JTG/T 365-02-2019), the Safety Technical Specifications for Highway Engineering Construction, (JTG F90-2015), the Specifications for Bridge Design Wind Speed Calculations (QX/T 438-2018), the Design Code of the Municipal Bridge (CJJ 11-2011), and the results of previous research of early warning systems [26].

2.2. Introduction to the RS. The RS, a data analysis theory proposed by Polish mathematician Pawlak, is able to deal with the uncertainty, incompleteness, and incompatibility between information and knowledge. The RS-based attribute reduction process involves deleting unimportant or irrelevant redundant attributes while maintaining the classification or decision-making ability of information systems unchanged and deducing the classification or decision-making of the problem to be solved [16, 17]. Therefore, theoretically speaking, applying the RS to the intensive prewarning indicators of bridge construction safety risks can reduce the unimportant indicators while maintaining the prewarning ability, thus improving the calculation accuracy of the subsequent risk prewarning model.

In the RS, information systems can be represented by 4 tuples [16]:

$$S = (U, A, V, f_S), \quad (1)$$

where U is the domain of discourse; $A = C \cup D = \{a_1, a_2, \dots, a_n\}$ is a finite set of non-empty attributes, $C \cap D = \emptyset$, C is a conditional attribute set, and D is a decision attribute set; $V = \cup_{a \in A} V_a$ is the set of attribute values, and V_a is the range of attribute $a \in A$. Function f_S is used to assign corresponding attribute values to each object attribute in theory.

The support degree of conditional attribute C to decision attribute D is an important concept of rough set theory [16]:

$$\gamma_C(D) = \frac{POS_C(D)}{|U|}, \quad (2)$$

where $POS_C(D)$ is denoted as the positive domain of D about C , which describes all the element sets in U that can be exactly classified into the $U|D$ class according to the knowledge of C , and $\gamma_C(D)$ indicates the ratio of objects that can be classified into the $U|D$ decision class under conditional attribute C and expresses the degree of support of the conditional attribute to the decision attribute.

Assume that there exists $q \in C$ and $C \subseteq A$ in information system S , if $PCS_C(D) \neq POS_{(C-q)}(D)$, then it is said that q is a necessary attribute in C and must be kept; otherwise, q is an unnecessary attribute in C and can be deleted [16].

In information system S , $E \subseteq C \subseteq A$ and E are independent and satisfy $(\gamma_E(D) = \gamma_C(D)) \wedge (\forall E' \subset E) \implies (\gamma_{E'}(D) \neq \gamma_C(D))$. E is denoted as the reduction of C , $Red(C)$, and the set of essential attributes in C forms the core of C , $Core(C)$. If E is independent, it is considered as the minimum set required to maintain the classification ability of universe U [16].

Although the mathematical theory of RS is very complex, the development of Rosetta, which is a computing software integrating rough set principle, facilitates data set classifications and minimum set searches.

2.3. Introduction to the SSA. The SSA is a novel swarm intelligence optimization algorithm [20]. Compared with classical algorithms, such as the PSO, it exhibits a superior computing performance due to the addition of discoverer and early warnings [21, 22].

At each SSA, iteration the location update of the discoverer is described as follows [20]:

$$X_{i,j}^{t+1} = \begin{cases} X_{i,j}^t \cdot \exp\left(\frac{-i}{\alpha \cdot \text{iter}_{\max}}\right), & \text{if } R_2 < ST, \\ X_{i,j}^t + Q \cdot L, & \text{if } R_2 \geq ST, \end{cases} \quad (3)$$

where t represents the current iteration number, iter_{\max} is a constant indicating the maximum iteration number, $X_{i,j}$ represents the position information of the i -th sparrow in the j -th dimension, $\alpha \in (0, 1]$ is a random number, R_2 and ST represent the warning and safety values, respectively, Q is a random number that obeys a normal distribution, L represents a $1 \times d$ matrix, and d is the dimensions of the problem to be optimized.

During each iteration, the position update of the enrollee is described as follows [20]:

$$X_{i,j}^{t+1} = \begin{cases} Q \cdot \exp\left(\frac{X_{\text{worst}}^t - X_{i,j}^t}{i^2}\right), & \text{if } i > \frac{n}{2}, \\ X_p^{t+1} + |X_{i,j}^t - X_p^{t+1}| \cdot A^+ \cdot L, & \text{if otherwise,} \end{cases} \quad (4)$$

where X_p is the best current position occupied by the discoverer, X_{worst} is the worst position in the world at present, and

TABLE 1: Primary early-warning indicators of bridge construction safety risk.

Primary indicator	Secondary indicator	Unit	Indicator type	Data collection method
A1: Men	A11: Rate of operation violation	%	Quantitative benefit indicator	On-site investigation and statistics
	A12: Rate of improper emergency handling	%	Quantitative benefit indicator	On-site investigation and statistics
	A13: Acceptance rate of worker technology	%	Quantitative cost-based indicators	On-site investigation and statistics
	A14: Safety skills of managers	—	Qualitative cost indicator	Expert investigation
A2: Machines	A21: Unqualified rate of mechanical quality	%	Quantitative benefit indicator	Field test and statistics
	A22: Failure rate of mechanical installation	%	Quantitative benefit indicator	Field test and statistics
	A23: Rate of mechanical operation error	%	Quantitative benefit indicator	On-site investigation and statistics
	A24: Rate of mechanical failure	%	Quantitative benefit indicator	On-site investigation and statistics
A3: Materials	A31: Qualified rate of concrete	%	Quantitative cost-based indicators	Field test and statistics
	A32: Qualified rate of steel	%	Qualitative cost-based indicator	Field test and statistics
	A33: Rationality of material stacking	—	Qualitative cost-based indicator	Expert investigation
	A34: Sampling inspection of materials	—	Qualitative cost-based indicator	Expert investigation
A4: Methods	A41: Rationality of monitoring method	—	Qualitative cost-based indicator	Expert investigation
	A42: Advancement of calculation method	—	Qualitative cost-based indicator	Expert investigation
	A43: Rate of technical disclosure	%	Quantitative cost-based indicators	On-site investigation and statistics
	A44: Proportion of new construction scheme	%	Quantitative benefit indicator	On-site investigation and statistics
A5: Environment	A51: Disaster frequency	—	Quantitative benefit indicator	Consult design data, local yearbook, etc.
	A52: Wind load grade	—	Quantitative benefit indicator	Field experiment and reference specification
	A53: Sustainability of engineering project	—	Qualitative cost-based indicator	Expert investigation
	A54: Social and economic sustainability	—	Qualitative cost-based indicator	Expert investigation

TABLE 2: Division of early warning indicators of bridge construction safety risk.

Division of warning degree	Descriptive explanation
No (I)	Very low risk and project managers do not need to take any measures.
Mild (II)	Risks are accepted, yet some early warning indicators have a small probability of causing bridge construction safety accidents. Project managers must focus some of their attention of the risks.
Moderate (III)	High-risk and some early-warning indicators exhibit a certain probability of causing bridge construction safety accidents. Project managers must make initially targeted measures.
Severe (IV)	Very high-risk and some early warning indicators have a high probability of causing bridge construction safety accidents. Project managers should take effective measures immediately; otherwise, construction safety accidents will easily occur.

A is a $1 \times d$ matrix, in which each element is randomly assigned 1 or -1 .

When aware of the danger, the sparrow population will exhibit antipredation behaviour, which is described as follows [20]:

$$X_{i,j}^{t+1} = \begin{cases} X_{\text{best}}^t + \beta \cdot |X_{i,j}^t - X_{\text{best}}^t|, & \text{if } f_i > f_g, \\ X_{i,j}^t + K \cdot \frac{|X_{i,j}^t - X_{\text{worst}}^t|}{f_i - f_w + \varepsilon}, & \text{if } f_i = f_g, \end{cases} \quad (5)$$

where X_{best} is the current global optimal position, β is the step control parameter, K is a random number, f_i is the fitness value of the current sparrows, f_g and f_w are the best and worst fitness values in the world, respectively, and ε is the smallest constant required to avoid a zero denominator.

Compared with other classical meta-heuristic optimization algorithms, the SSA algorithm possesses advantages, including good stability, strong global search ability, and minimal parameters. The bionics principle of the SSA algorithm simulates the foraging process of sparrows, which is similar to other classical meta-heuristic optimization algorithms and is based on “discoverer-follower” optimization. However, the SSA algorithm further simulates the detection and warning behaviour of sparrows during the foraging process. Not all sparrows are constantly approaching the current optimal solution in each iteration, yet some sparrows will experience detection and early warning. This mechanism enhances the global search ability and faster optimization speed of the SSA algorithm.

2.4. Introduction to the LSSVM. Assume that there is a training set $\{(x_i, y_i) | i = 1, 2, \dots, n\}$, where $x_i \in R^d$, $y_i \in R$, d is the input space dimension, and n is the number of training samples. $x_i \in R^d$ is projected into feature space H using nonlinear mapping ϕ and constructed in H following the structural risk minimization criterion. This process can be described as the following constrained optimization problem [13]:

$$\min \left(\frac{1}{2}w^2 + C \frac{1}{2} \sum_{i=1}^n \xi_i^2 \right), \quad (6)$$

$$\text{s.t. } y_i = w^T \phi(x_i) + b + \xi_i,$$

where C is the compromise coefficient between the empirical risk and confidence interval, that is, the regularization parameter, ξ_i is the uncorrelated random error, w is the weight variable of the prediction function, $\phi(x)$ is the nonlinear mapping function, and b is the deviation coefficient.

This constrained optimization problem can be transformed into the following form by the Lagrange method [13]:

$$L = \frac{1}{2}w^2 + C \frac{1}{2} \sum_{i=1}^n \xi_i^2 - \sum_{i=1}^n \alpha_i (w^T \phi(x_i) + b + \xi_i - y_i), \quad (7)$$

where α_i is a Lagrange multiplier.

Using the Karush–Kuhn–Tucker condition, equation (7) can be transformed into equality form, allowing us to obtain the linear model [13] by solving α_i and b via the least square method.

$$y = \sum_{i=1}^n \alpha_i K(x, x_i) + b, \quad (8)$$

where $K(x, x_i) = \phi(x)^T \phi(x_i)$ is the kernel function.

The radial basis function (RBF) is selected as the kernel function, namely, $(x, y) = \exp(-x - y/(2\sigma^2))$, where σ^2 is

the kernel width parameter reflecting the distribution characteristics of the training samples. Because the RBF kernel function satisfies the Mercer condition, calculating the kernel function in the original input space can replace the inner product operation in the mapping feature space.

To ensure the generalization performance of the LSSVM, it is necessary to optimize the regularization and kernel width parameters to determine the optimal parameter combination. At present, the K-fold calculation method or meta-heuristic optimization algorithm are commonly used to determine the optimal calculation parameters.

2.5. Implementation of the Early-Warning Model. The core concepts of the proposed early-warning model are described as follows: (1) The RS is used as the preprocessing system of the LSSVM, which preprocesses the safety risk data of the bridge construction and eliminates the redundant attributes and conflict attributes, thus simplifying the early-warning model structure of the LSSVM, shortening the training and improving the classification performance. (2) The LSSVM model is optimized via the global optimization ability of the SSA, and the parameter combination with the highest calculation accuracy is obtained to construct the optimal early-warning model of bridge construction safety risk. Figure 1 presents the architecture diagram of the proposed early-warning model.

In particular, the key steps of the proposed early-warning model for bridge construction safety risk are described in the following.

Step 1. Training and test sets are built, and the research object is determined. The original engineering data are collected based on the bridge construction safety risk early warning indicator system detailed in Section 2.1. Some samples are randomly selected from the original data as training sets and the remaining data are taken as the test sets.

Step 2. Data preprocessing and attribute set. The original engineering data are normalized as the database of early warning research. On the premise of guaranteeing the original classification ability, the redundant or conflicting attributes in the decision table are eliminated via a rough set theory and the minimum conditional attribute set is obtained.

Step 3. The early-warning model based on the LSSVM is trained and optimized. In particular, the early-warning model and kernel function parameters are initialized, the training sample set is input into the model, and the SSA algorithm is implemented to optimize the calculation parameters. Note that the iterative optimization calculation only occurs in the SSA, not in the LSSVM. The optimal calculation parameters and engineering data are input into the LSSVM to determine the early warning results.

Step 4. Early warning identification. The test sets are input into the optimal LSSVM model for early warning identification to obtain the early warning results of bridge construction safety risks.

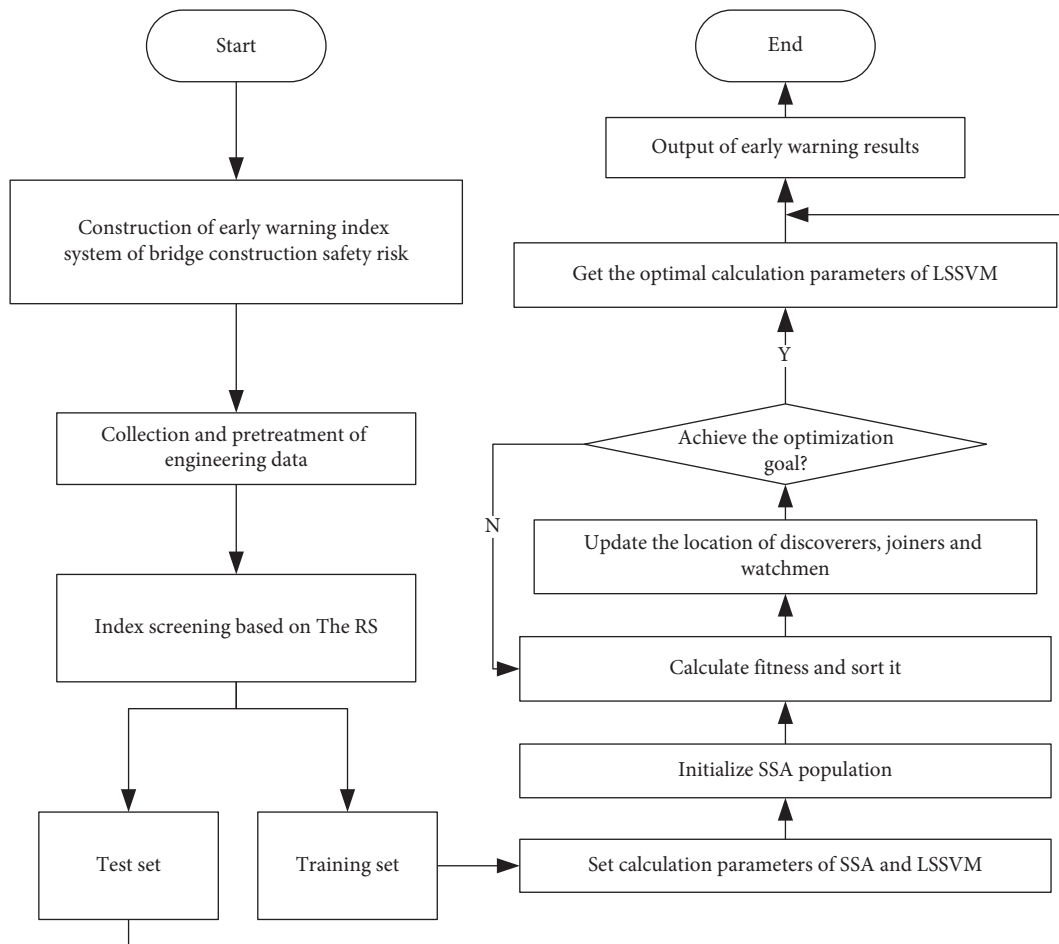


FIGURE 1: Flow chart of the early-warning model proposed in this study.

It should be emphasized that although the three algorithms (RS, SSA, and LSSVM) worked almost independently, these three algorithms belonged to the research framework of bridge construction safety risk early warning. The RS was to solve the problem of many factors affecting early warning and also to simplify the subsequent prediction model. LSSVM optimized by SSA was used to solve the problem of low prediction accuracy. Or it could be considered that both RS and SSA were used to optimize the LSSVM model, in which RS was used to optimize the input variables of LSSVM, and the SSA was used to optimize the optimal calculation parameters of LSSVM.

3. Case Study

3.1. Introduction of the Case Study. The Longlingshan Bridge Project in Wuhan and the Shihe Bridge Project in Xinyang, China were selected as the case studies.

The Longlingshan Bridge Project adopts four two-way lanes, with a standard width of 18.5 m and a total length of 1678.5 m. Its structural form is a prestressed concrete continuous beam. The project is located in Wuhan, Hubei Province, China. There are almost no earthquakes, yet heavy rains often occur. Limestone karst caves are located around the project and are generally 0.3–8.1 m high. The main

construction technology of this pile cap is summarized as follows: measure and support the position of the lofting steel sheet, construct the purlin (which also serves as the guide beam), insert the steel sheet pile to the design elevation, and excavate the foundation pit to pour in cushion concrete. Cranes are used as vertical transportation tools during the pier construction process, while scaffolding is set up as an operation platform. The concrete is commercial concrete, and piers lower (higher) than 11 m are cast by day pump once (twice). The basic construction steps of the concrete box girder are the erection of the supports, the one-time pouring, and overall tensioning. According to the site construction conditions, there are two forms of box girder support: (1) the floor-type bracket with full buckle and (2) the combined bracket (smaller steel pipe bracket for the door opening buckle bracket).

The Shihe Bridge Project in Xinyang is located in Xinyang City, Henan Province, China, with a total length of 203 m. It is a typical thrust concrete-filled steel tube arch bridge with a deck width of 37.5 m and six lanes in both directions. The construction procedures of the concrete-filled steel tubular arch bridge typically include pouring, reinforced, concrete, V-shaped piers and box girders, closing hollow steel tubular arch ribs, installing and tensioning tie bars, pouring concrete into arch ribs, installing and

tensioning suspenders, hoisting bridge deck beams and longitudinal beams, laying prefabricated hollow slabs on the bridge deck, pouring bridge deck concrete, installing anti-collision walls, paving bridge deck asphalt concrete, and so on. The construction of multispan, continuous, concrete-filled, steel, tubular arch bridges generally adopts the construction sequence of flowing water from the side span to the middle span. The subsequent construction process can be carried out once the entire bridge is completed. The advantage of this construction scheme is that the uniform loading between spans is realized to the maximum extent, thus effectively ensuring the arch rib line type and increasing the uniformity of the V-shaped buttress and arch.

3.2. Data Acquisition and Preprocessing

3.2.1. Data Acquisition and Reliability Analysis. The Longlingshan Bridge and Shihe Bridge Projects were constructed in 700 and 360 days, respectively. 1,060 groups of data from each day during the construction phase of these two projects were collected. Incomplete and questionable data sets were eliminated, and a total of 372 data sets were obtained; 300 (80.64%) of which were randomly selected as training sets, and the remaining 72 (19.36%) as test sets. Table 3 presents an example of the raw data.

Obtaining engineering data has always been one of the main difficulties in the engineering field. According to different engineering data sources or data acquisition methods, the 20 secondary indicators were roughly divided into the following three categories.

- (1) The index data of A51 (Disaster frequency) and A52 (Wind load grade) were obtained by consulting local yearbooks or design data.

Taking Long Lingshan Bridge Project in Wuhan as an example, this study illustrated the data acquisition processes of A51 and A52. According to the statistics of Wuhan Yearbook (<http://tjj.wuhan.gov.cn/tjfw/tjnj/>) published by Wuhan Municipal Government, during the period from 2001 to 2020, there were 47 natural disasters in the urban area of Wuhan, so the score of A51 was 2.35, and 2.35 natural disasters occurred every year on average. The data of A52 was the wind forecast data released by Wuhan Meteorological Bureau (<http://hubei.weather.com.cn/wuhan/index.shtml>).

- (2) Data of A11 (Rate of operation violation), A12 (Rate of improper emergency handling), A13 (Acceptance rate of worker technology), A21 (Unqualified rate of mechanical quality), A22 (Failure rate of mechanical installation), A23 (Rate of Mechanical operation error), A24 (Rate of mechanical failure), A31 (Qualified rate of concrete), A32 (Qualified rate of steel), A43 (Rate of technical disclosure), and A44 (Proportion of new construction scheme) were obtained by field investigation or field investigation combined with standard calculation. Taking Long Lingshan Bridge Project in Wuhan as an example,

this study illustrated the data acquisition process of A11 and A31. Project managers randomly checked the operation of workers in daily inspection. If there were 53 unqualified workers' operations in 125 random checks, the score of A11 should be 0.424 ($0.424 = 53/125$). Project managers randomly checked the quality of concrete. If 2453 of the 2500 selected times were qualified, the score of A31 should be 98.12 ($98.12 = 2453/2500 * 100$). The data of other indicators were also calculated according to the daily management data of the project.

- (3) Data of A14 (Safety skills of managers), A33 (Rationality of material stacking), A34 (Sampling inspection of materials), A41 (Rationality of calculation method), A53 (Sustainability of engineering project), and A54 (Social and economic sustainability) were obtained via questionnaires. According to their rich engineering experience, the experts graded the qualitative indicators with reference to Table 2. The average score of 20 experts was taken as the final score of the input variable. To ensure the validity of the expert scoring data, the invited 20 experts had more than 15 years of work experience and were senior engineers. The reliability of the qualitative indicator data is evaluated by determined the Cronbachs' α coefficient (Table 4).

The Cronbachs' α coefficients of all qualitative indicators exceed 0.7, proving the high reliability of the questionnaire survey results [27]. The acquisition methods of other indicator data are based on field statistics, standard calculations, and official statistics; thus, their reliability is well guaranteed.

3.2.2. Data Preprocessing and Attribute Intensive. To eliminate the influence of dimensional and data-level differences of early warning indicators on the performance of early-warning models, the data are preprocessed by the normalization methods in equations (9) and (10) for indicators with beneficial type or cost type, respectively:

$$x'_{ik} = \frac{x_{i\max} - x_{ik}}{x_{i\max} - x_{i\min}}, \quad (9)$$

$$x'_{ik} = \frac{x_{ik} - x_{i\min}}{x_{i\max} - x_{i\min}}, \quad (10)$$

where x_{ik} and x'_{ik} are the k -th indicator value of the i -th indicator and its normalized value, and $x_{i\min}$ and $x_{i\max}$ are the minimum and maximum values of the i -th indicator value, respectively.

Linear correlations may be observed among the 20 secondary indicators. These redundant or interfered secondary indicators are likely to affect the prediction accuracy of the early-warning model. Therefore, this study adopted an attribute reduction algorithm based on the RS. More specifically, redundant irrelevant or unimportant attributes were deleted, and warning indicators that were sensitive to the water state of bridge construction safety risks were identified.

TABLE 3: Original data of the case studies.

Secondary indicator	1	2	3	4	5	6	...	371	372
A11	0.424	1.223	0.872	0.313	2.342	4.873	...	0.291	0.742
A12	9.583	2.135	4.293	3.421	5.231	2.123	...	0.234	1.882
A13	93.21	90.31	85.74	89.07	79.42	95.25	...	76.48	89.25
A14	86.25	72.55	83.85	94.25	69.35	86.65	...	79.95	68.55
A21	1.451	0.832	2.425	5.317	3.427	2.512	...	0.982	0.428
A22	12.48	10.42	0.342	4.124	0.523	16.25	...	3.411	7.234
A23	25.25	18.14	9.413	17.94	24.31	4.510	...	7.223	5.861
A24	4.112	9.379	2.345	0.512	4.294	2.512	...	0.316	3.184
A31	98.12	97.52	98.65	99.05	96.59	94.50	...	98.52	99.50
A32	99.52	98.95	99.74	99.39	99.47	97.52	...	98.83	99.05
A33	84.75	74.45	86.25	69.15	48.55	86.05	...	79.55	73.45
A34	38.55	75.25	65.85	42.45	65.25	62.85	...	58.25	79.45
A41	67.55	74.25	85.65	75.35	79.35	78.75	...	84.75	78.35
A42	85.25	79.35	95.25	72.15	85.45	69.25	...	78.45	83.65
A43	98.41	99.58	95.25	96.23	97.14	95.42	...	99.74	98.68
A44	25	30	30	45	25	40	...	35	20
A51	2.35	2.35	2.35	2.35	2.35	2.520	...	2.520	2.520
A52	5	7	7	5	4	9	...	4	6
A53	68.35	84.25	60.55	75.35	82.45	48.95	...	68.45	84.25
A54	75.25	90.45	84.55	78.05	68.75	25.45	...	70.25	89.35
Warning degree	I	II	I	II	III	II	...	II	II

TABLE 4: Reliability analysis of the qualitative indicators.

Secondary indicator	A14	A33	A34	A41
Cronbachs' α	0.704	0.823	0.734	0.785
Result	Pass	Pass	Pass	Pass
Secondary indicator	A42	A53	A54	-
Cronbachs' α	0.824	0.864	0.723	-
Result	Pass	Pass	Pass	-

The preprocessed 372 data sets were imported into Rosetta, and the attribute reduction was performed via Johnson's algorithm. Table 5 reports the attribute reduction results, namely, the most important indicators based on the RS analysis.

The eight secondary indicators in Table 5 were also identified as the most important indicators affecting the construction safety risks in previous research [24, 25]. This acts as a validation of our results.

As the RS is a data processing tool, the final RS-based screening of the indicator system may differ for different engineering data sets. Thus, the final early warning indicator system in Table 5 is only applicable to the two engineering cases selected in this study.

3.3. Early Warning of Bridge Construction Safety Risks

3.3.1. Optimization of LSSVM Parameters Based on the SSA. The SSA specifications are as follows [22, 23]: population size of 100, maximum iteration number of 200, safety threshold of 0.7, discoverers account equal to 30% of the population size, the maximum permissible error is 0.00001, and 10 sparrows aware of danger. Calculations were performed in Matlab 2016a (MathWorks) on a computer with the Intel i7 processor configured at 3.40 GHz and a memory of 31 GB. In the LSSVM model, the range of regularization parameters

was limited to [0.01, 1000], and the range of the kernel function width coefficient was limited to [0.001,10000].

In the iterative optimization process of the SSA, the average value of four warning errors was selected as the fitness function of the SSA. The lower the average value of early warning errors, the lower the function value of fitness function and the better parameter combination.

In order to optimize the LSSVM model parameters for the early warning of the bridge construction safety risks, 170 sets of preprocessed training data were input into the calculation program in Matlab. Figure 2 depicts the adaptive function curve of the SSA. In the enlarged view of Figure 2, the filled rectangular points represented the points with the minimal fitness function.

The fitness function of the SSA is observed to decline rapidly from 44% to approximately 3% at the initial stage. Table 6 tracks the optimization calculation process of the SSA algorithm.

The SSA is observed to reach convergence in the 51th generation, converging to 3.657321%. Figure 2 and Table 6 reveal the ability of the SSA to effectively optimize the LSSVM model parameters in the 51th generation. Following the optimization, the optimal parameter combination is determined with kernel function and penalty factor parameters equal to 13.42 and 3.24, respectively.

3.3.2. Early Warning Calculations. The kernel function and penalty factor parameters (13.42 and 3.24, respectively) were input into the LSSVM model to construct the optimized early-warning model. Table 7 reports the results of the 72 preprocessed sets of test data imported into the optimized LSSVM model.

The parameters results reveal the high calculation accuracy of the proposed prediction model, with a very low misjudgement ratio for different warning degrees. The

TABLE 5: Final early warning indicator system based on the RS.

Primary indicators	Secondary indicators
A1: Men	A11: Rate of operation violation A14: Safety skills of managers
A2: Machines	A21: Unqualified rate of mechanical quality A24: Rate of mechanical failure
A3: Materials	A31: Qualified rate of concrete A32: Qualified rate of steel
A4: Methods	A44: Proportion of new construction scheme
A5: Environment	A52: Wind load grade

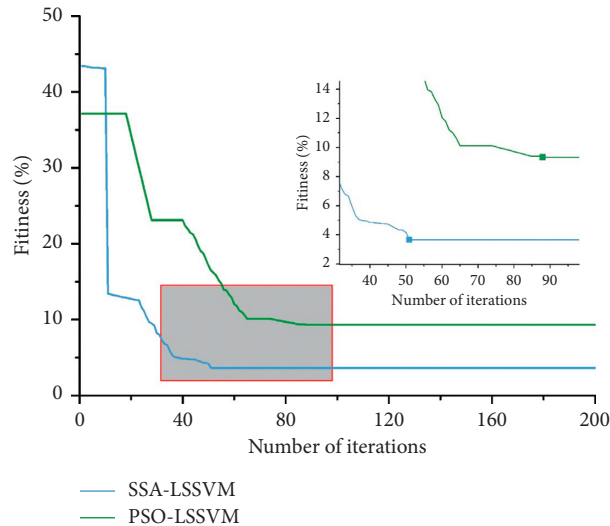


FIGURE 2: Adaptive function curve of different meta-heuristic algorithms.

TABLE 6: Detailed optimization process of the SSA.

Iterations	Fitness ($n-1$)	Fitness (n)	Fitness (n) - Fitness ($n-1$)
49	4.336809	4.332868	0.003941001 > 0.00001
50	4.332868	4.166309	0.166559012 > 0.00001
51	4.166309	3.657321	0.508988 > 0.00001
52	3.657321	3.657321	0 < 0.00001
200	3.657321	3.657321	0 < 0.00001

highest proportion of prediction errors occurred in No (I), which fully met the needs of the engineering practices. For the moderate (III) and severe (IV) cases, two important warning degrees, the proposed prediction model was completely correct. Thus, the proposed model has strong potential in engineering applications.

The proposed model is based on data; thus, the statistical analysis of the prediction results is required, and the calculations were repeated 1,000 times. Table 8 reports the average of the 1,000 calculations.

The proposed prediction model exhibits a high calculation accuracy for the 1,000 repeated calculations, with extremely low misjudgment ratios for different alarm levels. The highest proportion of prediction errors equals just 1.97%, occurring for no (I). This low error rate fully meets the needs of engineering practices. The high calculation accuracies for the moderate (III) and severe (IV) levels also

fully meet the needs of engineering practices. These results further demonstrate the high accuracy of the proposed model and its corresponding potential applicability in the field of engineering.

To further analyse the calculation accuracy of different prediction methods, this study calculated the average value of prediction errors. The calculation results showed that the average prediction error of the prediction model proposed in this study was only 1.025%, which was the lowest among all the results.

Computational time and stability are additional key indicators of the computational ability of prediction models. Table 9 reports the average calculation time of 1,000 calculations and the standard deviation of the prediction results.

The running time of our prediction model is observed to be just 3.241 s. Furthermore, the standard deviation of the prediction model results is very low, indicating the high stability of the model.

For this case study, the data structure characteristics of randomly selected training sets may exert a strong influence on the prediction performance of the model. We thus repeated the above calculation 10 times, with the training set randomly selected each time (Table 10).

The difference of the 10 repeated calculations is observed to be minimal, indicating the limited influence of the data structure characteristics from the randomly selected training

TABLE 7: Results of the early-warning model proposed in this study.

Warning degree	Actual warning degree	The model proposed in this study	
		Predicted warning degree	Rate of prediction errors (%)
I	27	28	3.70
II	34	33	2.94
III	8	8	0.00
IV	3	3	0.00

TABLE 8: Average value of the 1000 early warning results of different models.

Warning degree	Actual	Predicted	Rate of errors (%)	Predicted	Rate of errors (%)	Predicted	Rate of errors (%)
The proposed model							
I	27	27.531	1.97	25.024	7.32	16.952	37.2
II	34	33.524	1.40	36.084	6.13	42.084	23.8
III	8	7.944	0.70	7.840	2.00	8.716	8.95
IV	3	3.001	0.03	3.052	1.73	4.248	41.6
SSA-BP							
I	27	36.723	36.0	21.414	20.7	34.482	33.5
II	34	26.521	22.0	36.498	7.35	26.567	21.9
III	8	5.667	29.2	10.036	25.45	7.011	12.4
IV	3	3.089	29.7	4.052	49.2	3.940	3.13
LSSVM							
The proposed model without RS							
SSA-BPNN							
PSO-LSSVM							
PSO-BP							

TABLE 9: Average calculation time and standard deviation of 1000 calculations.

Model	The proposed model	The proposed model without RS	LSSVM	SSA-BPNN	PSO-LSSVM	PSO-BPNN
Average calculation time (s)	3.241	3.826	0.937	4.856	4.642	5.752
Standard deviation of I	0.00305	0.00524	0.02221	0.00552	0.01245	0.01046
Standard deviation of II	0.00731	0.00793	0.02597	0.00723	0.02213	0.01475
Standard deviation of III	0.00645	0.00830	0.02424	0.01420	0.04174	0.09422
Standard deviation of IV	0.01023	0.01384	0.04552	0.01525	0.01463	0.02425

TABLE 10: Prediction accuracy of repeated randomly selected training sets.

Warning degree	Rate of errors (%)									
	1st	2nd	3rd	4th	5th	6th	7th	8th	9th	10th
I	1.97	1.93	1.96	2.12	1.92	1.90	2.01	1.99	1.93	1.97
II	1.40	1.39	1.39	1.41	1.39	1.41	1.40	1.38	1.40	1.30
III	0.70	0.73	0.69	0.71	0.69	0.72	0.68	0.71	0.70	0.68
IV	0.03	0.04	0.03	0.04	0.02	0.03	0.05	0.03	0.03	0.03

sets of the case study on the model prediction performance. The maximum prediction error is 2.12%, fully meeting the needs of engineering practices.

4. Discussion

4.1. Comparative Analysis of the Attribute Intensive Calculation Results. Correlation analysis [28] and the mean impact value (MIV) [29] are commonly employed as index screening tools. For the former, the Pearson correlation coefficient (r) is typically used to investigate the linear correlation between different variables [28]:

$$r = \frac{\sum_{i=1}^n (x_i - \bar{x})(y_i - \bar{y})}{\sqrt{\sum_{i=1}^n (x_i - \bar{x})^2 (y_i - \bar{y})^2}} \quad (11)$$

where x_i and y_i are the values of the first and second variables, respectively, and \bar{x} and \bar{y} are the average values of the first and second variables, respectively.

The absolute value of r can effectively characterize the linear correlation between variables: $r > 0.8$ denotes a strong linear correlation between two variables, $r > 0.7$ denotes a moderate correlation, and $r < 0.7$ denotes almost no linear correlation. Moreover, $r > 0$ ($r < 0.8$) represents a positive (negative) correlation.

The normalized engineering data in Table 3 was taken to calculate the Pearson correlation coefficient between an index and the warning degree on equation (11). This also denotes the correlation coefficient between input and output variables. Table 11 reports the results, where bold values indicate absolute values greater than 0.7.

Alarm degrees A12, A13, A23, A32, A33, A41, A44, and A54 are observed to correlate strongly with the output index. Therefore, the remaining 12 indicators were selected as the key risk early warning indicators and input into the SSA-LSSVM model for subsequent calculations. Table 12 reports the results of the calculations repeated 1,000 times.

TABLE 11: Pearson correlation coefficient between an index and the alarming degree.

Secondary indicator Correlation coefficient	A11 0.3144	A12 0.7812	A13 - 0.8250	A14 0.2275
Secondary indicator Correlation coefficient	A21 0.7424	A22 0.5384	A23 0.8462	A24 -0.6380
Secondary indicator Correlation coefficient	A31 0.3127	A32 - 0.7263	A33 0.7422	A34 -0.0125
Secondary indicator Correlation coefficient	A41 0.7423	A42 -0.4352	A43 -0.2354	A44 0.7421
Secondary indicator Correlation coefficient	A51 0.3261	A52 0.2742	A53 -0.4630	A54 0.9031

TABLE 12: Results determined from 1,000 repeated calculations of different variable screening methods.

Warning degree	The proposed model		The SSA-LSSVM with the correlation analysis		The SSA-LSSVM with MIV	
	Predicted	Rate of errors (%)	Predicted	Rate of errors (%)	Predicted	Rate of errors (%)
I	27.531	1.97	29.411	8.91	26.242	2.81
II	33.524	1.40	39.036	14.8	34.654	1.92
III	7.944	0.70	10.381	29.8	8.091	1.14
IV	3.001	0.03	3.172	5.73	3.013	0.43

Following the method of [29], the MIV method was employed to screen out the key risk indicator and input them into the SSA-LSSVM model for subsequent calculations (Table 12).

Compared with the correlation analysis and the MIV method, this study adopted RS to screen key risk indicators and obtained the best calculation accuracy. These results prove the advancement of the RS presented in this study.

4.2. Comparative Analysis of Different Early-Warning Models.

To demonstrate the advancement of the early-warning model proposed in this study, a comparative analysis was performed based on two factors: the advancement of the optimization algorithm and the advancement of the nonlinear modelling method. The proposed model without the RS, the LSSVM, the SSA-BPNN, the PSO-LSSVM, and the PSO-BPNN were systematically ran. Tables 9 and 10 report the results, respectively. Based on the parameter setting method of [10], the sigmoid activation function was adopted for the BPNN, with a minimum convergence error of 10^{-5} . For the PSO algorithm, following the parameter setting method of references [15, 30], the maximum iteration number was set as 200, the weight factor varied linearly from 0.4 to 0.9, and the acceleration constants C1 and C2 were both equal to 2.

4.2.1. Advancement of the Selected Optimization Algorithm.

Figure 2 reveals that the fitness function of the SSA converged to approximately 3.5% in the 60–80 generation during the LSSVM parameter search, whereas the PSO fitness function converged in 110–120 generations. Thus, the SSA converged faster than the PSO, which is consistent with results from the previous literature [21, 22].

Table 9 demonstrates the running time of the proposed prediction model to be 1.401 s lower than that of the PSO-LSSVM. More specifically, for the typical nonlinear

optimization problem of optimizing the LSSVM parameters, the SSA exhibited a better global fast retrieval ability than the PSO. Comparing the average running times of the PSO-BPNN and SSA-BPNN, the SSA algorithm revealed to save 0.896 s. The SSA exhibited an improved global fast retrieval ability in searching for the optimal initial threshold and initializing the BPNN.

These results prove the superior ability of the SSA algorithm for global fast retrievals.

4.2.2. Advancement of the Selected Nonlinear Modelling Method.

Table 9 demonstrates the running time of the proposed prediction model to be 1.625 s, 1.401 s, and 2.511 s lower than that of SSA-BPNN, PSO-LSSVM, and PSO-BPNN, respectively. This highlights the global fast retrieval ability of the SSA and the simple structure of the LSSVM.

The running time of the proposed prediction model is clearly superior to that without the RS. This can be attributed to the removed redundant attributes of the original data from the attribute reduction of the RS. The reduced minimum conditional attribute set was consequently more representative and reduced the complexity of the LSSVM model. Note that the LSSVM exhibited the shortest running time because it does not involve iterative optimization calculations.

The LSSVM exhibited an improved calculation accuracy and stability compared with the BPNN (Tables 9 and 10). This is linked to the distinct calculation principles of the two methods. The LSSVM class prediction method determines the segmentation hyperplane with less support vectors, whereas the neural network-based prediction method follows the law of large numbers in nonlinear modelling. More specifically, the more training data samples, the higher the accuracy of the prediction results, with sample sets often required to be more than ten times the number of input variables. Therefore, under sufficient historical data and

large research samples, the neural network-based prediction method has an advantage over LSSVM prediction methods in terms of nonlinear modelling ability and computational performance. However, for insufficient historical data and small research samples, the nonlinear modelling ability and computational performance of the LSSVM prediction methods are significantly superior to those based on artificial neural networks.

5. Conclusions

In the current study, an early-warning model of bridge engineering construction safety risk based on the RS, SSA, and LSSVM was constructed. The RS was used to effectively solve the problem of multiple risk early warning factors, whereas the LSSVM model optimized via the SSA overcame the low precision of traditional early warning methods. The construction safety risks of two typical bridge projects in China were predicted. Results demonstrated the warning error of the proposed warning model for bridge construction safety risk to be low for different warning levels. In addition, the number of misjudged samples was less than or equal to one. Compared with the LSSVM, SSA-BP, PSO-LSSVM, PSO-BP, and other models, the proposed model exhibits a fast calculation speed, high early warning accuracy, and strong robustness.

In addition, by employing 4M1E, the early warning index system of bridge construction safety risk was constructed, including 20 secondary indexes. Based on the engineering data of the research object, the index system was screened by the RS, removing the redundant or unrealistic attributes of the original data and effectively improving the early warning accuracy of the LSSVM model. For the prestressed concrete continuous beam project and concrete-filled steel tubular arch bridge selected in this study, the operation violation rate, management safety skills, unqualified rate of mechanical quality, mechanical failure rate, concrete qualified rate, steel qualified rate, promotion of new construction schemes, and the wind load grade were the most important risk warning indicators.

Despite the substantial advancement made by this study in the research field, our proposed model faces several limitations. For example, just two case studies (the Longlingshan Bridge Project in Wuhan and the Shihe Bridge Project in Xinyang) were selected. However, bridges can take the form of numerous structural types and construction techniques. Further research will apply the research results of this study to additional bridges with different structural types or construction techniques. Moreover, the expert experience method, which is typically subjective, was adopted to determine the warning limit of early warnings for bridge construction safety risk. Although the conclusion of the case study was consistent with the actual situation, the determination of the early warning threshold requires further quantification. Lastly, the classification accuracy and performance of the LSSVM depend on the calibration of its parameters. Future work will focus on exploring effective multiobjective optimization techniques to optimize the LSSVM parameter combination and improve its prediction performance.

Abbreviations

AHP:	Analytic hierarchy process
ANNs:	Artificial neural networks
BPNN:	Back propagation neural network
GA:	Genetic algorithm
GM:	Grey model
LSSVM:	Least squares support vector machine
MIV:	Mean impact value
PSO:	Particle swarm optimization
RS:	Rough set
SSA:	Sparrow search algorithm
SVM:	Support vector machine
4M1E:	Men, machines, materials, methods and environment.

Data Availability

The case analysis data used to support the findings of this study are available from the corresponding author upon request.

Conflicts of Interest

The authors declare that there are no conflicts of interest regarding the publication of this paper.

Acknowledgments

This study was supported by the Science and Technology Project of Wuhan Urban and Rural Construction Bureau, China (201943).

References

- [1] S.-y. Song, J. Guo, Q.-k. Su, and G. Liu, "Technical challenges in the construction of bridge-tunnel sea-crossing projects in China," *Journal of Zhejiang University - Science*, vol. 21, no. 7, pp. 509–513, 2020.
- [2] A. P. C. Chan, Y. Yang, and A. Darko, "Construction accidents in a large-scale public infrastructure project: severity and prevention," *Journal of Construction Engineering and Management*, vol. 144, no. 10, Article ID 05018010, 2018.
- [3] S. S. Lin, S. L. Shen, A. Zhou, and Y. S. Xu, "Risk assessment and management of excavation system based on fuzzy set theory and machine learning methods," *Automation in Construction*, vol. 122, Article ID 103490, 2021.
- [4] C. Yan, L. Wang, W. Liu, and M. Qi, "Financial early warning of non-life insurance company based on RBF neural network optimized by genetic algorithm," *Concurrency and Computation: Practice and Experience*, vol. 30, no. 23, e4343 pages, 2018.
- [5] Y. Zhang, "Food safety risk intelligence early warning based on support vector machine," *Journal of Intelligent and Fuzzy Systems*, vol. 38, no. 6, pp. 6957–6969, 2020.
- [6] Z. Y. Cheng, Y. L. Li, and B. Wu, "Early warning method and model of inland ship collision risk based on coordinated collision-avoidance actions," *Journal of Advanced Transportation*, vol. 2020, Article ID 5271794, 14 pages, 2020.
- [7] Q. Zhang, J. Zhang, C. Wang, L. Cui, and D. Yan, "Risk early warning of maize drought disaster in Northwestern Liaoning

- Province, China,” *Natural Hazards*, vol. 72, no. 2, pp. 701–710, 2014.
- [8] M. Sattelle, M. Krautblatter, M. Brundl, and D. Straub, “Forecasting rock slope failure: how reliable and effective are warning systems?” *Landslides*, vol. 13, no. 4, pp. 37–750, 2016.
- [9] Q. Ding, “Risk early warning management and intelligent real-time system of financial enterprises based on fuzzy theory,” *Journal of Intelligent and Fuzzy Systems*, vol. 40, no. 4, pp. 6017–6027, 2021.
- [10] X. Yan, X. W. Deng, and S. H. Sun, “Analysis and simulation of the early warning model for human resource management risk based on the BP Neural Network,” *Complexity*, vol. 2020, Article ID 8838468, 11 pages, 2020.
- [11] L. N. Wang, R. F. Mou, X. Z. Yu, and R. Yang, “The design and implementation of security risk warning and prevention system for railway service system,” *Agro Food Industry Hi-Tech*, vol. 28, no. 3, pp. 264–267, 2017.
- [12] J. Z. Chen and H. Z. Zhang, “Study on early warning of cultural and creative crowdfunding defaults based on logistic - SVM,” *Journal of Systems Science and Mathematical Sciences*, vol. 40, no. 12, pp. 2320–2331, 2020.
- [13] Y. P. Zhao, J. J. Wang, X. Y. Li, G. J. Peng, and Z. Yang, “Extended least squares support vector machine with applications to fault diagnosis of aircraft engine,” *ISA Transactions*, vol. 97, pp. 189–201, 2020.
- [14] H. Ahmadi, H. Ahmadi, and A. Baghban, “Modeling vaporization enthalpy of pure hydrocarbons and petroleum fractions using LSSVM approach,” *Energy Sources, Part A: Recovery, Utilization, and Environmental Effects*, vol. 42, no. 5, pp. 569–576, 2020.
- [15] C. B. Yu, Z. W. Xi, Y. L. Lu, and K. Tao, “K/S value prediction of cotton fabric using PSO-LSSVM,” *Textile Research Journal*, vol. 90, no. 23–24, pp. 2581–2591, 2020.
- [16] H. Cao, “The utilization of rough set theory and data reduction based on artificial intelligence in recommendation system,” *Soft Computing*, vol. 25, no. 3, pp. 2153–2164, 2020.
- [17] X. Zhu, S.-q. Ma, Q. Xu, and W.-d. Liu, “A WD-GA-LSSVM model for rainfall-triggered landslide displacement prediction,” *Journal of Mountain Science*, vol. 15, no. 1, pp. 156–166, 2018.
- [18] W. Deng, S. F. Shang, X. Cai, and H. Zhao, “Quantum differential evolution with cooperative coevolution framework and hybrid mutation strategy for large scale optimization,” *Knowledge-Based Systems*, vol. 224, Article ID 107080, 2021.
- [19] X. H. Xue, “Evaluation of concrete compressive strength based on an improved PSO-LSSVM model,” *Computers and Concrete*, vol. 21, no. 5, pp. 505–511, 2018.
- [20] J. Xue and B. Shen, “A novel swarm intelligence optimization approach: sparrow search algorithm,” *Systems Science & Control Engineering*, vol. 8, no. 1, pp. 22–34, 2020.
- [21] G. B. Li, T. Y. Hu, and D. W. Bai, “BP neural network improved by sparrow search algorithm in predicting debonding strain of FRP-Strengthened RC beams,” *Advances in Civil Engineering*, vol. 2021, Article ID 9979028, 13 pages, 2021.
- [22] B. Liu and D. Rodriguez, “Renewable energy systems optimization by a new multi-objective optimization technique: a residential building,” *Journal of Building Engineering*, vol. 35, Article ID 102094, 2021.
- [23] T. Wumaier, C. Xu, H. Y. Guo, J. Zhijie, and Z. Huajian, “Fault diagnosis of wind turbines based on a support vector machine optimized by the sparrow search algorithm,” *IEEE Access*, vol. 9, pp. 69307–69315, 2021.
- [24] H. Zhou, Y. H. Zhao, Q. Shen, Y. Liu, and H. Cai, “Risk assessment and management via multi-source information fusion for undersea tunnel construction,” *Automation in Construction*, vol. 111, Article ID 103050, 2020.
- [25] P. Liu, M. C. Xie, J. Bian, and H. Li, “A hybrid PSO-SVM model based on safety risk prediction for the design process in metro station construction,” *International Journal of Environmental Research and Public Health*, vol. 17, no. 5, 1714 pages, 2020.
- [26] L. Y. Ding and C. Zhou, “Development of web-based system for safety risk early warning in urban metro construction,” *Automation in Construction*, vol. 34, pp. 45–55, 2013.
- [27] L. Su and S. Peng, “Metallogenic correlations for the Fe-Nb-ree mineralization in the west mine of the bayan obo deposit, inner Mongolia, China,” *Acta Geologica Sinica - English Edition*, vol. 92, no. 2, pp. 614–626, 2018.
- [28] H. Wu and J. W. Wang, “A method for prediction of waterlogging economic losses in a subway station project,” *Mathematics*, vol. 9, no. 12, p. 1421, 2021.
- [29] M. A. Bujang, E. D. Omar, E. D. Omar, and N. A. Baharum, “A review on sample size determination for Cronbach’s Alpha test: a simple guide for researchers,” *Malaysian Journal of Medical Sciences*, vol. 25, no. 6, pp. 85–99, 2018.
- [30] W. Deng, J. Xu, H. Zhao, and X. Z. Gao, “A novel gate resource allocation method using improved PSO-based QEA,” *IEEE Transactions on Intelligent Transportation Systems*, 2020.